Doctoral Dissertation

Studies on Unique Redox Systems Based on Multiply Aligned *Para*-Quinodimethane Units

（*p*-キノジメタンの集積化を基軸とした
特異なレドックス応答系に関する研究）

Takashi HARIMOTO

Laboratory of Organic Chemistry I
Graduate School of Chemical Sciences and Engineering
Hokkaido University

2024

Table of Contents

Chapter 1.

General Introduction

1-1. Redox-Active π-Conjugated Systems

Over the past couple of decades, various stimuli-responsive organic molecules have been developed as a result of remarkable advances in synthetic and material sciences (Figure 1-1),[1,2] and these molecules are attracting attention for their potential application in optoelectronic devices or medical materials.[3-8] Such stimuli-responsive molecules change their properties in response to changes in physical stimuli such as heat, light, and electric potential, or to a change in the chemical environment such as in pH or concentration. Therefore, these molecules function as nano-actuators that can change their form in response to external input. Electrical stimulation is particularly suitable for controlling the physical properties of a specific molecule because electrons can be used for precise manipulation and target selectivity at the nano-level.[9,10] In this regard, various redox-active species that respond to electric potential have been developed. Since the precise control of the redox properties is essential for achieving the high performance of electronic devices, switching behavior as well as the characteristics such as crystal structure, charge distribution, and spin density of redox-active species have been studied for a long time.

In 1965, Gomes *et al.* achieved the structural determination of the ClO_4^- salt of triphenylmethylium by a single-crystal X-ray structure analysis.[11] This was the first direct observation of the structure of a π-conjugated carbocation. Since then, the physical properties of cations based on aromatic hydrocarbons such as naphthalene, fluoranthene and perylene have been actively investigated by experimental and theoretical approaches,[12-14] and their crystal structures have been successfully determined.[15-20] Since it is difficult to stabilize such charged species without heteroatoms, the development of pure hydrocarbon-based redox systems is challenging from the viewpoint of the stability of cationic (anionic) species. Therefore, the successful isolation of charged species composed of pure hydrocarbons and elucidation of their intrinsic redox properties have led to significant advances in the field of redox chemistry (Figure 1-2).[21-25]

On the other hand, the incorporation of heteroatoms, for example, nitrogen and oxygen atoms, into the molecule is an effective method for stabilizing charged species and modulating the electronic properties of organic molecules. In addition, delocalization of a charge over an extended π-conjugation is effective for the synthesis and isolation of charged species as stable entities with carbon-centered ions. Indeed, aromatic hydrocarbons are known to exhibit unique electrochemical and spectroscopic properties based on their π-conjugated systems, and several systems capable of redox interconversion between neutral and cationic (anionic) states have been reported by effectively stabilizing the charged-

state(s) by embedding heteroatoms or introducing heteroatom-substituents into the π-skeleton (Figure 1-3).[26-36] These redox-active molecules have potential applications in electronic equipment such as semiconductors, batteries, and memory devices, due to the high reversibility of electron transfer among two or more redox states.[37-43]

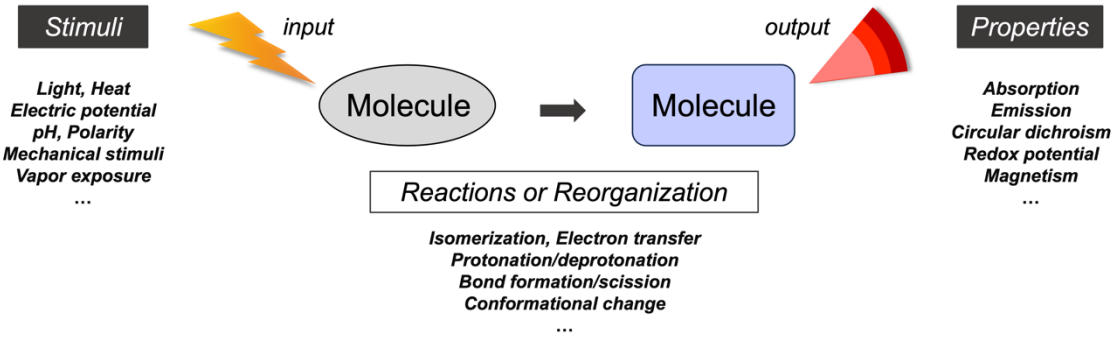

Figure 1-1. Schematic illustration of stimuli-responsive molecules.

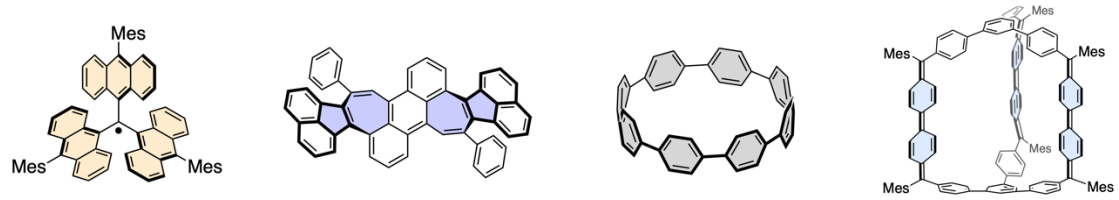

π-Extended trityl radical
Kubo *et al.*[22]

Azulene-based system
Würthner *et al.*[23]

Cycloparaphenylene
Yamago *et al.*[24]

3D-Caged hydrocarbon
Wu *et al.*[25]

Figure 1-2. Examples of previously reported well-designed redox-active π-conjugated hydrocarbons.

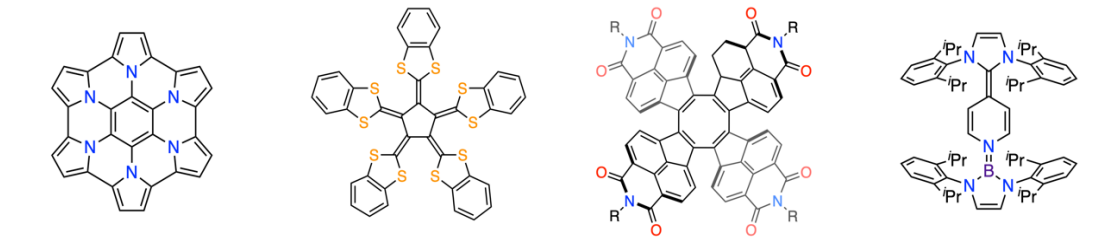

Hexapyrrolohexaazacoronene
Müllen *et al.*[27]

1,3-Dithiol-2-ylidenes
Misaki *et al.*[28]

Tridecacyclene tetraimide
Stępień *et al.*[30]

BN-Doped Thiele's analogue
Aldridge *et al.*[35]

Figure 1-3. Examples of previously reported well-designed redox-active π-conjugated systems with heteroatoms.

1-2. Near-Infrared (NIR) Electrochromic Systems

Electrochromic systems can induce a drastic change in color based on interconversion among differently charged species upon electron transfer (Figure 1-1).[44-47] Representative examples include robust inorganic compounds, such as tungsten oxide (WO_3), which have been used in auto-dimming mirrors, smart windows, and displays.[48-52] On the other hand, due to the advantages of organic molecules in terms of affordability, flexibility, modularity, and biocompatibility, organic and related materials with redox activity have also been actively studied in the past decades.[53-58]

Especially, NIR absorbing properties in the range of 750–2500 nm can be utilized to increase the efficiency of photovoltaic power generation by harvesting NIR light in sunlight.[59-61] In addition, since NIR light shows a superior penetration of biological tissues, they are also expected to be applied to chemotherapy and imaging of deep tissues in vivo.[62-70] Since organic dyes such as cyanines, squaliums and diimmonium, and organometallic complexes such as phthalocyanines and dithiolenes exhibit NIR-absorbing properties due to a narrow energy gap, they have attracted much attention from the viewpoint of various optical applications in electronics and life sciences to date (Figure 1-4).[71-73]

In this context, some organic polymeric materials including covalent organic frameworks (COF) and/or metal-organic frameworks (MOF) have been reported as NIR switchable electrochromic systems (Figure 1-5).[74-79] In these systems, multiple electrophores are needed to be integrated and controlled by the corresponding operating potential to output multiple colors. On the other hand, a well-designed single molecule, which can adopt multiple redox states with different colors, would be very useful, since it could work under a simple setup without the fabrication of multiple layers (Figure 1-6).[80-84] Despite this attractiveness, since stabilization and/or isolation of all redox states (neutral and anionic and/or cationic states) is needed for the modulation of NIR absorption based on reversible redox interconversion, it remains challenging to establish a smart guideline of molecular design for organic dyes that enable ON/OFF switching of NIR absorption, especially when some of the states are open-shell species.

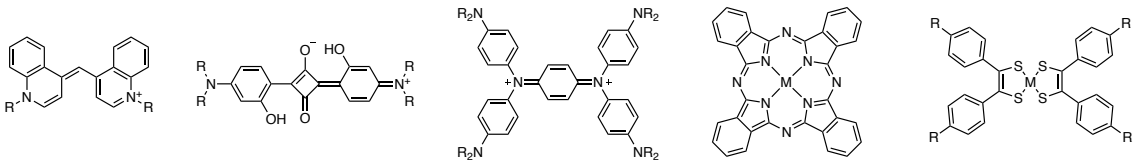

Figure 1-4. Examples of well-studied NIR dyes.

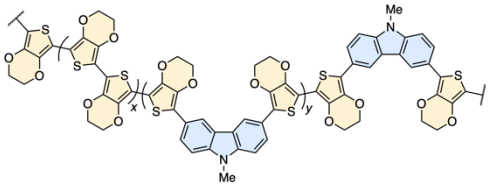

(3,4-Ethylenedioxy-thiophene-based polymer

Reynolds *et al.*[74]

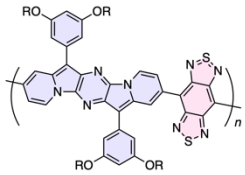

Heterocyclic π-conjugated polymer

Liu *et al.*[75]

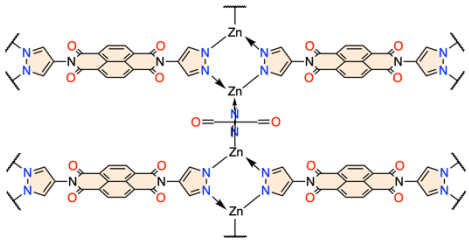

MOF containing naphthalene-diimide-based linkers

Dincă *et al.*[76]

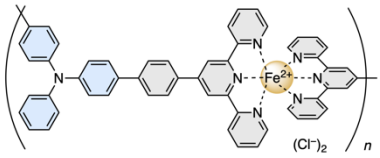

Metallo-supramolecular polymer

Higuchi *et al.*[77]

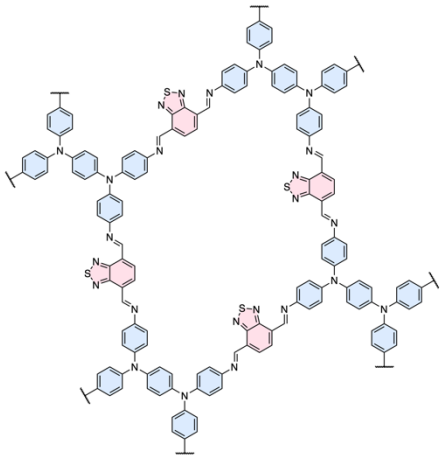

COF based on triphenylamines and benzothiadiazoles

Zhang *et al.*[78]

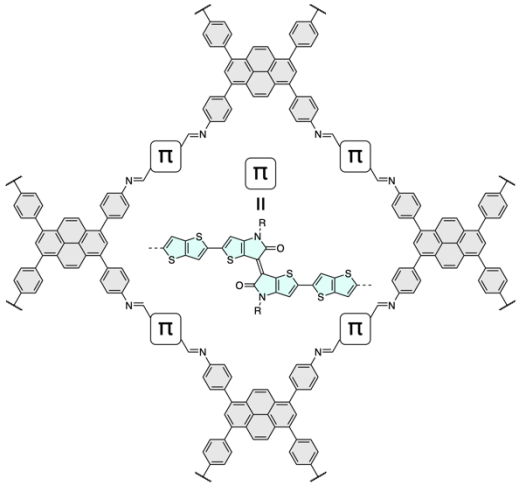

COF based on pyrenes and thienoisoindigos

Bein *et al.*[79]

Figure 1-5. Examples of previously reported organic polymeric NIR electrochromic materials.

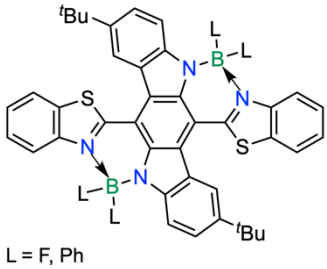

L = F, Ph

Nanographenes with BN coordination

Fang *et al.*[80]

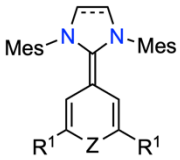

Z = O, N-R²
R¹ = Ar, alkyl, H
R² = Ar, alkyl

Carbene-based systems

Hansmann *et al.*[81-83]

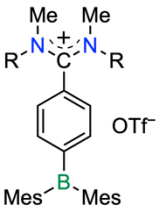

R = Dip, ⁱPr

BN-Doped *p*-phenylenes

Jana *et al.*[84]

Figure 1-6. Examples of previously reported well-designed NIR multi-electrochromic systems.

1-3. *p*-Quinodimethanes

Para-quinodimethane (*p*-QD),[85,86] a representative skeleton in cross-conjugated systems, is known to have a contribution of resonance structure with a planar aromatic sextet ring. Therefore, the *p*-QD skeleton is expected to be useful for the design of advanced π-conjugated systems that can switch photophysical and electrochemical properties based on different electronic structures induced by external stimuli as an input.[87] However, the parent *p*-QDs are highly reactive species that can be easily converted into oligomers/polymers, by C–C bond formation between *α*-carbons. When four phenyl groups are attached to these reactive sites, as in *p*-Ph_4QD, substantial stabilization is achieved to make their observation/isolation possible. While *p*-Ph_4QD (Thiele's hydrocarbon) is more long-lived than the parent *p*-QDs,[88,89] it is still susceptible to light and oxygen due to its expected biradical character (Figure 1-7).

On the other hand, in the case of the 9,10-anthraquinodimethane (AQD) skeleton, which is a dibenzo analogue of *p*-QD, the neutral state is further stabilized thanks to the less contribution of a biradical character based on the local aromaticity of both benzene rings (Figure 1-7). Therefore, organic π-systems with the AQD skeleton have attracted wide attention as synthetic precursors for polycyclic aromatic hydrocarbons (PAHs) such as benzocoronenes,[90,91] as scaffolds for aggregation-induced emission (AIE) dyes[92] and magnetic molecules (Figure 1-8).[93-96]

From the viewpoint of steric and electronic properties of stable AQD skeletons, the author proposes several reasons why π-conjugated systems containing *p*-QD units are suitable for constructing unique redox-responsive systems and controlling their physical properties (Figure 1-9).[97,98] First, electrochemical oxidation of tetraarylated AQD (Ar_4AQD) **1** leads to the formation of two diarylmethylium (Ar_2C^+) chromophores. The Ar_2C^+ chromophores exhibit the strong absorption band in the visible region, which is attributed to the π-π* transition, resulting in the observation of vivid color change in the UV/Vis region.[99-102] Second, electrochemical oxidation of folded Ar_4AQD **1** leads to aromatization of the central six-membered ring, i.e., the formation of the anthracene (=[3]acene) skeleton in the AQD core. As a result, the generated cationic center is kinetically protected by the steric effect of not only the aryl groups but also the [3]acene core in their twisted dicationic states $\mathbf{1}^{2+}$. Importantly, the HOMO of the dication $\mathbf{1}^{2+}$ is mainly located on the [3]acene framework, and the corresponding LUMO is delocalized in two diarylmethylium units. Thus, a low-energy absorption band based on an intramolecular charge transfer (CT) interaction from HOMO to LUMO can also be observed in the NIR region, which allow these redox pairs to exhibit electrochromism in the entire UV/Vis/NIR region. Third, since the neutral and cationic states adopt different conformations with thermodynamically most stable geometries, electrochemical bistability is imparted in these dynamic redox (*dyrex*) systems based on a large difference between the oxidation potential of folded Ar_4AQD **1** and the reduction potential of twisted dication $\mathbf{1}^{2+}$, which leads to

drastic changes in electronic structures and physical properties during redox interconversion. Another feature is that a facile two-electron (2e) transfer process occurs nearly at the same potential in both redox processes due to such a dynamic change in structures. Furthermore, their frontier orbital levels can be easily controlled by the modulation of the aryl groups and central framework, which provides a promising scaffold for fine-tuning of photophysical and electrochemical properties. In particular, by controlling the electronic structure of the neutral state as well as the dicationic state, it would be possible to modulate the physical properties not only by electric potential but also by external stimuli such as heat and light. Based on these attractive points, a study on cationic states of π-electron systems with multiply aligned *p*-QD units and their intrinsic redox properties will lead to the development of unprecedent *dyrex* systems, the frontier orbital levels of which can be precisely controlled by input of external stimuli such as electric potential and heat.

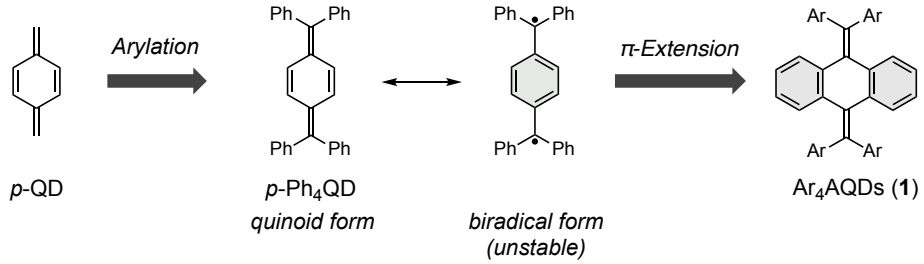

Figure 1-7. *p*-QD skeletons for the design of stable Ar_4AQDs.

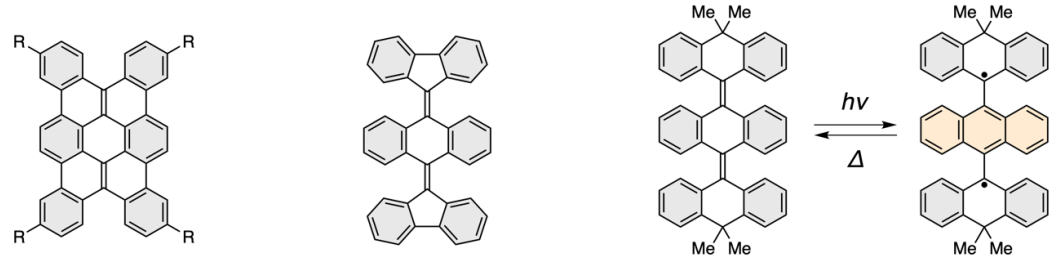

Figure 1-8. Examples of functional aromatic compounds containing the AQD skeleton.

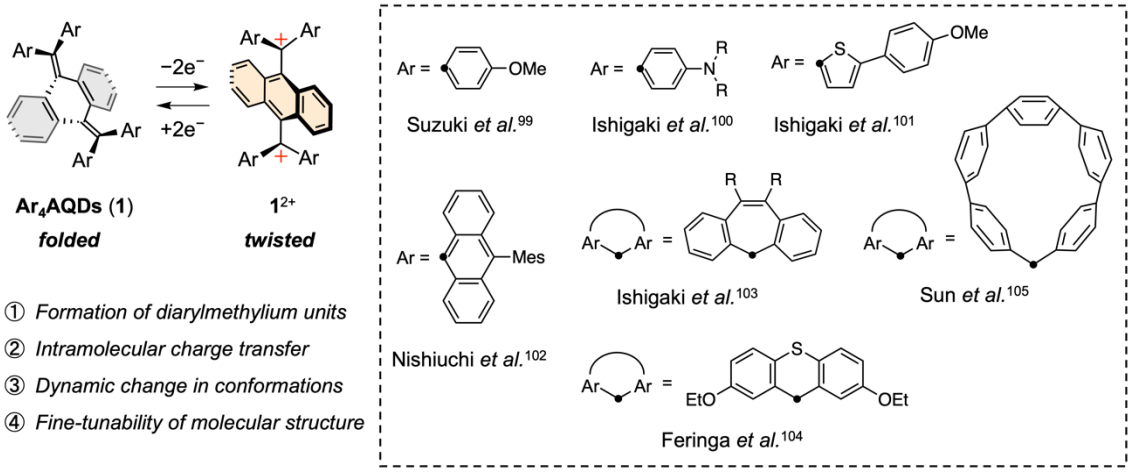

Figure 1-9. Redox scheme of Ar_4AQDs and previously reported redox-active AQDs.

1-4. Contents of This Dissertation

Based on such background, the author reports several studies on unique redox systems with multiply aligned *p*-QD units.

In chapter 2, the author revealed the steric effects of *ortho*-substituents of the aryl groups in AQD derivatives **1** on the electronic and structural properties of the dicationic dyes $\mathbf{1}^{2+}$ (Figure 1-10). The author designed and synthesized a series of anthraquinodimethane derivatives with various substituents introduced into the *ortho*-position(s) of the 4-methoxyphenyl group. X-ray and spectroscopic analyses revealed that their molecular conformations and photophysical properties can be drastically changed by the introduction of the *ortho*-substituents. Thus, the modulation of the steric and electronic effects of the *ortho* substituents on the 4-methoxyphenyl groups was demonstrated to be an effective strategy for fine-tuning the HOMO and LUMO levels for both neutral AQDs and twisted dications, respectively, resulting in the modification of electrochemical and spectroscopic properties. This "*ortho*-substitution strategy" also provides an effective guideline for the control of molecular conformations and *dyrex* properties, which is also discussed in chapter 4.

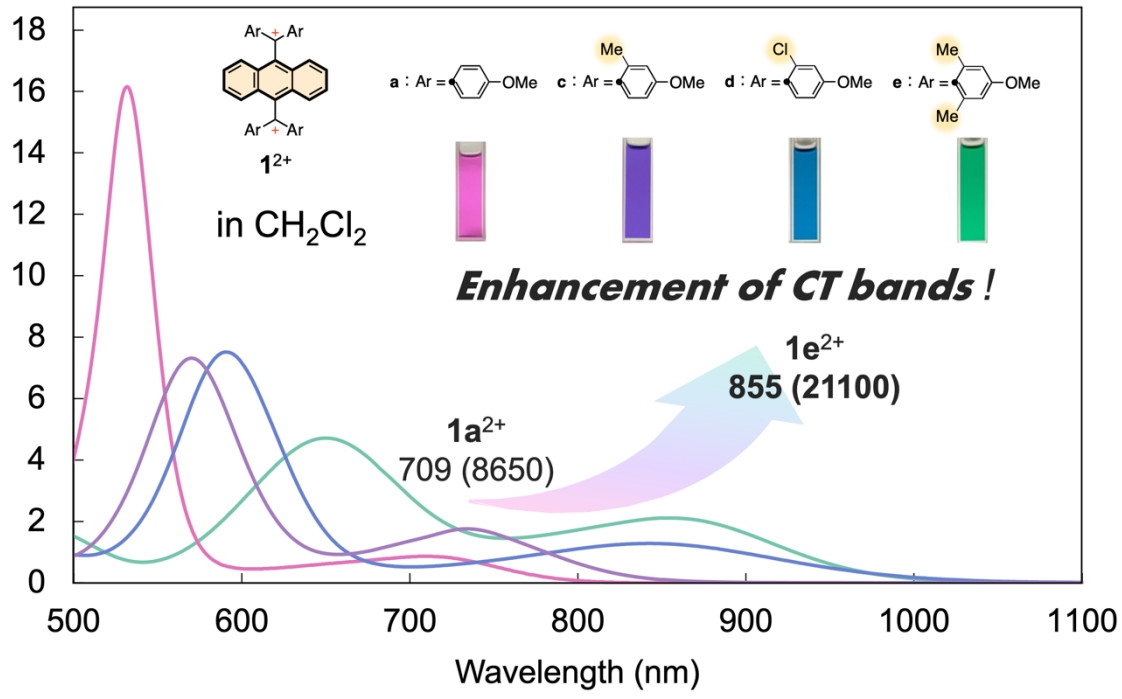

Figure 1-10. *Ortho*-substitution strategy for controlling NIR-absorbing properties of dications $\mathbf{1}^{2+}$.

In chapter 3, the author designed and synthesized octaaryl-substituted bisquinodimethanes (Ar_8BQDs) **2** with a zigzag structure containing doubly aligned *p*-QD units connected by a benzene spacer, and realized to produce tetracationic [5]acenes $\mathbf{2}^{4+}$ with a doubly twisted conformation upon the one-stage four-electron (4e) oxidation (Figure 1-11). When tetracationic [5]acenes $\mathbf{2}^{4+}$ were reduced, two-stage 2e-reduction occurred via dicationic [3]acenes $\mathbf{2}^{2+}$ to the original BQDs **1**. Such hysteretic three-state redox interconversion among them demonstrates perfect control of *n* (1→5→3→1) in the [*n*]acene structure by redox conversion. Moreover, since these cations exhibit significantly red-shifted NIR absorptions (~1400 nm) based on an intramolecular CT interaction, changes in the structure as well as UV/Vis/NIR absorptions can be stepwise controlled by an electrochemical input. All structures were determined by X-ray analyses, and their properties were characterized by spectroscopic and theoretical studies. In addition, the author elucidated the reason why the intermediary dications $\mathbf{2}^{2+}$ adopt a charge-localized geometry with both a *p*-QD unit and [3]acene skeleton by investigating the redox behavior of hybrid AQDs, which consist of two types of aryl groups with different electron-donating abilities on each diarylmethylene unit. Furthermore, the author designed hybrid BQD derivatives with aminophenyl and alkoxyphenyl groups. Thanks to the different oxidation potential in each quinodimethane unit, the apparent 2e-oxidation proceed in a stepwise manner with "double" drastic changes in the structure of the *p*-QD skeleton, the dicationic and tetracationic states were generated and isolated quantitatively due to the negligible steady-state concentration of intermediary open-shell species. When two electrophores with different donating abilities are attached to the BQD skeleton, a dicationic state is allowed to be generated not only by the 2e-reduction of a tetracationic state, but also by the 2e-oxidation of neutral states. Each of these three redox states exhibits distinct absorption properties depending on the combination of chromophores and [*n*]acene structures. Thus, tricolor UV/Vis/NIR electrochromic systems were successfully constructed by the interconversion among neutral (colorless), dicationic (blue, NIR OFF), and tetracationic (violet, NIR ON) states with a "double" structural change ("*double dyrex*" behavior).

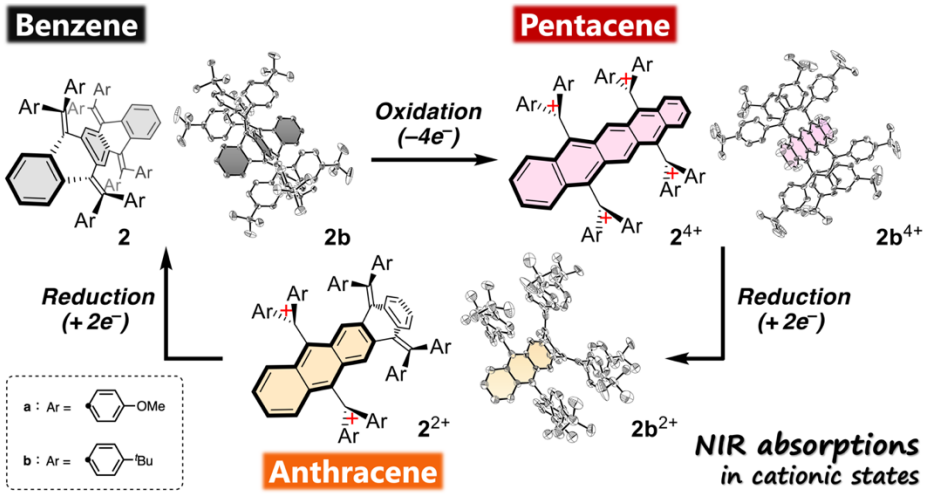

Figure 1-11. Dynamic redox interconversion among three redox states of octaarylated BQDs **2**.

In chapter 4, the author designed and synthesized SS-BQD derivatives **3**, in which the redox-active QD units are connected by a nonplanar dithiin skeleton, which allows steric repulsion and/or electronic interaction between electrophores for specific conformers, such as folded (**F**) and twisted (**T**) forms with different electronic structures. The author envisaged that the flexibility of the dithiin backbone and the change in electronic structures could be utilized to precisely control the redox behavior. Indeed, variable temperature (VT)-electrochemical measurements showed that SS-BQD **3a** with a flexible structure exhibits temperature-dependent redox properties, unlike *ortho*-substituted SS-BQD **3d**, which is less flexible. To clarify the redox mechanism, a dynamic motion of SS-BQDs in solution was investigated in detail. Actually, VT-^{1}H NMR measurements revealed that **3a** undergoes a smooth change in conformation, and thus the metastable **T-F** conformer can be partially generated with an increase in temperature (activation), which undergoes facile apparent 2e-transfer (trigger). In the resulting dication **3a**$^{2+}$, the steric repulsion and interelectrophore interaction cause a facile change in structure from the as-generated **T**$^{2+}$**-F** conformer to the **T**$^{2+}$**-T** conformer (domino), which facilitates the subsequent oxidation (domino) to **3a**$^{4+}$ of the **T**$^{2+}$**-T**$^{2+}$ conformer (Figure 1-12). This is the first successful demonstration of the domino-redox reaction of multi-redox systems consisting of the same kind of electrophores based on a change in the HOMO level due to a drastic change in the molecular conformation.

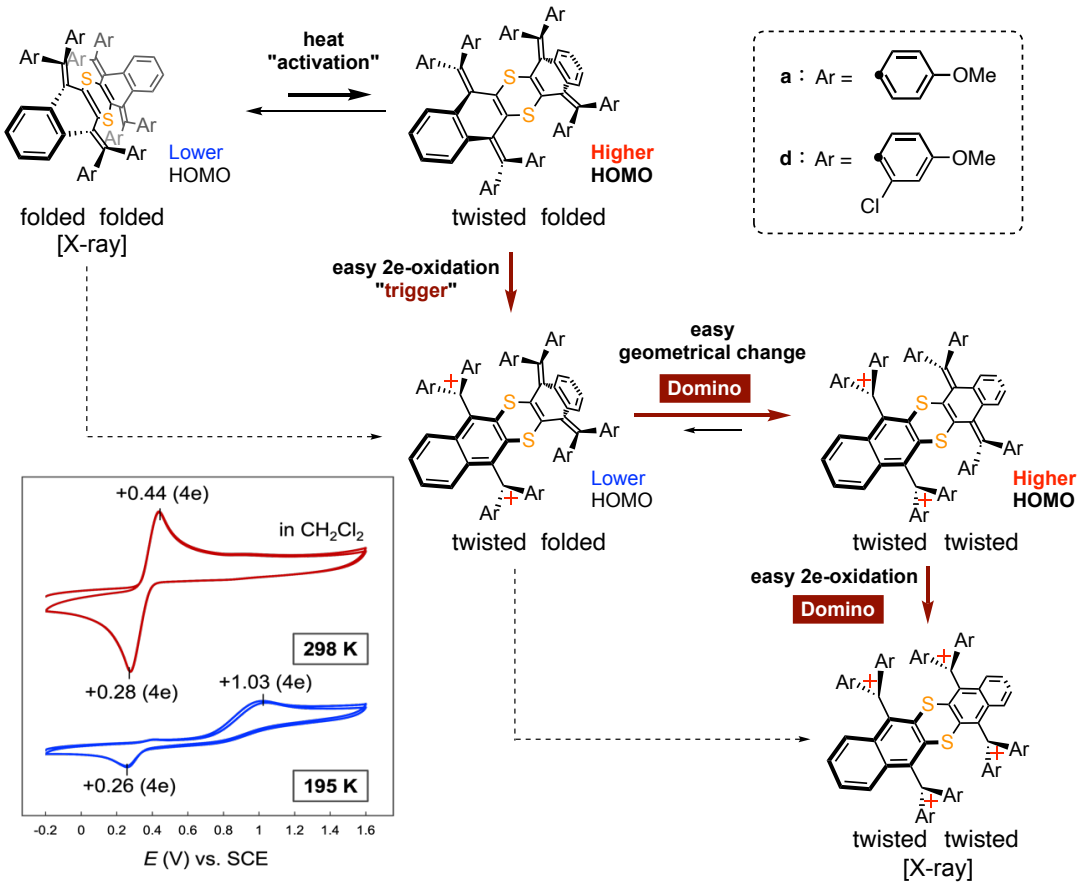

Figure 1-12. SS-BQD **3a** induces domino-redox reaction, unlike *ortho*-substituted SS-BQD **3d**.

1-5. References

[1] M. Wei, Y. Gao, X. Li, M. J. Serpe, *Polym. Chem.* **2017**, *8*, 127–143.
[2] L. Hu, T. Shu, Y. Wan, C. Fang, F. Gao, M. J. Serpe, *Mol. Syst. Des. Eng.* **2021**, *6*, 108–121.
[3] Y. Shirota, *J. Mater. Chem.* **2000**, *10*, 1–25.
[4] T.-P. Nguyen, *Surf. Coat. Technol.* **2011**, *206*, 742–752.
[5] O. Ostroverkhova, *Chem. Rev.* **2016**, *116*, 13279–13412.
[6] S. Park, Y. J. Kang, S. Majd, *Adv. Mater.* **2015**, *27*, 7583–7619.
[7] A. M. Grumezescu, *Organic Materials as Smart Nanocarriers for Drug Delivery*, Elsevier, **2018**.
[8] X. Zhang, C. Gong, O. U. Akakuru, Z. Su, A. Wu, G. Wei, *Chem. Soc. Rev.* **2019**, *48*, 5564–5595.
[9] L. Sun, Y. A. Diaz-Fernandez, T. A. Gschneidtner, F. Westerlund, S. Lara-Avila, K. Moth-Poulsen, *Chem. Soc. Rev.* **2014**, *43*, 7378–7411.
[10] Y. Kobayashi, Y. Yokota, R. A. Wong, M. Hong, J. Takeya, S. Osawa, F. Ishiwari, Y. Shoji, T. Harimoto, K. Sugimoto, Y. Ishigaki, T. Suzuki, T. Fukushima, Y. Kim, *J. Phys. Chem. C* **2023**, *127*, 746–758.
[11] A. H. Gomes de Mesquita, C. H. MacGillavry, K. Eriks, *Acta Crystallogr.* **1965**, *18*, 437–443.
[12] J. L. Courtneidge, A. G. Davies, *Acc. Chem. Res.* **1987**, *20*, 90–97.
[13] Y. Sato, M. Kinoshita, M. Sano, H. Akamatu, *Bull. Chem. Soc. Jpn.* **1969**, *42*, 3051–3055.
[14] T. Bally, C. Carra, M. P. Fülscher, Z. Zhu, *J. Chem. Soc. Perkin Trans. 2* **1998**, 1759–1766.
[15] H. P. Fritz, H. Gebauer, P. Friedrich, P. Ecker, R. Artes, U. Schubert, *Z. Naturforsch. B* **1978**, *33*, 498–506.
[16] C. Kröhnke, V. Enkelmann, G. Wegner, *Angew. Chem. Int. Ed. Engl.* **1980**, *19*, 912–919.
[17] V. Enkelmann, B. S. Morra, C. Kröhnke, G. Wegner, J. Heinze, *Chem. Phys.* **1982**, *66*, 303–313.
[18] H. J. Keller, D. Nöthe, H. Pritzkow, D. Wehe, M. Werner, P. Koch, D. Schweitzer, *Mol. Cryst. Liq. Cryst.* **1980**, *62*, 181–199.
[19] D. Schweitzer, I. Hennig, K. Bender, H. Endres, H. J. Keller, *Mol. Cryst. Liq. Cryst.* **1985**, *120*, 213–220.
[20] J. K. Kochi, R. Rathore, P. Le Maguères, *J. Org. Chem.* **2000**, *65*, 6826–6836.
[21] T. Harimoto, Y. Ishigaki, *ChemPlusChem* **2022**, *87*, e202200013.
[22] T. Nishiuchi, S. Aibara, T. Kubo, *Angew. Chem. Int. Ed.* **2018**, *57*, 16516–16519.
[23] C. Zhu, K. Shoyama, F. Würthner, *Angew. Chem. Int. Ed.* **2020**, *59*, 21505–21509.
[24] E. Kayahara, T. Kouyama, T. Kato, H. Takaya, N. Yasuda, S. Yamago, *Angew. Chem. Int. Ed.* **2013**, *52*, 13722–13726.
[25] Y. Ni, F. Gordillo-Gámez, M. Peña Alvarez, Z. Nan, Z. Li, S. Wu, Y. Han, J. Casado, J. Wu, *J. Am. Chem. Soc.* **2020**, *142*, 12730–12742.
[26] R. Rathore, P. Le Magueres, S. V. Lindeman, J. K. Kochi, *Angew. Chem. Int. Ed.* **2000**, *39*, 809–812.
[27] M. Takase, V. Enkelmann, D. Sebastiani, M. Baumgarten, K. Müllen, *Angew. Chem. Int. Ed.* **2007**, *46*, 5524–5527.
[28] K. Kano, T. Sugimoto, Y. Misaki, T. Enoki, H. Hatakeyama, H. Oka, Y. Hosotani, Z.Yoshida, *J. Phys. Chem.* **1994**, *98*, 252–258.
[29] K. Oki, M. Takase, S. Mori, H. Uno, *J. Am. Chem. Soc.* **2019**, *141*, 16255–16259.
[30] R. Kumar, P. J. Chmielewski, T. Lis, D. Volkmer, M. Stępień, *Angew. Chem.Int. Ed.* **2022**, *61*, e202207486.
[31] Y. Ishigaki, T. Harimoto, K. Sugimoto, L. Wu, W. Zeng, D. Ye, T. Suzuki, *Chem. Asian J.* **2020**, *15*, 1147–1155.

[32] Y. Ni, T. Y. Gopalakrishna, H. Phan, T. Kim, T. S. Herng, Y. Han, T. Tao, J. Ding, D. Kim, J. Wu, *Nat. Chem.* **2020**, *12*, 242–248.
[33] B. Li, C. Yang, X. Wang, G. Li, W. Peng, H. Xiao, S. Luo, S. Xie, J. Wu, Z. Zeng, *Angew. Chem. Int. Ed.* **2021**, *60*, 19790–19796.
[34] M. B. S. Wonink, B. P. Corbet, A. A. Kulago, G. B. Boursalian, B. de Bruin, E. Otten, W. R. Browne, B. L. Feringa, *J. Am. Chem. Soc.* **2021**, *143*, 18020–18028.
[35] Y. K. Loh, P. Vasko, C. McManus, A. Heilmann, W. K. Myers, S. Aldridge, *Nat. Commun.* **2021**, *12*, 7052.
[36] S. H. Pun, K. M. Cheung, D. Yang, H. Chen, Y. Wang, S. V. Kershaw, Q. Miao, *Angew. Chem. Int. Ed.* **2022**, *61*, e202113203.
[37] B. Fabre, *Chem. Rev.* **2016**, *116*, 4808–4849.
[38] H. Bronstein, C. B. Nielsen, B. C. Schroeder, I. McCulloch, *Nat. Chem. Rev.* **2020**, *4*, 66–77.
[39] G. L. Soloveichik, *Chem. Rev.* **2015**, *115*, 11533–11558.
[40] Y. Ding, C. Zhang, L. Zhang, Y. Zhou, G. Yu, *Chem. Soc. Rev.* **2018**, *47*, 69–103.
[41] J. Heiska, M. Nisula, M. Karppinen, *J. Mater. Chem. A* **2019**, *7*, 18735–18758.
[42] P. Poizot, J. Gaubicher, S. Renault, L. Dubois, Y. Liang, Y. Yao, *Chem. Rev.* **2020**, *120*, 6490–6557.
[43] Y. Li, Q. Qian, X. Zhu, Y. Li, M. Zhang, J. Li, C. Ma, H. Li, J. Lu, Q. Zhang, *InfoMat* **2020**, *2*, 995–1033
[44] C. G. Granqvist, *Handbook of Inorganic Electrochromic Materials*, Elsevier, Amsterdam, The Netherlands, **1995**.
[45] P. Monk, R. Mortimer, D. Rosseinsky, *Electrochromism and Electrochromic Devices*, Cambridge University Press, Cambridge, **2007**.
[46] R. J. Mortimer, *Annu. Rev. Mater. Res.* **2011**, *41*, 241–268.
[47] D. R. Rosseinsky, P. M. S. Monk, R. J. Mortimer, *Electrochromic Materials and Devices*, Wiley-VCH, Weinheim, Germany, **2013**.
[48] K. Bange, T. Gambke, *Adv. Mater.* **1990**, *2*, 10–16.
[49] R. J. Mortimer, A. L. Dyer, J. R. Reynolds, *Displays* **2006**, *27*, 2–18.
[50] Z. Wang, X. Wang, S. Cong, J. Chen, H. Sun, Z. Chen, G. Song, F. Geng, Q. Chen, Z. Zhao, *Nat. Commun.* **2020**, *11*, 302.
[51] V.-T. Nguyen, B. K. Min, S. K. Kim, Y. Yi, C.-G. Choi, *J. Mater. Chem. C* **2021**, *9*, 3183–3192.
[52] Y. Wang, H. Nie, J. Han, Y. An, Y.-M. Zhang, S. X.-A. Zhang, *Light-Sci. Appl.* **2021**, *10*, 33.
[53] P. M. S. Monk, *The Viologens: Physicochemical Properties, Synthesis and Applications of the Salts of 4,4'-Bipyridine*, Wiley, Chichester, New York, **1998**.
[54] P. M. Beaujuge, J. R. Reynolds, *Chem. Rev.* **2010**, *110*, 268–320.
[55] H. Meng, *Organic Electronics for Electrochromic Materials and Devices*, Wiley-VCH, Weinheim, **2021**.
[56] K. Madasamy, D. Velayutham, V. Suryanarayanan, M. Kathiresan, K.-C. Ho, *J. Mater. Chem. C* **2019**, *7*, 4622–4637.
[57] M. Stolar, *Pure Appl. Chem.* **2020**, *92*, 717–731.
[58] T. A. Welsh, E. R. Draper, *RSC Adv.* **2021**, *11*, 5245–5264.
[59] G. Chen, H. Sasabe, T. Igarashi, Z. Hong, J. Kido, *J. Mater. Chem. A* **2015**, *3*, 14517–14534.
[60] J. He, Y. J. Jo, X. Sun, W. Qiao, J. Ok, T. Kim, Z. Li, *Adv. Funct. Mater.* **2021**, *31*, 2008201.
[61] D. Meng, R. Zheng, Y. Zhao, E. Zhang, L. Dou, Y. Yang, *Adv. Mater.* **2022**, *34*, 2107330.
[62] R. R. Anderson B.S. AND J. A. Parrish M.D., *J. Invest. Dermatol.*, *1981*, 77, 13–19.
[63] J. O. Escobedo, O. Rusin, S. Lim, R. M. Strongin, *Curr. Opin. Chem. Biol.* **2010**, *14*, 64–70.

[64] S. Luo, E. Zhang, Y. Su, T. Cheng, C. Shi, *Biomaterials* **2011**, *32*, 7127–7138.
[65] A. Yuan, J. Wu, X. Tang, L. Zhao, F. Xu, Y. Hu, *J. Pharm. Sci.* **2013**, *102*, 6–28.
[66] L. Wu, Y. Sun, K. Sugimoto, Z. Luo, Y. Ishigaki, K. Pu, T. Suzuki, H.-Y. Chen, D. Ye, *J. Am. Chem. Soc.* **2018**, *140*, 16340–16352.
[67] H.-B. Cheng, Y. Li, B. Z. Tang, J. Yoon, *Chem. Soc. Rev.* **2020**, *49*, 21–31.
[68] L. Wu, Y. Ishigaki, Y. Hu, K. Sugimoto, W. Zeng, T. Harimoto, Y. Sun, J. He, T. Suzuki, X. Jiang, H.-Y. Chen, D. Ye, *Nat. Commun.* **2020**, *11*, 446.
[69] L. Wu, Y. Ishigaki, W. Zeng, T. Harimoto, B. Yin, Y. Chen, S. Liao, Y. Liu, Y. Sun, X. Zhang, Y. Liu, Y. Liang, P. Sun, T. Suzuki, G. Song, Q. Fan, D. Ye, *Nat. Commun.* **2021**, *12*, 6145.
[70] L. Wu, W. Zeng, Y. Ishigaki, J. Zhang, H. Bai, T. Harimoto, T. Suzuki, D. Ye, *Angew. Chem. Int. Ed.* **2022**, *61*, e202209248.
[71] J. Fabian, H. Nakazumi, M. Matsuoka, *Chem. Rev.* **1992**, *92*, 1197–1226.
[72] K. Y. Law, *Chem. Rev.* **1993**, *93*, 449–486.
[73] L. Li, X. Dong, J. Li, J. Wei, *Dye. Pigment.* **2020**, *183*, 108756.
[74] A. A. Argun, P.-H. Aubert, B C. Thompson, I. Schwendeman, C. L. Gaupp, J. Hwang, N. J. Pinto, D. B. Tanner, A. G. MacDiarmid, J. R. Reynolds, *Chem. Mater.* **2004**, *16,* 4401–4412.
[75] C. L. Anderson, T. Zhang, M. Qi, Z. Chen, C. Yang, S. J. Teat, N. S. Settineri, E. A. Dailing, A. Garzón-Ruiz, A. Navarro, Y. Lu, Yi Liu, *J. Am. Chem. Soc.* **2023**, *145*, 5474−5485.
[76] C. R. Wade, M. Li, M. Dincă, *Angew. Chem. Int. Ed.* **2013**, *52*, 13377–13381.
[77] S. Mondal, D. C. Santra, Y. Ninomiya, T. Yoshida, M. Higuchi, *ACS Appl. Mater. Interfaces* **2020**, *12*, 58277−58286.
[78] F. Yu, W. Liu1, S.-W. Ke, M. Kurmoo, J.-L. Zuo, Q. Zhang *Nat. Commun.* **2020**, *11*, 5534.
[79] D. Bessinger, K. Muggli, M. Beetz, F. Auras, T. Bein, *J. Am. Chem. Soc.* **2021**, *143*, 7351−7357.
[80] C. Zhu, X. Ji, D. You, T. L. Chen, A. U. Mu, K. P. Barker, L. M. Klivansky, Y. Liu, L. Fang, *J. Am. Chem. Soc.* **2018**, *140*, 18173–18182.
[81] P. W. Antoni, M. M. Hansmann, *J. Am. Chem. Soc.* **2018**, *140*, 14823–14835.
[82] P. W. Antoni, T. Bruckhoff, M. M. Hansmann, *J. Am. Chem. Soc.* **2019**, *141*, 9701–9711.
[83] P. W. Antoni, C. Golz, M. M. Hansmann, *Angew. Chem. Int. Ed.* **2022**, *61*, e202203064.
[84] A. Maiti, F. Zhang, I. Krummenacher, M. Bhattacharyya, S. Mehta, M. Moos, C. Lambert, B. Engels, A. Mondal, H. Braunschweig, P. Ravat, A. Jana, *J. Am. Chem. Soc.* **2021**, *143*, 3687–3692.
[85] S. Patai and Z. Rappoport, Eds., *The Quinonoid Compounds: Vol. 1*, John Wiley & Sons, Inc., Chichester, UK (1988), **1988**, vol. 1.
[86] S. Patai and Z. Rappoport, Eds., *The Quinonoid Compounds: Vol. 2*, John Wiley & Sons, Inc., Chichester, UK (1988) , **1988**, vol. 2.
[87] K. Deuchert and S. Hünig, *Angew. Chem. Int. Ed. Engl.* **1978**, *17*, 875−886.
[88] L. K. Montgomery, J. C. Huffman, E. A. Jurczak and M. P. Grendze, *J. Am. Chem. Soc.* **1986**, **108**, 6004−6011.
[89] W. Sümmermann, G. Kothe, H. Baumgärtel and H. Zimmermann, *Tetrahedron Lett.* **1969**, *10*, 3807−3810.
[90] X. Zhang, X. Jiang, K. Zhang, L. Mao, J. Luo, C. Chi, H. S. O. Chan and J. Wu, *J. Org. Chem.* **2010**, *75*, 8069−8077.
[91] S. Pola, C.-H. Kuo, W.-T. Peng, M. M. Islam, I. Chao and Y.-T. Tao, *Chem. Mater.* **2012**, *24*, 2566−2571.
[92] X. Yin, J. Z. Low, K. J. Fallon, D. W. Paley and L. M. Campos, *Chem. Sci.* **2019**, *10*, 10733−10739.

[93] Z. Zeng, Y. M. Sung, N. Bao, D. Tan, R. Lee, J. L. Zafra, B. S. Lee, M. Ishida, J. Ding, J. T. López Navarrete, Y. Li, W. Zeng, D. Kim, K.-W. Huang, R. D. Webster, J. Casado and J. Wu, *J. Am. Chem. Soc.* **2012**, *134*, 14513−14525.
[94] M. Desroches, P. Mayorga Burrezo, J. Boismenu-Lavoie, M. Peña Álvarez, C. J. Gómez-García, J. M. Matxain, D. Casanova, J.-F. Morin and J. Casado, *Angew. Chem. Int. Ed.* **2017**, *56,* 16212−16217.
[95] T. Nishiuchi, R. Ito, E. Stratmann and T. Kubo, *J. Org. Chem.* **2020**, *85*, 179–186.
[96] Y. Ishigaki, T. Harimoto, T. Shimajiri, T. Suzuki, *Chem. Rev.* **2023**, *in press*
(DOI: 10.1021/acs.chemrev.3c00376)
[97] Y. Ishigaki, K. Sugawara, T. Tadokoro, Y. Hayashi, T. Harimoto, T. Suzuki, *Chem. Commun.*, **2021**, *57*, 7201–7214.
[98] T. Harimoto, Y. Ishigaki, *J. Synth. Org. Chem. Jpn.* **2023**, *81*, 963–977.
[99] Y. Sakano, R. Katoono, K. Fujiwara and T. Suzuki, *Chem. Lett.* **2014**, *43*, 1143–1145.
[100] Y. Ishigaki, K. Sugawara, M. Yoshida, M. Kato and T. Suzuki, *Bull. Chem. Soc. Jpn.* **2019**, *92*, 1211–1217.
[101] Y. Ishigaki, T. Hashimoto, K. Sugawara, S. Suzuki, T. Suzuki, *Angew. Chem. Int. Ed.* **2020**, *59*, 6581–6584.
[102] T. Nishiuchi, S, Aibara, H. Sato, T. Kubo, *J. Am. Chem. Soc.* **2022**, *144*, 7479–7488.
[103] Y. Ishigaki, Y, Hayashi, T. Suzuki, *J. Am. Chem. Soc.* **2019**, *141*, 18293–18300.
[104] M. B. S. Wonink, B. P. Corbet, A. A. Kulago, G. B. Boursalian, B. de Bruin, E. Otten, W. R. Browne, B. L. Feringa, *J. Am. Chem. Soc.* **2021**, *143*, 18020–18028.
[105] K. Li, Z. Xu, J. Xu, T. Weng, X. Chen, S. Sato, J. Wu, Z. Sun, *J. Am. Chem. Soc.* **2021**, *143*, 20419–20430.

Chapter 2

Enhancement of NIR-Absorbing Ability of Bis(diarylmethylium)-Type Dicationic Dyes Based on an *Ortho*-Substitution Strategy

2-1. Introduction

Organic dyes such as cyanines,[1–3] squaliums,[4,5] and diimmoniums,[6,7] and organometallic complexes such as phthalocyanines[8], and dithiolenes[9] show a narrow energy gap which has been attributed to a long-range π-conjugation based on the effective delocalization of N/O-based cations and charge-transfer (CT) interactions based on metal ions, respectively. Thus, they are known to exhibit near-infrared (NIR) absorption in the range of 750–2500 nm.[10–12] These dyes are expected to be applied to various optical applications such as security marking,[13,14] lithography,[15] optical filters[16,17] and photovoltaic cells.[18–22] Furthermore, to increase the efficiency of photovoltaic power generation, it would be desirable to make effective use of NIR light in sunlight. Thus, the development of NIR-absorbing materials is of essential importance.[23–25] In addition, since NIR light shows a superior penetration of biological tissues, NIR dyes are also expected to be applied to chemotherapy and imaging of deep tissues in vivo.[26–34]

Electrochromic systems, on the other hand, induce drastic color changes based on the redox interconversion between neutral and charged species.[35,36] Electrochromic systems capable of switching NIR absorption are attractive from the viewpoint of applications for material and life science, and thus several examples have been reported to date.[37–40] Since most of the inorganic systems contain heavy metals, the development of organic-based electrochromic materials is needed to reduce the environmental impact and improve biocompatibility.

However, since the redox states of organic NIR dyes are generally unstable, the reversible modulation of NIR absorption based on quantitative redox interconversion is still a challenging issue regarding reversibility and durability during their interconversion. Indeed, there is an increasing interest in organic electrochromic systems that enable ON/OFF switching of NIR absorption.[41–51]

It was reported that 11,11,12,12-tetraaryl-9,10-anthraquinodimethanes (AQDs) **1** with a folded form undergo one-stage two-electron (2e) oxidation to produce twisted dications $\mathbf{1}^{2+}$ with a planar anthracene skeleton (Scheme 2-1).[48,52,53] The HOMO of the dication $\mathbf{1}^{2+}$ is mainly located on the anthracene framework, and the corresponding LUMO is delocalized in two diarylmethylium units. As a result, a NIR absorption band (~800 nm) based on an intramolecular CT interaction from HOMO to LUMO was observed in the dication $\mathbf{1a}^{2+}$ with 4-methoxyphenyl groups. Therefore, lowering the LUMO level of dicationic dyes is an effective approach for the observation of longer-wavelength absorption in the NIR region.

In this chapter, the author aimed to obtain advanced design guidelines to control the wavelength of NIR bands by an introduction of proper substituents to 4-methoxyphenyl groups. Thus, the author newly designed and synthesized a series of AQD-based electrochromic systems with *ortho*-substituents on 4-methoxyphenyl groups. X-ray, electrochemical, and spectroscopic measurements of both neutral and cationic species revealed their detailed structural and electronic properties both experimentally and theoretically. As a result, both the electronic and steric effects of the *ortho*-substituents were proven to be effective way for controlling the CT bands in the NIR region. Notably, not only an electron-withdrawing substituent such as chlorine atom but also an electron-donating substituent such as methyl group can lower the LUMO level of the dication $\mathbf{1}^{2+}$ to exhibit longer-wavelength absorption. Since lowering the LUMO level with electron-withdrawing groups often leads to the undesirable consequence of decreased stability of dicationic dyes, this "*ortho*-substitution strategy", which enables the enhancement of NIR-absorbing abilities by lowering the LUMO levels of the chromophores, would be a key for constructing reversible NIR electrochromic materials.

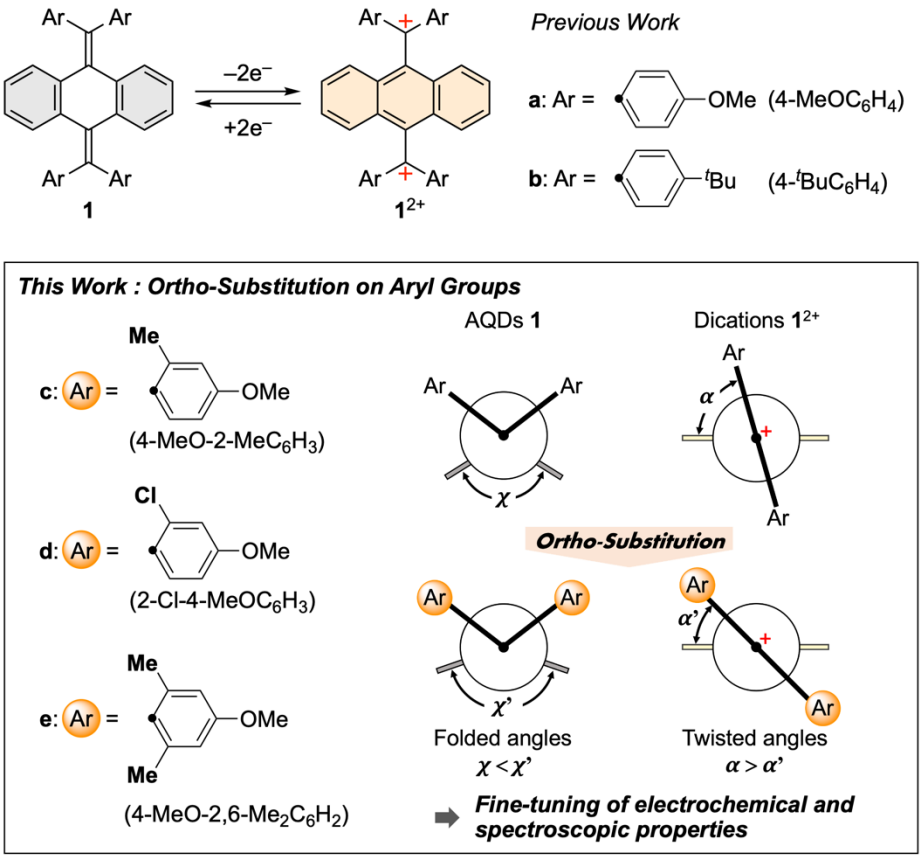

Scheme 2-1. Redox interconversion of anthraquinodimethane derivatives and designed molecules based on an "*ortho*-substitution strategy".

2-2. Results and Discussion

2-2-1. Preparation and X-ray analysis

The target compounds **1c** and **1d** with a methyl group and chlorine atom at the *ortho*-position of a 4-methoxyphenyl group, respectively, were obtained in good yields by the Suzuki-Miyaura cross-coupling reaction of tetrabromoanthraquinodimethane **1Br$_4$**[54] with the corresponding aryl boronic acid (Scheme 2-2). An *ortho*-disubstituted derivative **1e** was synthesized by the Negishi cross-coupling reaction (Scheme 2-2). Single-crystal X-ray structure analyses revealed that all these derivatives **1c**–**1e** adopt a folded conformation, as in 4-methoxyphenyl derivative **1a** (Figure 2-1). Notable differences in the structural features of these AQD derivatives were found in **1e** with two *ortho*-substituents (Table 2-1), e.g., the bent angles θ_{exp} between the central plane and diarylethene moieties decrease due to the steric effects in **1e** with two *ortho*-substituents (39.04(11)°, 44.39(10)° for **1a**, 36.65(5)° for **1c**, 33.16(14)°, 33.45(14)° for **1d** and 27.04(10)°, 29.79(11)° for **1e**). In particular, **1e** has a unique torsion angle ϕ and folded angle χ [ϕ = 13.05(9)° and 18.24(8)°, χ = 34.85(13)°], which suggests that neutral **1e** has a folded-twisted conformation with smaller *p*-orbital overlap for the exomethylene bonds.

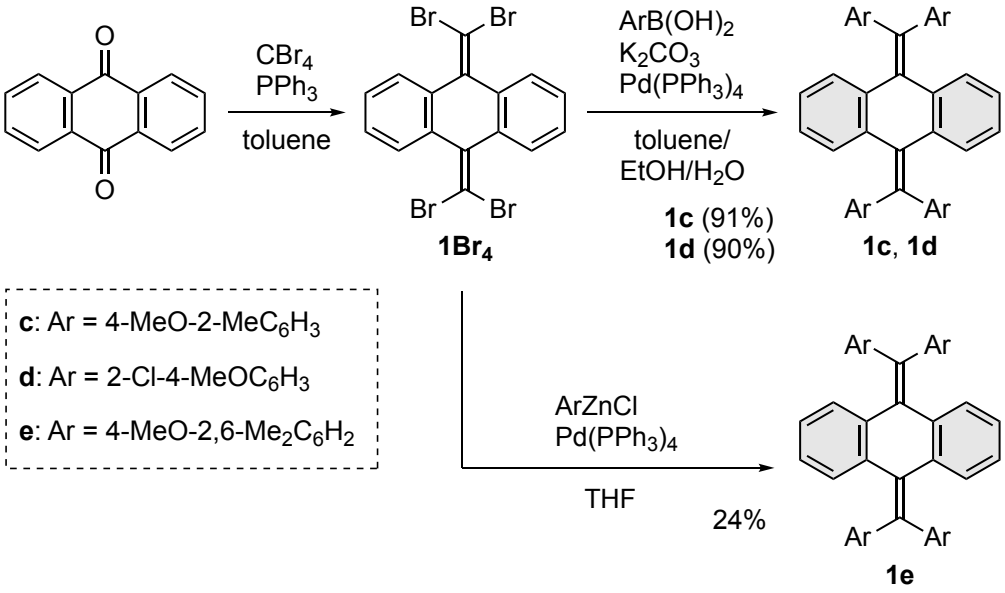

Scheme 2-2. Preparation of *ortho*-substituted derivatives **1c**–**1e**.

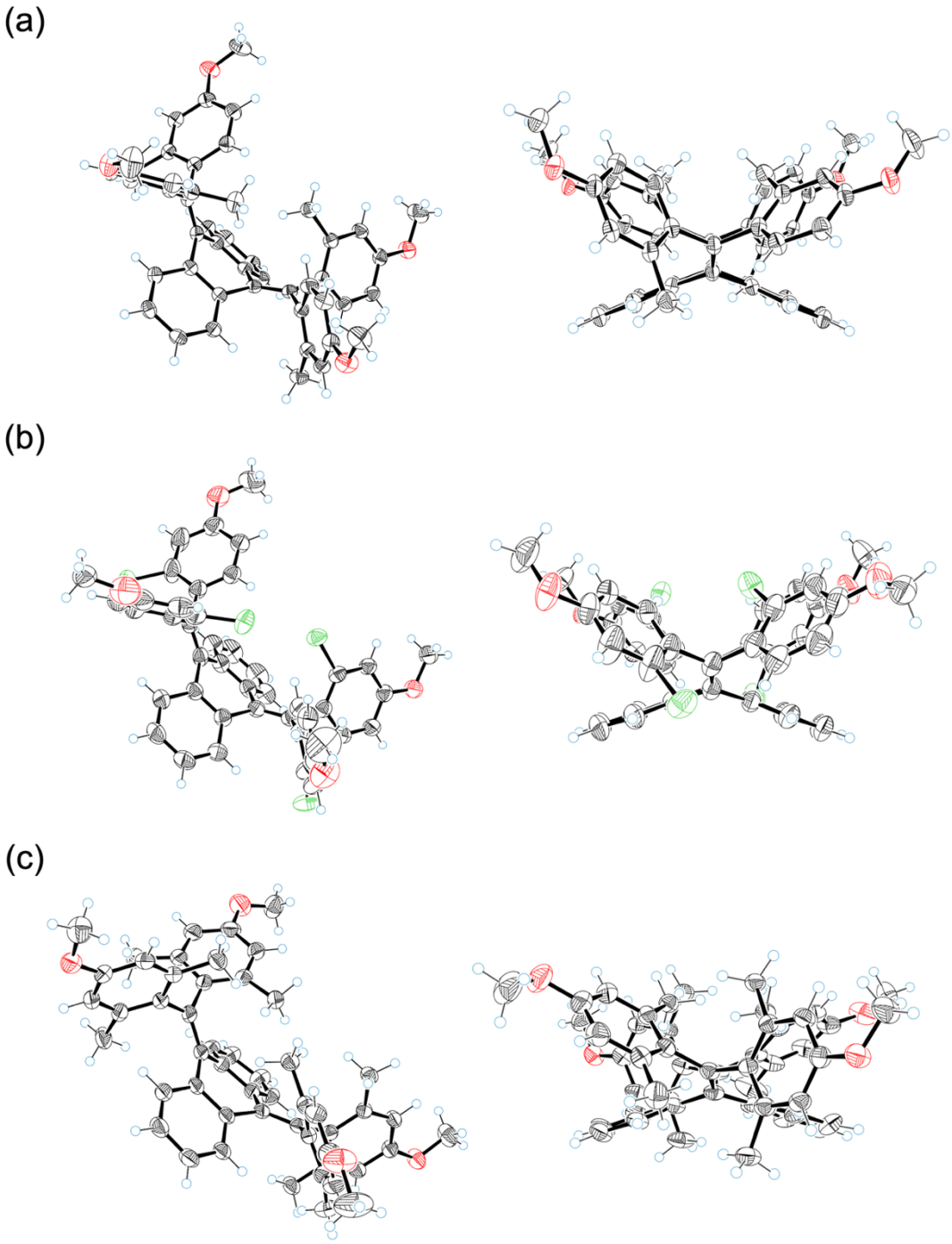

Figure 2-1. X-ray crystal structures (ORTEP drawings) of (a) **1c**, (b) **1d**, and (c) **1e** determined at 150 K. Thermal ellipsoids are shown at the 50% probability level. Solvent mask procedures were used for the analyses of **1c** and **1e**. Disordered atoms are omitted for clarity in the X-ray structure of **1d**.

Table 2-1. Structural parameters determined by X-ray analyses and DFT calculations (CAM-B3LYP/6-31G*). The calculated values are shown in italics.

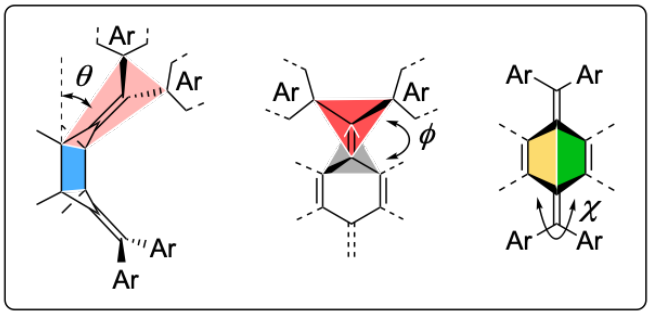

		θ (°)	ϕ (°)	χ (°)
1a	Expt.	44.39(10)	7.32(8)	47.22(12)
		39.04(11)	9.45(9)	-
	Calcd.	*39.11*	*7.236*	*45.13*
		39.11	*7.240*	-
1c	Expt. [a]	36.65(5)	3.72(7)	41.84(16)
	Calcd.	*34.91*	*4.132*	*41.91*
		34.91	*4.126*	-
1d	Expt.	33.16(14)	4.73(11)	38.66(17)
		33.45(14)	7.21(11)	-
	Calcd.	*37.68*	*6.444*	*42.87*
		36.62	*6.630*	-
1e	Expt.	27.04(10)	18.24(8)	34.85(13)
		29.79(11)	13.05(9)	-
	Calcd.	*27.36*	*15.71*	*34.73*
		27.06	*15.87*	-

[a] Centrosymmetric.

2-2-2. Redox behavior

To investigate the redox behavior of *ortho*-substituted AQDs **1c**–**1e** in detail, cyclic voltammetry (CV) measurements were performed in CH_2Cl_2 (Figure 2-2). Cyclic voltammograms of **1c** and **1d** showed 2e-oxidation peaks at +1.06 V and +1.32 V vs. SCE, respectively, for which a 2e-process was confirmed using ferrocene as an external standard. The value of *ortho*-monomethylated derivative **1c** is similar to that of parent **1a** (+1.03 V) whereas the higher oxidation potential of *ortho*-monochlorinated derivative **1d** can be accounted for by the introduction of electron-withdrawing chlorine atoms. As a result of changes in their structures, return peaks, at which twisted dications undergo 2e-reduction to give folded neutral species, appeared in the far cathodic region (+0.59 V for $\mathbf{1c}^{2+}$ and +0.87 V for $\mathbf{1d}^{2+}$). Such peak separation is a characteristic feature of dynamic redox (*dyrex*) systems such as $\mathbf{1a}/\mathbf{1a}^{2+}$, in which the steady-state concentration of an intermediary radical cationic species is negligible.[55]

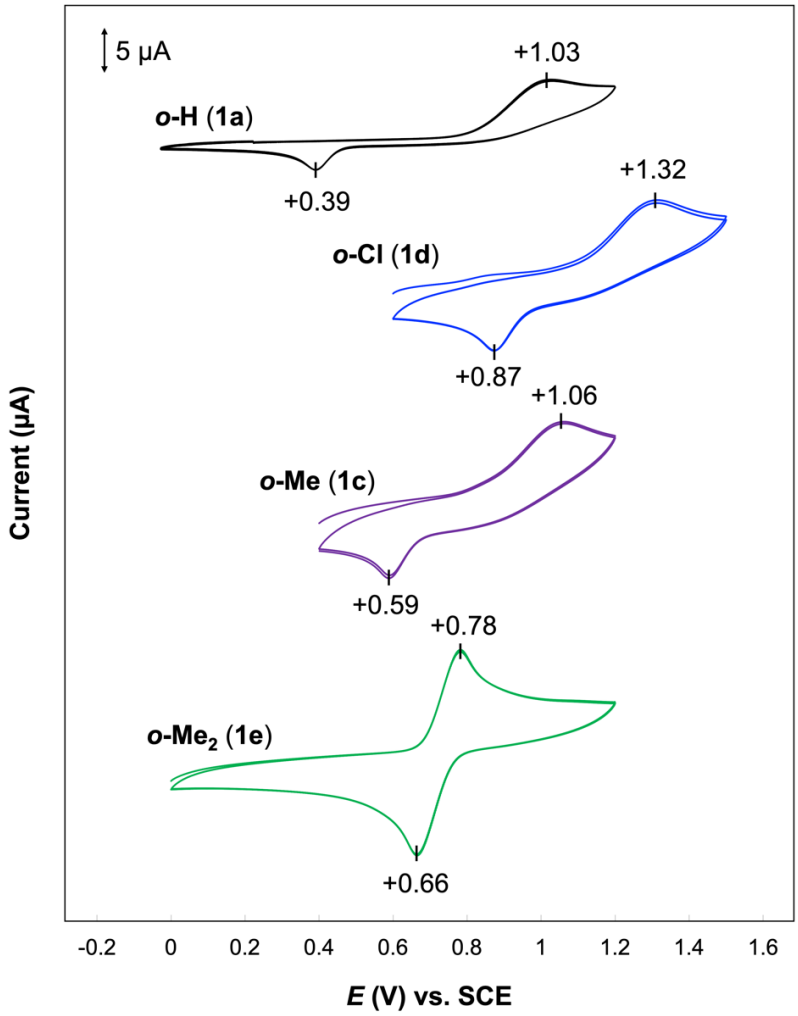

Figure 2-2. Cyclic voltammograms of neutral donors ***o*-H** (**1a**), ***o*-Cl** (**1d**), ***o*-Me** (**1c**), and ***o*-Me$_2$** (**1e**) at 297 K in CH_2Cl_2 containing 0.1 M Bu_4NBF_4 as a supporting electrolyte (scan rate 0.1 V s^{-1}, Pt electrodes).

The most important finding is that both $\mathbf{1c}^{2+}$ with methyl groups and $\mathbf{1d}^{2+}$ with chlorine atoms exhibit higher reduction potentials than $\mathbf{1a}^{2+}$, proving that electron-donating groups at the *ortho*-position can also lower the LUMO level of the dication. Actually, the reduction peak corresponding to $\mathbf{1e}^{2+}$ with two methyl groups on each aryl group exhibits a much higher reduction peak at +0.66 V, showing that steric effects of the *ortho*-substituents can lower the LUMO level of the dications even if they have electron-donating substituents on the 4-methoxyphenyl group. In contrast to **1c** and **1d** with a large separation of redox peaks, the voltammogram of $\mathbf{1e}/\mathbf{1e}^{2+}$ showed almost no separation. This would result from the easy oxidation of **1e** with a folded-twisted geometry at +0.78 V. Such a small separation might suggest that there is no significant structural change that accompanies redox interconversion between **1e** and $\mathbf{1e}^{2+}$. However, this is not the case, as proven in the next section by isolation and analysis of the X-ray structure of $\mathbf{1e}^{2+}$ salt as well as other dications.

2-2-3. Redox interconversion and X-ray analysis

The dication salts $\mathbf{1}^{2+}(SbCl_6^-)_2$ were successfully synthesized and isolated quantitatively by treatment of the neutral donor with 2 equivalents of $(4\text{-}BrC_6H_4)_3N^{+\bullet}SbCl_6^-$ (Scheme 2-3). X-ray analysis showed that, in common with dication $\mathbf{1a}^{2+}$, dications $\mathbf{1c}^{2+}$–$\mathbf{1e}^{2+}$ adopt a fully conjugated planar anthracene core (Figure 2-3). Notably, the steric repulsion of the *ortho*-substituents leads to a decrease in the average twist angles α_{exp} between the anthracene core and the diarylmethylium moiety (76.7° for $\mathbf{1a}^{2+}$, 67.0° for $\mathbf{1c}^{2+}$, 66.6° for $\mathbf{1d}^{2+}$ and 50.7° for $\mathbf{1e}^{2+}$). Moreover, the torsion angles β_{exp} between the aryl group and methylium moiety increase to avoid steric repulsion between *ortho*-substituents (24.3(3)° for $\mathbf{1a}^{2+}$, 27.5(7)° and 31.6(8)° for $\mathbf{1c}^{2+}$, 30.0(4)° and 38.6(8)° for $\mathbf{1d}^{2+}$ and 43.35(9)° and 43.36(9)° for $\mathbf{1e}^{2+}$, see p.25). Density functional theory (DFT) calculations[56] at the CAM-B3LYP/6-31G* level showed dihedral angles α and β similar to those observed (Table 2-2). Treatment of the dications with an excess amount of Zn powder quantitatively regenerated the original neutral AQDs **1**. This result indicates that a reversible redox interconversion proceeds between neutral state **1** and dicationic state $\mathbf{1}^{2+}$, resulting in a dynamic structural change upon electron transfer.

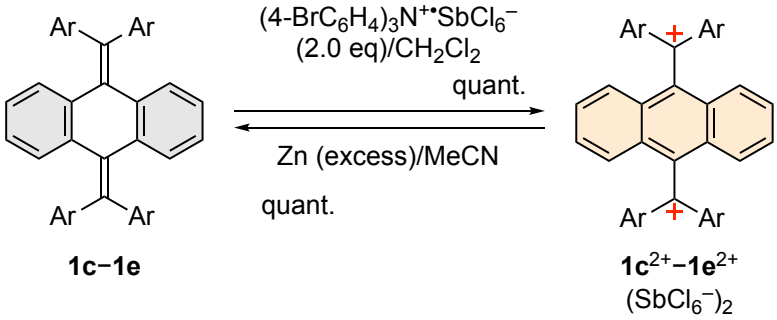

Scheme 2-3. Redox interconversion of *ortho*-substituted derivatives $\mathbf{1c}/\mathbf{1c}^{2+}(SbCl_6^-)_2$, $\mathbf{1d}/\mathbf{1d}^{2+}(SbCl_6^-)_2$, and $\mathbf{1e}/\mathbf{1e}^{2+}(SbCl_6^-)_2$.

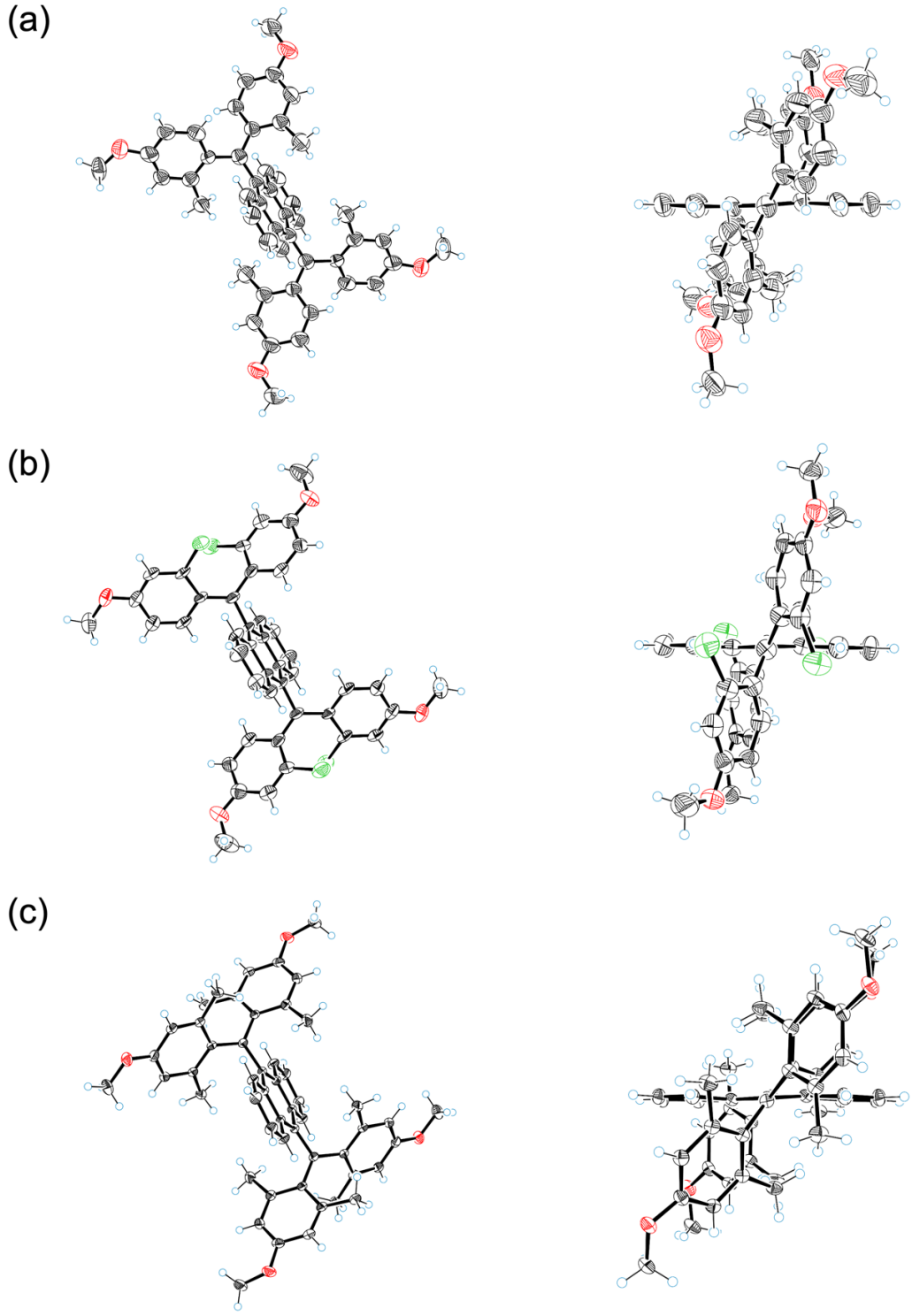

FIgure 2-3. X-ray crystal structures (ORTEP drawings) of (b) $\mathbf{1c}^{2+}(SbCl_6^-)_2$, (c) $\mathbf{1d}^{2+}(SbCl_6^-)_2$, and (d) $\mathbf{1e}^{2+}(SbCl_6^-)_2$ determined at 150 K. Thermal ellipsoids are shown at the 50% probability level. Solvent mask procedures were used for the analysis of $\mathbf{1c}^{2+}(SbCl_6^-)_2$. The counterions (all cases) and disordered atoms ($\mathbf{1d}^{2+}(SbCl_6^-)_2$, and $\mathbf{1e}^{2+}(SbCl_6^-)_2$) are omitted for clarity in the X-ray structures.

Table 2-2. Structural parameters determined by X-ray analyses and DFT calculations (CAM-B3LYP/6-31G*). The calculated values are shown in italics.

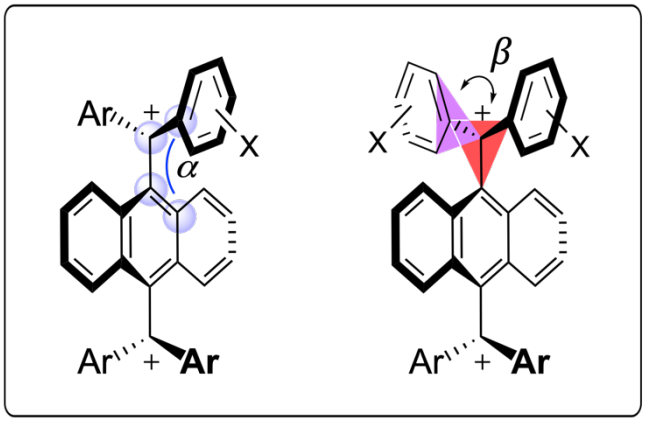

		α_{ave} (°)	β (°)
1a^{2+}	Expt.[a]	76.7	24.3(3)
	Calcd.	*71.69*	*24.87*, *24.88*
1c^{2+}	Expt. [a]	67.0	33.8(5), 34.4(4)
	Calcd.	*64.42*	*30.35*, *35.18*
1d^{2+}	Expt. [a]	66.6	30.0(4), 38.1(4)
	Calcd.	*69.30*	*32.67*, *33.85*
1e^{2+}	Expt. [a]	50.7	43.35(9), 43.36(9)
	Calcd.	*54.89*	*40.95*, *40.96*

[a] Centrosymmetric.

2-2-4. Absorbing properties

The *ortho*-monosubstituted neutral compounds **1c** and **1d** in CH_2Cl_2 exhibit absorption mainly in the UV region, and no significant difference in absorption properties was observed compared to parent AQD **1a**. In contrast, *ortho*-disubstituted neutral **1e** shows a more red-shifted absorption band (λ_{max} = 394 nm) into the visible region compared to *ortho*-monosubstituted derivatives **1c** and **1d** (Figure 2-5). The observed red-shift for **1e** can be explained by the adoption of a folded-twisted conformation which has a higher HOMO and a lower LUMO than the corresponding folded structure, resulting in a decrease in the HOMO-LUMO gap. Elevation of the HOMO level was experimentally demonstrated by CV measurement (see above).

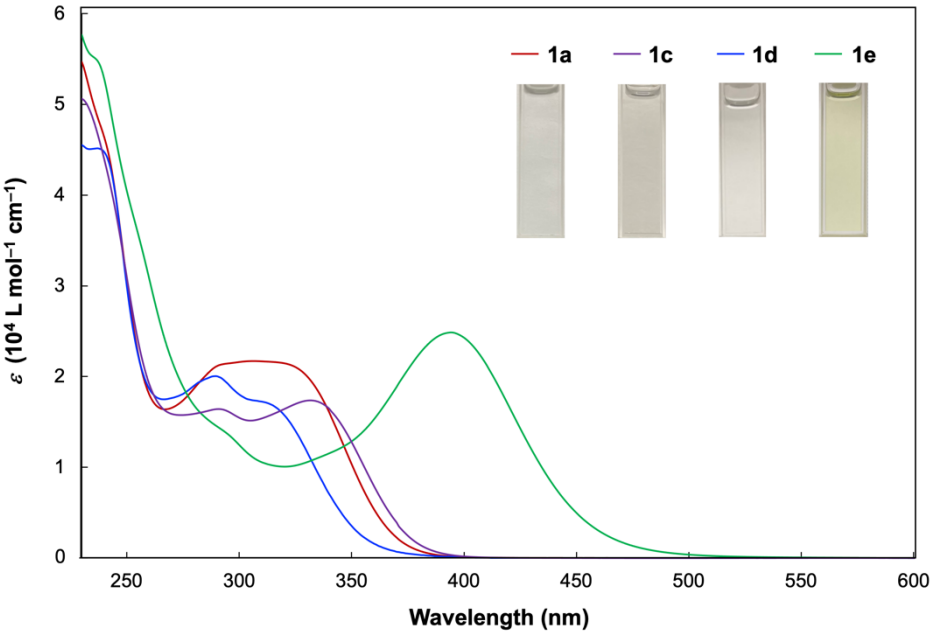

Figure 2-4. UV/Vis spectra of **1a** (red), **1c** (violet), **1d** (blue), and **1e** (green) in CH_2Cl_2.

On the other hand, dication salts $\mathbf{1c}^{2+}(SbCl_6^-)_2$–$\mathbf{1e}^{2+}(SbCl_6^-)_2$ in CH_2Cl_2 exhibit strong absorption, mainly in the Vis/NIR region (Figure 2-5). The red-shift of the strong absorption band in the visible region, which is attributed to the π-π* transition derived from the diarylmethylium chromophore, was observed from λ_{max} (nm) = 532 ($\mathbf{1a}^{2+}$) to 650 ($\mathbf{1e}^{2+}$) (Table 2-3), accompanied by a decrease in the molar absorption coefficient ε ($Lmol^{-1}cm^{-1}$) from 162000 ($\mathbf{1a}^{2+}$) to 47100 ($\mathbf{1e}^{2+}$) (Table 2-3). The significant changes in the values of λ_{max} and ε can be explained by perturbation of the frontier orbital level due to the steric effect of the *ortho*-substituents. The steric repulsion between *ortho*-substituents increases the torsion angle β between the aryl group and methylium moiety (Table 2-1), which weakens the effective delocalization of the positive charge and the oscillator strength of the π-π* transition. The NHOMO-LUMO gap and oscillator strength corresponding to the π-π* transition are reproduced by TD-DFT calculations at the CAM-B3LYP/6-31G* level (Figure 2-6).

Another striking result is the NIR absorption of $\mathbf{1e}^{2+}(SbCl_6^-)_2$. The first absorption band in the NIR region is attributed to the intramolecular CT transition from HOMO mainly located on the anthracene core to LUMO delocalized on diarylmethylium units. The CT band was red-shifted from λ_{max} (ε) = 709 nm (8650) for $\mathbf{1a}^{2+}$ to 855 nm (21100) for $\mathbf{1e}^{2+}$ (Table 2-3), which is due to the narrower HOMO-LUMO gap induced by the steric effects of *ortho*-substituents.

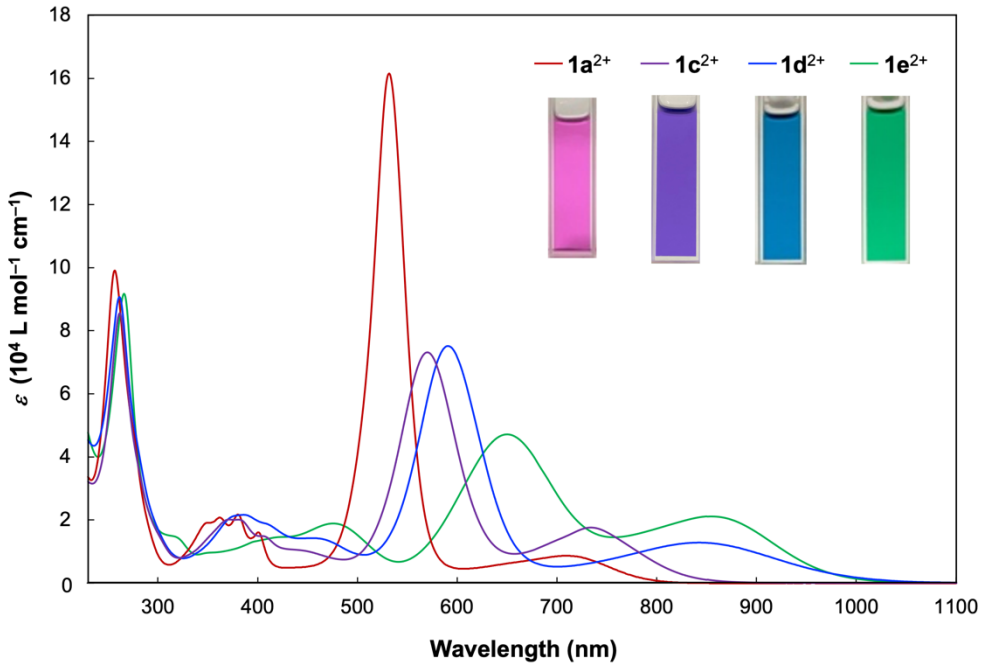

Figure 2-5. UV/Vis/NIR spectra of $\mathbf{1a}^{2+}(SbCl_6^-)_2$ (red), $\mathbf{1c}^{2+}(SbCl_6^-)_2$ (blue), $\mathbf{1d}^{2+}(SbCl_6^-)_2$ (violet), and $\mathbf{1e}^{2+}(SbCl_6^-)_2$ (green) in CH_2Cl_2.

Table 2-3. UV/Vis/NIR spectral data of the dication salts in CH_2Cl_2.

	λ_{max} (ε)
$\mathbf{1a}^{2+}(SbCl_6^-)_2$	709 nm (8650), 532 nm (162000)
$\mathbf{1c}^{2+}(SbCl_6^-)_2$	734 nm (17600), 570 nm (73100)
$\mathbf{1d}^{2+}(SbCl_6^-)_2$	843 nm (12800), 591 nm (75100)
$\mathbf{1e}^{2+}(SbCl_6^-)_2$	855 nm (21100), 650 nm (47100)

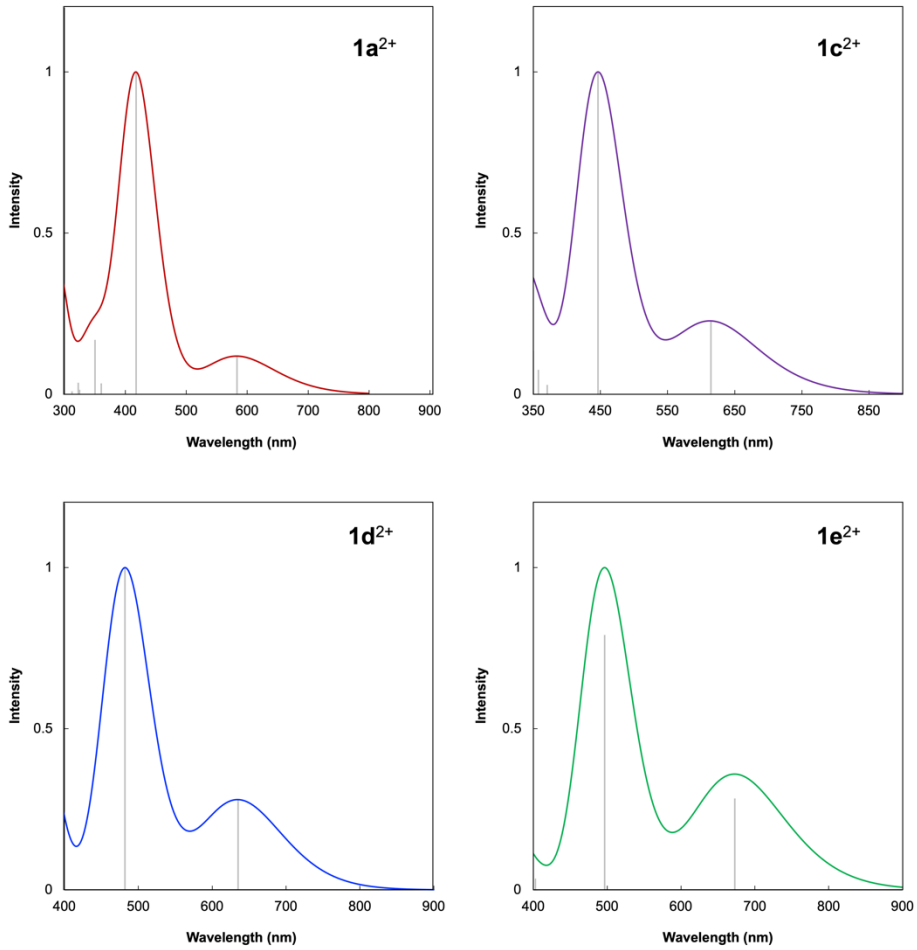

Figure 2-6. Simulated UV/Vis/NIR spectra by TD-DFT calculations (CAM-B3LYP/6-31G*) for corresponding dications $\mathbf{1}^{2+}$.

In this way, the author could successfully extend the NIR absorption band by lowering the LUMO level without attaching electron-withdrawing substituents to the aryl group. The author previously reported that a red-shift of the NIR absorption band extending to 1000 nm could be achieved for another dication $\mathbf{1b}^{2+}$ with *tert*-butylphenyl groups (Scheme 2-1), by lowering the LUMO level due to the absence of a methoxy group.[48] However, the dication $\mathbf{1b}^{2+}$ is too moisture-sensitive because it is composed of pure hydrocarbon without electron-donating heteroatoms. Another merit of the use of an *ortho*-substitution strategy is the enhancement of ε of the NIR absorption bands. In general, for twisted dications such as $\mathbf{1a}^{2+}$, the CT transitions are virtually forbidden because the two units of diarylmethylium are attached to the anthracene in an almost orthogonal manner, and the transition intensities are relatively minimal. Thus, the much larger ε in $\mathbf{1e}^{2+}$ can also be explained by the steric effect, which reduced the twist angle α between the diarylmethylium unit and the anthracene core (Table 2-1) and increased the overlap of the HOMO-LUMO orbitals, resulting in an increase in the oscillator strength of the CT transitions. As a result, the terminus of the CT band of $\mathbf{1e}^{2+}$ reaches 1100 nm, and the corresponding ε is approximately 2.4 times greater than that of $\mathbf{1a}^{2+}$.

2-2-5. DFT calculations

To obtain further information regarding the effect of the twist angle *a* between the diarylmethylium unit and the central anthracene core on the frontier orbital levels, we performed DFT calculations. For example, in the case of **1a**$^{2+}$, the author predicts that reducing its twist angle α can induce a red-shift and an enhancement of the oscillator strength in the CT band, when optimizations were performed by varying the twist angle α ∠C1-C2-C3-C4 in steps of 20° from the initial optimized structure (α = 71.69°) while keeping the four aryl *ipso*-carbons C4, C5, C6, and C7 fixed on the same plane (Figure 2-7). According to DFT calculations, the HOMO-LUMO gap (ΔE) becomes narrower as the twist angle α decreases [α = 71.69° (ΔE = 4.27 eV), 51.69° (4.16 eV), 31.69° (4.02 eV), 11.69° (3.86 eV), Figure 2-8]. In fact, TD-DFT calculations for each of the optimized structures revealed that the CT bands show a constant red-shift as the twist angle α decreases from 71.69° to 11.69°. In addition, it was also demonstrated that the oscillator strength *f* of the first absorption band gradually increases from 0.1681 to 0.4053. Notably, with a decrease in the twist angle α, the average torsion angle β_{ave} increases [α = 71.69° (β_{ave} = 24.88°), 51.69° (26.64°), 31.69° (29.14°), 11.69° (32.33°), Figure 2-8], leading to a red-shift in the second absorption band and a decrease in the oscillator strength *f* from 1.4114 to 0.5508.

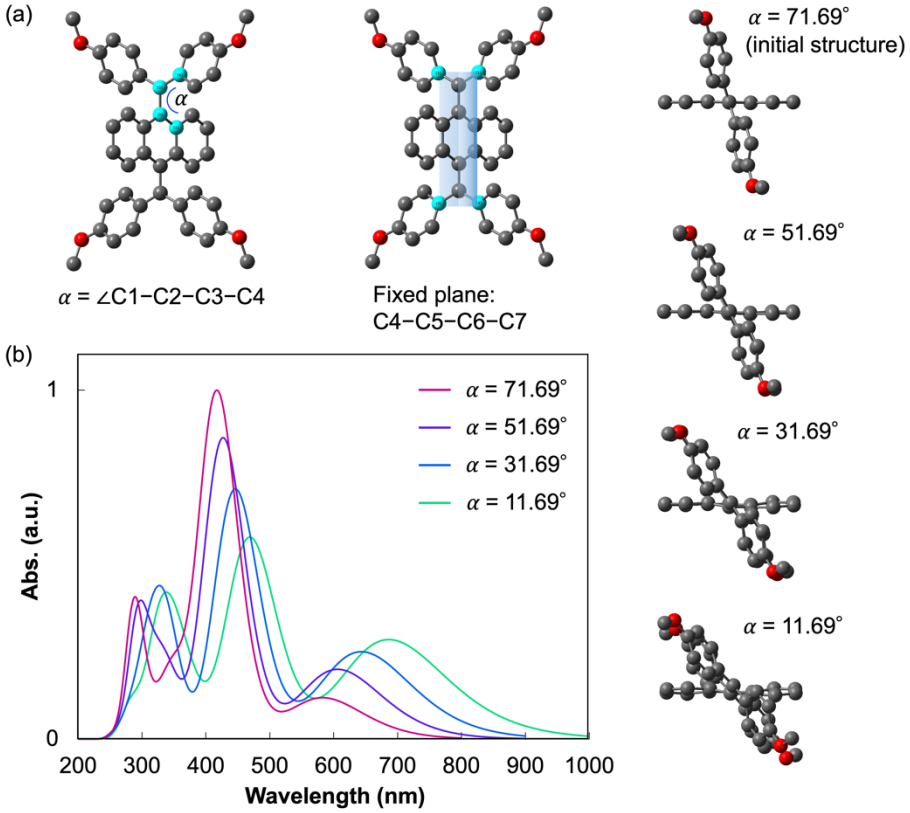

Figure 2-7. (a) Optimized structures obtained by varying the twist angle α ∠C1-C2-C3-C4 with the fixed plane C4-C5-C6-C7 from the energy-minimized structure (α = 71.69°) for **1a**$^{2+}$. (b) A change in UV/Vis/NIR spectrum simulated by TD-DFT calculations of **1a**$^{2+}$ while varying the twist angle α.

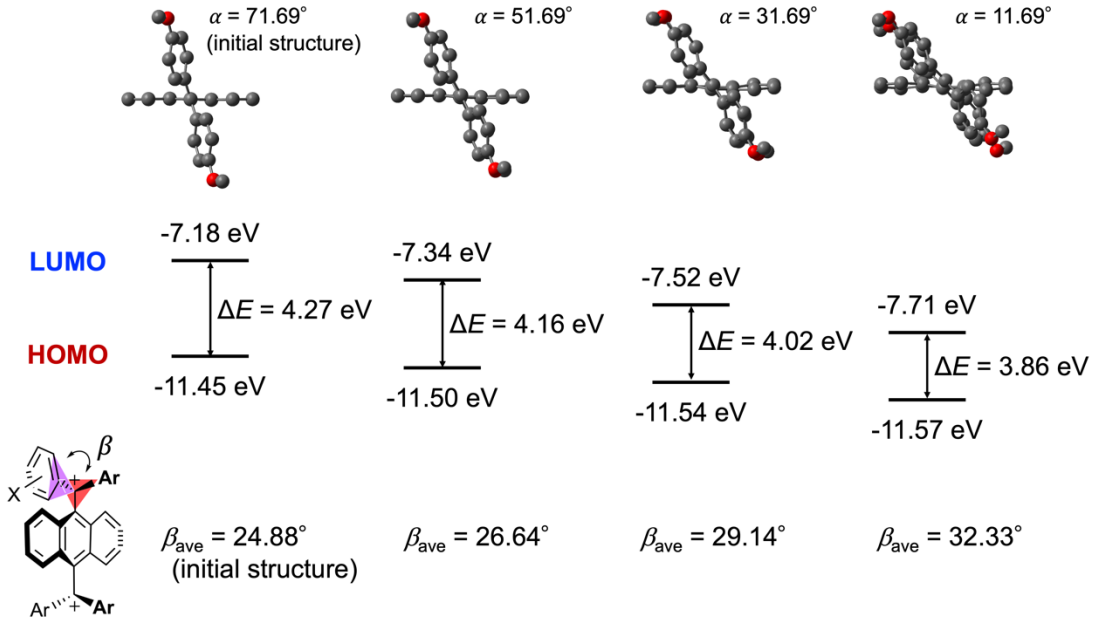

Figure 2-8. Optimized structures obtained by varying the twist angle α ∠C1-C2-C3-C4 with the fixed plane C4-C5-C6-C7 from the energy-minimized structure ($\alpha = 71.69°$) for **1a**$^{2+}$. The corresponding HOMO and LUMO levels and the average torsion angles β_{ave} calculated by the DFT method.

Based on this theoretical result, for *ortho*-disubstituted **1e**$^{2+}$, to confirm whether the experimentally observed red-shift was due to a decrease in the twist angle α, theoretical calculations with varying of the corresponding angle were conducted in the same procedure. As a result, TD-DFT calculations carried out under conditions of varying the twist angle α ∠C1-C2-C3-C4 in steps of 10° from the initial optimized structure ($\alpha = 54.89°$) show a constant blue-shift accompanied by a decrease in the oscillator strength *f* from 0.2840 to 0.1604 (Figure 2-9). Therefore, the energy levels of frontier orbitals are significantly affected by the twist angles *a* between the diarylmethylium units and anthracene cores. Thus, modulation of the steric and electronic effects of *ortho*-substituents is an effective strategy that allows a fine-tuned red-shift of both the first and second absorption bands. A similar behavior was also observed for biaryl-type molecules.[57,58]

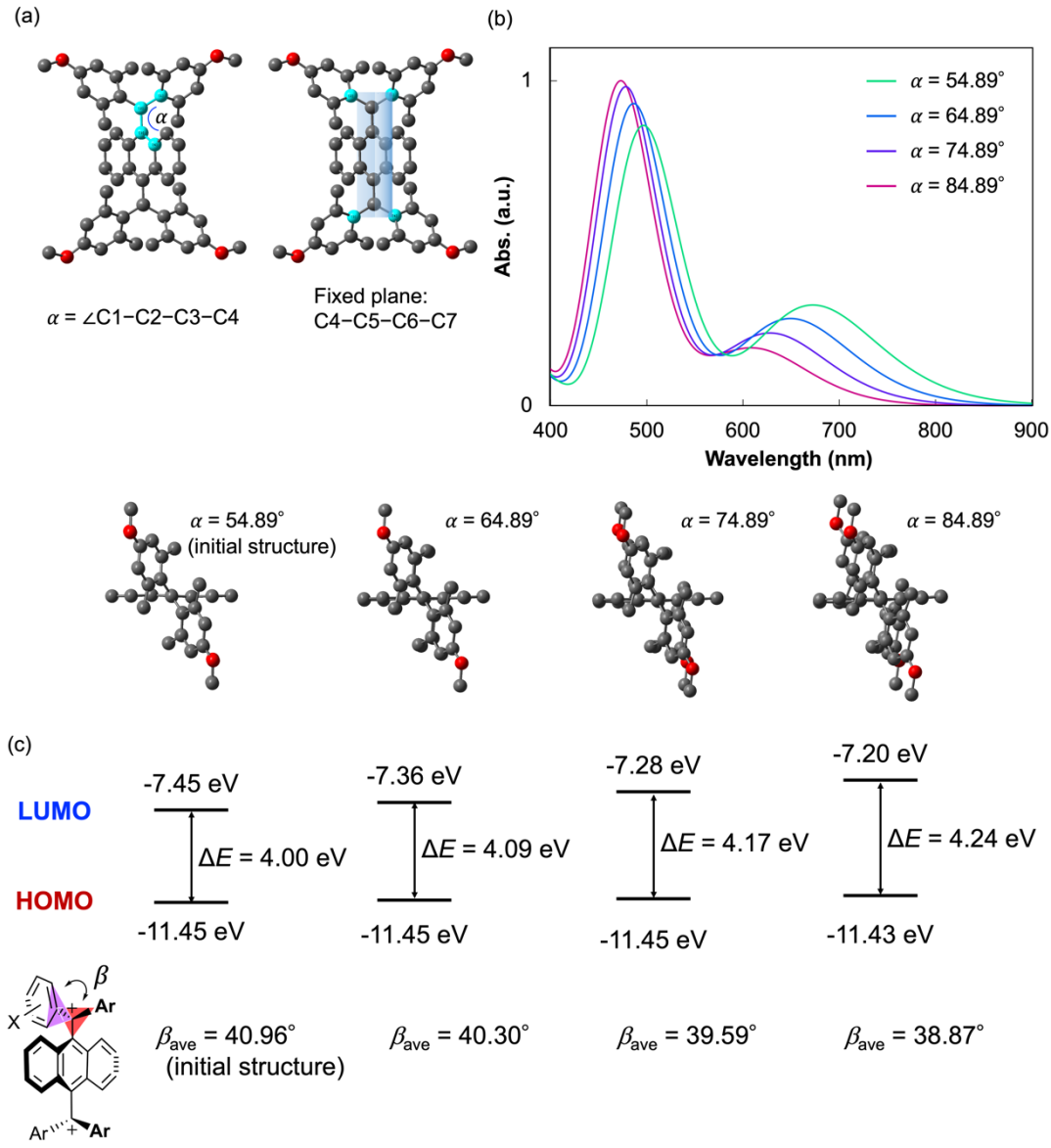

Figure 2-9. (a) Optimized structures obtained by varying the twist angle α ∠C1-C2-C3-C4 with the fixed plane C4-C5-C6-C7 from the energy-minimized structure (α = 54.89°) for $\mathbf{1e}^{2+}$. (b) A change in UV/Vis/NIR spectrum simulated by TD-DFT calculations of $\mathbf{1e}^{2+}$ while varying the twist angle α. (c) The corresponding HOMO and LUMO levels and the average torsion angles β_{ave} calculated by the DFT method.

2-2-6. Electrochromic behavior

Finally, constant-current electrochemical oxidation of the *ortho*-monosubstituted electron donor **1c** was monitored by UV/Vis/NIR spectroscopy in CH_2Cl_2 (Figure 2-10a). The colorless solution gradually turned deep violet with several isosbestic points, demonstrating that an intermediary radical cationic species is short-lived in this process, as in other dyrex systems such as **1a**/**1a**$^{2+}$. Regeneration of **1c** accompanied by a color change from deep violet color to nearly colorless was confirmed by reduction of as-prepared **1c**$^{2+}$ when the polarity of the electrodes was reversed (Figure 2-10b). Therefore, by introducing a substituent on the *ortho*-position of 4-methoxyphenyl groups, it is possible to induce an even longer wavelength-shifted NIR absorption upon electrochemical stimulation.

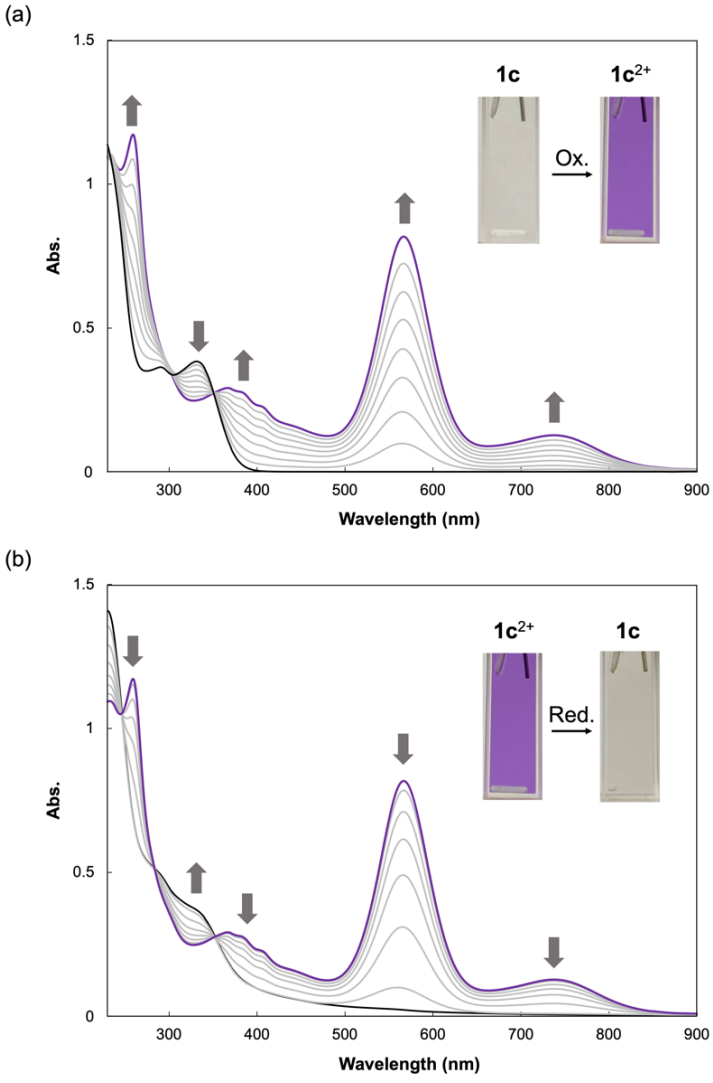

Figure 2-10. Changes in the UV/Vis/NIR spectrum of (a) **1c** (22.1 μM, 30 μA, every 16 min) upon constant-current electrochemical oxidation and (b) as-prepared **1c**$^{2+}$ (30 μA, every 16 min) upon constant-current electrochemical reduction in CH_2Cl_2 containing 0.05 M Bu_4NBF_4 as a supporting electrolyte.

2-3. Conclusion

In summary, the author has designed and synthesized a series of AQD derivatives with various substituents at the *ortho*-position of the 4-methoxyphenyl group.[63] Quantitative redox interconversions between neutral *ortho*-substituted AQDs and the corresponding dications were demonstrated on a preparative scale. X-ray crystallographic analyses of these derivatives revealed that the *ortho*-substituents have a significant steric effect on both the neutral and dicationic states. Electrochemical measurements suggest that the steric and electronic effects of *ortho*-substituents can modify both the redox behavior and potential, especially for *ortho*-disubstituted derivative **1e**/**1e**$^{2+}$. Furthermore, UV/Vis/NIR spectroscopy showed that the two main absorption bands of the dicationic dye can be controlled by adjusting the steric effects of the *ortho*-substituents. In particular, the end-absorption of the CT band of **1e**$^{2+}$ reaches 1100 nm, and the corresponding ε is enhanced up to 2.4 times larger than that of **1a**$^{2+}$. The *ortho*-substitution strategy, which allows fine-tuning of the HOMO/LUMO levels, is expected to lead to NIR absorption-switchable redox systems, paving the way for the development of functional organic dyes in materials and life science.

2-4. Experimental Section

2-4-1. General

All reactions were carried out under an argon atmosphere. All commercially available compounds were used without further purification. Dry MeCN was obtained by distillation from CaH_2 prior to use. Column chromatography was performed on silica gel 60N (KANTO KAGAKU, spherical neutral) of particle size 40-50 μm or Wakogel® 60N (neutral) of particle size 38-100 μm. ^1H and ^{13}C NMR spectra were recorded on a BRUKER Ascend™ 400 (^1H/400 MHz and ^{13}C/100MHz) spectrometer at 296 K unless otherwise indicated. IR spectra were measured on a Shimadzu IRAffinity-1S spectrophotometer using the attenuated total reflection (ATR) mode. Mass spectra were recorded on a JMS-T100GCV spectrometer in FD mode by Dr. Eri Fukushi and Mr. Yusuke Takata (GS-MS & NMR Laboratory, Research Faculty of Agriculture, Hokkaido University). Melting points were measured on a Yamato MP-21 and are uncorrected. UV/Vis/NIR spectra were recorded on a JASCO V-770 spectrophotometer. Redox potentials (E^{ox} and E^{red}) were measured on a BAS ALS-612EX by cyclic voltammetry in dry CH_2Cl_2 containing 0.1 M Bu_4NBF_4 as a supporting electrolyte. All of the values shown in the text are in E/V vs. SCE measured at the scan rate of 100 mVs^{-1}. Pt electrodes were used as the working (disk) and counter electrodes. The working electrode was polished using a water suspension of aluminum oxide (0.05 μm) before use. DFT calculations were performed with the Gaussian 16W program package.[56] The geometries of the compounds were optimized by using the CAM-B3LYP method in combination with the 6-31G* basis set unless otherwise indicated.

2-4-2. Synthetic procedures

11,11,12,12-Tetrakis(4-methoxy-2-methylphenyl)-9,10-anthraquinodimethane (1c)

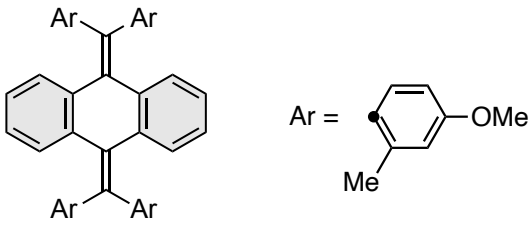

1c

A mixture of 11,11,12,12-tetrabromo-9,10-anthraquinodimethane[54] (780 mg, 1.50 mmol), 4-methoxy-2-methylphenylboronic acid (1.49 g, 9.00 mmol), K_2CO_3 (1.66 g, 12.0 mmol) and $Pd(PPh_3)_4$ (86.7 mg, 75.0 μmol) in toluene (15 mL), EtOH (1.5 mL), and H_2O (1.5 mL) was stirred at reflux for 14 h. After cooling to 25 ºC, the mixture was diluted with water and extracted with EtOAc five times. The combined organic layers were washed with water and brine, and dried over anhydrous Na_2SO_4. After filtration, the solvent was concentrated under reduced pressure. The crude product was purified by column chromatography on silica gel (hexane/CH_2Cl_2 = 1) to give **1c** (926 mg) as a white solid in 90% yield.

1c; Mp: 259-260 ºC; ^{1}H NMR (400 MHz, $CDCl_3$ at 330 K): δ/ppm 7.35 (4H, brs), 7.10 (4H, brs), 6.70 (12H, m), 3.75 (12H, s), 2.13 (12H, brs); ^{13}C NMR (100 MHz, $CDCl_3$): δ/ppm 158.21, 137.39, 136.00, 133.49, 130.98, 128.56, 126.43, 125.48, 125.06, 115.45, 111.48, 55.06, 21.57; IR (ATR): ν/cm^{-1} 3065, 3011, 2993, 2953, 2934, 2906, 2831, 1605, 1568, 1496, 1463, 1448, 1416, 1375, 1311, 1288, 1261, 1230, 1173, 1157, 1118, 1098, 1044, 988, 934, 864, 842, 829, 815, 797, 769, 749, 731, 726, 704, 668, 654, 630, 603, 585, 564, 541, 493, 446; LR-MS(FD) m/z (%): 687.38 (5), 686.38 (17), 685.38 (54), 684.37 (M^+, bp), 343.19 (1), 342.69 (4), 342.19 (M^{2+}, 7); HR-MS (FD) Calcd. for $C_{48}H_{44}O_4$: 684.32396; Found: 684.32260; UV/Vis (CH_2Cl_2): λ_{max}/nm (ε/Lmol^{-1}cm^{-1}) 332 (17400), 291 (16400).

11,11,12,12-Tetrakis(2-chloro-4-methoxyphenyl)-9,10-anthraquinodimethane (1d)

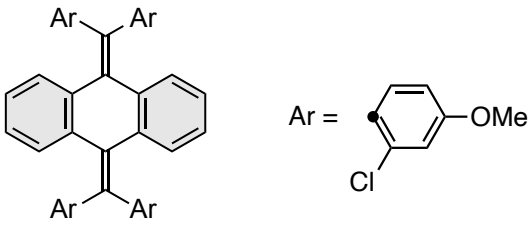

1d

A mixture of 11,11,12,12-tetrabromo-9,10-anthraquinodimethane[54] (1.04 mg, 2.00 mmol), 2-chloro-4-methoxyphenylboronic acid (1.79 g, 9.60 mmol), K_2CO_3 (1.77 g, 12.8 mmol) and $Pd(PPh_3)_4$ (116 mg, 100 μmol) in toluene (20 mL), EtOH (2.0 mL), and H_2O (2.0 mL) was stirred at 80 ºC for 20 h. After cooling to 25 ºC, the mixture was diluted with water and extracted with EtOAc five times. The combined organic layers were washed with water and brine, and dried over anhydrous Na_2SO_4. After filtration, the solvent was concentrated under reduced pressure. The crude product was purified by column chromatography on silica gel (hexane/EtOAc = 5) to give **1d** (1.39 g) as a white solid in 91% yield.

1d; Mp: 261-263 ºC; ^{1}H NMR (400 MHz, $CDCl_3$): δ/ppm 8.18 (2H, d, J = 8.4 Hz), 7.41-7.28 (4H, m), 7.08 (2H, d, J = 7.6 Hz), 7.03 (2H, d, J = 2.0 Hz), 6.77 (2H, d, J = 7.6 Hz), 6.73 (2H, d, J = 2.0 Hz), 6.69 (2H, d, J = 8.4 Hz), 3.77 (6H, s), 3.74 (6H, s); ^{13}C NMR (100 MHz, $CDCl_3$): δ/ppm 159.10, 158.93, 139.35, 136.94, 136.44, 134.63, 134.34, 133.41, 132.82, 132.04, 131.45, 130.62, 127.68, 126.57, 125.97, 125.51, 115.09, 114.81, 113.18, 113.03, 55.41, 55.38; IR (ATR): ν/cm^{-1} 3074, 3005, 2956, 2935, 2905, 2834, 1599, 1555, 1490, 1458, 1437, 1399, 1284, 1256, 1220, 1182, 1039, 976, 949, 894, 882, 873, 854, 845, 833, 810, 794, 766, 732, 719, 685, 655, 626, 610, 594, 573, 559, 483, 457; LR-MS(FD) m/z (%): 771.15 (8), 770.15 (18), 769.15 (26), 768.15 (57), 767.15 (48), 766.15 (bp), 765.15 (36), 764.15 (M^+, 69), 383.08 (7), 382.08 (M^{2+}, 5); HR-MS (FD) Calcd. for $C_{44}H_{32}Cl_4O_4$: 764.10547; Found: 764.10540; UV/Vis (CH_2Cl_2): λ_{max}/nm (ε/Lmol^{-1}cm^{-1}) 310 (sh, 17200), 290 (20000).

11,11,12,12-Tetrakis(4-methoxy-2,6-dimethylphenyl)-9,10-anthraquinodimethane (1e)

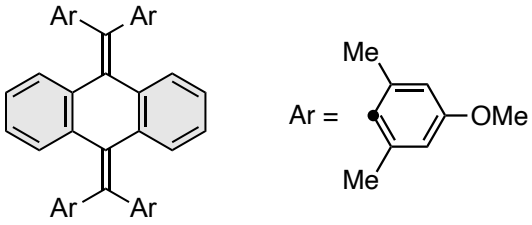

1e

To a solution of 2-bromo-5-methoxy-1,3-dimethylbenzene[57] (1.33 g, 6.19 mmol) in dry THF (30 mL) was added *n*BuLi (1.59 M solution in hexane, 3.9 mL, 6.19 mmol) dropwise over 5 min at -78 ºC, and the mixture was stirred for 1 h. To the solution was added dichloro(*N*,*N*,*N*',*N*'-tetramethylethane-1,2-diamine)zinc(II) (suspension in THF, 15 mL, 6.19 mmol) dropwise over 5 min at -78 ºC. The mixture was gradually warmed up to -50 ºC, and stirred for 1 h. To the solution were added 11,11,12,12-tetrabromo-9,10-anthraquinodimethane[54] (535 mg, 1.03 mmol) and $Pd(PPh_3)_4$ (119 mg, 103 μmol), and the mixture was stirred at reflux for 44 h. After cooling to 25 ºC, the mixture was diluted with water and extracted with EtOAc five times. The combined organic layers were washed with water and brine, and dried over anhydrous Na_2SO_4. After filtration, the solvent was concentrated under reduced pressure. The crude product was purified by column chromatography on silica gel (hexane/EtOAc = 7) to give **1e** (181 mg) as a yellow solid in 24% yield.

1e; Mp: 230-231 ºC; ^{1}H NMR (400 MHz, $CDCl_3$): δ/ppm 7.35 (4H, dd, *J* = 3.4, 6.1 Hz), 6.74 (4H, dd, *J* = 3.4, 6.1 Hz), 6.48 (8H, s), 3.75 (12H, s), 2.32 (12H, brs), 1.98 (12H, brs); ^{13}C NMR (100 MHz, $CDCl_3$): δ/ppm 158.05, 140.56, 140.31, 137.53, 137.05, 136.64, 135.22, 127.79, 125.61, 114.91, 112.37, 54.92, 22.96, 22.02; IR (ATR): ν/cm^{-1} 3051, 3003, 2934, 2917, 2834, 1600, 1569, 1476, 1456, 1437, 1371, 1309, 1273, 1195, 1154, 1138, 1112, 1070, 1064, 1032, 996, 947, 854, 842, 835, 770, 740, 716, 693, 664, 654, 631, 603, 586, 512; LR-MS(FD) m/z (%): 743.46 (6), 742.45 (20), 741.44 (60), 740.44 (M^+, bp); HR-MS (FD) Calcd. for $C_{52}H_{52}O_4$: 740.38656; Found: 740.38881; UV/Vis (CH_2Cl_2): λ_{max}/nm (ε/Lmol^{-1}cm^{-1}) 394 (24900).

Anthracene-9,10-diyl-bis[bis(4-methoxy-2-methylphenyl)methylium] bis(hexachloroantimonate) [$\mathbf{1c}^{2+}(SbCl_6^-)_2$]

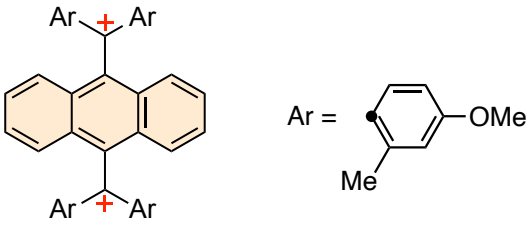

$\mathbf{1c}^{2+}(SbCl_6^-)_2$

To a solution of **1c** (119 mg, 174 μmol) in dry CH_2Cl_2 (5.1 mL) was added tris(4-bromophenyl)aminium hexachloroantimonate (283 mg, 347 μmol), and the mixture was stirred at 25 ºC for 30 min. The addition of dry ether led to precipitation of the dication salt. The precipitates were washed with dry ether five times, and collected by filtration to give $\mathbf{1c}^{2+}(SbCl_6^-)_2$ (229 mg) as a dark-violet powder in 97% yield.

$\mathbf{1c}^{2+}(SbCl_6^-)_2$; Mp: 164-165 ºC; ^{1}H NMR (400 MHz, CD_3CN): δ/ppm 7.62 (4H, dd, *J* =3.3, 6.9 Hz), 7.54 (4H, dd, *J* =3.3, 6.9 Hz), 7.47 (4H, d, *J* = 8.3 Hz), 7.20 (4H, brs), 7.09 (4H, d, *J* = 8.3 Hz), 4.12 (12H, s), 2.04 (12H, brs); ^{13}C NMR (100 MHz, CD_3CN): δ/ppm 190.70, 173.45, 152.46, 146.19, 142.11, 139.15, 132.40, 130.04, 126.62, 122.14, 116.43, 58.32, 22.50; IR (ATR, KBr pellet): ν/cm^{-1} 3078, 2978, 2941, 2841, 1603, 1583, 1559, 1522, 1456, 1441, 1423, 1358, 1301, 1266, 1226, 1188, 1174, 1105, 1065, 1031, 997, 944, 927, 858, 818, 767, 730, 562, 513; LR-MS(FD) m/z (%): 685.32 (12), 684.31 ($[M^{2+}+e^-]^+$, 29), 344.16 (2), 343.66 (6), 343.16 (16), 342.66 (56), 342.16 (M^{2+}, bp); HR-MS (FD) Calcd. For $C_{48}H_{44}O_4$: 684.32396; Found: 684.32558; UV/Vis/NIR (CH_2Cl_2): λ_{max}/nm (ε/Lmol^{-1}cm^{-1}) 734 (17600), 570 (73100), 262 (85500).

Reduction of dication salt $\mathbf{1c}^{2+}(SbCl_6^-)_2$ to **1c**:

To a solution of $\mathbf{1c}^{2+}(SbCl_6^-)_2$ (30.3 mg, 22.4 μmol) in dry MeCN (1.1 mL) was added activated zinc powder (146 mg, 2.23 mmol). The mixture was stirred at 25 ºC for 30 min, and then diluted with water. The whole mixture was extracted with EtOAc five times. The combined organic layers were washed with water and brine, and dried over anhydrous Na_2SO_4. After filtration through silica gel, the solvent was concentrated under reduced pressure to give **1c** (15.1 mg) as a white solid in 98% yield.

Anthracene-9,10-diyl-bis[bis(2-chloro-4-methoxyphenyl)methylium] bis(hexachloroantimonate) [$\mathbf{1d}^{2+}(SbCl_6^-)_2$]

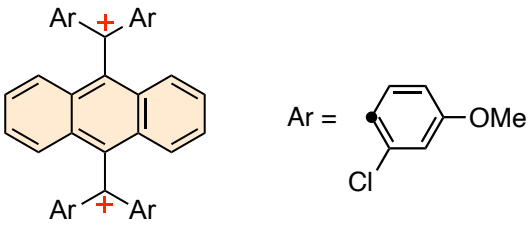

$\mathbf{1d}^{2+}(SbCl_6^-)_2$

To a solution of **1d** (218 mg, 284 μmol) in dry CH_2Cl_2 (5.7 mL) was added tris(4-bromophenyl)aminium hexachloroantimonate (464 mg, 568 μmol), and the mixture was stirred at 25 ºC for 30 min. The addition of dry ether led to precipitation of the dication salt. The precipitates were washed with dry ether five times, and collected by filtration to give $\mathbf{1d}^{2+}(SbCl_6^-)_2$ (397 mg) as a dark-blue powder in 97% yield.

$\mathbf{1d}^{2+}(SbCl_6^-)_2$; Mp: 193-194 ºC; ^{1}H NMR (400 MHz, CD_3CN): δ/ppm 7.72-7.57 (12H, m), 7.46 (4H, d, J = 2.4 Hz), 7.18 (4H, d, J = 9.0 Hz), 4.17 (12H, s); ^{13}C NMR (100 MHz, CD_3CN): δ/ppm 187.10, 174.53, 146.72, 145.50, 142.59, 136.24, 133.17, 130.47, 126.75, 122.22, 117.38, 59.34; IR (ATR, KBr pellet): ν/cm^{-1} 3102, 2942, 2843, 1596, 1573, 1522, 1437, 1417, 1364, 1306, 1260, 1212, 1180, 1159, 1138, 1041, 1009, 928, 870, 816, 762, 736, 718, 608, 550; LR-MS(FD) m/z (%): 771.16 (6), 770.16 (16), 769.16 (22), 768.16 (50), 767.16 (42), 766.16 (86), 765.16 (32), 764.16 ([M^{2+}+e$^-$]$^+$, 59), 386.07 (5), 385.58 (9), 385.08 (19), 384.58 (27), 384.08 (58), 383.58 (47), 383.08 (bp), 382.58 (34), 382.08 (M^{2+}, 66); HR-MS (FD) Calcd. for $C_{44}H_{32}Cl_4O_4$: 764.10547; Found: 764.10426; UV/Vis/NIR (CH_2Cl_2): λ_{max}/nm (ε/Lmol^{-1}cm^{-1}) 843 (12800), 591 (75100), 385 (21600), 262 (90500).

Reduction of dication salt $\mathbf{1d}^{2+}(SbCl_6^-)_2$ to **1d**:

To a solution of $\mathbf{1d}^{2+}(SbCl_6^-)_2$ (20.6 mg, 14.4 μmol) in dry MeCN (1.4 mL) was added activated zinc powder (93.0 mg, 1.42 mmol). The mixture was stirred at 25 ºC for 30 min, and then diluted with water. The whole mixture was extracted with EtOAc five times. The combined organic layers were washed with water and brine, and dried over anhydrous Na_2SO_4. After filtration through silica gel, the solvent was concentrated under reduced pressure to give **1d** (10.6 mg) as a white solid in 96% yield.

Anthracene-9,10-diyl-bis[bis(4-methoxy-2,6-dimethylphenyl)methylium] bis(hexachloroantimonate) [$\mathbf{1e}^{2+}(SbCl_6^-)_2$]

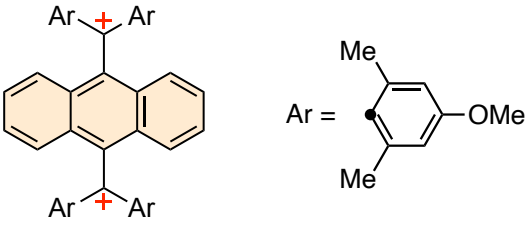

$\mathbf{1e}^{2+}(SbCl_6^-)_2$

To a solution of **1e** (43.0 mg, 58.0 μmol) in dry CH_2Cl_2 (1.2 mL) was added tris(4-bromophenyl)aminium hexachloroantimonate (94.6 mg, 116 μmol), and the mixture was stirred at 25 ºC for 30 min. The addition of dry ether led to precipitation of the dication salt. The precipitates were washed with dry ether five times, and collected by filtration to give $\mathbf{1e}^{2+}(SbCl_6^-)_2$ (397 mg) as a dark-green powder in 97% yield.

$\mathbf{1e}^{2+}(SbCl_6^-)_2$; Mp: 163-164 ºC; ^{1}H NMR (400 MHz, CD_3CN): δ/ppm 7.91 (4H, brs), 7.59 (4H, brs), 7.20 (4H, s), 6.81 (4H, s), 4.08 (12H, s), 2.21 (12H, brs), 1.58 (12H, brs); ^{13}C NMR (100 MHz, CD_3CN): δ/ppm 186.97, 171.95, 154.03, 150.24, 144.22, 134.29, 130.84, 130.52, 126.88, 126.51, 121.13, 120.40, 58.05, 23.72, 23.57; IR (ATR, KBr pellet): ν/cm^{-1} 3081, 2977, 2937, 2860, 2839, 1581, 1525, 1473, 1441, 1414, 1349, 1295, 1252, 1191, 1154, 1025, 990, 961, 929, 867, 844, 770, 752, 729, 706, 670, 605, 524, 475; LR-MS(FD) m/z (%): 742.44 (10), 741.43 (28), 740.43 ($[M^{2+}+e^-]^+$, 55), 739.42 (30), 738.41(21), 737.40 (8), 371.71 (8), 371.21(20), 370.71(60), 370.21(M^{2+}, bp); HR-MS (FD) Calcd. for $C_{52}H_{52}O_4$: 740.38656; Found: 740.38821; UV/Vis/NIR (CH_2Cl_2): λ_{max}/nm (ε/Lmol^{-1}cm^{-1}) 855 (21100), 650 (47100), 476 (18900), 266 (91700).

Reduction of dication salt $\mathbf{1e}^{2+}(SbCl_6^-)_2$ to **1e**:

To a solution of $\mathbf{1e}^{2+}(SbCl_6^-)_2$ (13.4 mg, 9.50 μmol) in dry MeCN (1.0 mL) was added activated zinc powder (62.2 mg, 951 μmol). The mixture was stirred at 25 ºC for 30 min, and then diluted with water. The whole mixture was extracted with EtOAc five times. The combined organic layers were washed with water and brine, and dried over anhydrous Na_2SO_4. After filtration through silica gel, the solvent was concentrated under reduced pressure to give **1e** (7.0 mg) as a yellow solid in 99% yield.

2-4-3. Crystal data

Method

A suitable crystal was selected and measured on a Rigaku XtaLAB Synergy (Cu-Kα radiation, λ = 1.54184 Å) with HyPix diffractometer. The crystal was kept at 150 K during data collection. Using Olex2,[58] the structure was solved with the SHELXT[59] structure solution program using Intrinsic Phasing and refined with the SHELXL[60] refinement package using Least Squares minimization.

*Crystal data of **1c***

Crystals were obtained by recrystallization from CH_2Cl_2/MeOH. MF: $C_{48}H_{44}O_4$, FW: 684.83, colorless plate, 0.12 × 0.05 × 0.01 mm^3, monoclinic *I*2/a, a = 22.0117(9) Å, b = 7.5538(3) Å, c = 25.9466(11) Å, β = 109.791(5)º, V = 4059.4(3) $Å^3$, ρ (Z = 4) = 1.121 g cm^{-3}. A total 13310 reflections were measured at T = 150 K. Numerical absorption correction was applied (μ = 0.548 mm^{-1}). The final R_1 and wR_2 values are 0.0468 (I > 2σI) and 0.1417 (all data) for 4065 reflections and 240 parameters Estimated standard deviations are 0.0018-0.002 Å for bond lengths and 0.12-0.16º for bond angles. Solvent mask procedure was used for the analysis. CCDC 2225557.

*Crystal data of **1d***

Crystals were obtained by recrystallization from $CHCl_3$/MeOH. MF: $C_{44}H_{32}Cl_4O_4$, FW: 766.49, colorless block, 0.13 × 0.10 × 0.08 mm^3, monoclinic $P2_1$/c, a = 13.00534(10) Å, b = 18.30266(16) Å, c = 15.93071(14) Å, β = 104.0340(8)º, V = 3678.84(6) $Å^3$, ρ (Z = 4) = 1.384 g cm^{-3}. A total 13470 reflections were measured at T = 150 K. Numerical absorption correction was applied (μ = 9.799 mm^{-1}). The final R_1 and wR_2 values are 0.0554 (I > 2σI) and 0.1471 (all data) for 13470 reflections and 529 parameters Estimated standard deviations are 0.002-0.011 Å for bond lengths and 0.17-0.5º for bond angles. CCDC 2225558.

*Crystal data of **1e***

Crystals were obtained by recrystallization from $CHCl_3$/Hexane. MF: $C_{52}H_{52}O_4$, FW: 740.93, yellow plate, 0.15 × 0.10 × 0.02 mm^3, monoclinic C2c, a = 48.3263(11) Å, b = 8.21941(16) Å, c = 22.3771(4) Å, β = 97.539(2)º, V = 8811.6(3) $Å^3$, ρ (Z = 8) = 1.117 g cm^{-3}. A total 13470 reflections were measured at T = 150 K. Numerical absorption correction was applied (μ = 0.538 mm^{-1}). The final R_1 and wR_2 values are 0.0528 (I > 2σI) and 0.1552 (all data) for 9069 reflections and 529 parameters Estimated standard deviations are 0.002-0.007 Å for bond lengths and 0.15-0.4º for bond angles. Solvent mask procedure was used for the analysis. CCDC 2225559.

Crystal data of ***1c***$^{2+}$*(*$SbCl_6^-$*)*$_2$

Crystals were obtained by recrystallization from dry CH_2Cl_2/ether. MF: $C_{48}H_{44}O_4Cl_{12}Sb_2$, FW: 1353.73, purple plate, 0.35 × 0.03 × 0.002 mm^3, monoclinic $P2_1/c$, a = 14.6910(5) Å, b = 10.3742(16) Å, c = 20.0759(8) Å, β = 105.698(4)º, V = 2945.59(19) Å^3, ρ (Z = 2) = 1.526 g cm^{-3}. A total 16702 reflections were measured at T = 150 K. Numerical absorption correction was applied (μ = 12.591 mm^{-1}). The final R_1 and wR_2 values are 0.0552 (I > 2σI) and 0.1679 (all data) for 5866 reflections and 387 parameters Estimated standard deviations are 0.0015-0.06 Å for bond lengths and 0.06-3.0º for bond angles. Solvent mask procedure was used for the analysis. CCDC 2225560.

Crystal data of ***1d***$^{2+}$*(*$SbCl_6^-$*)*$_2$

Crystals were obtained by recrystallization from dry CH_2Cl_2/ether. MF: $C_{44}H_{32}O_4Cl_{16}Sb_2$, FW: 1435.39, blue plate, 0.20 × 0.05 × 0.01 mm^3, triclinic $P\bar{1}$, a = 9.73711(15) Å, b = 11.1901(2) Å, c = 12.8218(3) Å, α = 100.7375(17)º, β = 91.7028(16)º, γ = 92.4705(14)º, V = 1370.30(5) Å^3, ρ (Z = 1) = 1.739 g cm^{-3}. A total 19756 reflections were measured at T = 150 K. Numerical absorption correction was applied (μ = 15.327 mm^{-1}). The final R_1 and wR_2 values are 0.1130 (I > 2σI) and 0.3519 (all data) for 5578 reflections and 310 parameters Estimated standard deviations are 0.002-0.014 Å for bond lengths and 0.09-0.8º for bond angles. CCDC 2225561.

Crystal data of ***1e***$^{2+}$*(*$SbCl_6^-$*)*$_2$

Crystals were obtained by recrystallization from dry MeCN/ether. MF: $C_{52}H_{52}O_4Cl_{12}Sb_2$, FW: 1409.83, green plate, 0.20 × 0.18 × 0.03 mm^3, triclinic $P\bar{1}$, a = 9.08563(8) Å, b = 11.33164(10) Å, c = 14.07306(13) Å, α = 95.4062(7)º, β = 100.5335(8)º, γ = 94.3919(7)º, V = 1411.61(2) Å^3, ρ (Z = 1) = 1.658 g cm^{-3}. A total 25128 reflections were measured at T = 100 K. Numerical absorption correction was applied (μ = 13.163 mm^{-1}). The final R_1 and wR_2 values are 0.0258 (I > 2σI) and 0.0730 (all data) for 5813 reflections and 326 parameters Estimated standard deviations are 0.0005-0.003 Å for bond lengths and 0.018-0.03º for bond angles. CCDC 2225562.

2-4-4. (TD-)DFT calculations at the CAM-B3LYP/6-31G* level

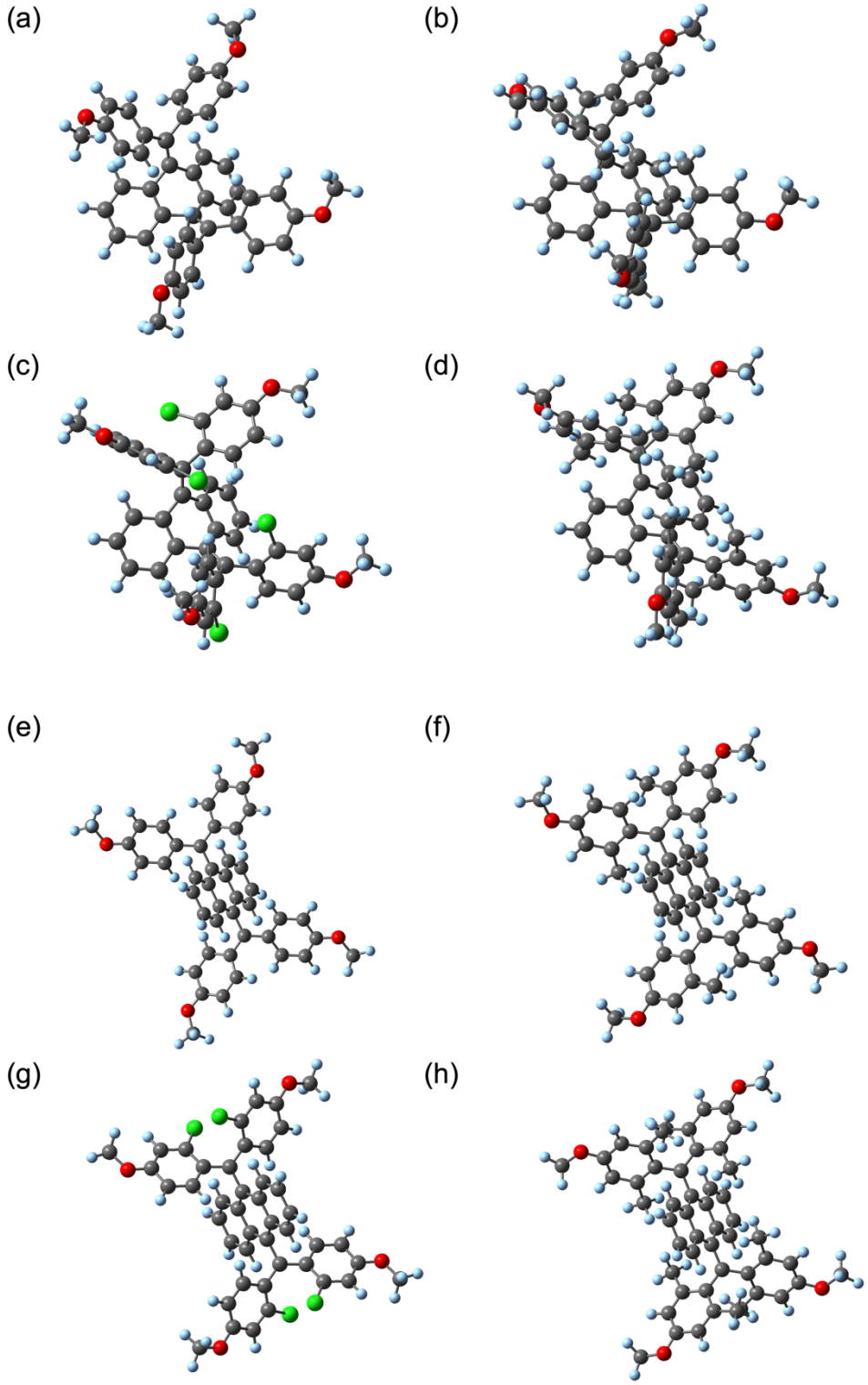

Figure 2-11. Optimized structures of (a) **1a**, (b) **1c**, (c) **1d**, (d) **1e**, (e) $\mathbf{1a}^{2+}$, (f) $\mathbf{1c}^{2+}$, (g) $\mathbf{1d}^{2+}$, and (h) $\mathbf{1e}^{2+}$obtained by DFT calculations (CAM-B3LYP/6-31G*).

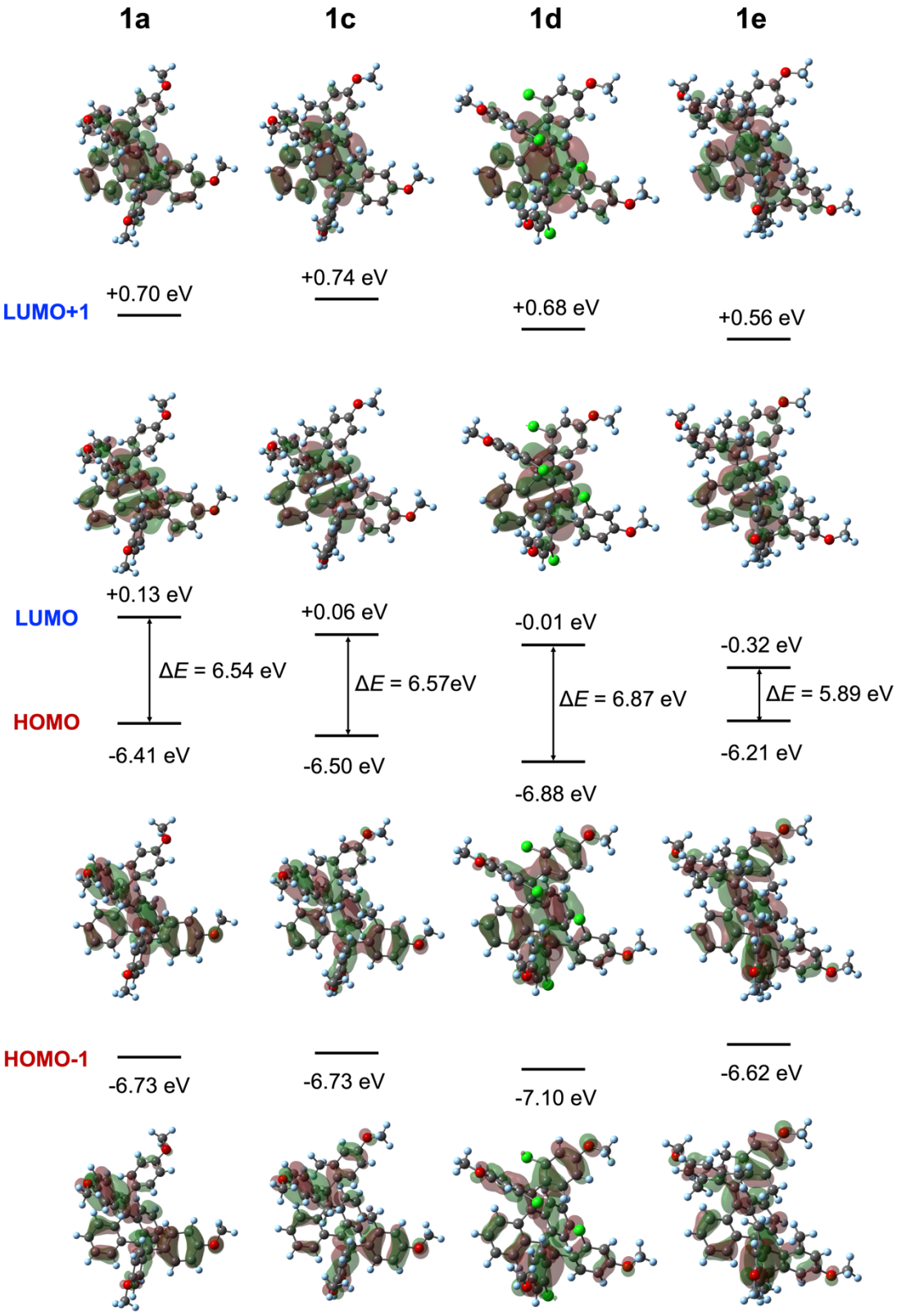

Figure 2-12. HOMO and LUMO levels calculated by the DFT method (CAM-B3LYP/6-31G*) based on the optimized structures of **1a**, **1c**, **1d**, and **1e**.

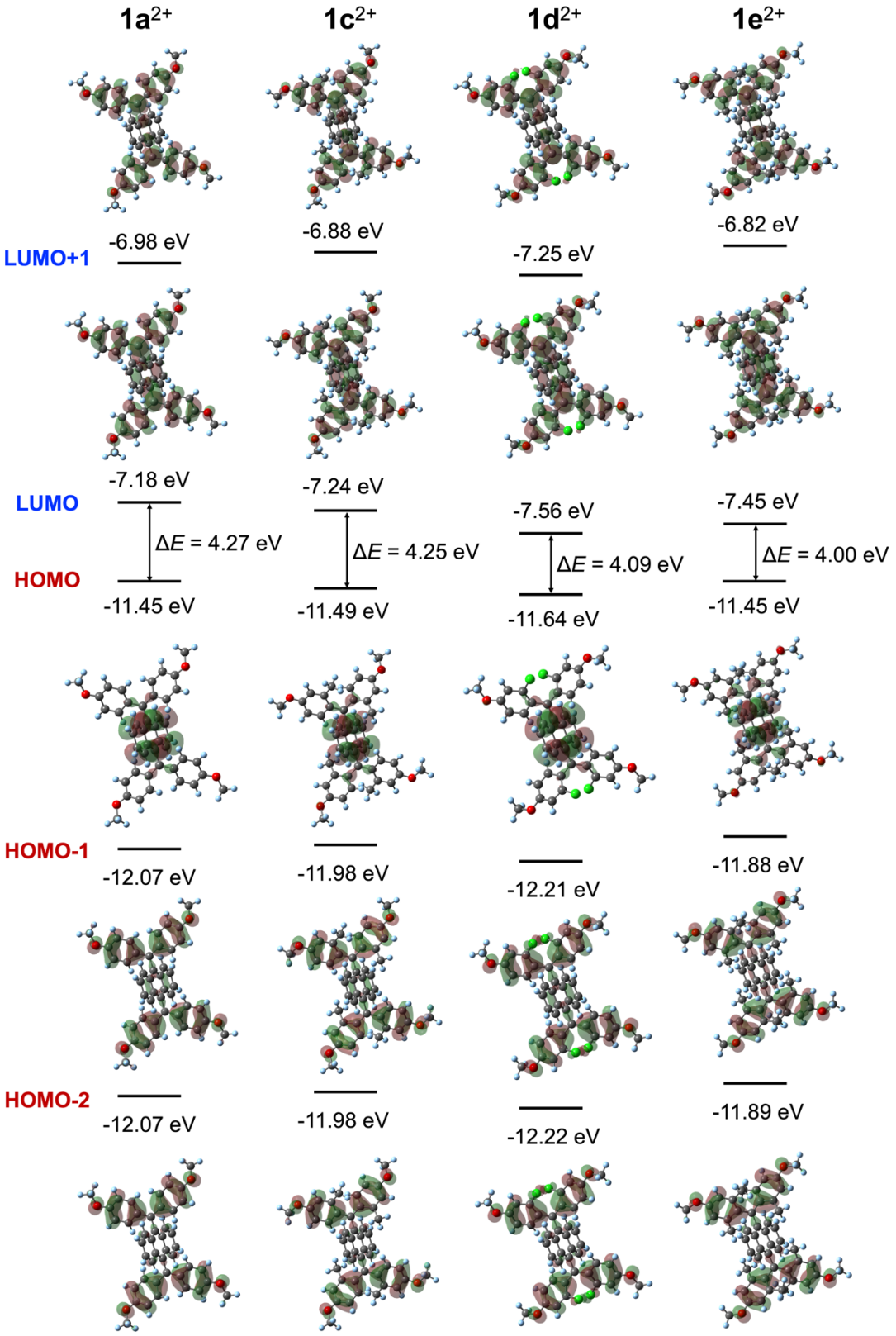

Figure 2-13. HOMO and LUMO levels calculated by the DFT method (CAM-B3LYP/6-31G*) based on the optimized structures of **1a**$^{2+}$, **1c**$^{2+}$, **1d**$^{2+}$, and **1e**$^{2+}$.

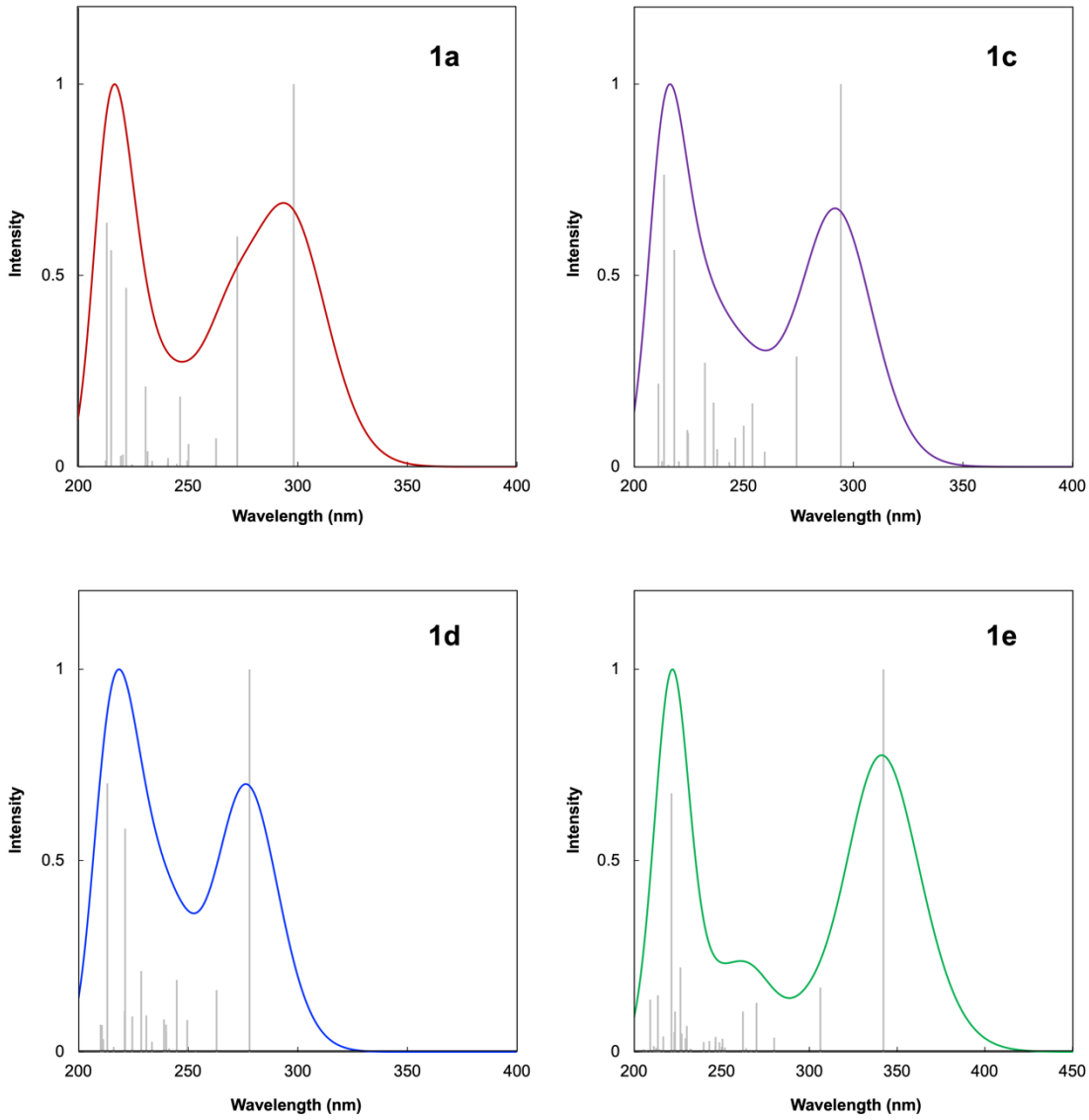

Figure 2-14. Simulated UV/Vis spectra by TD-DFT calculations (CAM-B3LYP/6-31G*) for corresponding neutral donors **1**. For detailed information on excitation energies and oscillator strengths, see Ref. [63].

2-5. References

[1] S. Hünig, M. Kemmer, H. Wenner, I. F. Perepichka, P. Bäuerle, A. Emge, G. Gescheid, *Chem. Eur. J.* **1999**, *5*, 1969–1973.

[2] S. Hünig, M. Kemmer, H. Wenner, F. Barbosa, G. Gescheidt, I. F. Perepichka, P. Bäuerle, A. Emge, K. Peters, *Chem. Eur. J.* **2000**, *6*, 2618– 2632.

[3] H. A. Shindy, *Dyes Pigm.* **2017**, *145*, 505–513.

[4] L. Hu, Z. Yan, H. Xu, *RSC Adv.* **2013**, *3*, 7667.

[5] S. Khopkar, G. Shankarling, *Dyes Pigm.* **2019**, *170*, 107645.

[6] M. Han, B. Kim, H. Lim, H. Jang, E. Kim, *Adv. Mater.* **2020**, *32*, 1905096.

[7] H. M. Kim, H. J. Lee, H. K. Lee, T. G. Hwang, J. W. Namgoong, J. M. Lee, S. Kim, J. P. Kim, *Dyes Pigm.* **2021**, *190*, 109288.

[8] Y. Liu, Z. Zhang, X. Chen, S. Xu, S. Cao, *Dyes Pigm.* **2016**, *128*, 179–189.

[9] N. Kobayashi, T. Furuyama, K. Satoh, *J. Am. Chem. Soc.* **2011**, *133*, 19642–19645.

[10] J. Fabian, H. Nakazumi, M. Matsuoka, *Chem. Rev.* **1992**, *92*, 1197–1226.

[11] K. Y. Law, *Chem. Rev.* **1993**, *93*, 449–486.

[12] L. Li, X. Dong, J. Li, J. Wei, *Dyes Pigm.* **2020**, *183*, 108756.

[13] S. Ghosh, S. Cherumukkil, C. H. Suresh, A. Ajayaghosh, *Adv. Mater.* **2017**, *29*, 1703783.

[14] H. Han, Y. J. Lee, J. Kyhm, J. S. Jeong, J. Han, M. K. Yang, K. M. Lee, Y. Choi, T. Yoon, H. Ju, S. Ahn, J. A. Lim, *Adv. Funct. Mater.* **2020**, *30*, 2006236.

[15] X. Han, X. Chen, T. Gordon, S. Holdcroft, *Macromol. Rapid Commun.* **2009**, *30*, 2089–2095.

[16] T. Okamura, T. Kitagawa, K. Koike, S. Fukuda, *J. Soc. Inf. Disp.* **2004**, *12*, 527–531.

[17] K. Yang, L. Wang, Q. Zhang, *J. Mater. Sci. Mater. Electron.* **2015**, *26*, 2222–2229.

[18] B. C. O'Regan, I. López-Duarte, M. V. Martínez-Díaz, A. Forneli, J. Albero, A. Morandeira, E. Palomares, T. Torres, J. R. Durrant, *J. Am. Chem. Soc.* **2008**, *130*, 2906–2907.

[19] N. Sekar, R. K. Raut, P. G. Umape, *Mater. Sci. Eng. B* **2010**, *168*, 259–262.

[20] M. Ince, J. Bartelmess, D. Kiessling, K. Dirian, M. V. Martínez-Díaz, T. Torres, D. M. Guldi, *Chem. Sci.* **2012**, *3*, 1472.

[21] H. Zhang, G. Wicht, C. Gretener, M. Nagel, F. Nüesch, Y. Romanyuk, J.-N. Tisserant, R. Hany, *Sol. Energy Mater. Sol. Cells* **2013**, *118*, 157–164.

[22] B. Hu, W. Zhang, J. Wu, Z. Pang, S. Zhao, Z. Lu, Y. Huang, *Dyes Pigm.* **2019**, *166*, 467–472.

[23] G. Chen, H. Sasabe, T. Igarashi, Z. Hong, J. Kido, *J. Mater. Chem. A* **2015**, *3*, 14517–14534.

[24] J. He, Y. J. Jo, X. Sun, W. Qiao, J. Ok, T. Kim, Z. Li, *Adv. Funct. Mater.* **2021**, *31*, 2008201.

[25] D. Meng, R. Zheng, Y. Zhao, E. Zhang, L. Dou, Y. Yang, *Adv. Mater.* **2022**, *34*, 2107330.

[26] J. O. Escobedo, O. Rusin, S. Lim, R. M. Strongin, *Curr. Opin. Chem. Biol.* **2010**, *14*, 64–70.

[27] S. Luo, E. Zhang, Y. Su, T. Cheng, C. Shi, *Biomaterials* **2011**, *32*, 7127–7138.

[28] A. Yuan, J. Wu, X. Tang, L. Zhao, F. Xu, Y. Hu, *J. Pharm. Sci.* **2013**, *102*, 6–28.

[29] L. Wu, Y. Sun, K. Sugimoto, Z. Luo, Y. Ishigaki, K. Pu, T. Suzuki, H.-Y. Chen, D. Ye, *J. Am. Chem. Soc.* **2018**, *140*, 16340–16352.

[30] H.-B. Cheng, Y. Li, B. Z. Tang, J. Yoon, *Chem. Soc. Rev.* **2020**, *49*, 21–31.
[31] B. Li, M. Zhao, F. Zhang, *ACS Materials Lett.* **2020**, *2*, 905–917.
[32] L. Wu, Y. Ishigaki, Y. Hu, K. Sugimoto, W. Zeng, T. Harimoto, Y. Sun, J. He, T. Suzuki, X. Jiang, H.-Y. Chen, D. Ye, *Nat. Commun.* **2020**, *11*, 446.
[33] L. Wu, Y. Ishigaki, W. Zeng, T. Harimoto, B. Yin, Y. Chen, S. Liao, Y. Liu, Y. Sun, X. Zhang, Y. Liu, Y. Liang, P. Sun, T. Suzuki, G. Song, Q. Fan, D. Ye, *Nat. Commun.* **2021**, *12*, 6145.
[34] L. Wu, W. Zeng, Y. Ishigaki, J. Zhang, H. Bai, T. Harimoto, T. Suzuki, D. Ye, *Angew. Chem. Int. Ed.* **2022**, *61*, e202209248.
[35] P. Monk, R. Mortimer, D. Rosseinsky, *Electrochromism and Electrochromic Devices*, Cambridge University Press, Cambridge, **2007**.
[36] D. R. Rosseinsky, P. M. S. Monk, R. J. Mortimer, *Electrochromic Materials and Devices*, Wiley-VCH, Weinheim, Germany, **2013**.
[37] S. Mujawar, P. Patil, *Electrochromism in Pristine and Doped Niobium Oxide Thin Films: Spray Pyrolytic Synthesis of Niobium Oxide Thin Films for Smart Window Application*, LAP LAMBERT Academic Publishing, **2016**.
[38] W. Zhang, H. Li, E. Hopmann, A. Y. Elezzabi, *Nat. Photonics* **2020**, *10*, 825–850.
[39] Z. Wang, X. Wang, S. Cong, J. Chen, H. Sun, Z. Chen, G. Song, F. Geng, Q. Chen, Z. Zhao, *Nat. Commun.* **2020**, *11*, 302.
[40] B. Li, J. Dang, Q. Zhuang, Z. Lv, *Chem. Asian J.* **2022**, *17*, e202200022.
[41] T. Suzuki, Y. Sakano, Y. Tokimizu, Y. Miura, R. Katoono, K. Fujiwara, N. Yoshioka, N. Fujii, H. Ohno, *Chem. Asian J.* **2014**, *9*, 1841–1846.
[42] C. Zhu, X. Ji, D. You, T. L. Chen, A. U. Mu, K. P. Barker, L. M. Klivansky, Y. Liu, L. Fang, *J. Am. Chem. Soc.* **2018**, *140*, 18173–18182.
[43] D. T. Christiansen, A. L. Tomlinson, J. R. Reynolds, *J. Am. Chem. Soc.* **2019**, *141*, 3859–3862.
[44] P. W. Antoni, T. Bruckhoff, M. M. Hansmann, *J. Am. Chem. Soc.* **2019**, *141*, 9701–9711.
[45] Y. Ishigaki, T. Harimoto, K. Sugimoto, L. Wu, W. Zeng, D. Ye, T. Suzuki, *Chem. Asian J.* **2020**, *15*, 1147–1155.
[46] P. Rietsch, S. Sobottka, K. Hoffmann, A. A. Popov, P. Hildebrandt, B. Sarkar, U. Resch-Genger, S. Eigler, *Chem. A Eur. J.* **2020**, *26*, 17361– 17365.
[47] R. Rausch, M. I. S. Röhr, D. Schmidt, I. Krummenacher, H. Braunschweig, F. Würthner, *Chem. Sci.* **2021**, *12*, 793–802.
[48] Y. Ishigaki, T. Harimoto, K. Sugawara, T. Suzuki, *J. Am. Chem. Soc.* **2021**, *143*, 3306–3311.
[49] B. Sk, M. Sarkar, K. Singh, A. Sengupta, A. Patra, *Chem. Commun.* **2021**, *57*, 13590–13593.
[50] P. W. Antoni, C. Golz, M. M. Hansmann, *Angew. Chem. Int. Ed.* **2022**, *61*, e202203064.
[51] Y. Ishigaki, M. Takata, T. Shimajiri, L. Wu, W. Zeng, D. Ye, T. Suzuki, *Chem. A Eur. J.* **2022**, *28*, e202202457.
[52] Y. Ishigaki, K. Sugawara, M. Yoshida, M. Kato, T. Suzuki, *Bull. Chem. Soc. Jpn.* **2019**, *92*, 1211–1217.

[53] Y. Ishigaki, K. Sugawara, T. Tadokoro, Y. Hayashi, T. Harimoto, T. Suzuki, *Chem. Commun.* **2021**, *57*, 7201–7214.
[54] R. Neidlein, M. Winter, *Synthesis* **1998**, *1998*, 1362–1366.
[55] Y. Sakano, R. Katoono, K. Fujiwara, T. Suzuki, *Chem. Lett.* **2014**, *43*, 1143–1145.
[56] M. J. Frisch, G. W. Trucks, H. B. Schlegel, G. E. Scuseria, M. A. Robb, J. R. Cheeseman, G. Scalmani, V. Barone, G. A. Petersson, X. Nakatsuji, H.; Li, M. Caricato, A. V. Marenich, J. Bloino, B. G. Janesko, R. Gomperts, B. Mennucci, H. P. Hratchian, J. V. Ortiz, A. F. Izmaylov, J. L. Sonnenberg, D. Williams-Young, F. Ding, F. Lipparini, F. Egidi, J. Goings, B. Peng, A. Petrone, T. Henderson, D. Ranasinghe, V. G. Zakrzewski, J. Gao, N. Rega, G. Zheng, W. Liang, M. Hada, M. Ehara, K. Toyota, R. Fukuda, J. Hasegawa, M. Ishida, T. Nakajima, Y. Honda, O. Kitao, H. Nakai, T. Vreven, K. Throssell, J. A. J. Montgomery, J. E. Peralta, F. Ogliaro, M. J. Bearpark, J. J. Heyd, E. N. Brothers, K. N. Kudin, V. N. Staroverov, T. A. Keith, R. Kobayashi, J. Normand, K. Raghavachari, A. P. Rendell, J. C. Burant, S. S. Iyengar, J. Tomasi, M. Cossi, J. M. Millam, M. Klene, C. Adamo, R. Cammi, J. W. Ochterski, R. L. Martin, K. Morokuma, O. Farkas, J. B. Foresman, D. J. Fox, *Gaussian 16, Revision B.01*, Gaussian, Inc., Wallingford CT, **2016**.
[57] M. R. Talipov, M. M. Hossain, A. Boddeda, K. Thakur, R. Rathore, *Org. Biomol. Chem.* **2016**, *14*, 2961–2968.
[58] L. V. Ivanova, T. S. Navale, D. Wang, S. Lindeman, M. V. Ivanov, R. Rathore, *Chem. Commun.* **2018**, *54*, 5851–5854.
[59] F. C. Görth, M. Rucker, M. Eckhardt, R. Brückner, *Eur. J. Org. Chem.* **2000**, 2605–2611.
[60] O. V. Dolomanov, L. J. Bourhis, R. J. Gildea, J. A. K. Howard, H. Pusch- mann, *J. Appl. Crystallogr.* **2009**, *42*, 339–341.
[61] G. M. Sheldrick, *Acta Crystallogr. Sect. A* **2015**, *71*, 3–8.
[62] G. M. Sheldrick, *Acta Crystallogr. Sect. C* **2015**, *71*, 3–8.
[63] T. Harimoto, T. Suzuki, Y. Ishigaki, *Chem. Eur. J.* **2023**, *29*, e202203899.

Chapter 3

Octaarylated Bisquinodimethanes: Double Dynamic Redox Systems Enabling the Control of [*n*]Acene Structures and NIR Absorptions

3-1. Introduction

[*n*]Acenes are a class of aromatic hydrocarbons composed of linearly fused benzene rings (e.g., anthracene, tetracene, pentacene, etc.; *n*: number of annulated benzene rings). [*n*]Acenes are highly attractive molecules because their HOMO/LUMO levels and small band gap can be easily modulated by π-extension and the introduction of various substituents or steric strain to the acene core.[1–11] Thus, their optical and electrochemical properties can be fine-tuned. As a result, [*n*]acenes are widely used as functional organic materials such as semiconductors,[12–15] fluorescent probes,[16–18] and optoelectronic devices.[19–25] There are two main approaches to their synthesis[26] (Scheme 3-1a): elimination of small molecule(s) such as carbon monoxide (CO) from precursors[27–30] and nucleophilic addition to quinones followed by reductive aromatization.[31,32] However, some problems may arise regarding the solubility and stability of the reaction intermediate with an increase in *n*.

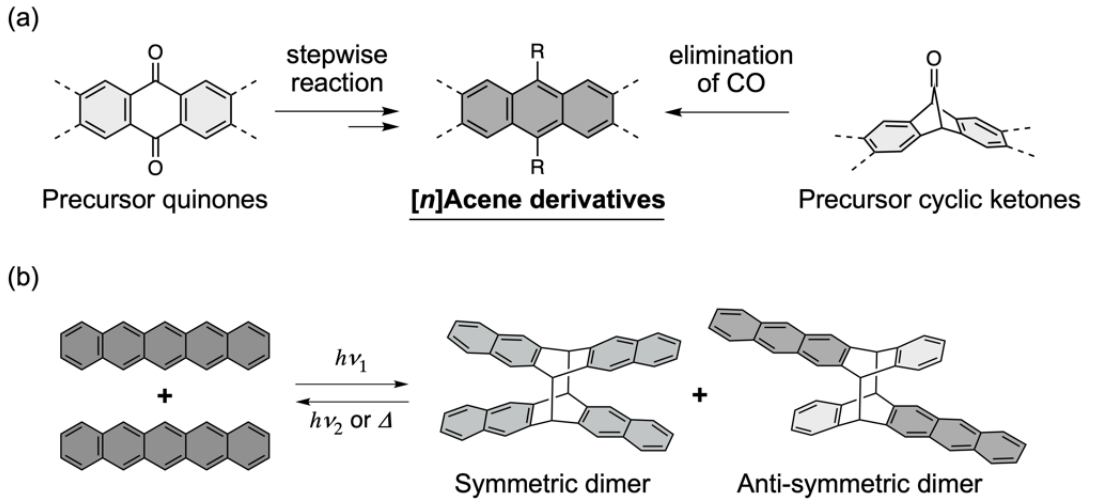

Scheme 3-1. Previous examples of (a) synthetic procedures for [*n*]acene derivatives and (b) intermolecular dimerization and dissociation of [5]acene by light/heat.

In addition, [*n*]acenes have been reported to show switching behavior based on dynamic interconversion through photo- and thermal dimerization/dissociation and reversible endoperoxidation reaction.[33–39] For example, [5]acenes are interconvertible with their dimers, where the [3]acene skeleton and/or naphthalene skeleton are unselectively formed by partial dearomatization (Scheme 3-1b). While these switching behaviors are fascinating from the viewpoint of control of HOMO/LUMO

levels arising from the change in acene units, it is difficult to control intermolecular reactions due to the existence of several reaction points in the case of n ≥ 4. Thus, it is still challenging to selectively obtain the desired structure and to attain reversible and selective switching of [*n*]acene units that can be observed in a unimolecular fashion rather than as an intermolecular reaction of two molecules.

On the other hand, the author's group reported that 11,11,12,12-tetraaryl-9,10-anthraquinodimethanes (AQDs) **1** with a folded form undergo one-stage two-electron (2e) oxidation to produce twisted dications with a planar [3]acene skeleton.[40–42] These results indicate that a [3]acene unit can be reversibly constructed by a redox reaction, accompanied by changes in both the structure and color of the molecule (Scheme 3-2). On the basis of such background, the author envisaged that extended [*n*]acenes could be formed in oligocationic states by one-stage oxidation of an accumulated structure composed of multiple AQD units, for instance, [5]acene derivative would be obtained by four-electron (4e) oxidation of bisquinodimethane (BQD) **2** with eight aryl groups (Scheme 3-2). In general, many extended [*n*]acenes are unstable due to the reactivity at the edges such as dimerization. However, this tetracationic molecule $\mathbf{2}^{4+}$ is expected to be sufficiently stable because its highly reactive edges are protected by almost orthogonally twisted diarylmethylium units. Here, the author chose 4-methoxyphenyl group **a** as an aryl group with the expectation of moderate electron-donating property to stabilize cationic species as well as characteristic signals of methyl group in ^{1}H NMR to easily identify both the precursors and target products. On the other hand, there are only a few examples of oligocations consisting of pure hydrocarbon,[46] due to the lack of effective charge delocalization by heteroatoms with an electron-donating ability. Therefore, it is a challenging issue to construct and isolate pure oligocationic hydrocarbons and to elucidate their intrinsic electronic and structural properties. To tackle this issue, the author chose 4-*tert*-butylphenyl group **b** as an aryl group, with the expectation that the stability and solubility of tetracationic hydrocarbons would be improved due to the bulkiness of the *tert*-butyl group. Furthermore, for hydrocarbonic tetracation $\mathbf{2b}^{4+}$, the author anticipated that lowering the LUMO level due to an increased electron-withdrawing property of less donating diarylmethyliums would result in a decrease in the HOMO-LUMO gap, and thus far red-shifted absorptions in the NIR region could be observed.

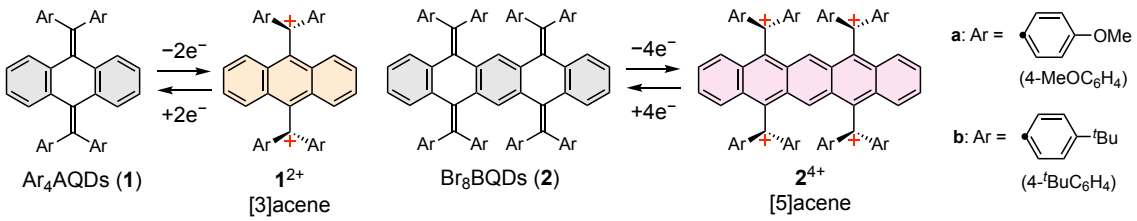

Scheme 3-2. A synthetic procedure for [5]acene derivatives: an electrochemical strategy in this study.

3-2. Results and Discussion

3-2-1. Preparation and X-ray analysis

As shown in Scheme 3-3, target molecules **2a** and **2b** were prepared from 5,7,12,14-pentacenetetraone over 4 steps, where stepwise introduction of aryl groups was conducted by Suzuki-Miyaura cross-coupling reaction following dibromoolefination (Scheme 3-3). It should be noted that in the synthesis of brominated BQD precursors **6**, unreacted quinones **5** were quantitatively recovered in both derivatives, indicating that the relatively low yields were not caused by any side reactions. The reason for the decrease in the yields is probably due to the incorporation of unreacted quinones **5** into precipitates produced in a reaction flask, making further reaction impossible. Additionally, in the synthesis of tetrabrominated quinone **4**, overreacted derivative **7**, in which dibromomethylene units were introduced in all carbonyl groups, was obtained as a by-product (5%) (Scheme 3-3).

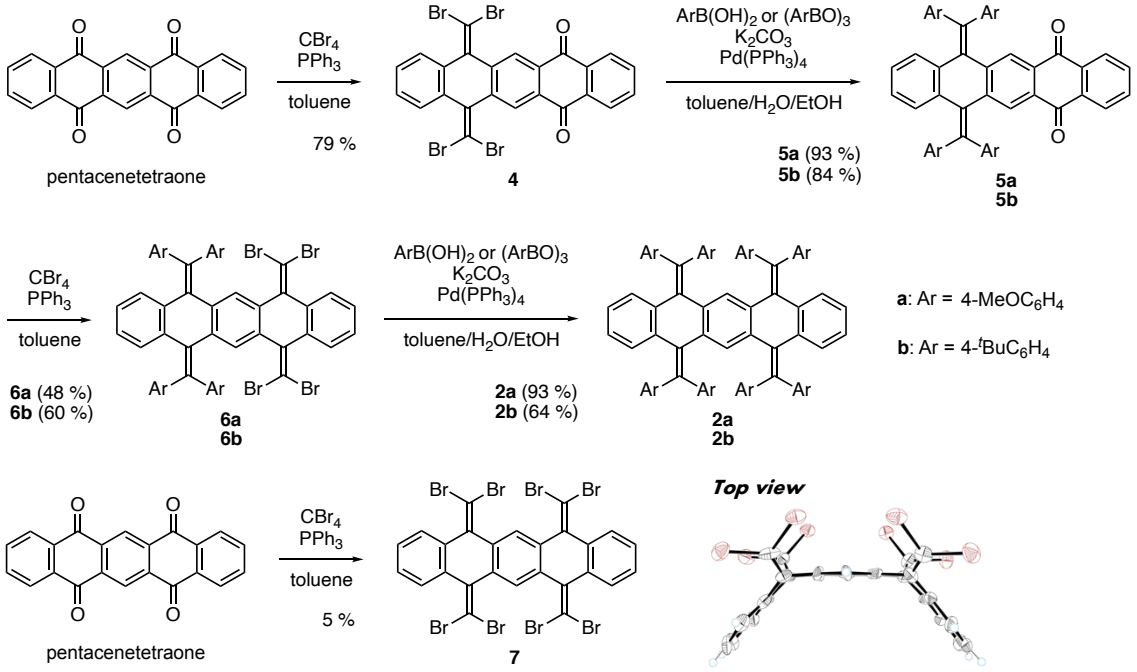

Scheme 3-3. Preparation of newly designed BQDs **2**.

An X-ray crystallographic analysis revealed that **7** has a curved structure. Although further dibromoolefination of **4** was also investigated to obtain a large amount of the octabrominated derivative **7**, a white solid with very poor solubility was produced. Mass spectrometric measurements of the obtained solid showed molecular weight peaks and patterns that could be assigned to **7**, but the extremely low solubility made following investigation unsuitable for the use of **7** as a reaction precursor. The author considered that such poor solubility might arise from a zigzag-structured isomer of **7**, which would be packed in crystal with a much stronger intermolecular interaction than the curved

isomer. Althouh the author has found that it is possible to introduce all aryl groups from the curved-type derivative **7**, the difficulty remains in supply due to the low yield. Moreover, there is an important advantage of the stepwise introduction of dibromomethylene and aryl groups, that is, different aryl groups can be introduced into the BQD skeleton to obtain unsymmetrically substituted derivatives (see below).

By treatment of **2a** and **2b** with four equivalents of $(4\text{-}BrC_6H_4)_3N^{+\bullet}SbCl_6^-$ (Magic Blue), tetracationic salts $\mathbf{2a}^{4+}(SbCl_6^-)_4$ and $\mathbf{2b}^{4+}(SbCl_6^-)_4$ were isolated in 100% and 96% yields, respectively. The original BQDs **2a** and **2b** were completely recovered when tetracations were treated with an excess amount of Zn powder, which demonstrates that reversible redox interconversion between $\mathbf{2}/\mathbf{2}^{4+}$ can proceed (Scheme 3-4).

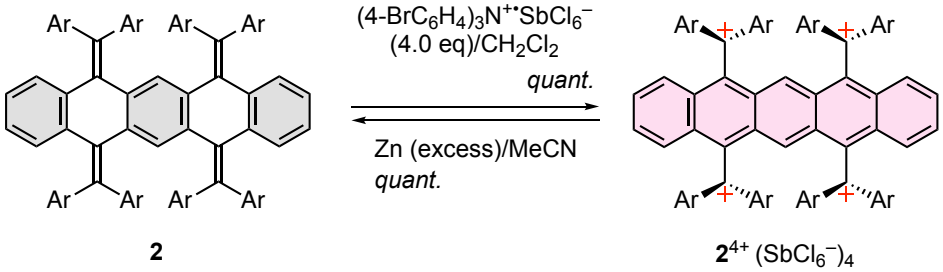

Scheme 3-4. Redox interconversion between neutral donors and tetracations. Four equivalents of $(4\text{-}BrC_6H_4)_3N^{+\bullet}SbCl_6^-$ were used for the oxidation of **2a** and **2b**, respectively.

According to X-ray analyses, these BQDs **2a** and **2b** with three non-fused benzene rings adopt a zigzag conformation as shown in Figure 3-1. The bent angles θ between the central plane in quinodimethane part and exomethylene moiety are 36.90(16)°, 37.25(19)° for **2a** and 33.96(11)°, 34.23(11)° for **2b**, respectively. Density functional theory (DFT) calculations at the CAM-B3LYP/6-31G* level showed similar values [36.2°, 37.4° for **2a** and 37.3°, 37.3° for **2b**] to those observed in single crystals (Table 3-1).

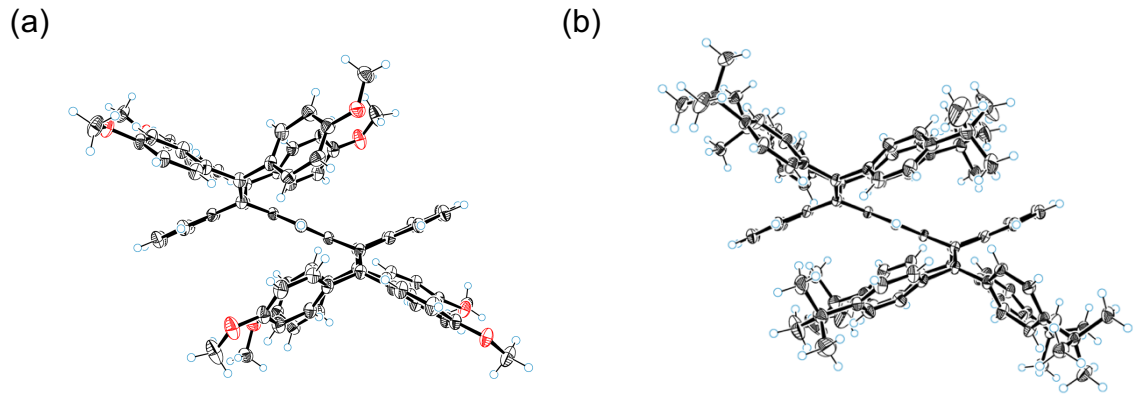

Figure 3-1. X-ray crystal structures (ORTEP drawings) of (a) **2a** and (b) **2b** at 150 K. Solvent molecules are omitted for clarity for **2b**. Thermal ellipsoids are shown at the 50% probability levels.

Table 3-1. Structural parameters of **2** determined by X-ray analyses and DFT calculations (CAM-B3LYP/6-31G*). The calculated values are shown in italics.

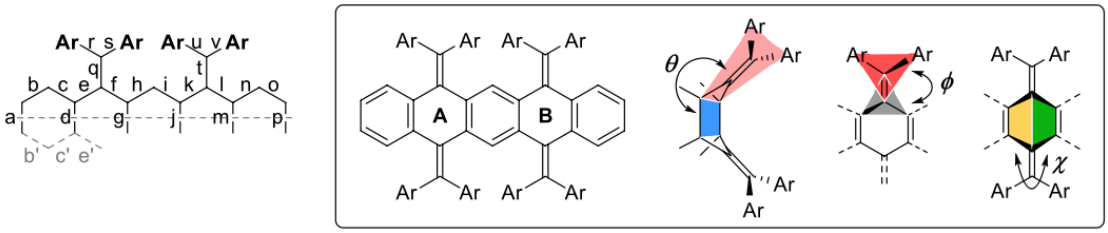

2a (Ar = 4-MeOC$_6$H$_4$)						**2b** (Ar = 4-^{t}BuC$_6$H$_4$)					
bond length (Å)			dihedral angle (°)			bond length (Å)			dihedral angle (°)		
	Expt.	*Calcd.*		Expt.	*Calcd.*		Expt.	*Calcd.*		Expt.	*Calcd.*
a	1.388(5)	*1.391*	θ_A	37.25(19)	*36.216*	**a**	1.393(2)	*1.390*	θ_A	34.23(11)	*37.256*
b	1.383(4)	*1.387*		36.90(16)	*37.446*	**b**	1.388(3)	*1.387*		33.96(11)	*37.264*
c	1.394(5)	*1.400*	ϕ_A	3.17(15)	*8.796*	**c**	1.398(3)	*1.395*	ϕ_A	2.35(7)	*6.944*
d	1.413(4)	*1.407*		3.43(11)	*8.726*	**d**	1.409(2)	*1.407*		5.20(9)	*5.335*
e	1.487(4)	*1.490*	χ_A	43.3(2)	*44.417*	**e**	1.489(3)	*1.490*	χ_A	40.94(14)	*43.928*
f	1.486(5)	*1.492*				**f**	1.489(2)	*1.490*			
g	1.399(4)	*1.407*	θ_B	$=\theta_A$	*35.528*	**g**	1.409(2)	*1.406*	θ_B	$=\theta_A$	*37.258*
h	1.397(3)	*1.392*			*37.275*	**h**	1.391(2)	*1.391*			*36.270*
i	1.392(5)	*1.391*	ϕ_B	$=\phi_A$	*10.541*	**i**	1.393(2)	*1.391*	ϕ_B	$=\phi_A$	*5.331*
j	=g	*1.405*			*6.419*	**j**	=g	*1.406*			*6.937*
k	1.495(3)	*1.490*	χ_B	$=\chi_A$	*42.692*	**k**	1.487(2)	*1.489*	χ_B	$=\chi_A$	*43.920*
l	1.486(4)	*1.492*				**l**	1.484(3)	*1.490*			
m	=d	*1.407*				**m**	=d	*1.407*			
n	1.401(4)	*1.396*				**n**	1.395(3)	*1.395*			
o	1.379(5)	*1.388*				**o**	1.387(3)	*1.388*			
p	=a	*1.391*				**p**	=a	*1.390*			
q	1.351(5)	*1.355*				**q**	1.3518(19)	*1.351*			
r	1.491(5)	*1.492*				**r**	1.496(2)	*1.494*			
s	1.502(4)	*1.497*				**s**	1.497(3)	*1.497*			
t	1.342(3)	*1.351*				**t**	1.349(3)	*1.350*			
u	1.502(4)	*1.493*				**u**	1.498(3)	*1.495*			
v	1.499(3)	*1.498*				**v**	1.502(2)	*1.497*			
b'	=o	*1.388*				**b'**	=o	*1.388*			
c'	=n	*1.396*				**c'**	=n	*1.395*			
e'	=l	*1.489*				**e'**	=l	*1.490*			
f'	=k	*1.489*				**f'**	=k	*1.489*			
h'	=i	*1.392*				**h'**	=i	*1.391*			
i'	=h	*1.390*				**i'**	=h	*1.391*			
k'	=f	*1.489*				**k'**	=f	*1.490*			
l'	=e	*1.491*				**l'**	=e	*1.490*			
n'	=c	*1.396*				**n'**	=c	*1.395*			
o'	=b	*1.387*				**o'**	=b	*1.387*			
q'	=t	*1.352*				**q'**	=t	*1.350*			
r'	=v	*1.497*				**r'**	=v	*1.497*			
s'	=u	*1.494*				**s'**	=u	*1.495*			
t'	=q	*1.351*				**t'**	=q	*1.351*			
u'	=s	*1.497*				**u'**	=s	*1.497*			
v'	=r	*1.493*				**v'**	=r	*1.494*			

On the othe hand, X-ray analyses revealed that the tetracations have a fully conjugated planar [5]acene core, which is almost orthogonal to the diarylmethylium moieties (Figure 3-2); there are only a few examples of the determination of the structure of oligocations in organic molecules,[43–45] especially pure hydrocarbons.[46] Their average dihedral angles ϕ between [5]acene and diarylmethylium units are 73.4° for $\mathbf{2a}^{4+}$ and 62.5° for $\mathbf{2b}^{4+}$, respectively. As in the cases of BQDs **2**, tetracations $\mathbf{2}^{4+}$ were very similar to the geometries obtained by DFT calculations at the CAM-B3LYP/6-31G* level [74.7° for $\mathbf{2a}^{4+}$ and 69.5° for $\mathbf{2b}^{4+}$] (Table 3-2).

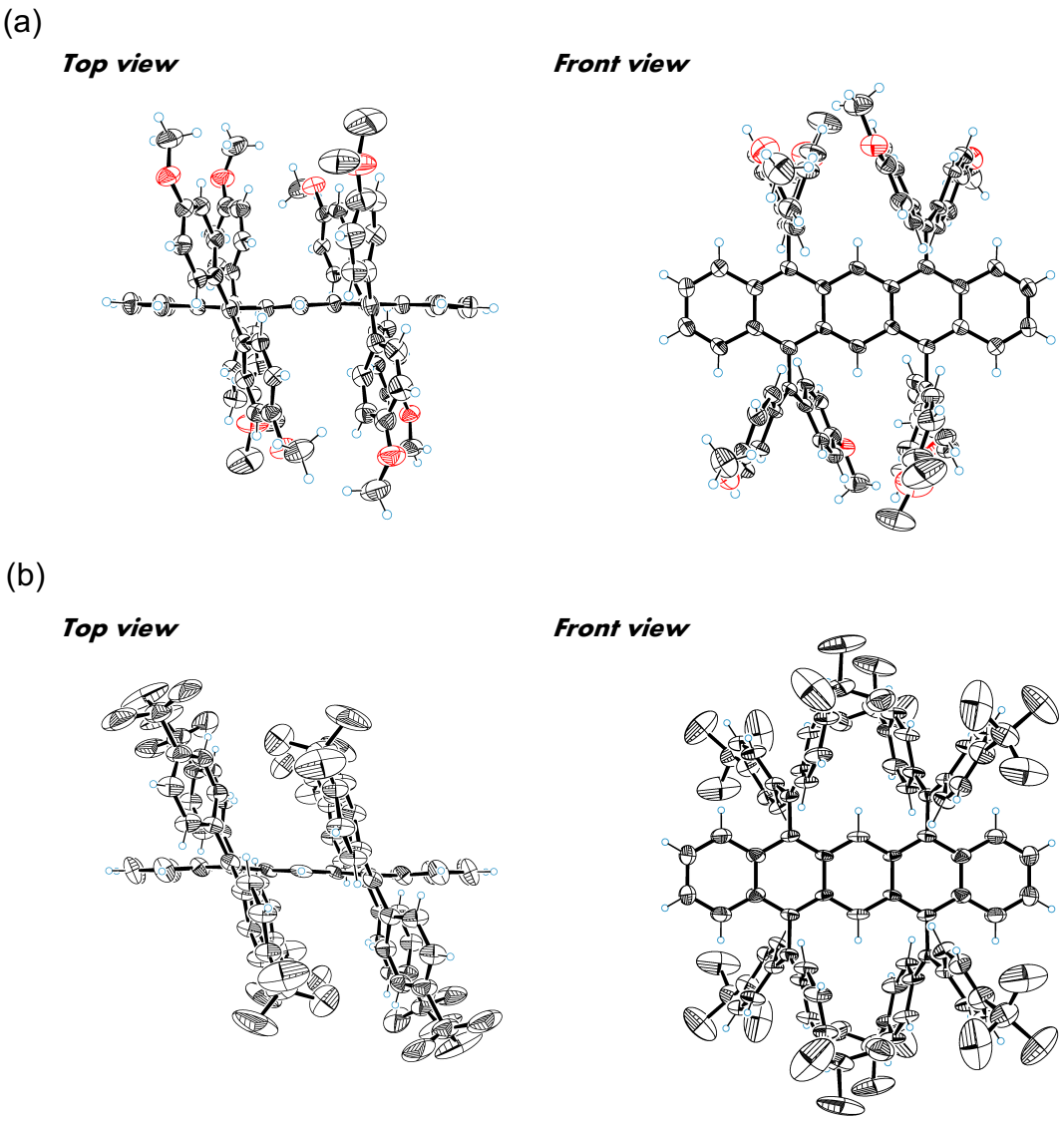

Figure 3-2. X-ray crystal structures (ORTEP drawings) of (a) $\mathbf{2a}^{4+}(SbCl_6^-)_4$ and (b) $\mathbf{2b}^{4+}(SbCl_6^-)_4$ determined at 150 K. The counterions are omitted for clarity and solvent mask procedures were used for the analyses in both cases. Thermal ellipsoids are shown at the 50% and 30% probability levels for $\mathbf{2a}^{4+}(SbCl_6^-)_4$ and $\mathbf{2b}^{4+}(SbCl_6^-)_4$, respectively.

Table 3-1. Structural parameters of $\mathbf{2}^{4+}$ determined by X-ray analyses and DFT calculations (CAM-B3LYP/6-31G*). The calculated values are shown in italics.

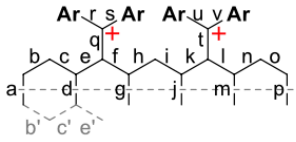

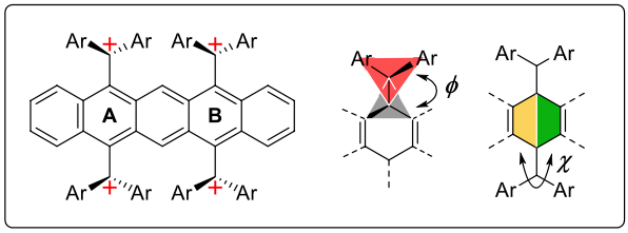

$\mathbf{2a}^{4+}$ (Ar = 4-$MeOC_6H_4$)						$\mathbf{2b}^{4+}$ (Ar = 4-^{t}BuC_6H_4)					
bond length (Å)			dihedral angle (°)			bond length (Å)			dihedral angle (°)		
	Expt.	*Calcd.*		Expt.	*Calcd.*		Expt.	*Calcd.*		Expt.	*Calcd.*
a	1.409(12)	*1.428*	θ_A	-	-	**a**	1.44(3)	*1.427*	θ_A	-	-
b	1.360(11)	*1.355*				**b**	1.39(2)	*1.355*			
c	1.440(9)	*1.439*	ϕ_A	82.1(3)	*74.675*	**c**	1.428(19)	*1.439*	ϕ_A	62.5(5)	*68.940*
d	1.446(9)	*1.451*		64.7(3)	*74.676*	**d**	1.427(19)	*1.452*			*70.066*
e	1.399(10)	*1.395*	χ_A	1.1(6)	*0.0859*	**e**	1.421(15)	*1.397*	χ_A	5.0(11)	*0.6129*
f	1.403(9)	*1.429*				**f**	1.428(13)	*1.431*			
g	1.440(11)	*1.447*	θ_B	-	-	**g**	1.420(15)	*1.445*	θ_B	-	-
h	1.413(10)	*1.400*				**h**	1.405(10)	*1.399*			
i	1.376(9)	*1.400*	ϕ_B	$=\phi_A$	*74.675*	**i**	=h	*1.399*	ϕ_B	$=\phi_A$	*69.294*
j	=g	*1.447*			*74.675*	**j**	=g	*1.445*			*68.549*
k	1.431(10)	*1.429*	χ_B	$=\chi_A$	*0.0859*	**k**	=f	*1.432*	χ_B	$=\chi_A$	*0.8171*
l	1.409(9)	*1.395*				**l**	=e	*1.398*			
m	=d	*1.451*				**m**	=d	*1.452*			
n	1.437(11)	*1.439*				**n**	=c	*1.439*			
o	1.346(11)	*1.355*				**o**	=b	*1.355*			
p	=a	*1.428*				**p**	=a	*1.427*			
q	1.501(9)	*1.498*				**q**	1.471(11)	*1.492*			
r	1.416(12)	*1.422*				**r**	1.427(14)	*1.430*			
s	1.421(10)	*1.423*				**s**	1.488(16)	*1.424*			
t	1.481(9)	*1.498*				**t**	=q	*1.491*			
u	1.427(11)	*1.423*				**u**	=s	*1.423*			
v	1.425(8)	*1.422*				**v**	=r	*1.431*			
b'	=o	*1.355*				**b'**	=b	*1.355*			
c'	=n	*1.439*				**c'**	=c	*1.439*			
e'	=l	*1.395*				**e'**	=e	*1.398*			
f'	=k	*1.429*				**f'**	=f	*1.432*			
h'	=i	*1.400*				**h'**	=h	*1.400*			
i'	=h	*1.400*				**i'**	=h	*1.400*			
k'	=f	*1.429*				**k'**	=f	*1.432*			
l'	=e	*1.395*				**l'**	=e	*1.398*			
n'	=c	*1.439*				**n'**	=c	*1.439*			
o'	=b	*1.355*				**o'**	=b	*1.355*			
q'	=t	1.498				**q'**	=q	1.492			
r'	=v	*1.422*				**r'**	=r	*1.430*			
s'	=u	*1.423*				**s'**	=s	*1.424*			
t'	=q	*1.498*				**t'**	=t	*1.492*			
u'	=s	*1.423*				**u'**	=u	*1.424*			
v'	=r	*1.422*				**v'**	=v	*1.430*			

3-2-2. Absorbing properties

When the absorption spectra were measured in CH_2Cl_2 (Figure 3-3), tetracations $\mathbf{2}^{4+}$ exhibited strong absorptions in the visible region characteristic to diarylmethylium units [λ_{max}/nm (log ε): 517 (5.30) for $\mathbf{2a}^{4+}$ and 498 (5.08) for $\mathbf{2b}^{4+}$] as well as intramolecular charge-transfer (CT) absorptions in the NIR region [λ_{max}/nm (log ε): 922 (4.06) for $\mathbf{2a}^{4+}$ and 1094 (4.11) for $\mathbf{2b}^{4+}$], whereas BQDs **2** have absorption maxima only in the UV region [λ_{max}/nm (log ε): 328 (4.60) for **2a** and 317 (4.59) for **2b**]. A large red shift and vivid color change were observed upon 4e-oxidation of **2**. Each absorption band in tetracations $\mathbf{2}^{4+}$ was assigned by time-dependent (TD)-DFT calculations (Figure 3-4). Note that the pure hydrocarbon $\mathbf{2b}^{4+}$ shows significantly red-shifted CT absorptions, which can be accounted for by a low-lying LUMO level due to the lower donating ability of *tert*-butyl groups for $\mathbf{2b}^{4+}$ than methoxy groups for $\mathbf{2a}^{4+}$, while the coefficients in HOMO are located on the same [5]acene core, as expected. The lower-energy CT bands for tetracationic [5]acenes $\mathbf{2}^{4+}$ compared to dicationic [3]acenes $\mathbf{1}^{2+}$ [λ_{max}/nm (log ε): 709 (3.94) for $\mathbf{1a}^{2+}$ and 836 (3.95) for $\mathbf{1b}^{2+}$] can be explained by the higher donating ability of [5]acene compared to the [3]acene core, which was also supported by TD-DFT calculations.

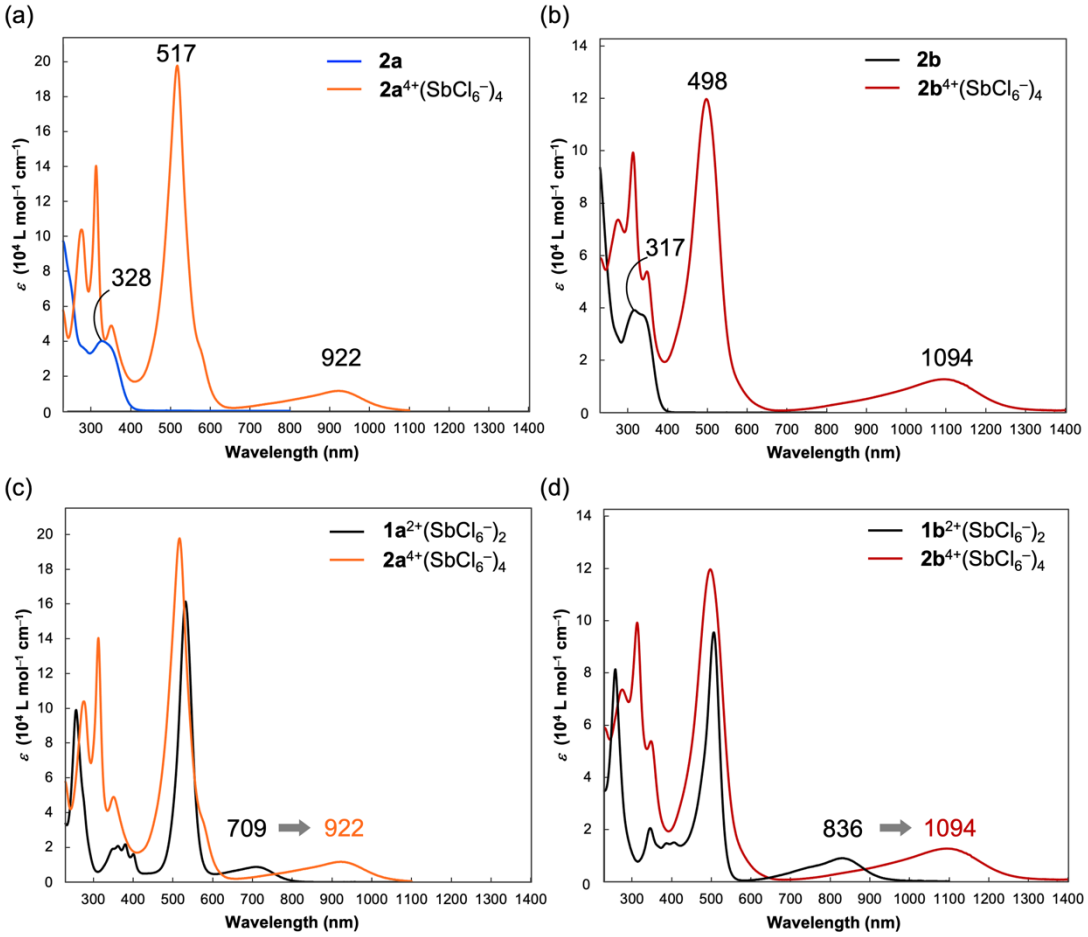

Figure 3-3. UV/Vis/NIR spectra of (a) **2a** and $\mathbf{2a}^{4+}(SbCl_6^-)_4$, (b) **2b** and $\mathbf{2b}^{4+}(SbCl_6^-)_4$, (c) $\mathbf{1a}^{2+}(SbCl_6^-)_2$ and $\mathbf{2a}^{4+}(SbCl_6^-)_4$ and (d) $\mathbf{1b}^{2+}(SbCl_6^-)_2$ and $\mathbf{2b}^{4+}(SbCl_6^-)_4$ in CH_2Cl_2. [**1a** and **2a**: Ar = 4-$MeOC_6H_4$; **1b** and **2b**: Ar = 4-^{t}BuC_6H_4]

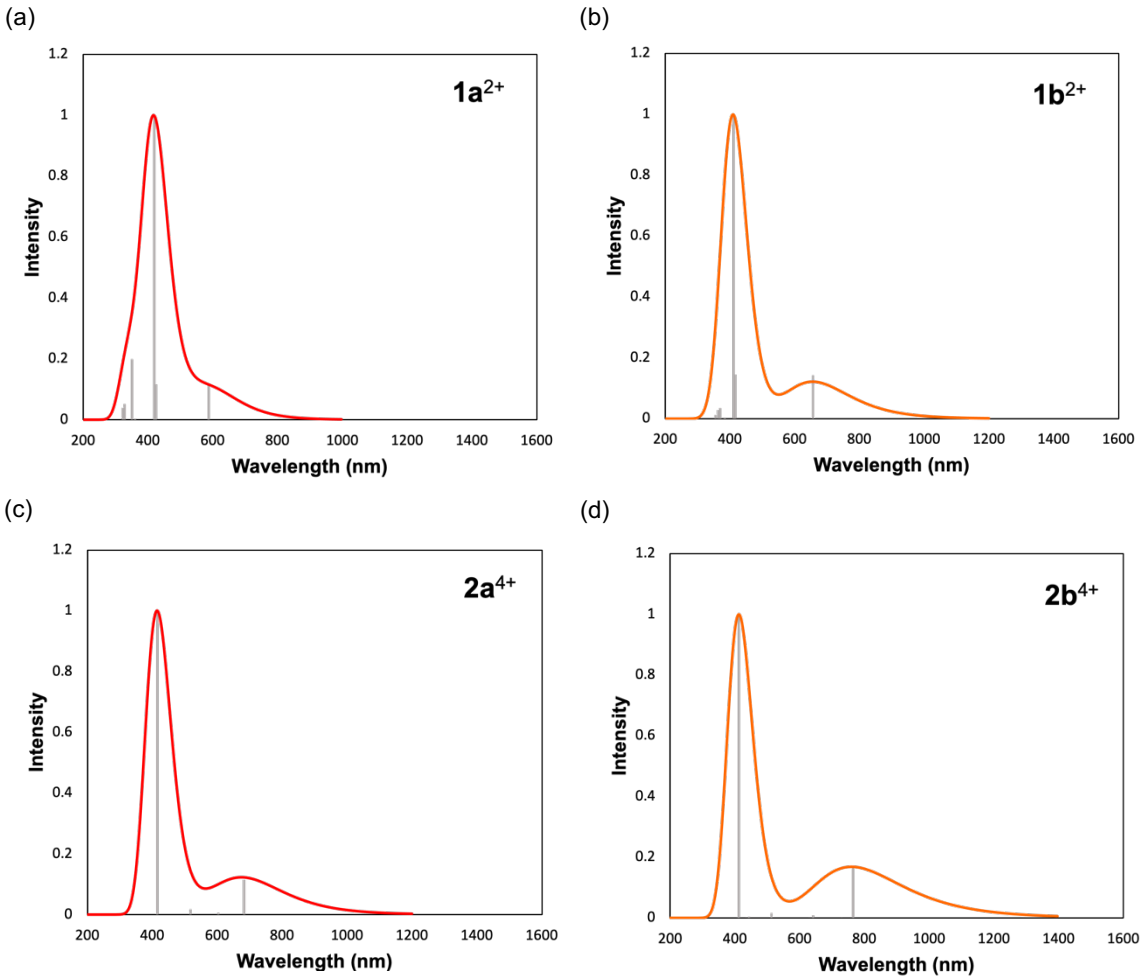

Figure 3-4. Simulated UV/Vis/NIR spectra by TD-DFT calculations (CAM-B3LYP/6-31G*) for (a) $\mathbf{1a}^{2+}$, (b) $\mathbf{1b}^{2+}$, (c) $\mathbf{2a}^{4+}$ and (d) $\mathbf{2b}^{4+}$. [$\mathbf{1a}^{2+}$ and $\mathbf{2a}^{4+}$: Ar = 4-$MeOC_6H_4$; $\mathbf{1b}^{2+}$ and $\mathbf{2b}^{4+}$: Ar = 4-^{t}BuC_6H_4] For detailed information on excitation energies and oscillator strengths, see Ref. [48].

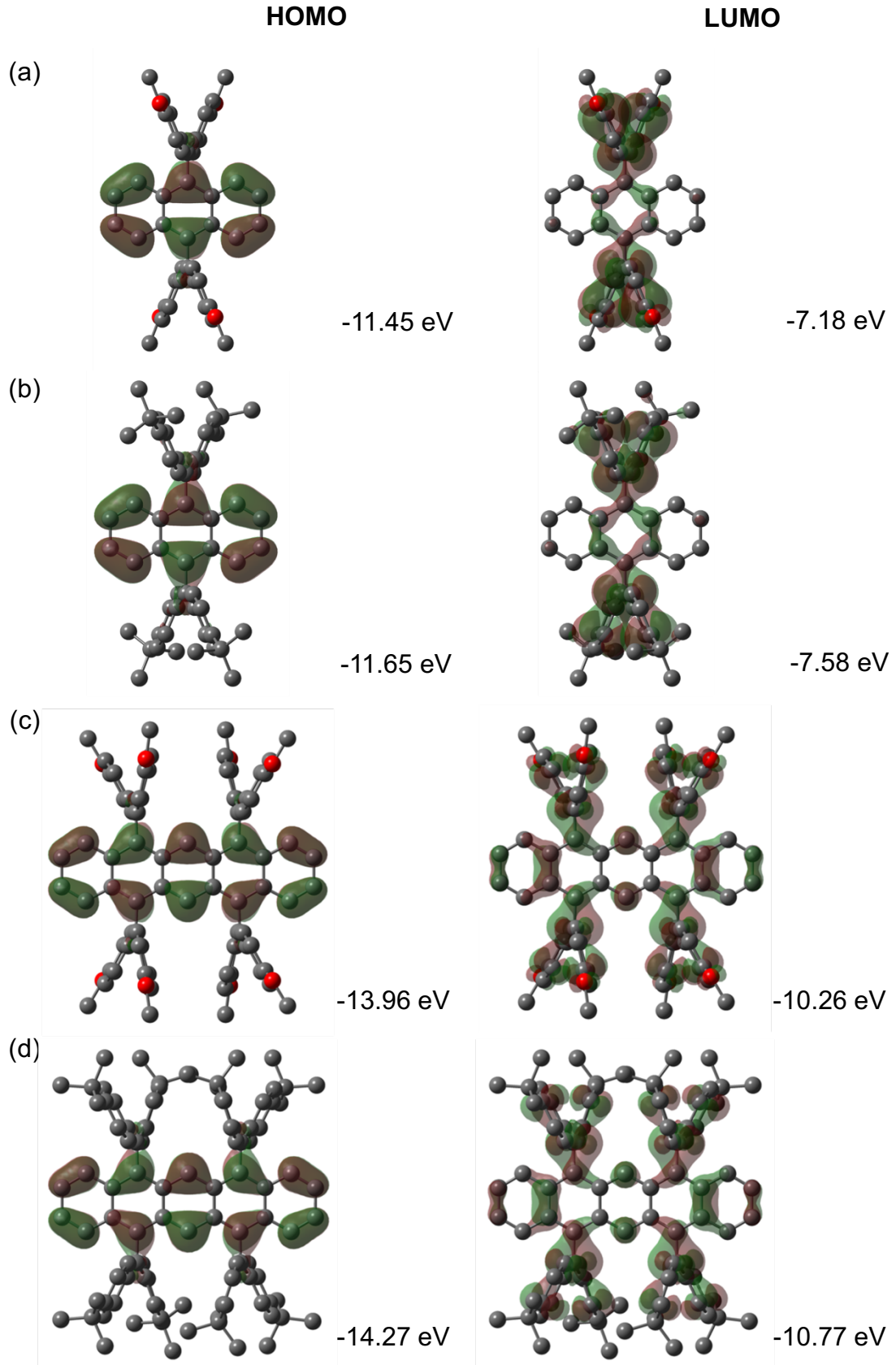

Figure 3-5. HOMO and LUMO levels calculated by the DFT method (CAM-B3LYP/6-31G*) based on the optimized structures of (a) **1a**$^{2+}$, (b) **1b**$^{2+}$, (c) **2a**$^{4+}$ and (d) **2b**$^{4+}$.

3-2-3. Redox behavior

To investigate the redox properties in detail, cyclic voltammetry (CV) was carried out in CH_2Cl_2 (Figure 3-6a). For **2a**, the voltammogram showed a one-wave 4e-oxidation peak at +1.12 V (vs. SCE), which is close to that of **1a** (+1.03 V).[40] The one-stage 4e-process for oxidation was verified by using ferrocene as an external standard and confirmed by differential pulse voltammetry (Figure 3-6b). As a result of the change in structures, return peaks, where two-stage 2e-reduction occurs via intermediate dication $\mathbf{2a}^{2+}$, appeared in the far cathodic region (E^{red}/V: +0.55 for $\mathbf{2a}^{4+}$ and +0.27 for $\mathbf{2a}^{2+}$). Such a cathodic peak shift is a characteristic feature of dynamic redox (*dyrex*) systems,[47] in which the steady-state concentration of intermediary radical cationic species ($\mathbf{2a}^{3+\bullet}$ or $\mathbf{2a}^{+\bullet}$) is negligible. The smaller current of the return peaks is due to the effects of diffusion, which is commonly found in *dyrex* systems. Similar redox behavior was observed for **2b** (E^{ox}/V: +1.26 for **2b**; E^{red}/V: +0.89 for $\mathbf{2b}^{4+}$ and +0.76 for $\mathbf{2b}^{2+}$).

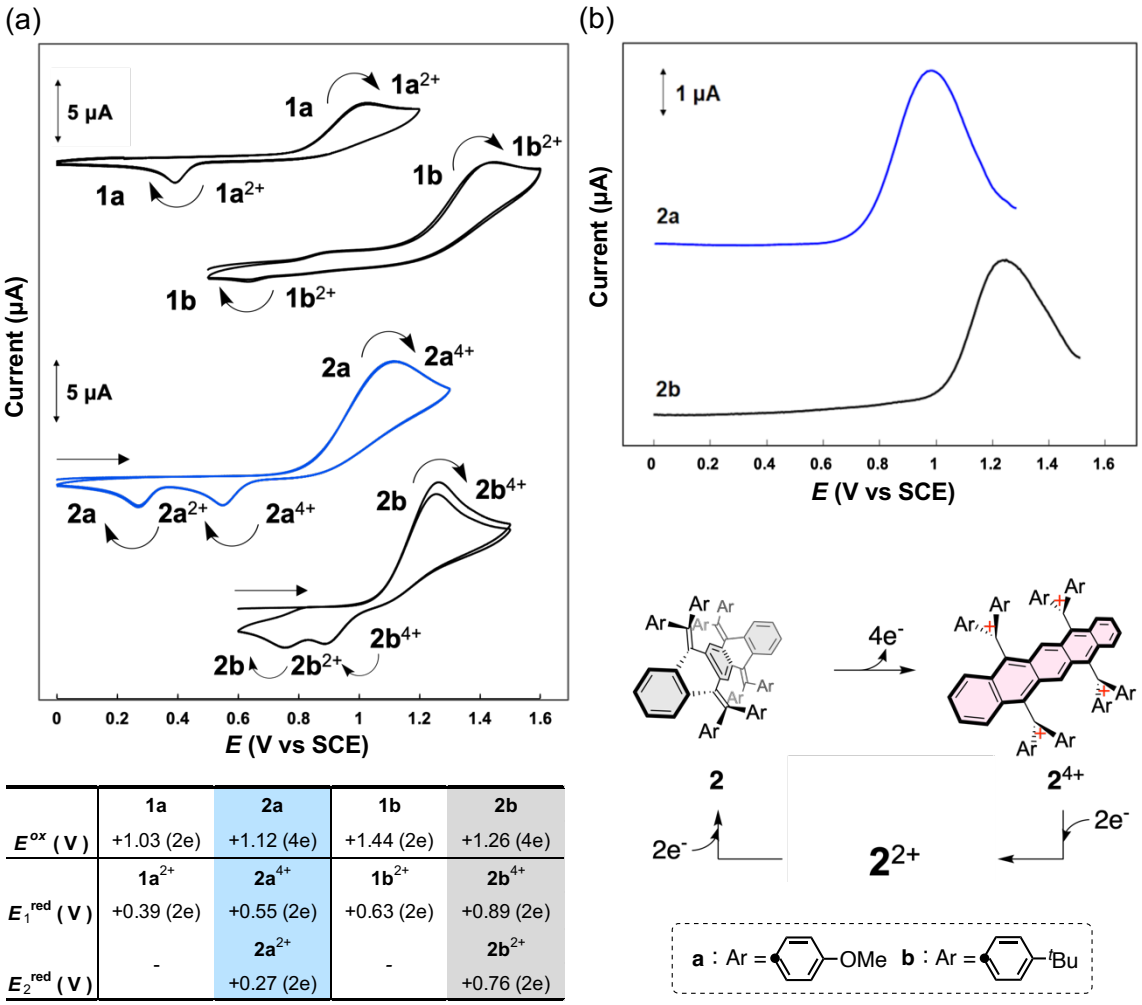

	1a	2a	1b	2b
E^{ox} (V)	+1.03 (2e)	+1.12 (4e)	+1.44 (2e)	+1.26 (4e)
	$\mathbf{1a}^{2+}$	$\mathbf{2a}^{4+}$	$\mathbf{1b}^{2+}$	$\mathbf{2b}^{4+}$
E_1^{red} (V)	+0.39 (2e)	+0.55 (2e)	+0.63 (2e)	+0.89 (2e)
		$\mathbf{2a}^{2+}$		$\mathbf{2b}^{2+}$
E_2^{red} (V)	-	+0.27 (2e)	-	+0.76 (2e)

Figure 3-6. (a) Cyclic voltammograms and (b) differential pulse voltammograms of **1a**, **1b**, **2a** and **2b** in CH_2Cl_2 containing 0.1 M Bu_4NBF_4 as a supporting electrolyte (scan rate 100 $mV \cdot s^{-1}$, Pt electrodes).

According to these observations, three structures can be considered as the intermediary dication $\mathbf{2}^{2+}$: (**A**) localized dication with an [3]acene skeleton fused with an AQD unit and (**B**) dication diradical with a [5]acene skeleton as in $\mathbf{2}^{4+}$ (Figure 3-7a). Both forms have some advantages: there would be an intramolecular CT interaction in form **A** and highly delocalized cations and radicals in form **B**. The author first investigated if these dications $\mathbf{2}^{2+}$ are diradical species having a [5]acene core via voltammetric analyses by immediately reoxidizing the as-prepared dicationic species that were generated at the first 2e-reduction peak (Figure 3-7b). There was no corresponding oxidation peak for either $\mathbf{2a}^{2+}$ or $\mathbf{2b}^{2+}$ with the [5]acene skeleton as in $\mathbf{2}^{4+}$, meaning that a significant structural change rapidly occurs in $\mathbf{2}^{2+}$ to lose the [5]acene structure when the tetracations are reduced, so that the possibility of diradical species **B** could be excluded.

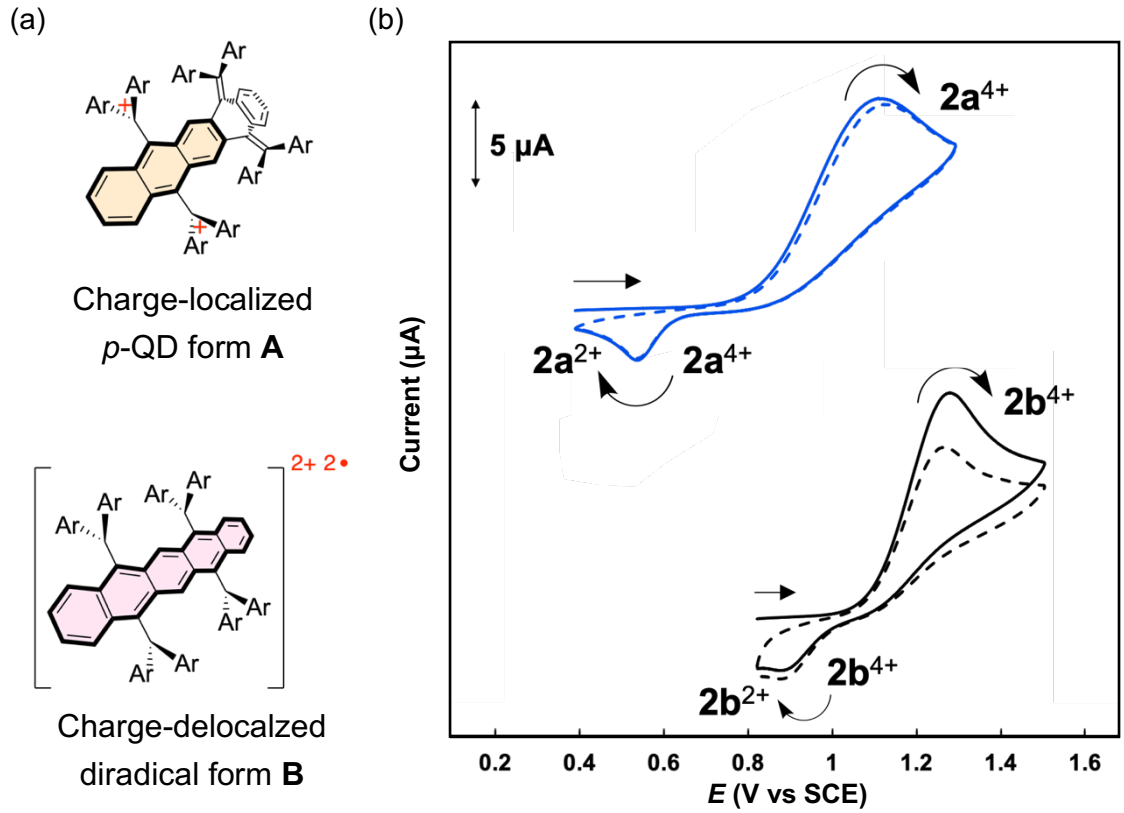

Figure 3-7. (a) Possible structures of dication : (**A**) localized dication with an [3]acene skeleton fused with an AQD unit and (**B**) dication diradical with a [5]acene skeleton. (b) Cyclic voltammograms of **2a** and **2b** in CH_2Cl_2 containing 0.1 M Bu_4NBF_4 as a supporting electrolyte (scan rate 100 $mV \cdot s^{-1}$, Pt electrodes).

3-2-4. Titration experiment of tetracations with a reducing agent

To obtain further information regarding the structure of the intermediary dications $\mathbf{2}^{2+}$ as expected by the voltammetric analyses of BQDs **2**, a titration experiment on the chemical reduction of $\mathbf{2}^{4+}$ was performed, which was monitored by UV/Vis/NIR spectroscopy. Upon the addition of aliquots of Bu_4NI (TBAI) into CH_2Cl_2 solution, the UV/Vis/NIR spectrum of $\mathbf{2b}^{4+}$ changed to that of **2b** via the intermediate dication $\mathbf{2b}^{2+}$ in a stepwise fashion, where several isosbestic points were observed in both stages. Especially in the first stage, the absorption maxima at 498 and 1094 nm for $\mathbf{2b}^{4+}$ in the visible and NIR region shifted to 509 and 1005 nm for $\mathbf{2b}^{2+}$, respectively (Figure 3-8a). Similar results were obtained by using $\mathbf{2a}^{4+}$ with decamethylferrocene ($Me_{10}Fc$) (Figure 3-8b). The NIR absorption of dications $\mathbf{2}^{2+}$ suggested that the form **A** with the intramolecular CT interaction would be likely. At the same time, titration experiments indicated that the intermediary dications $\mathbf{2}^{2+}$ have a long lifetime as observed by spectroscopic measurements and do not disproportionate into neutral BQDs **2** and tetracations $\mathbf{2}^{4+}$. Thus, the author envisaged that these dications should be able to be isolated and their structure could be determined by X-ray.

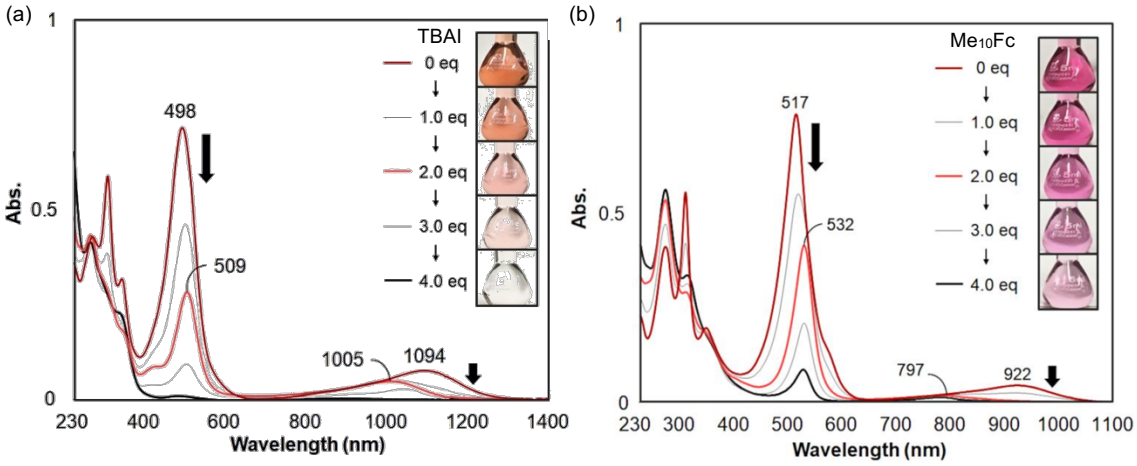

Figure 3-8. Changes in UV/Vis/NIR spectra of (a) $\mathbf{2b}^{4+}(SbCl_6^-)_4$ (6.00 μM) upon the addition of several aliquots of TBAI in CH_2Cl_2 and (b) $\mathbf{2a}^{4+}(SbCl_6^-)_4$ (3.87 μM) upon the addition of several aliquots of decamethylferrocene ($Me_{10}Fc$) in CH_2Cl_2.

3-2-5. Isolation and X-ray analyses of dications

Upon 2e-reduction of tetracationic salts $\mathbf{2a}^{4+}(SbCl_6^-)_4$ and $\mathbf{2b}^{4+}(SbCl_6^-)_4$ in MeCN with two equivalents of $Me_{10}Fc$ and TBAI, respectively, dicationic salts $\mathbf{2a}^{2+}(SbCl_6^-)_2$ and $\mathbf{2b}^{2+}(SbCl_6^-)_2$ were isolated in 99% and 95% yields, respectively (Figure 3-9a). For these experiments, it is of importance to choose the appropriate reducing agent. When the tetracation salt $\mathbf{2b}^{4+}(SbCl_6^-)_4$ was reduced with TBAI, iodide (I^-) was oxidized to iodine (1/2 I_2), which could be easily removed from the reaction mixture of dication salt $\mathbf{2b}^{2+}(SbCl_6^-)_2$. However, when TBAI was used for the tetracation salt $\mathbf{2a}^{4+}(SbCl_6^-)_4$ with a higher LUMO level, I^- could only be oxidized but not triiodide (I_3^-), resulting in a mixture of $SbCl_6^-$ and I_3^- for counterions of the dicationic salt $\mathbf{2a}^{2+}$. Furthermore, when ferrocene (Fc) was used instead of decamethylferrocene ($Me_{10}Fc$) for the reduction of $\mathbf{2a}^{4+}$, it was difficult to remove residues derived from Fc, and thus pure dicationic salt could not be obtained. After many trials, dications $\mathbf{2}^{2+}$ could be isolated in pure form by using the appropriate reductant. These structures of dications $\mathbf{2}^{2+}$ are form **A**, consisting of bis(diarylmethylium)-substituted [3]acene and a tetraarylquinodimethane unit, as characterized by NMR spectroscopy and finally determined by single-crystal X-ray analyses, as shown in Figure 3-9b. The bent angles θ between the central plane in quinodimethane part and exomethylene moiety in a single crystal of the $SbCl_6^-$ salt are 37.0(2)° for $\mathbf{2a}^{2+}$ and 37.8(4)° for $\mathbf{2b}^{2+}$. Their dihedral angles ϕ between antracene and diarylmethylium units are 67.3(3)° for $\mathbf{2a}^{2+}$ and 57.6(4)° for $\mathbf{2b}^{2+}$, respectively, both of which are smaller than those for tetracations $\mathbf{2}^{4+}$ probably due to the steric repulsion between aryl groups in the diarylmethylene and diarylmethylium moieties (Table 3-3).

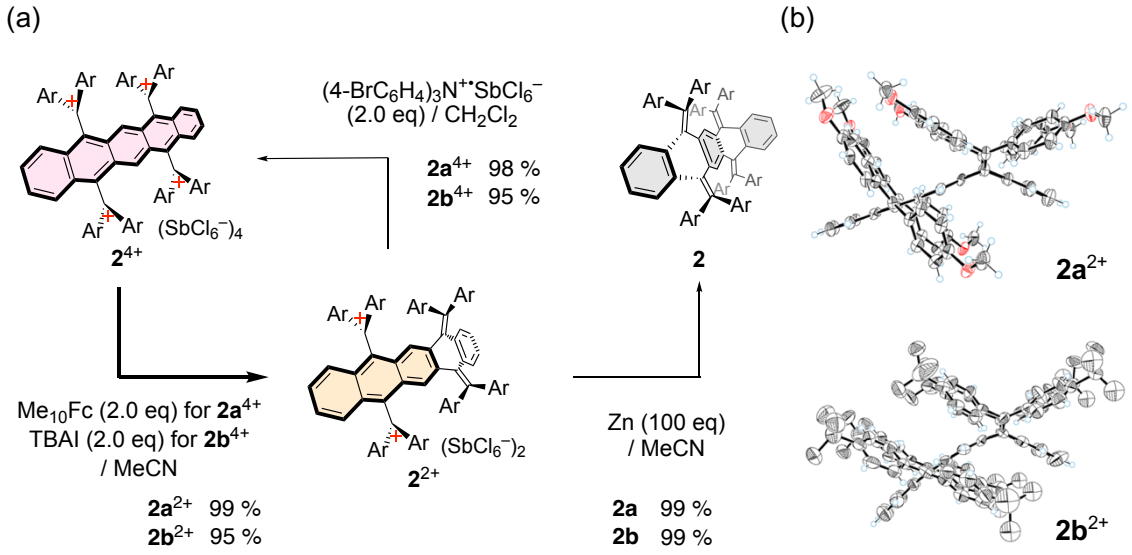

Figure 3-9. (a) Isolation of dications $\mathbf{2a}^{2+}(SbCl_6^-)_2$ and $\mathbf{2b}^{2+}(SbCl_6^-)_2$ and redox interconversion among $\mathbf{2}^{2+}$ and $\mathbf{2}/\mathbf{2}^{4+}$. (b) X-ray crystal structures (ORTEP drawings) of (a) $\mathbf{2a}^{2+}(SbCl_6^-)_2$ and (b) $\mathbf{2b}^{2+}(SbCl_6^-)_2$ determined at 150 K. The counterions and solvent molecules are omitted for clarity. Thermal ellipsoids are shown at the 50% and 30% probability levels, respectively.

Table 3-3. Structural parameters of $\mathbf{2}^{2+}$ determined by X-ray analyses and DFT calculations (CAM-B3LYP/6-31G*). The calculated values are shown in italics.

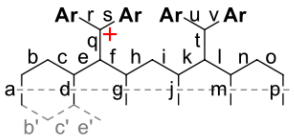

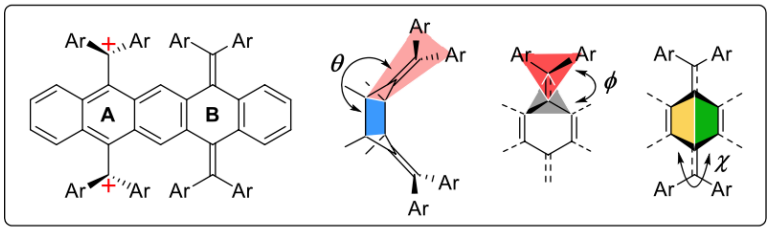

$\mathbf{2a}^{2+}$ (Ar = 4-$MeOC_6H_4$)						$\mathbf{2b}^{2+}$ (Ar = 4-^{t}BuC_6H_4)					
bond length (Å)			dihedral angle (°)			bond length (Å)			dihedral angle (°)		
	Expt.	*Calcd.*		Expt.	*Calcd.*		Expt.	*Calcd.*		Expt.	*Calcd.*
a	1.428(11)	*1.420*	θ_A	-	-	**a**	1.44(2)	*1.418*	θ_A	-	-
b	1.347(8)	*1.361*				**b**	1.341(14)	*1.362*			
c	1.421(8)	*1.430*	ϕ_A	67.3(3)	*84.066*	**c**	1.426(14)	*1.430*	ϕ_A	57.6(4)	*85.703*
d	1.440(11)	*1.435*			*75.289*	**d**	1.496(19)	*1.432*			*74.815*
e	1.411(8)	*1.408*	χ_A	2.3(6)	*0.9338*	**e**	1.369(14)	*1.410*	χ_A	6.0(12)	*0.5373*
f	1.421(8)	*1.405*				**f**	1.415(14)	*1.404*			
g	1.440(11)	*1.435*	θ_B	37.0(2)	*40.225*	**g**	1.462(19)	*1.441*	θ_B	37.8(4)	*39.779*
h	1.426(8)	*1.428*			*39.632*	**h**	1.426(14)	*1.430*			*40.997*
i	1.353(8)	*1.365*	ϕ_B	4.4(3)	*7.221*	**i**	1.316(13)	*1.365*	ϕ_B	3.4(5)	*5.706*
j	1.443(11)	*1.446*			*10.527*	**j**	1.538(19)	*1.441*			*12.671*
k	1.482(8)	*1.489*	χ_B	43.6(6)	*46.632*	**k**	1.478(13)	*1.487*	χ_B	43.5(9)	*48.489*
l	1.494(7)	*1.492*				**l**	1.463(14)	*1.499*			
m	1.413(11)	*1.405*				**m**	1.38(2)	*1.411*			
n	1.398(8)	*1.395*				**n**	1.392(16)	*1.394*			
o	1.370(8)	*1.388*				**o**	1.434(18)	*1.389*			
p	1.387(11)	*1.391*				**p**	1.36(3)	*1.389*			
q	1.492(8)	*1.497*				**q**	1.529(18)	*1.496*			
r	1.405(7)	*1.419*				**r**	1.445(15)	*1.423*			
s	1.436(7)	*1.425*				**s**	1.393(17)	*1.430*			
t	1.348(9)	*1.351*				**t**	1.372(17)	*1.352*			
u	1.502(8)	*1.492*				**u**	1.537(15)	*1.495*			
v	1.498(8)	*1.497*				**v**	1.521(16)	*1.500*			
b'	=b	*1.361*				**b'**	=b	*1.362*			
c'	=c	*1.430*				**c'**	=c	*1.429*			
e'	=e	*1.409*				**e'**	=e	*1.412*			
f'	=f	*1.407*				**f'**	=f	*1.408*			
h'	=h	*1.427*				**h'**	=h	*1.427*			
i'	=i	*1.364*				**i'**	=i	*1.364*			
k'	=k	*1.487*				**k'**	=k	*1.486*			
l'	=l	*1.489*				**l'**	=l	*1.490*			
n'	=n	*1.395*				**n'**	=n	*1.394*			
o'	=o	*1.387*				**o'**	=o	*1.389*			
q'	=q	*1.492*				**q'**	=q	*1.488*			
r'	=r	*1.419*				**r'**	=r	*1.422*			
s'	=s	*1.427*				**s'**	=s	*1.434*			
t'	=t	*1.354*				**t'**	=t	*1.348*			
u'	=u	*1.498*				**u'**	=u	*1.492*			
v'	=v	*1.489*				**v'**	=v	*1.495*			

3-2-6. Spectroscopic and electrochemical investigations of dications

The formation of dications with form **A** was also confirmed that the CT absorption bands for $\mathbf{2}^{2+}(SbCl_6^-)_2$ (794 nm for $\mathbf{2a}^{2+}$ and 1000 nm for $\mathbf{2b}^{2+}$) were observed at a longer-wavelength region than those for $\mathbf{1}^{2+}(SbCl_6^-)_2$ (709 nm for $\mathbf{1a}^{2+}$ and 836 nm for $\mathbf{1b}^{2+}$), the latter of which exhibits the intramolecular CT interaction between cationic moieties as an acceptor and [3]acene skeleton as a donor (Figure 3-10). Since the red-shifted NIR absorption bands for $\mathbf{2}^{2+}(SbCl_6^-)_2$ can be accounted for by the intramolecular CT interaction between electron-accepting cationic moieties and electron-donating diarylmethylene units by TD-DFT calculations at the CAM-B3LYP/6-31G* level (Figures 3-11, 3-12), the structures in solution are considered to be the same as those in crystals.

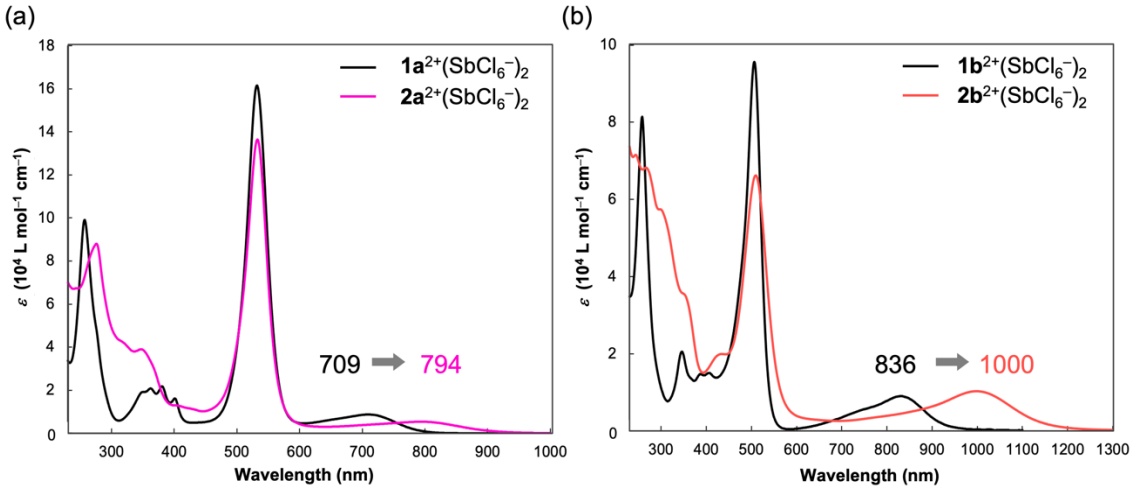

Figure 3-10. UV/Vis/NIR spectra of (a) $\mathbf{2a}^{2+}(SbCl_6^-)_2$ and $\mathbf{2a}^{4+}(SbCl_6^-)_4$, (b) $\mathbf{2b}^{2+}(SbCl_6^-)_2$ and $\mathbf{2b}^{4+}(SbCl_6^-)_4$ in CH_2Cl_2. [$\mathbf{1a}^{2+}$ and $\mathbf{2a}^{2+}$: Ar = 4-$MeOC_6H_4$; $\mathbf{1b}^{2+}$ and $\mathbf{2b}^{2+}$: Ar = 4-^{t}BuC_6H_4]

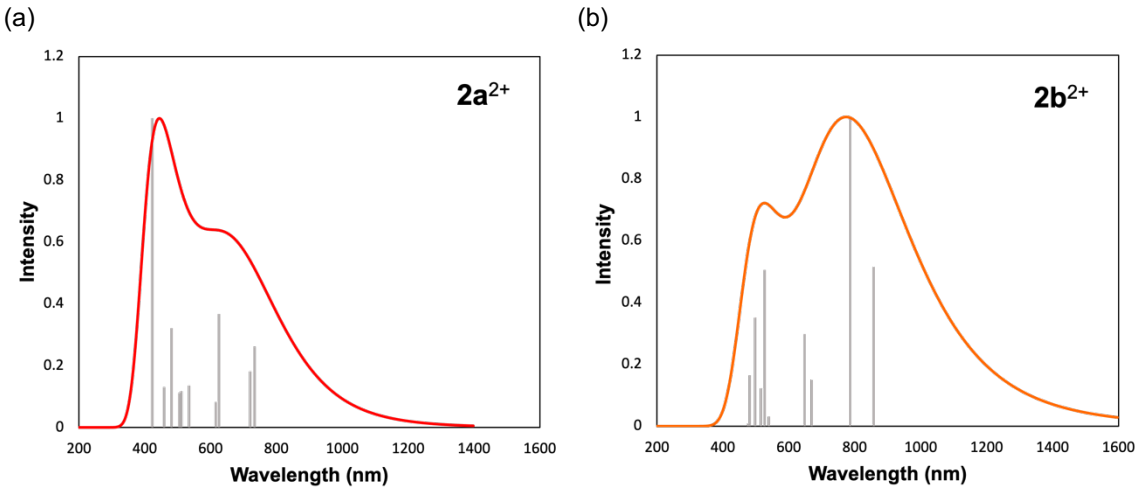

Figure 3-11. Simulated UV/Vis/NIR spectra by TD-DFT calculations (CAM-B3LYP/6-31G*) for (a) $\mathbf{2a}^{2+}$ and (d) $\mathbf{2b}^{2+}$. [$\mathbf{2a}^{2+}$: Ar = 4-$MeOC_6H_4$; $\mathbf{2b}^{2+}$: Ar = 4-^{t}BuC_6H_4] For detailed information on excitation energies and oscillator strengths, see Ref. [48].

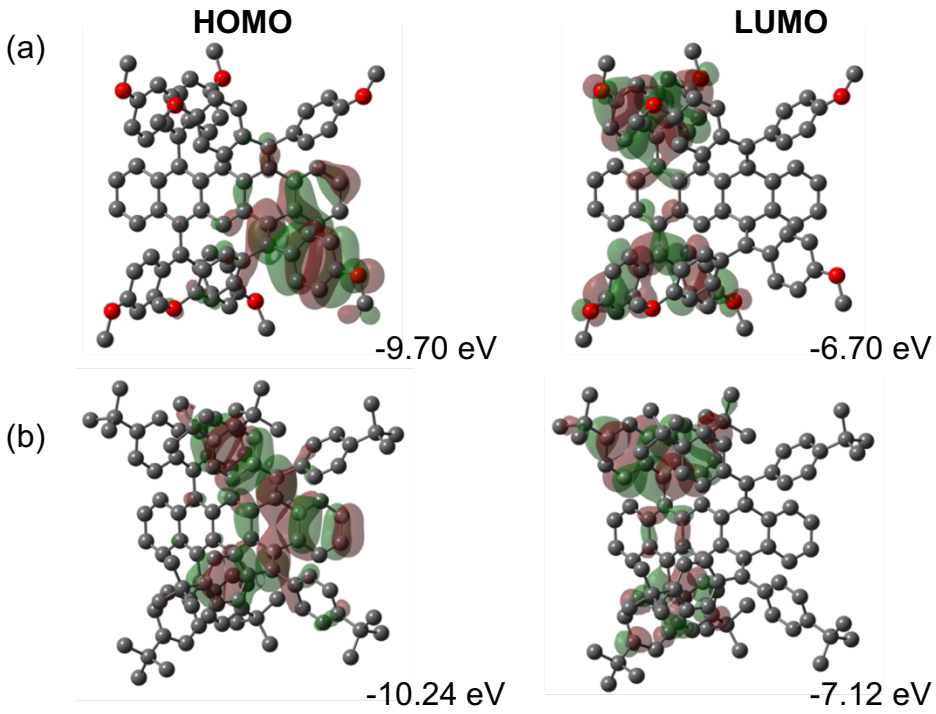

Figure 3-12. HOMO and LUMO levels calculated by the DFT method (CAM-B3LYP/6-31G*) based on the optimized structures of (a) **2a**$^{2+}$ and (d) **2b**$^{2+}$.

Variable-temperature (VT)-^{1}H NMR measurement revealed that there is no intramolecular electron-transfer because any broadening or coalescence of NMR signals of **2a**$^{2+}$($SbCl_6^-$)$_2$ in CD_3CN cannot be observed (Figure 3-13). Thus, each redox part behaves independently, and voltammetric analyses of **2**$^{2+}$ show that one-stage 2e-oxidation of the AQD unit occurred at +0.95 V for **2a**$^{2+}$ and +1.26 V for **2b**$^{2+}$, and one-stage 2e-reduction peaks of dicationic [3]acene were observed at +0.20 V for **2a**$^{2+}$ and +0.73 V for **2b**$^{2+}$ (Figure 3-14a, b). Actually, when dications **2**$^{2+}$ were treated with two equivalents of Magic Blue and with an excess amount of Zn powder, tetracations **2**$^{4+}$ and BQDs **2**, respectively, were isolated quantitatively for both reactions (Scheme 3-8a). Thus, unprecedented hysteretic three-state redox interconversion among tetracationic [5]acenes **2**$^{4+}$, dicationic [3]acenes **2**$^{2+}$, and neutral BQDs ([1]acenes) **2**, as shown by CV measurements, was demonstrated on a preparative scale. With the exact structure and detailed redox properties of dications **2**$^{2+}$ in hand, the author can now explain why BQDs **2** undergo one-stage 4e-oxidation. The HOMOs of **2** have coefficients on the atoms in both AQD units (Figure 3-14c), and thus 2e-oxidation of **2** does not occur to form dications **2**$^{2+}$ of form **A**. Moreover, based on the similar oxidation potentials of **2**$^{2+}$ and **2**, the author can rule out the possibility that orthogonally attached cationic units cause on-site Coulombic repulsion to retard multiple-electron transfer.

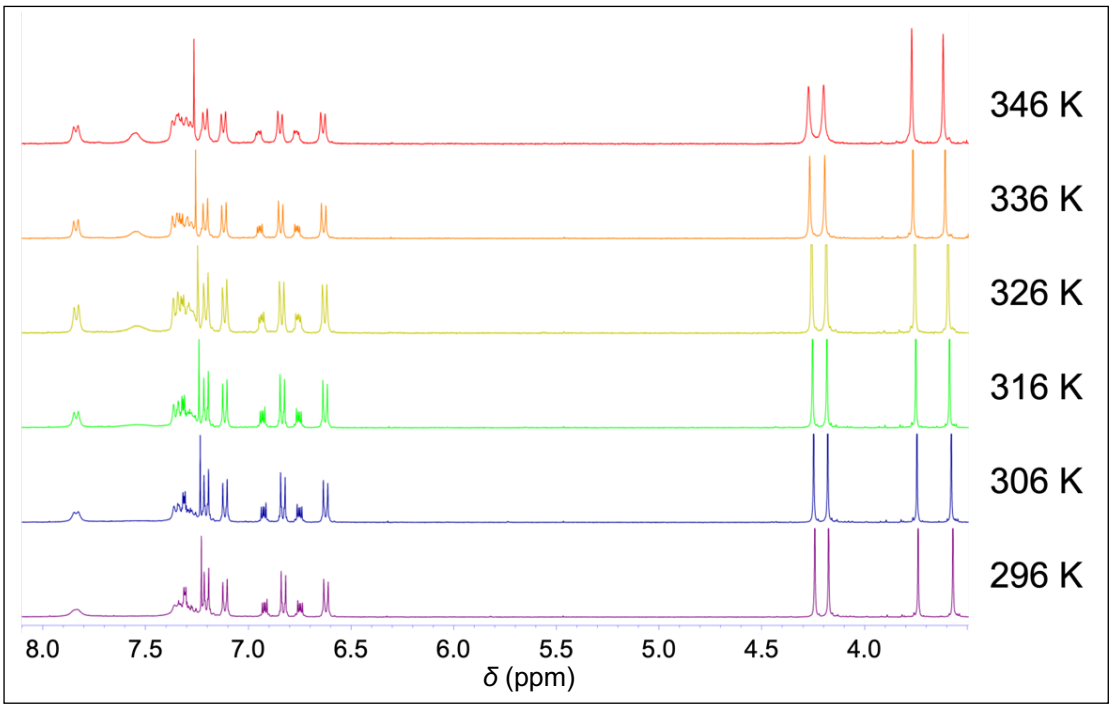

Figure 3-13. VT-^{1}H NMR spectra of $\mathbf{2a}^{2+}$ $(SbCl_6^-)_2$ in CD_3CN from 296 K to 346 K (every 10 K).

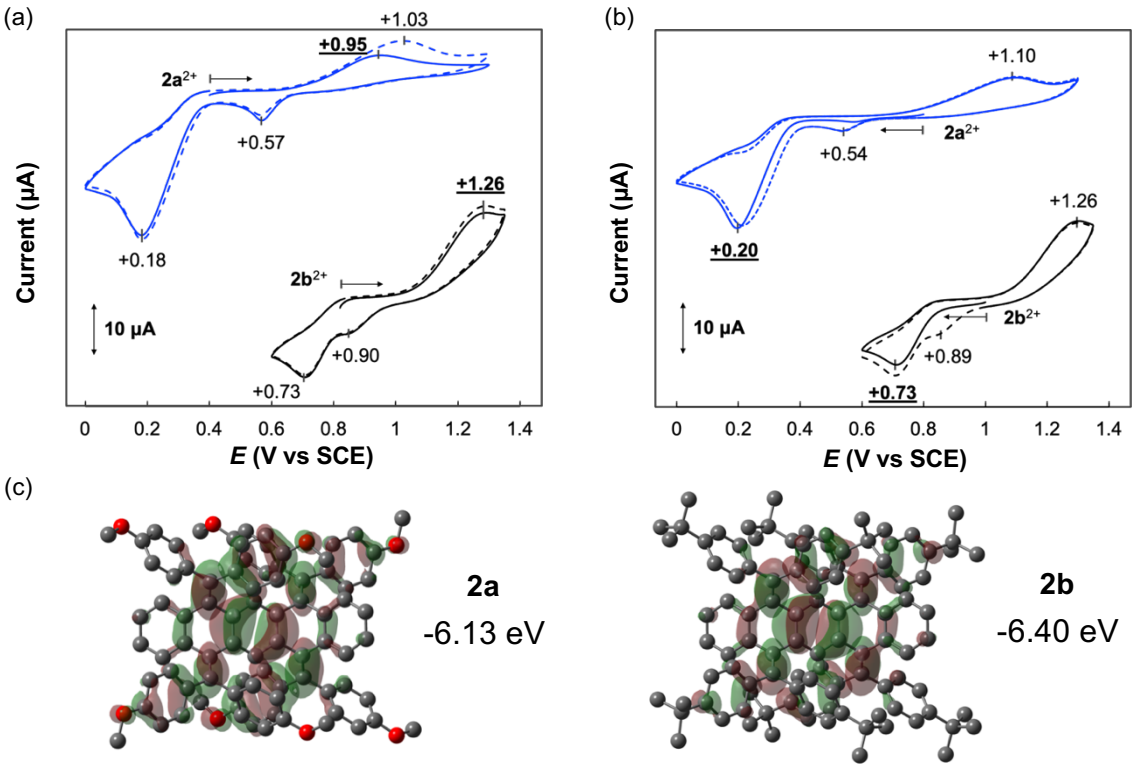

Figure 3-14. Cyclic voltammograms of $\mathbf{2a}^{2+}(SbCl_6^-)_2$ and $\mathbf{2b}^{2+}(SbCl_6^-)_2$ in CH_2Cl_2 containing 0.1 M Bu_4NBF_4 as a supporting electrolyte (scan rate 100 mV·s^{-1}, Pt electrodes). (a) $\mathbf{2}^{2+} \rightarrow \mathbf{2}^{4+} \rightarrow \mathbf{2}^{2+} \rightarrow \mathbf{2} \rightarrow \mathbf{2}^{4+} \rightarrow \mathbf{2}^{2+} \rightarrow \mathbf{2}$ and (b) $\mathbf{2}^{2+} \rightarrow \mathbf{2} \rightarrow \mathbf{2}^{4+} \rightarrow \mathbf{2}^{2+} \rightarrow \mathbf{2} \rightarrow \mathbf{2}^{4+}$ (c) HOMO levels calculated by the DFT method (CAM-B3LYP/6-31G*) based on the optimized structures of **2a** and **2b**

3-2-7. Study on the conformational preferences of dications

Based on the investigation shown above, the pentacenequinodimethane-type dication (**A**) has a quite peculiar structure, in which the two positive charges are located on the one side of the molecular skeleton (Scheme 3-5). Compared to the isomeric dication diradical structure (**B**), the charges in form **A** are less delocalized over the π-skeleton with an anthracene core on the skeleton. The number of Clar sextet in form **A** is larger than in form **B**, which may, if possibly, account for preference of form **A**. By considering that form **B** consists of two units of the cation radical of redox-active AQD (**1**), the authors envisaged that the detailed examination of the geometrical and electronic structure on $\mathbf{1}^{+\bullet}$ would provide a valuable information to account for the unique structure of form **A**. Since the cation radical $\mathbf{1}^{+\bullet}$ is a transient species in the cases of symmetric compounds with the same four aryl groups [**1a**: Ar^1=Ar^2=4-$MeOC_6H_4$; **1f**: Ar^1=Ar^2=4-$Me_2NC_6H_4$; **1g**: Ar^1=Ar^2=4-$O(CH_2CH_2)_2NC_6H_4$] due to successive 2e-transfer in both oxidation and reduction steps (Scheme 3-5),[40] the author has designed here the unsymmetric analogues (**1af**, **1ag**), in anticipation that the lifetime of the corresponding cation radicals would be extended. The aryl substituents of **1af** (Ar^1=4-$Me_2NC_6H_4$, Ar^2=4-$MeOC_6H_4$) are selected so that the 2e-process of **1** to $\mathbf{1}^{2+}$ or $\mathbf{1}^{2+}$ to **1** would occur in a stepwise manner by the different electron-donating properties of dimethylamino and methoxy groups as shown by the oxidation peak potential of **1f** (+0.50 V vs SCE in CH_2Cl_2) and **1a** (+1.03 V). The author also designed **1ag** [Ar^1=4-$O(CH_2CH_2)_2NC_6H_4$, Ar^2=4-$MeOC_6H_4$] with the expectation that the donating properties of morpholino group are intermediary between the above two (+0.71 V for **1g**).

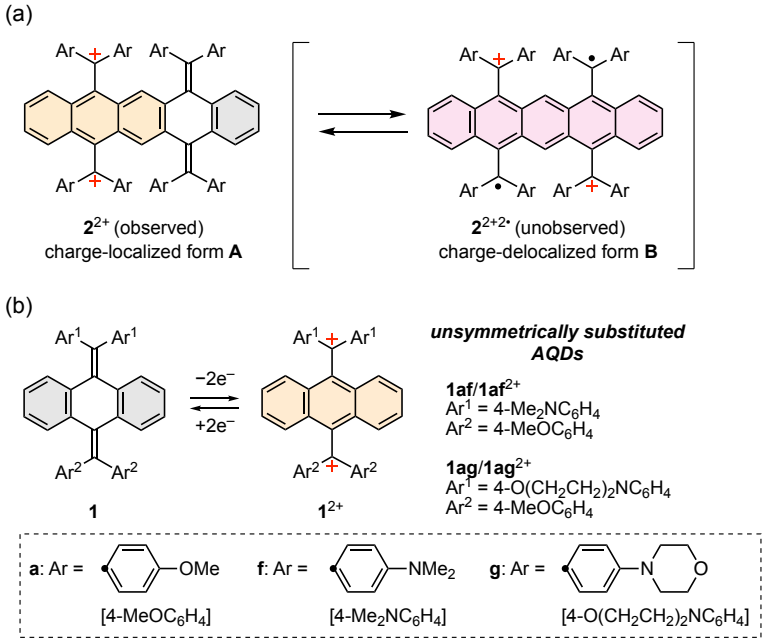

Scheme 3-5. (a) Charge-localized and -delocalized form (**A** and **B**) of extended dications $\mathbf{2}^{2+}$ based on bisquinodimethane derivatives. (b) Redox interconversion of anthraquinodimethane derivatives.

The voltammogram would exhibit a 2e-oxidation wave upon conversion of **1af** to $\mathbf{1af}^{2+}$, whereas the two separated 1e-reduction waves would be observed in the reverse cycle for the transformation of $\mathbf{1af}^{2+}$ to **1af** via $\mathbf{1af}^{+\bullet}$. As shown in Figure 3-15, this holds true for the voltammogram of **1ad** (1 mM in CH_2Cl_2 at 298 K) with the scan rate of 1 V s^{-1}. Based on the external standard of ferrocene/ferrocenium, oxidation wave of **1af** was confirmed to be a 2e-process, and the oxidation peak at +0.69 V is close to that of **1f** (+0.50 V) with four 4-dimethylaminophenyl groups. In the return cycle, there are two peaks corresponding to the reduction of $\mathbf{1af}^{2+}$ to $\mathbf{1af}^{+\bullet}$ and the reduction of $\mathbf{1af}^{+\bullet}$ to **1af** at +0.12 V and −0.19 V vs SCE, respectively. The former value is less positive but still close to the reduction peak of $\mathbf{1a}^{2+}$ (+0.42 V) with four 4-methoxyphenyl groups, whereas the latter value is similar to that of $\mathbf{1f}^{2+}$ (−0.27 V). It should be noted that the reduction wave of $\mathbf{1af}^{2+}/\mathbf{1af}^{+\bullet}$ at +0.12 V is reversible when the sweep direction was switched just after the first reduction peak (Figure 3-15), thus confirming that $\mathbf{1af}^{+\bullet}$ generated from $\mathbf{1af}^{2+}$ maintains its twisted geometry. In contrast, the similar reversible wave did not appear when the direction was switched after the second reduction wave, showing that the geometrical change of twisted $\mathbf{1af}^{2\bullet}$ to folded **1af** is very fast, as expected.

Based on the potential difference (ΔE) of 0.31 V for the two reduction peaks, the intermediary twisted cation radical $\mathbf{1af}^{+\bullet}$ should be thermodynamically stable ($\log K$=5.34 where $K=[\mathbf{1af}^{+\bullet}]^2/[\mathbf{1af}^{2\bullet}][\mathbf{1af}^{2+}]$). However, the author found that disproportionation of $\mathbf{1af}^{+\bullet}$ into $\mathbf{1af}^{2\bullet}$ and $\mathbf{1af}^{2+}$ proceeds easily, and the second reduction peak became ambiguous when the voltammogram was measured at 100 mV s^{-1} (Figure 3-15). Such observation should be related to the very fast geometrical change from twisted $\mathbf{1af}^{2\bullet}$ to folded **1af**. Further evidence for the disproportionation process was obtained by measuring the voltammogram at different scan rate, and at different temperatures, showing that the second reduction peak almost disappeared at low scan rate and at higher temperature. In the voltammograms for the conversion of $\mathbf{1ag}^{2+}$ to **1ag**, the second reduction peak is more ambiguous than in the case of $\mathbf{1af}^{2+}$ to **1af**, since the disproportionation of $\mathbf{1ag}^{+\bullet}$ into $\mathbf{1ag}^{2\bullet}$ and $\mathbf{1ag}^{2+}$ is thermodynamically more favored due to the smaller potential difference for the reduction processes of bis(4-methoxyphenyl)methylium and bis(4-morpholinophenyl)methylium (E^{red} of −0.11 V for $\mathbf{1g}^{2+}$ is more positive than that for $\mathbf{1f}^{2+}$). Thanks to the unsymmetric substitution and the different electronic properties of amino and methoxy groups, the present dications $\mathbf{1af}^{2+}$ and $\mathbf{1ag}^{2+}$ with a twisted geometry undergo stepwise reduction to generate thermodynamically stabilized cation radicals $\mathbf{1af}^{+\bullet}$ and $\mathbf{1ag}^{+\bullet}$. By considering the twisted geometry of $\mathbf{1}^{2+}$, it is highly likely that spectroscopically observed $\mathbf{1}^{+\bullet}$ would adopt a twisted geometry similar to that of $\mathbf{1}^{2+}$. In this way, the redox process between **1** and $\mathbf{1}^{2+}$ would involve the geometrical change as shown in Scheme 3-6, which includes the knowledge that neutral quinodimethane **1** has no contribution from the twisted diradical form $\mathbf{1}^{2+}$.

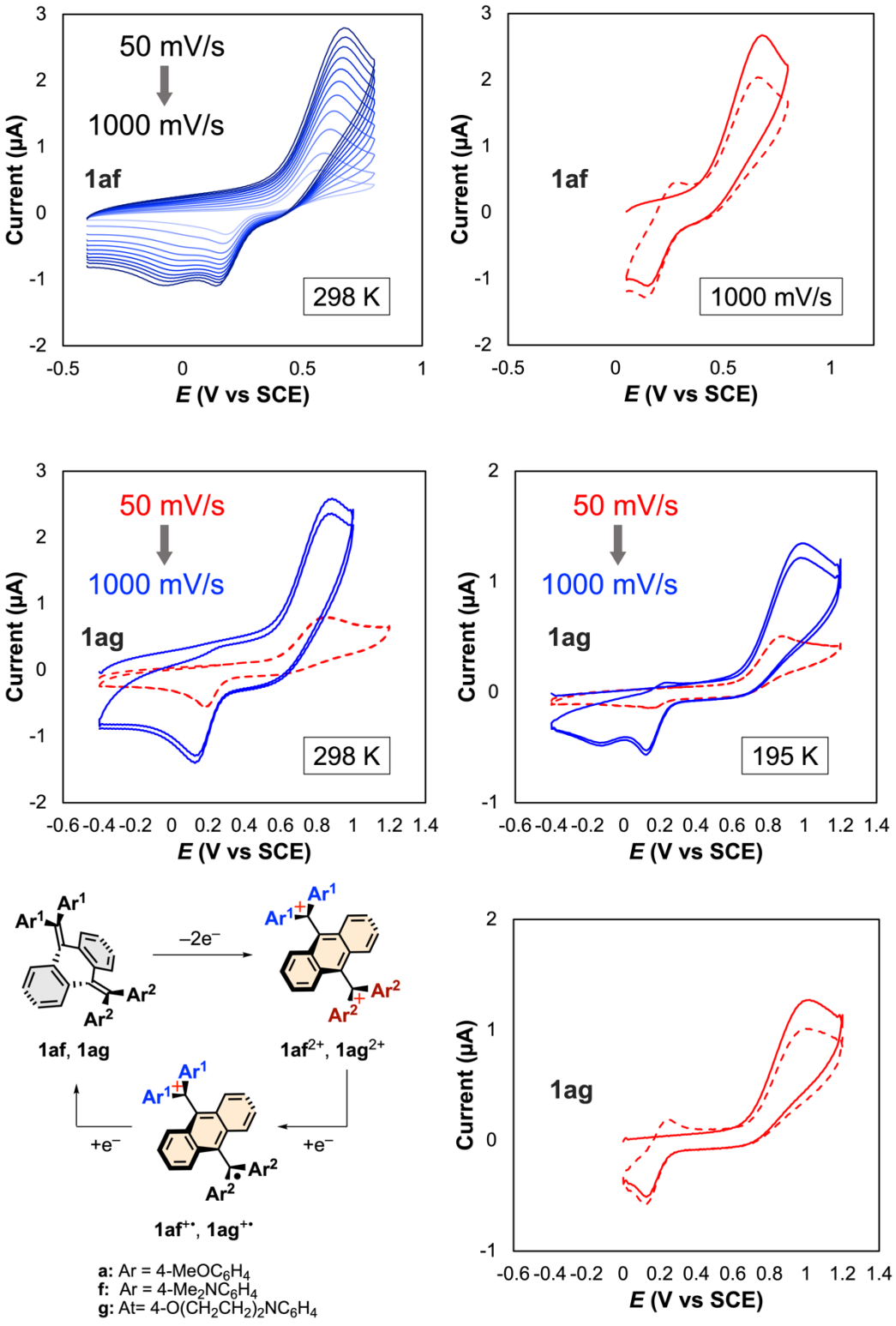

Figure 3-15. Cyclic voltammograms of **1af** and **1ag** in CH_2Cl_2 containing 0.1 M Bu_4NBF_4 as a supporting electrolyte (Pt electrodes).

If the author considers that the hypothetical dication diradical **B** consists of two units of $\mathbf{1}^{+\bullet}$ which are confined in a proximity, the form **B** should undergo intramolecular disproportionation to give another dication diradical **C** (Scheme 3-7). Because of the rapid conversion of geometry from twisted form ($\mathbf{1}^{2\bullet}$) to folded form (**1**), the form **C** would be easily transformed to the form **A** with a pentacenequinodimethane skeleton. Once the form **A** is produced, the oxidation potential of its quinodimethane unit is more positive than that of the diradical unit in the form **C**, and thus intramolecular electron transfer in the form **A** to the form **B** is energetically disfavored. In this way, we could now clarify the reason why the charge-localized dication with the [3]acene core (**A**) was observed and isolated, while the form **B** was not discovered at all.

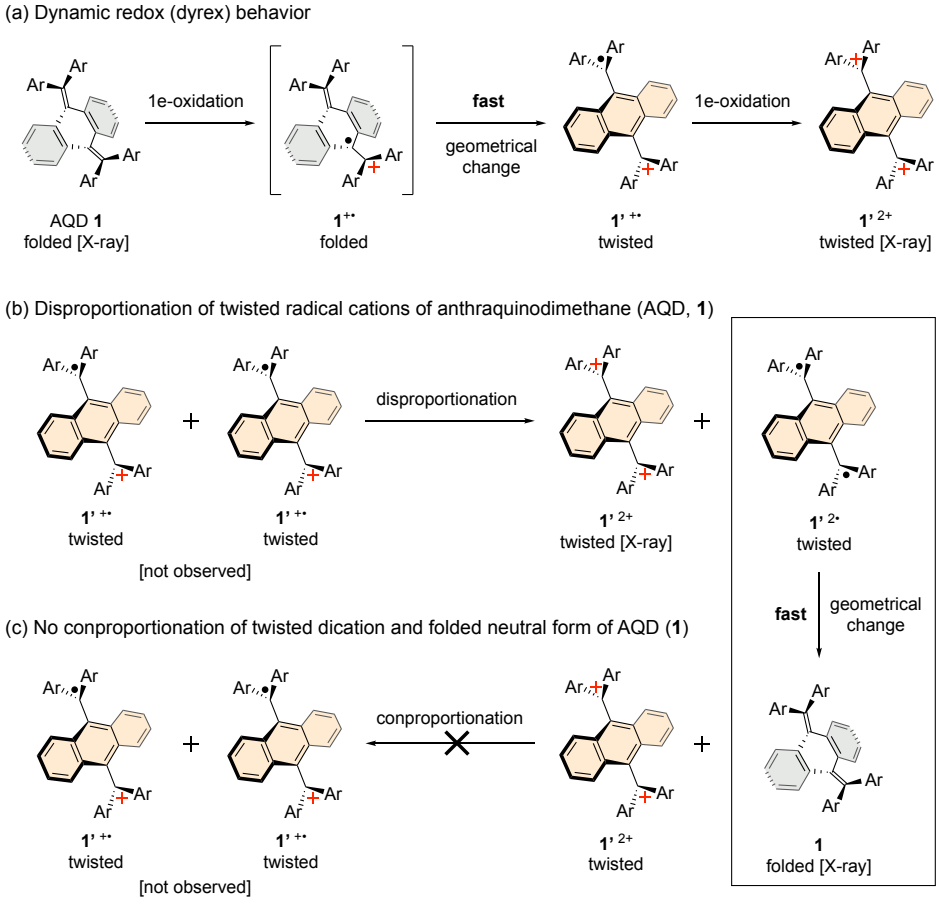

Scheme 3-6. A plausible mechanism of redox interconversion between **1** and $\mathbf{1}^{2+}$.

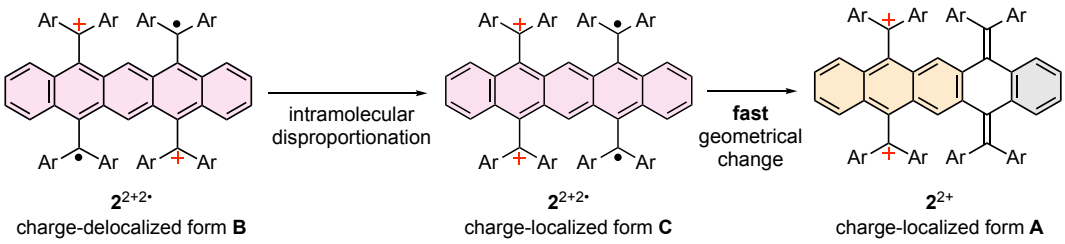

Scheme 3-7. A plausible mechanism of intramolecular disproportionation from the form **B** to **C**.

3-2-8. Hybridization of BQDs for tricolor chromism

The BQDs **2** were found to be converted into dicationic and tetracationic states with negligible steady-state concentrations of intermediary open-shell species such as monocation radical or trication radical. Thus, the BQD skeleton would be the best platform for constructing tricolor electrochromic systems with high reversibility due to the apparent 2e-transfer for mutual interconversion among three-color states. However, based on a consideration of the similar absorption bands [λ_{max}/nm (log ε) in CH_2Cl_2: 517(5.30) for **2a**$^{4+}$($SbCl_6^-$)$_4$ and 498 (5.08) for **2b**$^{4+}$($SbCl_6^-$)$_4$], a methoxyphenyl group and a *tert*-butylphenyl group would not make a good combination to construct a tricolor electrochromic system. Based on this result, the author newly designed BQD-based tricolor electrochromic molecules **2af** and **2ag**, which have four 4-methoxyphenyl groups and four 4-aminophenyl groups, by considering that quite different colors are expected for the aryl groups when incorporated in the diarylmethylium unit (Figure 3-16). Before we examined such hybrid compounds, the author also examined octakis(4-dimethylaminophenyl) and octakis(4-morpholinophenyl) derivatives **2f** and **2g**.

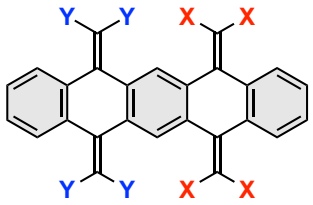

Ar$_8$BQDs **2**

2a : **X** = **Y** = 4-$MeOC_6H_4$

2b : **X** = **Y** = 4-^{t}BuC_6H_4

2f : **X** = **Y** = 4-$Me_2NC_6H_4$

2g : **X** = **Y** = 4-$O(C_2H_4)_2NC_6H_4$

2af
X = 4-$MeOC_6H_4$
Y = 4-$Me_2NC_6H_4$

2ag
X = 4-$MeOC_6H_4$
Y = 4-$O(CH_2CH_2)_2NC_6H_4$

Figure 3-16. Newly designed BQD-based tricolor electrochromic molecules **2af** and **2ag**.

The hybrid compounds **2af** and **2ag** were synthesized by the Suzuki-Miyaura cross-coupling reaction using the key intermediate **6a** described above. As in the parent neutral donor **2a**, **2f**, **2g**, these hybrid compounds exhibit absorption mainly in the UV region [λ_{max}/nm (log ε) in CH_2Cl_2: 347 (4.59) for **2af** and 337 (4.60) for **2ag**] (Figure 3-17a). In contrast to the neutral state, hybrid tetracations **2af**$^{4+}$($SbCl_6^-$)$_4$ and **2ag**$^{4+}$($SbCl_6^-$)$_4$, both of which were obtained by treatment of **2af** and **2ag** with four equivalents of Magic Blue, exhibit two strong absorptions in the visible region [λ_{max}/nm (log ε) in CH_2Cl_2: 656 (4.97) and 532 (5.23) for **2af**$^{4+}$ and 659 (5.01) and 534 (5.22) for **2ag**$^{4+}$] (Figure 3-17a). The absorption around 650 nm and that around 530 nm are characteristic to bis(aminophenyl)methylium- and bis(methoxyphenyl)methylium-based chromophores, respectively. When the bands of bis(aminophenyl)methylium in **2af**$^{4+}$ and **2ag**$^{4+}$ were compared to those in BQD tetracations with eight aminophenyl groups [592 for **2f**$^{4+}$(I_3^-)$_4$ and 600 (5.29) for **2g**$^{4+}$(I_3^-)$_4$], considerable red-shifts were observed in both hybrid tetracations. This holds true for the absorption band of bis(methoxyphenyl)methylium since BQD tetracation **2a**$^{4+}$($SbCl_6^-$)$_2$ shows absorption at 517 nm (log ε 5.30) (Figure 3-17b). These results clearly show that the intramolecular interaction between two different diarylmethyliums in **2af**$^{4+}$ and **2ag**$^{4+}$ induces a red-shift of the intrinsic absorptions of

these chromophores. A hypochromic shift of the absorption band of bis(aminophenyl)methylium would also be related to such interchromophore interactions, and the differences in the oscillator strength *f* were reproduced by time-dependent (TD)-DFT calculations (Figures 3-26, 3-28, see p.115 and p.117).

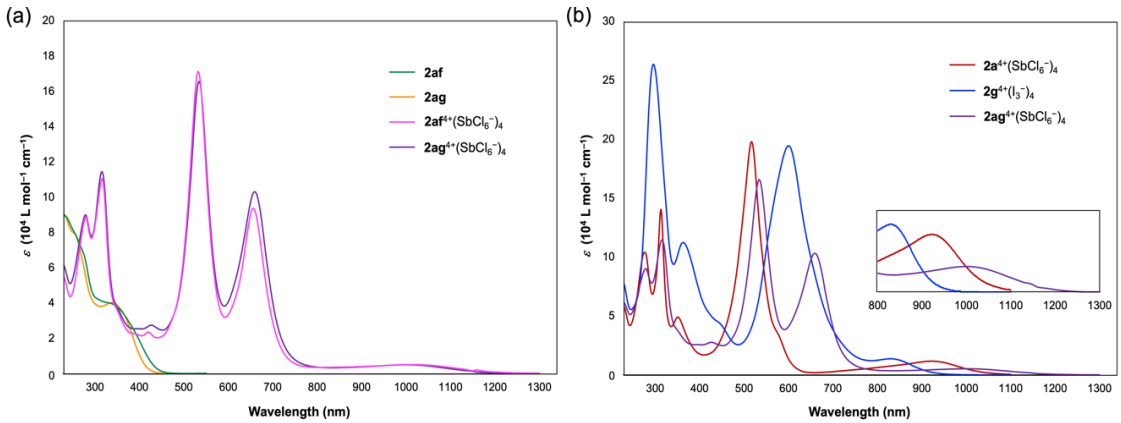

Figure 3-17. (a) UV/Vis/NIR spectra of **2af**, **2ag**, **2af**$^{4+}$$(SbCl_6^-)_4$ and **2ag**$^{4+}$$(SbCl_6^-)_4$ in CH_2Cl_2. (b) UV/Vis/NIR spectra of **2a**$^{4+}$$(SbCl_6^-)_4$, **2g**$^{4+}$$(I_3^-)_4$ and **2ag**$^{4+}$$(SbCl_6^-)_4$ in CH_2Cl_2. [**2a**: X=Y=4-$MeOC_6H_4$; **2g**: X=Y=4-$O(C_2H_4)_2NC_6H_4$; **2af**: X=4-$MeOC_6H_4$, Y=4-$Me_2NC_6H_4$; **2ag**: X=4-$MeOC_6H_4$, Y=4-$O(C_2H_4)_2NC_6H_4$].

Table 3-1. UV/Vis/NIR spectral data of the tetracationic salts in CH_2Cl_2.

	Substituents	λ_{max}/nm (ε)
2a^{4+}$(SbCl_6^-)_4$	Ar = 4-$MeOC_6H_4$	922 (4.06), 517 (5.30)
2f^{4+}$(I_3^-)_4$	X = Y = 4-$Me_2NC_6H_4$	780 [a], 592 [a]
2g^{4+}$(I_3^-)_4$	X = Y = 4-$O(C_2H_4)_2NC_6H_4$	830 (4.13), 600 (5.29)
2af^{4+}$(SbCl_6^-)_4$	X = 4-$MeOC_6H_4$, Y = 4-$Me_2NC_6H_4$	1025 (3.71), 656 (4.97), 532 (5.23)
2ag^{4+}$(SbCl_6^-)_4$	X = 4-$MeOC_6H_4$, Y = 4-$O(C_2H_4)_2NC_6H_4$	1000 (3.71), 659 (5.01), 534 (5.22)

[a] The molar extinction coefficients were not determined due to low solubility.

In addition to the bands in the visible region, all of the BQD tetracations exhibit NIR absorptions, which are assigned to the intramolecular CT transition from the pentacene core (major contribution of HOMO) to the electron-deficient diarylmethyliums (major contribution of nearly degenerated LUMOs), as assigned by TD-DFT calculations at the CAM-B3LYP/6-31G* level. Notably, such NIR absorption bands are also red-shifted in **2af**$^{4+}$ [1025 (3.71)] and **2ag**$^{4+}$ [1000 (3.71)] compared to those of tetracations with the same eight aryl groups [922 (4.06) for **2a**$^{4+}$, 780 for **2g**$^{4+}$, and 830 (4.13) for **2f**$^{4+}$] (Figures 3-17b). The red-shift of the NIR band in the hybrid tetracations can be qualitatively

accounted for by considering that the strongly electron-deficient bis(methoxyphenyl)methylium can warrant a cation-based lower LUMO in **2af**$^{4+}$, **2ag**$^{4+}$, and **2a**$^{4+}$. Although four-fold substitution of bis(methoxyphenyl)methylium in **2a**$^{4+}$ simultaneously causes lowering of the HOMO level by its electron-withdrawing effects, these red-shifts in hybrid tetracations **2af**$^{4+}$ and **2ag**$^{4+}$ indicate that the HOMO level can be maintained to be higher due to the strong electron-donating ability of two bis(aminophenyl)methyliums. In this way, the author found that all of the first band around 1000 nm, the second band around 650 nm, and the third band around 420 nm in hybrid tetracations can be red-shifted relative to the corresponding bands in the simple BQD tetracations by attaching two different diarylmethylium chromophores on the pentacene core. This finding can provide useful guidelines, especially in terms of the red-shift of the NIR band, which is the cause of the recent attention regarding potential application as functional dyes.

To investigate the redox behavior of newly synthesized BQDs, CV measurements were performed in CH_2Cl_2 with ferrocene as an external standard. BQDs **2f** and **2g** with eight aminophenyl groups exhibit voltammograms as shown in Figure 3-18 that are quite similar to that of methoxyphenyl analogue **2a**. Thus, one-wave 4e-electron oxidation peak as well as two-stage 2e-reduction peaks were observed. The anodic peak potential (E_{peak}^{ox}/V vs SCE: +0.50 for **2f** and +0.68 for **2g**, respectively) is less positive than that for **2a** (+1.12), which corresponds to the electron-donating ability of aryl groups. The DFT calculations show that, for BQDs **2** with the same eight aryl groups, the HOMO is widely delocalized over the same two units of tetraarylquinodimethane, so that the oxidation process apparently proceeds as a one-wave 4e process to produce the corresponding tetracationic states (see above). Accordingly, the dicationic states **2**$^{2+}$ are short-lived during the oxidation process and could be generated only upon 2e-reduction of the tetracations **2**$^{4+}$.

In contrast, the redox behavior of hybrid BQDs **2af** and **2ag** is quite different from that of simple BQDs **2** shown above, due to the different electronic natures of the two kinds of aryl substituents (Figure 3-18). Thus, two-stage 2e-processes occur in both oxidation and reduction waves. The two-stage oxidation processes were also supported by differential pulse voltammetry measurements. Thus, the dications **2ag**$^{2+}$ and **2af**$^{2+}$ would be generated not only by 2e-reduction of the tetracations, but also by 2e-oxidation of the neutral forms. The oxidation peaks of **2ag** (E_{peak}^{ox} /V vs SCE: +0.42 and +0.95) can be characterized by considering the combination of AQDs with dimethylaminophenyl groups (+0.50) and methoxyphenyl groups (+1.03), respectively, suggesting that the first 2e-oxidation of **2af** proceeds at the more easily oxidized dimethylaminophenyl units, followed by the 2e-oxidation of the methoxyphenyl units. As a result of the dynamic change in structure between the zigzag pentacyclic core for the neutral state and planar pentacene for the tetracation, return peaks appeared in the far cathodic region (E_{peak}^{red}/ V: +0.53 and –0.40), where two-step 2e-reduction occurs with a negligible steady-state concentration of intermediate open-shell species (**2af**$^{+\bullet}$ or **2af**$^{3+\bullet}$). This holds true for another hybrid compound **2ag**, with a slight change in redox potentials (E_{peak}^{ox}/ V: +0.66 and +0.97;

E_{peak}^{red}/ V: +0.54 and –0.20), which were tuned by the electronic properties of the amino substituents. The energies of the HOMO and LUMO levels of each redox state were qualitatively reproduced by DFT calculations (Figures 3-25, 3-26, 3-27, see pp.114－116).

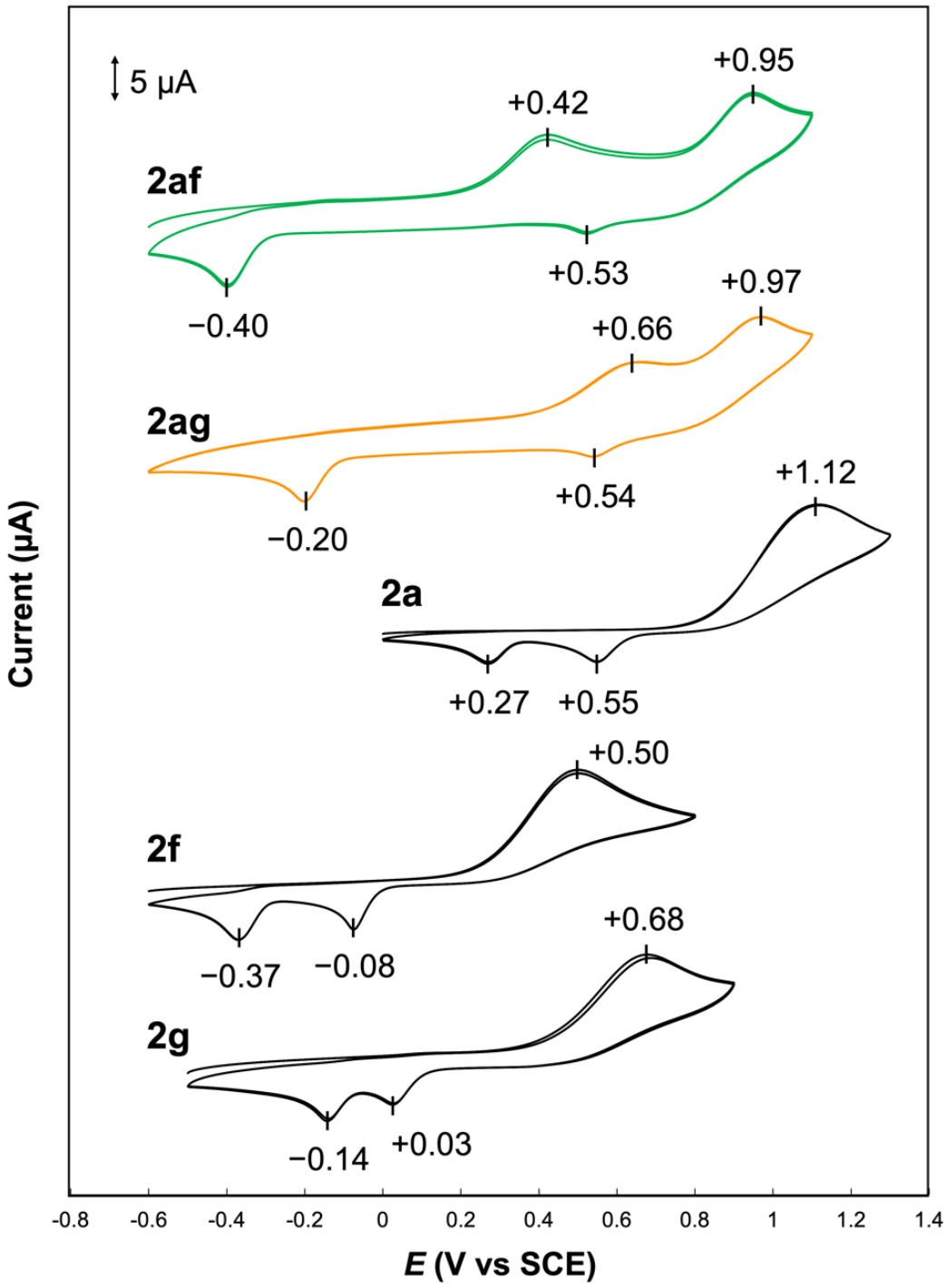

Figure 3-18. Cyclic voltammograms of **2a**, **2f**, **2g**, **2af** and **2ag** in CH_2Cl_2 containing 0.1 M Bu_4NBF_4 as a supporting electrolyte (scan rate 100 $mV \cdot s^{-1}$, Pt electrodes).

Based on the stepwise redox processes observed in the voltammograms of hybrid BQDs **2af** and **2ag**, their dications would be isolated not only upon 2e-reduction of the tetracations, but also upon 2e-oxidation of neutral BQDs under preparative conditions. In fact, treatment of neutral **2af** and **2ag** with two equivalents of Magic Blue allowed isolation of the dicationic salts **2af**$^{2+}$($SbCl_6^-$)$_2$ and **2ag**$^{2+}$($SbCl_6^-$)$_2$ in respective yields of 95% and 95%. Meanwhile, treatment of the tetracation salts **2af**$^{4+}$($SbCl_6^-$)$_4$ and **2ag**$^{4+}$($SbCl_6^-$)$_4$ with two equivalents of cobaltocene as a reducing agent gave the same dicationic salts in respective yields of 88% and 82%. In addition, the obtained dicationic salts can be oxidized to the tetracationic salts **2af**$^{4+}$($SbCl_6^-$)$_4$ and **2ag**$^{4+}$($SbCl_6^-$)$_4$ in yields of 96% and 97%, whereas Zn-reduction regenerated **2af** and **2ag** in yields of 100% and 96% yields. Therefore, the dication of hybrid BQDs is the isolable intermediate in a three-state redox interconversion in both the oxidation and reduction cycles (Figure 3-19a).

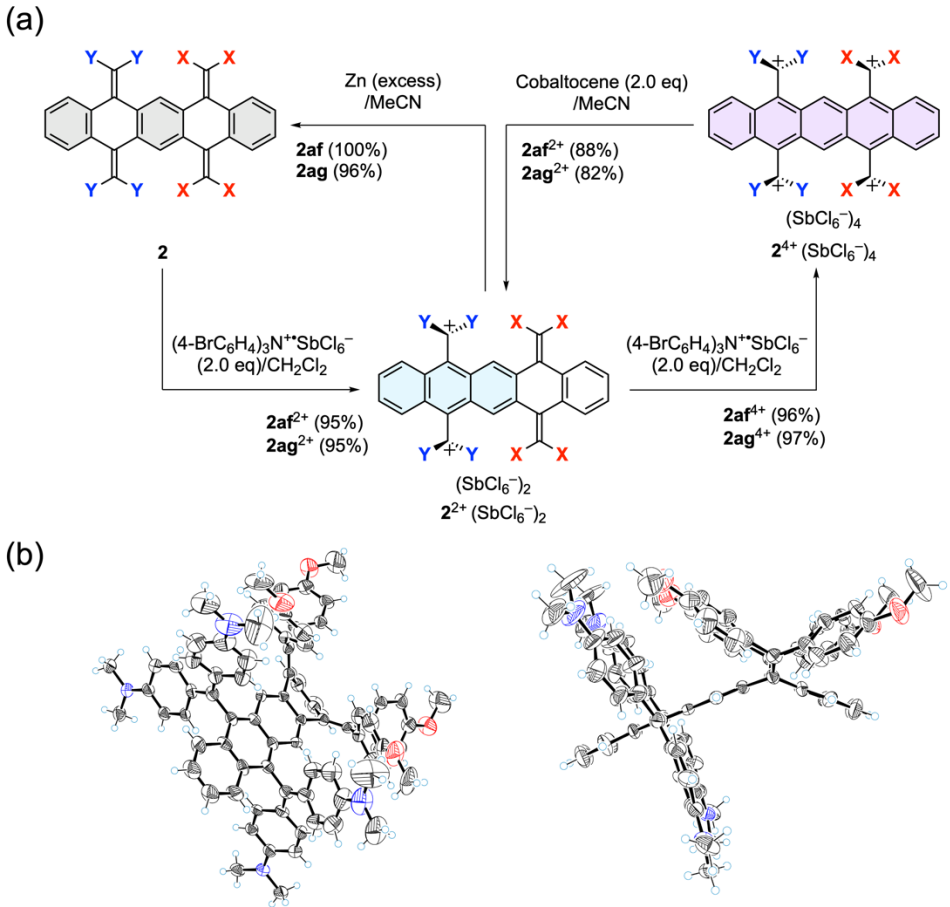

Figure 3-19. (a) Isolation of dication salts **2af**$^{2+}$($SbCl_6^-$)$_2$ and **2ag**$^{2+}$($SbCl_6^-$)$_2$ and redox interconversion among dicationic states **2**$^{2+}$ and other redox states **2**/**2**$^{4+}$. (b) X-ray crystal structures (ORTEP drawings) of **2af**$^{2+}$($SbCl_6^-$)$_2^{\#}$ determined at 150 K. The counterions solvent molecules, and disordered atoms are omitted for clarity. Thermal ellipsoids are shown at the 50% probability level. $^{\#}$One of the two crystallographically independent molecules. [**2af**: X = 4-$MeOC_6H_4$, Y = 4-$Me_2NC_6H_4$; **2ag**: X = 4-$MeOC_6H_4$, Y = 4-$O(C_2H_4)_2NC_6H_4$]

The ^{1}H NMR spectra of **2af**$^{2+}$($SbCl_6^-$)$_2$ and **2ag**$^{2+}$($SbCl_6^-$)$_2$ indicate that positive charges are located on the aminophenyl moieties, which is in accord with the expectation based on voltammetric analyses. There were no signs of a contribution from the open-shell species for the dications. Finally, X-ray analysis of the dicationic salt **2af**$^{2+}$($SbCl_6^-$)$_2$ revealed that it consists of an [3]acene skeleton attached to two bis(dimethylaminophenyl)methylium units, to which tetrakis(methoxyphenyl)quinodimethane unit is annulated (Figure 3-19b). Thus, the dicationic states of hybrid BQDs with two kinds of electrophores of different donating properties are closed-shell species with localized positive charges on the diarylmethylium moieties with more strongly donating aryl groups.

As expected from the X-ray structure of **2af**$^{2+}$($SbCl_6^-$)$_2$, the absorption band based on bis(methoxyphenyl)methylium units would disappear for both dicationic salts. Indeed, only the absorption bands attributed to bis(aminophenyl)methylium units were observed [λ_{max}/nm (log ε) in CH_2Cl_2: 640 (5.37) for **2af**$^{2+}$ and 642 (5.32) for **2ag**$^{2+}$, respectively] (Figure 3-20). The NIR absorption band is absent in dications **2af**$^{2+}$ and **2ag**$^{2+}$ because the intramolecular CT bands overlap the local absorption bands of bis(aminophenyl)methyliums. The blue-shift of the CT bands can be accounted for by the higher LUMO level of these dications due to the lower electron-accepting ability of the bis(aminophenyl)methylium groups and by the lower HOMO level by changing the acene unit from pentacene in the tetracations to anthracene in the dications. In this way, a sharp difference in the absorption band for the three interconvertible closed-shell states is realized for neutral states (only UV), dications (blue without NIR), and tetracations (violet with NIR).

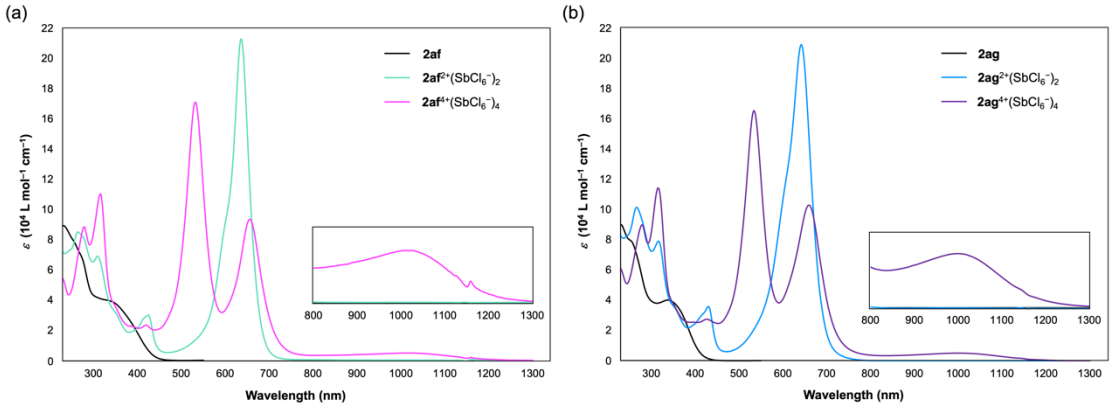

Figure 3-20. UV/Vis/NIR spectra of (a) **2af**, **2af**$^{2+}$($SbCl_6^-$)$_2$, and **2af**$^{4+}$($SbCl_6^-$)$_4$ in CH_2Cl_2 and (b) **2ag**, **2ag**$^{2+}$($SbCl_6^-$)$_2$, and **2ag**$^{4+}$($SbCl_6^-$)$_4$ in CH_2Cl_2. [**2af**: X=4-$MeOC_6H_4$, Y=4-$Me_2NC_6H_4$; **2ag**: X=4-$MeOC_6H_4$, Y=4-$O(C_2H_4)_2NC_6H_4$].

To demonstrate the redox-dependent color changes of hybrid BQDs, a titration experiment was conducted for **2ag** by using Magic Blue in CH_2Cl_2, which was monitored by UV/Vis/NIR spectroscopy (Figure 3-21a). Upon the addition of several aliquots of oxidant, sequential and drastic spectral changes were observed. First, a strong band at 642 nm grew to give blue solution with an isosbestic point at 389 nm (1st stage), and then strong absorption at 534 nm gradually grew to give a purple solution with several isosbestic points at 663, 577, 435, and 266 nm (2nd stage). Such a spectral change can be accounted for by considering the quantitative conversion to **2ag** to $\mathbf{2ag}^{2+}$ in the 1st stage until the addition of two equivalents of Magic Blue, whereas the 2nd stage shows the quantitative conversion of $\mathbf{2ag}^{2+}$ to $\mathbf{2ag}^{4+}$ with concomitant growth of the NIR band. In both stages, steady-state concentrations of open-shell intermediates ($\mathbf{2ag}^{+\bullet}$ and $\mathbf{2ag}^{3+\bullet}$) are negligible.

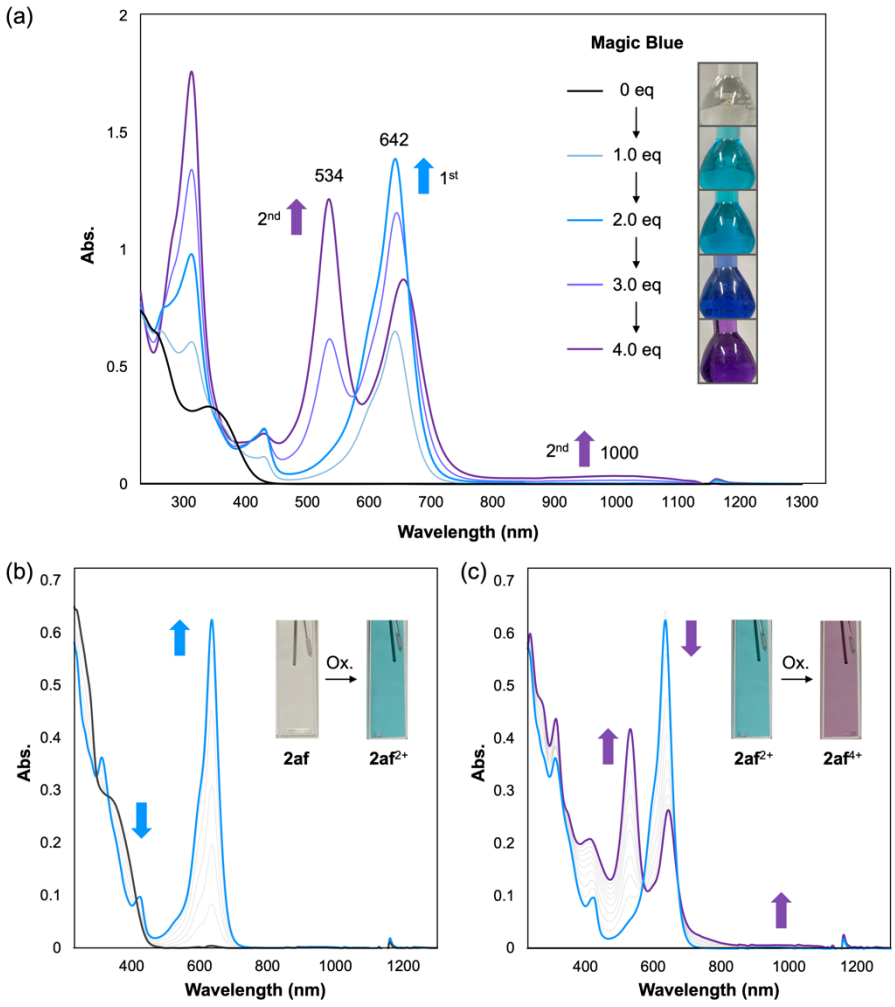

Figure 3-21. (a) Change in UV/Vis/NIR spectrum of **2ag** (8.00 μM) upon the addition of several aliquots of Magic Blue in CH_2Cl_2 [**2ag**: X = 4-$MeOC_6H_4$, Y = 4-$O(C_2H_4)_2NC_6H_4$]. Changes in UV/Vis/NIR spectra upon constant-current electrochemical oxidation of (b) **2af** (7.23 μM, 30 μA, every 2 min) and (c) as-prepared $\mathbf{2af}^{2+}$ (30 μA, every 8 min) in CH_2Cl_2 containing 0.05 M Bu_4NBF_4 as a supporting electrolyte. [**2af**: X = 4-$MeOC_6H_4$, Y = 4-$Me_2NC_6H_4$]

In addition to the titration experiments, the constant-current electrochemical oxidation of **2af** in CH_2Cl_2 was conducted, and this was monitored by UV/Vis/NIR spectroscopy. The 1st-stage spectroelectrogram with isosbestic points showed that the spectrum could be accounted for simply by considering the presence of **2af** and **2af**$^{2+}$ (Figure 3-21b). The 2nd-stage spectroelectrogram also exhibits the isosbestic points, indicating only the presence of **2af**$^{2+}$ and **2af**$^{4+}$ with an increase in NIR absorption (Figure 3-21c). During the electrochemical reduction of as-generated **2af**$^{4+}$, sequential spectral changes were observed; initially, the bands at 534 nm and those in the NIR region disappeared to give a blue solution of **2af**$^{2+}$, and then the absorption at 640 nm gradually faded to give a colorless solution of **2af**. Thus, by using the hybrid BQDs **2af** and **2ag**, reversible interconversion among the three closed-shell species (neutral, dicationic, and tetracationic states) can demonstrate tricolor UV/Vis/NIR electrochromism in both oxidation and reduction processes, for which apparent 2e-transfer is accompanied by a change in color. Compared to the previously reported tricolor electrochromic systems in which the intermediary state is an open-shell species that undergoes disproportionation, all of the neutral, dicationic, and tetracationic states in the present systems exhibit thermodynamic stability, as demonstrated by isolation and X-ray analysis of each state including the intermediary dicationic state. Drastic geometrical changes among the redox states are another characteristic that facilitates the apparent 2e-transfer (Scheme 3-8). In the oxidation process, as-generated **2af**$^{+\bullet}$ and **2af**$^{3+\bullet}$ are more easily oxidized than **2af** and **2af**$^{2+}$ due to the rapid structural change. In the reduction process, cation radical species **2af**$^{3+\bullet}$ and **2af**$^{+\bullet}$ can be generated upon the reduction of **2af**$^{4+}$ and **2af**$^{2+}$, however, they rapidly disproportionate into **2af**$^{4+}$/**2af**$^{2+2\bullet}$ and **2af**$^{2+}$/**2af**$^{2\bullet}$, respectively, under ambient conditions. The structural change of the resulting diradical species is very fast, and thus a steady-state concentration of intermediary open-shell species is negligibly small in both oxidation and reduction processes. Geometrical changes would be also associated with high electrochemical bistability, as suggested by CV measurements, between the neutral and dicationic states as well as between the dicationic and tetracationic states.

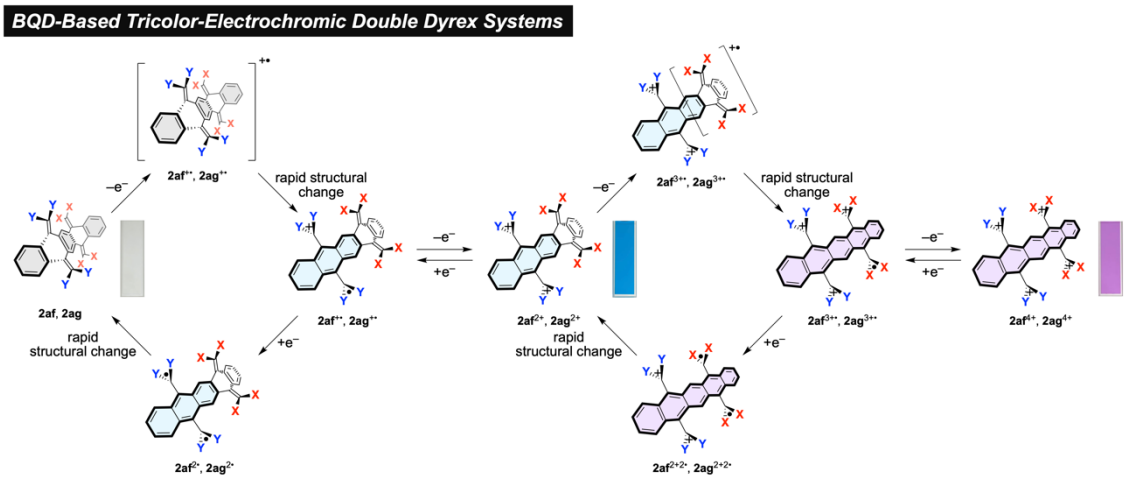

Scheme 3-8. Dynamic redox interconversion among three redox states of hybrid BQDs.

3-3. Conclusion

In conclusion, the author designed and synthesized symmetrically substituted BQD derivatives **2** with a zigzag structure, which undergo one-stage 4e-oxidation to produce tetracationic pentacene derivatives $\mathbf{2}^{4+}$ with a doubly twisted conformation. When tetracationic [5]acenes $\mathbf{2}^{4+}$ were reduced, two-stage 2e-reduction occurs via dicationic [3]acenes $\mathbf{2}^{2+}$ to the original BQDs **2**. Such hysteretic three-state redox interconversion among them demonstrates perfect control of the number of fused benzene rings ([1] → [5] → [3] → [1]) in the [*n*]acene structure by redox conversion. It is noteworthy that cationic species $\mathbf{2b}^{2+}$ and $\mathbf{2b}^{4+}$ can be isolated even for pure hydrocarbons. Furthermore, since the cationic states of **2** exhibit significantly red-shifted NIR absorptions (~1,400 nm) based on intramolecular CT interaction, changes in structure as well as UV/Vis/NIR absorptions can be controlled by redox switching. These results provide a new tactic for creating [*n*]acene-based redox switches with fully controlled multiple-electron transfer, and for dynamically interconverting their structures and properties in a unimolecular fashion.[48]

In addition, the author investigated the redox behavior of hybrid AQDs **1af** and **1ag**, which consist of two types of aryl groups with different electron-donating abilities on each quinodimethane unit. The electrochemical measurements suggested that the geometrical change of twisted form $\mathbf{1}^{2+}$ to folded form **1** upon reduction facilitates the disproportionation of $\mathbf{1}^{+\bullet}$ to $\mathbf{1}^{2\bullet}$ and $\mathbf{1}^{2+}$, which rationalizes the presence of peculiar dicationic species and why the intermediary dications $\mathbf{2}^{2+}$ adopt a charge-localized geometry with both a *p*-QD unit and [3]acene skeleton.[49]

Furthermore, the author designed hybrid BQD derivatives **2af** and **2ag** with dialkylaminophenyl and alkoxyphenyl groups. Thanks to apparent 2e-transfer accompanied by double dramatic changes in the structure of the arylated quinodimethane skeleton, the dicationic and tetracationic states were generated and isolated quantitatively because of the negligible steady-state concentration of intermediary open-shell species such as monocation or trication radicals in both oxidation and reduction processes. When two electrophores with different donating abilities are attached to the BQD skeleton, a dicationic state with a different color can be isolated in addition to the neutral and tetracationic states. For these tetracations, an interchromophore interaction induces a red-shift of the NIR absorptions, thus realizing tricolor UV/Vis/ NIR electrochromic behavior involving only closed-shell states.[50]

3-4. Experimental Section

3-4-1. General

All reactions were carried out under an argon atmosphere. All commercially available compounds were used without further purification. Dry MeCN was obtained by distillation from CaH_2 prior to use. Column chromatography was performed on silica gel 60N (KANTO KAGAKU, spherical neutral) of particle size 40-50 μm or Wakogel® 60N (neutral) of particle size 38-100 μm. ^1H and ^{13}C NMR spectra were recorded on a BRUKER Ascend™ 400 (^1H/400 MHz and ^{13}C/100MHz) spectrometer at 296 K unless otherwise indicated. IR spectra were measured on a Shimadzu IRAffinity-1S spectrophotometer using the attenuated total reflection (ATR) mode. Mass spectra were recorded on a JMS-T100GCV spectrometer in FD mode by Dr. Eri Fukushi and Mr. Yusuke Takata (GS-MS & NMR Laboratory, Research Faculty of Agriculture, Hokkaido University). Melting points were measured on a Yamato MP-21 or a Stanford Research Systems OptiMelt MPA100 and are uncorrected. UV/Vis/NIR spectra were recorded on a JASCO V-770 spectrophotometer. Redox potentials (E^{ox} and E^{red}) were measured on a BAS ALS-612EX by cyclic voltammetry in dry CH_2Cl_2 containing 0.1 M Bu_4NBF_4 as a supporting electrolyte. All of the values shown in the text are in E/V vs. SCE measured at the scan rate of 100 mVs^{-1}. Pt electrodes were used as the working (disk) and counter electrodes. The working electrode was polished using a water suspension of aluminum oxide (0.05 μm) before use. DFT calculations were performed with the Gaussian 16W program package.[51] The geometries of the compounds were optimized by using the CAM-B3LYP method in combination with the 6-31G* basis set unless otherwise indicated.

3-4-2. Synthetic procedures

7,12-Bis(dibromomethylene)-7,12-dihydropentacene-5,14-dione 4 and 5,7,12,14-Tetra(dibromomethylene)-5,7,12,14-tetrahydropentacene 7

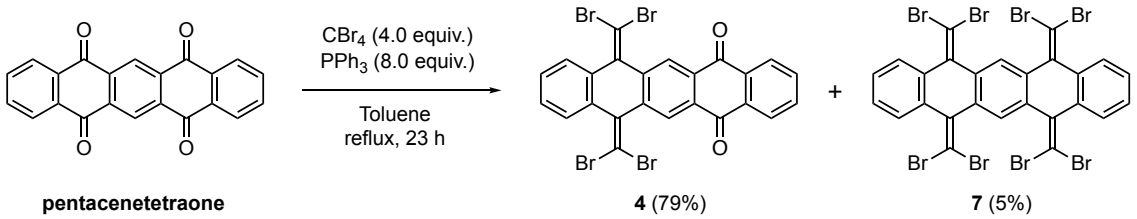

pentacenetetraone **4** (79%) **7** (5%)

A mixture of CBr_4 (6.63 g, 20.0 mmol) and PPh_3 (10.5 g, 40.0 mmol) in dry toluene (200 mL) was stirred at 25 °C for 1.5 h. To the suspension was added pentacene-5,7,12,14-tetraone (1.69 g, 5.00 mmol), and the mixture was heated at reflux for 23 h. After cooling to 25 °C, the reaction mixture was diluted with water. Then, the solvent was concentrated under reduced pressure and the resulting residue was extracted with CH_2Cl_2 five times. The combined organic layers were washed with water and brine, and dried over anhydrous $MgSO_4$. After filtration, the solvent was concentrated under reduced pressure. The crude product was purified by column chromatography on silica gel (hexane/CH_2Cl_2 = 1) to give **4** (2.57 g) and **7** (217 mg) as a yellow solid in 79 % and a white solid in 5 % yield, respectively.

4; Mp: 289-293 °C (decomp.) ^{1}H NMR ($CDCl_3$): δ/ppm 8.80 (2H, s), 8.32 (2H, dd, *J* = 3.3, 5.8 Hz), 7.89 (2H, dd, *J* = 3.3, 5.8 Hz), 7.82 (2H, dd, *J* = 3.3, 5.8 Hz), 7.35 (2H, dd, *J* = 3.3, 5.8 Hz); ^{13}C NMR ($CDCl_3$): δ/ppm 182.33, 141.19, 138.42, 134.97, 134.32, 133.52, 131.55, 127.84, 127.66, 127.35, 126.83, 93.23; IR (ATR): ν/cm^{-1} 3095, 3080, 3061, 3033, 2930, 1675, 1584, 1562, 1458, 1450, 1331, 1309, 1287, 1258, 1159, 953, 940, 921, 795, 771, 764, 735, 712, 691, 684, 638, 514; LR-MS (FD) m/z (%):654.62 (6), 653.62 (20), 652.62 (20), 651.62 (69), 650.62 (29), 649.62 (bp), 648.63 (19), 647.62 (68), 646.63 (5), 645.62 (M^+, 17); HR-MS (FD) Calcd. for $C_{24}H_{10}Br_4O_2$: 645.74143; Found: 645.74200.

7; Mp: > 300 °C; ^{1}H NMR ($CDCl_3$): δ/ppm 7.84 (4H, dd, *J* = 3.3, 5.8 Hz), 7.45 (2H, s), 7.35 (4H, dd, *J* = 3.3, 5.8 Hz); ^{13}C NMR ($CDCl_3$): δ/ppm 138.94, 135.51, 134.73, 127.54, 127.19, 126.33, 91.11; IR (ATR): ν/cm^{-1} 3084, 3064, 2946, 2922, 1584, 1559, 1452, 1289, 1279, 1260, 1197, 1160, 1098, 1043, 978, 938, 902, 821, 776, 756, 746, 730, 704, 668, 650, 632, 611, 585, 503, 460, 442, 426, 419, 416; LR-MS (FD) m/z (%):967.49 (14), 966.49 (13), 965.49 (41), 964.50 (23), 963.49 (77), 962.50 (30), 961.50 (bp), 960.50 (24), 959.50 (81), 958.50 (12), 957.50 (41), 955.50 (11), 953.51 (M^+, 1); HR-MS (FD) Calcd. for $C_{26}H_{10}Br_8$: 953.42495; Found: 953.42389.

7,12-Bis[bis(4-methoxyphenyl)methylene]-7,12-dihydropentacene-5,14-dione 5a

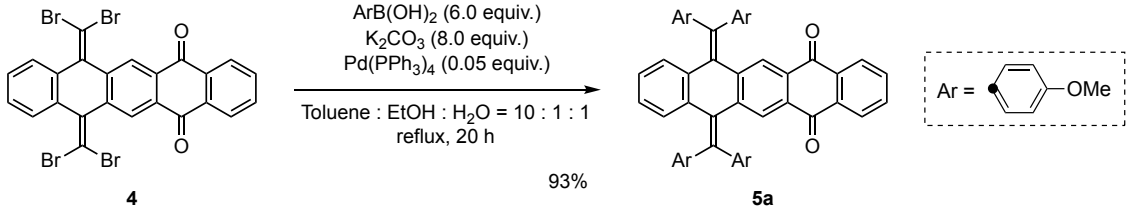

A mixture of **4** (381 mg, 0.586 mmol), 4-methoxyphenylboronic acid (535 mg, 3.52 mmol), K_2CO_3 (649 mg, 4.69 mmol), and $Pd(PPh_3)_4$ (35.2 mg, 30.5 μmol) in toluene (6.0 mL), EtOH (0.60 mL), and H_2O (0.60 mL) was heated at reflux for 20 h. After cooling to 25 °C, the mixture was diluted with water and extracted with CH_2Cl_2 five times. The combined organic layers were washed with water and brine, and dried over anhydrous Na_2SO_4. After filtration, the solvent was concentrated under reduced pressure. The crude product was washed with a mixed solvent (hexane/EtOAc = 1) five times, and dried in vacuo to give **5a** (414 mg) as a yellow solid in 93 % yield.

5a; Mp: > 300 °C; ^{1}H NMR ($CDCl_3$): δ/ppm 8.15 (2H, dd, *J* = 3.3, 5.8 Hz), 8.00 (2H, s), 7.69 (2H, dd, *J* = 3.3, 5.8 Hz), 7.31 (4H, d, *J* = 8.8 Hz), 7.28 (4H, d, *J* = 8.8 Hz), 7.07 (2H, dd, *J* = 3.3, 5.8 Hz), 6.85 (4H, d, *J* = 8.8 Hz), 6.84 (4H, d, *J* = 8.8 Hz), 6.81 (2H, dd, *J* = 3.3, 5.8 Hz), 3.80 (6H, s), 3.76 (6H, s); ^{13}C NMR ($CDCl_3$): δ/ppm 182.60, 158.73, 158.58, 144.45, 141.85, 137.18, 134.40, 134.26, 134.23, 133.77, 133.64, 130.76, 130.73, 130.14, 127.95, 127.06, 126.98, 125.73, 113.97, 113.75, 55.26, 55.25; IR (ATR): ν/cm^{-1} 3031, 2999, 2930, 2835, 1676, 1654, 1602, 1586, 1559, 1506, 1457, 1441, 1331, 1312, 1285, 1241, 1171, 1108, 1068, 1030, 991, 954, 927, 920, 849, 827, 813, 805, 773, 761, 733, 711, 702, 690, 656, 632, 599, 588, 559, 531, 509, 452; LR-MS (FD) m/z (%): 761.27 (5), 760.26 (19), 759.26 (58), 758.25 (M^+, bp), 380.12 (7), 379.62 (19), 379.12 (M^{2+}, 33); HR-MS (FD) Calcd. for $C_{52}H_{38}O_6$: 758.26684; Found: 758.26605.

5,14-Bis(dibromomethylene)-7,12-bis[bis(4-methoxyphenyl)methylene]-5,7,12,14-tetrahydropentacene 6a

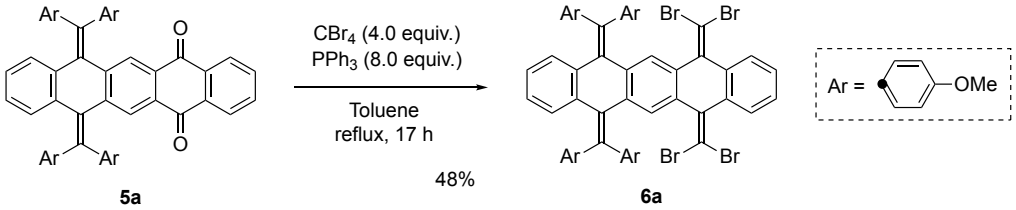

A mixture of CBr_4 (2.06 g, 6.21 mmol) and PPh_3 (3.26 g, 12.4 mmol) in dry toluene (31 mL) was stirred at 25 °C for 1.5 h. To the suspension was added **5a** (1.18 g, 1.55 mmol), and the mixture was heated at reflux for 17 h. After cooling to 25 °C, the reaction mixture was diluted with water. Then, the solvent was concentrated under reduced pressure and the resulting residue was extracted with CH_2Cl_2 five times. The combined organic layers were washed with water and brine, and dried over anhydrous Na_2SO_4. After filtration, the solvent was concentrated under reduced pressure. The crude product was purified by column chromatography on silica gel (CH_2Cl_2/hexane =3) to give **6a** (800 mg) as a white solid in 48 % yield.

6a; Mp: 183-204 °C (decomp.); ^{1}H NMR ($CDCl_3$): δ/ppm 7.67 (2H, s), 7.62 (2H, dd, *J* = 3.3, 5.8 Hz), 7.41 (4H, d, *J* = 8.8 Hz), 7.23 (4H, d, *J* = 8.8 Hz), 7.13 (2H, dd, *J* = 3.3, 5.8 Hz), 6.92 (2H, dd, *J* = 3.3, 5.8 Hz), 6.87 (4H, d, *J* = 8.8 Hz), 6.81 (4H, d, *J* = 8.8 Hz), 6.66 (2H, dd, *J* = 3.3, 5.8 Hz), 3.79 (6H, s), 3.78 (6H, s); ^{13}C NMR ($CDCl_3$): δ/ppm 158.31, 158.23, 140.01, 139.42, 137.72, 137.61, 135.84, 135.34, 135.14, 135.05, 132.90, 131.18, 130.62, 128.32, 127.62, 127.36, 126.76, 125.18, 114.43, 113.73, 90.17, 55.40, 55.20; IR (ATR): ν/cm^{-1} 3031, 2953, 2928, 2834, 1607, 1507, 1458, 1438, 1285, 1245, 1173, 1106, 1032, 957, 946, 861, 847, 823, 811, 780, 765, 756, 740, 668, 659, 645, 615, 589, 578, 558, 505; LR-MS (FD) m/z (%): 1075.94 (5), 1074.94 (14), 1073.93 (28), 1072.94 (39), 1071.93 (75), 1070.94 (56), 1069.93 (bp), 1068.94 (37), 1067.94 (64), 1066.94 (10), 1065.94 (M^+, 16), 536.46 (8), 535.96 (13), 535.46 (10), 534.96 (16), 534.46 (7), 533.96 (11), 533.46 (2), 532.96 (M^{2+}, 2); HR-MS (FD) Calcd. for $C_{54}H_{38}Br_4O_4$: 1065.95036; Found: 1065.95146

5,7,12,14-Tetrakis[bis(4-methoxyphenyl)methylene]-5,7,12,14-tetrahydropentacene 2a

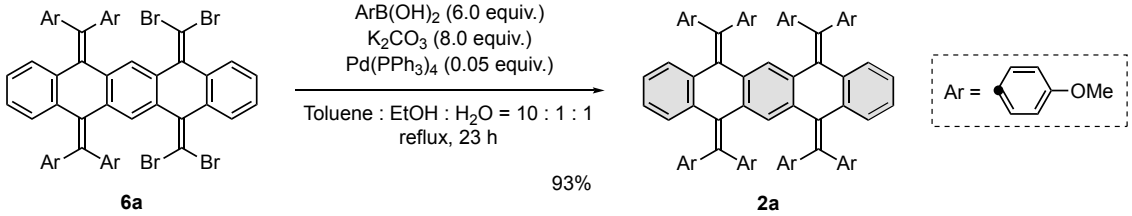

6a **2a**

A mixture of **6a** (325 mg, 303 μmol) , 4-methoxyphenylboronic acid (276 mg, 1.82 mmol), K_2CO_3 (332 mg, 2.40 mmol), and $Pd(PPh_3)_4$ (17.5 mg, 15.1 μmol) in toluene (6.0 mL), EtOH (0.60 mL), and H_2O (0.60 mL) was heated at reflux for 23 h. After cooling to 25 °C, the mixture was diluted with water and extracted with EtOAc five times. The combined organic layers were washed with water and brine, and dried over anhydrous Na_2SO_4. After filtration, the solvent was concentrated under reduced pressure. The crude product was washed with hexane/CH_2Cl_2 = 1.5 five times, and dried *in vacuo* to give **2a** (333 mg) as a white solid in 93 % yield.

2a; Mp: 271-290 °C (decomp.); ^{1}H NMR ($CDCl_3$): δ/ppm 7.11 (8H, d, J = 8.8 Hz), 7.02 (8H, d, J = 8.7 Hz), 6.84 (4H, dd, J = 3.3, 5.8 Hz), 6.76 (8H, d, J = 8.7 Hz), 6.76 (8H, d, J = 8.8 Hz), 6.68 (4H, dd, J = 3.3, 5.8 Hz), 6.55 (2H, s), 3.76 (12H, s), 3.76 (12H, s); ^{13}C NMR ($CDCl_3$): δ/ppm 158.23, 158.12, 138.34, 138.04, 135.51, 135.32, 134.64, 134.46, 130.96, 130.76, 127.98, 127.68, 124.63, 113.55, 113.49, 55.30, 55.20; IR (ATR): ν/cm^{-1} 3030, 2998, 2958, 2931, 2906, 2834, 1603, 1572, 1505, 1462, 1456, 1439, 1284, 1239, 1171, 1108, 1029, 901, 847, 823, 811, 771, 757, 725, 651, 634, 615, 591, 559, 520; LR-MS (FD) m/z (%): 1182.46 (6), 1181.45 (15), 1180.45 (44), 1179.45 (92), 1178.44 (M^+, bp), 590.21 (5), 589.71 (10), 589.21 (M^{2+}, 11); HR-MS (FD) Calcd. for $C_{82}H_{66}O_8$: 1178.47577; Found: 1178.47418; UV/Vis (CH_2Cl_2): λ_{max}/nm (ε/L mol^{-1} cm^{-1}) 328 (40100).

Reduction of **2a**$^{4+}$($SbCl_6^-$)$_4$ to **2a**:

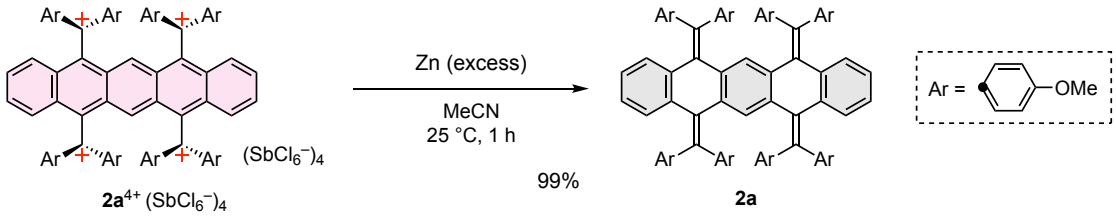

2a^{4+} ($SbCl_6^-$)$_4$ **2a**

To a solution of **2a**$^{4+}$($SbCl_6^-$)$_4$ (39.3 mg, 15.6 μmol) in dry MeCN (1.0 mL) was added activated zinc powder (102 mg, 1.57 mmol) at 25 °C. The mixture was stirred at 25 °C for 1 h, and then diluted with water. The whole mixture was extracted with CH_2Cl_2 five times. The combined organic layers were washed with water and brine, and dried over anhydrous Na_2SO_4. After filtration through silica gel, the solvent was concentrated under reduced pressure to give **2a** (17.9 mg) as a white solid in 99% yield.

Reduction of **2a**$^{2+}$($SbCl_6^-$)$_2$ to **2a**:

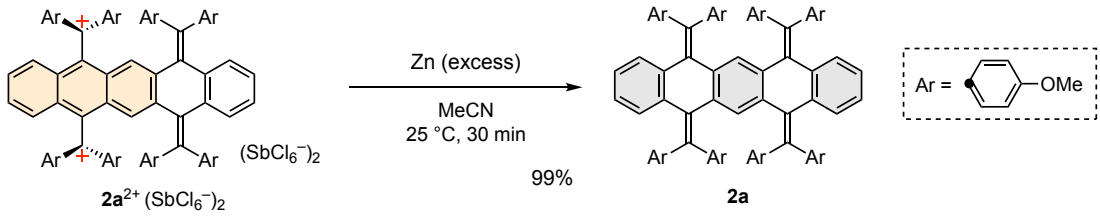

2a^{2+} ($SbCl_6^-$)$_2$ **2a**

To a solution of **2a**$^{2+}$($SbCl_6^-$)$_2$ (18.0 mg, 9.74 μmol) in dry MeCN (2.0 mL) was added activated zinc powder (63.7 mg, 974 μmol) at 25 °C. The mixture was stirred at 25 °C for 30 min, and then diluted with water. The whole mixture was extracted with CH_2Cl_2 five times. The combined organic layers were washed with water and brine, and dried over anhydrous Na_2SO_4. After filtration through silica gel, the solvent was concentrated under reduced pressure to give **2a** (11.4 mg) as a white solid in 99% yield.

Pentacene-5,7,12,14-tetrayl-tetrakis[bis(4-methoxyphenyl)methylium] tetrakis(hexachloroantimonate) 2a^{4+}($SbCl_6^-$)$_4$

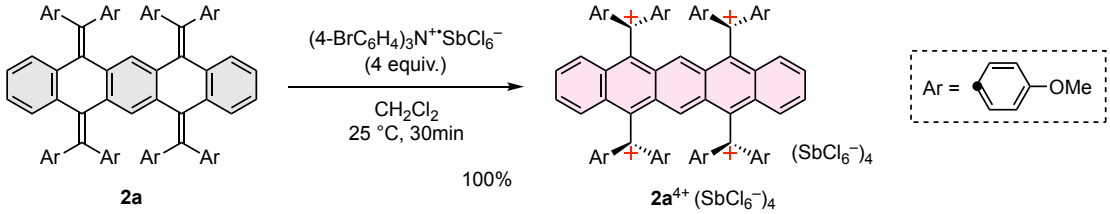

2a **2a**$^{4+}$ ($SbCl_6^-$)$_4$

To a solution of **2a** (184 mg, 156 μmol) in dry CH_2Cl_2 (24 mL) was added tris(4-bromophenyl)aminium hexachloroantimonate (510 mg, 625 μmol) at 25 ℃ to generate a deep red solution, and the mixture was stirred at 25 ℃ for 30 min. The addition of dry ether led to precipitation of the tetracation salt. The precipitates were collected, washed with dry ether three times, and dried *in vacuo* to give **2a**$^{4+}$($SbCl_6^-$)$_4$ (393 mg) as a dark green powder in 100% yield.

2a^{4+}($SbCl_6^-$)$_4$; Mp: 204-206 °C (decomp.); ^{1}H NMR (CD_3CN): δ/ppm 7.72 (16H, brs), 7.66 (2H, s), 7.44-7.35 (8H, m), 7.21 (16H, brd, J = 7.6 Hz), 4.15 (24H, s); ^{13}C NMR (CD_3CN): δ/ppm 185.59, 174.80, 144.86, 138.39, 134.67, 132.99, 130.33, 129.69, 127.24, 126.88, 119.05, 58.85; IR (ATR, KBr pellet): ν/cm^{-1} 3096, 2938, 2847, 1607, 1576, 1540, 1507, 1448, 1374, 1280, 1181, 1155, 1133, 996, 911, 847, 802, 758, 702, 622, 608, 528; LR-MS (FD) m/z (%): 1182.45 (7), 1181.45 (16), 1180.44 (45), 1179.44 (85), 1178.43 ([M^{4+}+3e$^-$]$^+$, bp), 590.21 (10), 589.71 (24), 589.21 ([M^{4+}+2e$^-$]$^{2+}$, 19); HR-MS (FD) Calcd. for $C_{82}H_{66}O_8$: 1178.47577; Found: 1178.47642; UV/Vis/NIR (CH_2Cl_2): λ_{max}/nm (ε/L mol^{-1} cm^{-1}) 922 (11600), 517 (198000), 351 (49000), 313 (140300), 276 (104000).

Oxidation of **2a**$^{2+}$(SbCl$_6^-$)$_2$ to **2a**$^{4+}$(SbCl$_6^-$)$_4$:

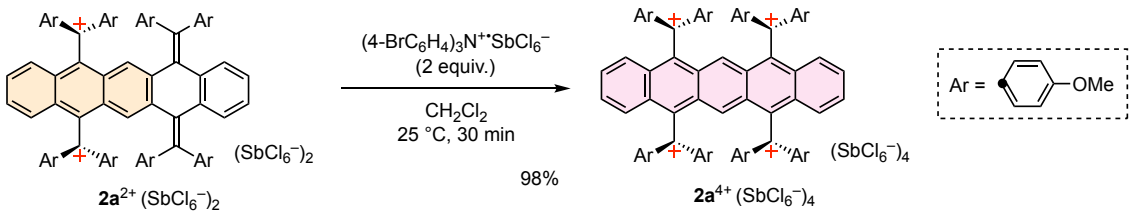

To a solution of **2a**$^{2+}$(SbCl$_6^-$)$_2$ (36.8 mg, 19.9 μmol) in dry CH_2Cl_2 (3.0 mL) was added tris(4-bromophenyl)aminium hexachloroantimonate (32.5 mg, 39.8 μmol) at 25 °C to generate a deep red solution, and the mixture was stirred at 25 °C for 30 min. The addition of dry ether led to precipitation of the tetracation salt. The precipitates were collected, washed with dry ether three times, and dried *in vacuo* to give **2a**$^{4+}$(SbCl$_6^-$)$_4$ (49.3 mg) as a dark green powder in 98% yield.

7,12-Bis[bis(4-methoxyphenyl)methylene]-7,12-dihydropentacene-5,14-diyl-bis[bis(4-methoxyphenyl)methylium] bis(hexachloroantimonate) 2a^{2+}(SbCl$_6^-$)$_2$

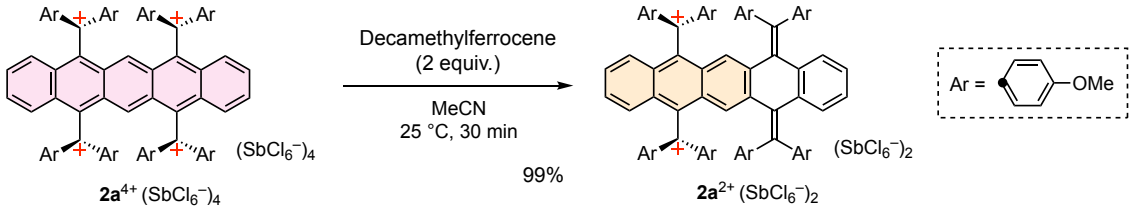

To a solution of **2a**$^{4+}$(SbCl$_6^-$)$_4$ (52.6 mg, 20.9 μmol) in dry MeCN (2 mL) was added decamethylferrocene (13.7 mg, 42.0 μmol) at 25 °C, and the mixture was stirred at 25 °C for 30 min. The addition of dry ether led to precipitation of the dication salt. The precipitates were collected, washed with dry ether three times, and dried *in vacuo* to give **2a**$^{2+}$(SbCl$_6^-$)$_2$ (38.3 mg) as a dark green powder in 99 % yield.

2a^{2+}(SbCl$_6^-$)$_2$; Mp: 174-179 °C (decomp.); ^{1}H NMR (CD_3CN, 336 K): δ/ppm 7.85 (4H, d, J = 8.7 Hz), 7.56 (4H, brs), 7.40-7.25 (12H, m), 7.26 (2H, s), 7.22 (4H, d, J = 8.7 Hz), 7.13 (4H, d, J = 8.7 Hz), 6.95 (2H, dd, J = 3.3, 5.8 Hz), 6.85 (4H, d, J = 8.7 Hz), 6.77 (2H, dd, J = 3.3, 5.8 Hz), 6.64 (4H, d, J = 8.7 Hz), 4.27 (6H, s), 4.20 (6H, s), 3.77 (6H, s), 3.61 (6H, s); ^{13}C NMR (CD_3CN): δ/ppm 190.28, 175.15, 174.65, 159.30, 158.71, 144.50, 142.90, 138.99, 137.81, 137.76, 135.45, 135.16, 134.47, 134.40, 133.68, 131.55, 131.12, 130.57, 129.15, 128.85, 128.80, 126.75, 126.40, 124.98, 119.00, 118.92, 114.39, 114.20, 58.64, 58.54, 55.53, 55.32; IR (ATR, KBr pellet): ν/cm^{-1} 3064, 2951, 2837, 1606, 1575, 1505, 1446, 1373, 1280, 1245, 1180, 1154, 1134, 1028, 998, 908, 881, 844, 810, 755, 602, 592, 530; LR-MS (FD) m/z (%): 1182.46 (7), 1181.43 (21), 1180.43 (50), 1179.43 (93), 1178.42 ([M^{2+}+e$^-$]$^+$, bp), 590.71 (13), 590.20 (26), 589.71 (36), 589.21 (M^{2+}, 36); HR-MS (FD) Calcd. for $C_{82}H_{66}O_8$: 1178.47577; Found: 1178.47608; UV/Vis/NIR (CH_2Cl_2): λ_{max}/nm (ε/L mol^{-1} cm^{-1}) 794 (5400), 532 (136000), 347 (39000), 276 (87900).

7,12-Bis[bis(4-*tert*-butylphenyl)methylene]-7,12-dihydropentacene-5,14-dione 5b

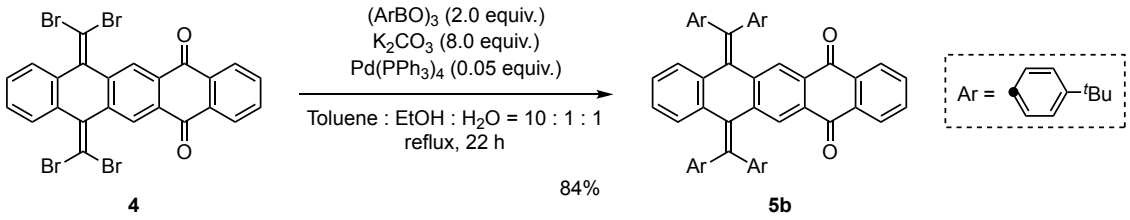

4 **5b**

A mixture of **4** (652 mg, 1.00 mmol), tris(4-*tert*-butylphenyl)boroxin[52] (964 mg, 2.01 mmol), K_2CO_3 (1.11 g, 8.03 mmol), and $Pd(PPh_3)_4$ (58.7 mg, 50.8 μmol) in toluene (10 mL), EtOH (1.0 mL), and H_2O (1.0 mL) was heated at reflux for 22 h. After cooling to 25 °C, the mixture was diluted with water and extracted with CH_2Cl_2 five times. The combined organic layers were washed with water and brine, and dried over anhydrous Na_2SO_4. After filtration, the solvent was concentrated under reduced pressure. The crude product was washed with a mixed solvent (hexane/EtOAc = 1) five times, and dried *in vacuo* to give **5b** (727 mg) as a yellow solid in 84 % yield.

5b; Mp: > 300 °C; ^{1}H NMR ($CDCl_3$): δ/ppm 8.10 (2H, dd, *J* = 3.3, 5.8 Hz), 7.86 (2H, s), 7.65 (2H, dd, *J* = 3.3, 5.8 Hz), 7.40-7.30 (16H, m), 7.04 (2H, dd, *J* = 3.3, 5.8 Hz), 6.77 (2H, dd, *J* = 3.3, 5.8 Hz), 1.32 (18H, s), 1.28 (18H, s); ^{13}C NMR ($CDCl_3$): δ/ppm 182.34, 150.09, 149.81, 144.00, 142.63, 138.89, 138.86, 137.00, 134.07, 133.82, 133.51, 129.89, 129.09, 128.20, 127.14, 126.81, 125.55, 125.41, 125.21, 34.53, 31.37, 31.28; IR (ATR): ν/cm^{-1} 3080, 3025, 2960, 2901, 2865, 1673, 1580, 1507, 1473, 1457, 1405, 1395, 1363, 1330, 1318, 1292, 1267, 1261, 1222, 1203, 1142, 1110, 1068, 1017, 993, 957, 936, 926, 856, 843, 824, 801, 781, 771, 715, 694, 685, 668, 647, 630, 583, 562, 542, 536, 506; LR-MS (FD) m/z (%): 865.48 (6), 864.47 (28), 863.47 (73), 862.46 (M^+, bp), 431.73 (13), 431.22 (M^{2+}, 18); HR-MS (FD) Calcd. for $C_{64}H_{62}O_2$: 862.47498; Found: 862.47564.

5,14-Bis(dibromomethylene)-7,12-bis[bis(4-*tert*-butylphenyl)methylene]-5,7,12,14-tetrahydropentacene 6b

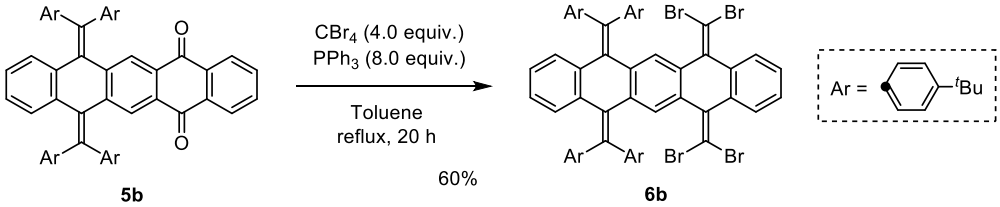

5b **6b**

A mixture of CBr_4 (1.51 g, 4.57 mmol) and PPh_3 (2.40 g, 9.14 mmol) in dry toluene (23 mL) was stirred at 25 °C for 1.5 h. To the suspension was added **5b** (985 mg, 1.14 mmol), and the mixture was heated at reflux for 22 h. After cooling to 25 °C, the reaction mixture was diluted with water. Then, the solvent was concentrated under reduced pressure and the resulting residue was extracted with CH_2Cl_2 five times. The combined organic layers were washed with water and brine, and dried over anhydrous Na_2SO_4. After filtration, the solvent was concentrated under reduced pressure. The crude

product was purified by column chromatography on silica gel (hexane/CH_2Cl_2 = 7) to give **6b** (802 mg) as a white solid in 60 % yield.

6b; Mp: 183-204 °C (decomp.); ^{1}H NMR ($CDCl_3$): δ/ppm 7.69 (2H, s), 7.62 (2H, dd, *J* = 3.3, 5.9 Hz), 7.48 (4H, d, *J* = 8.5 Hz), 7.34 (4H, d, *J* = 8.5 Hz), 7.30 (4H, d, *J* = 8.8 Hz), 7.27 (4H, d, *J* = 8.8 Hz), 7.12 (2H, dd, *J* = 3.3, 5.9 Hz), 6.82 (2H, dd, *J* = 3.3, 5.9 Hz), 6.58 (2H, dd, *J* = 3.3, 5.9 Hz), 1.32 (18H, s), 1.30 (18H, s); ^{13}C NMR ($CDCl_3$): δ/ppm 1149.41, 149.07, 140.58, 139.73, 139.68, 139.18, 137.59, 135.80, 135.00, 132.75, 129.84, 129.07, 128.63, 127.56, 127.43, 126.72, 125.85, 125.15, 124.89, 90.38, 34.47, 31.63, 31.38; IR (ATR): ν/cm^{-1} 3080, 3064, 3026, 2959, 2902, 2865, 1505, 1454, 1394, 1362, 1267, 1202, 1108, 1022, 992, 958, 943, 900, 863, 854, 820, 799, 773, 758, 740, 718, 695, 646, 636, 615, 583, 557, 534, 503, 426; LR-MS (FD) m/z (%): 1080.07 (6), 1079.06 (16), 1178.07 (32), 1077.06 (47), 1075.07 (80), 1175.07 (68), 1174.07 (bp), 1173.07 (47), 1172.07 (63), 1171.07 (12), 1170.07 (M^+, 15), 588.02 (5), 587.52 (5), 587.02 (6), 586.52 (2), 586.02 (4), 585.02 (M^{2+}, 1); HR-MS (FD) Calcd. for $C_{66}H_{62}Br_4$: 1170.15850; Found: 1170.15906.

5,7,12,14-Tetrakis[bis(4-*tert*-butylphenyl)methylene]-5,7,12,14-tetrahydropentacene 2b

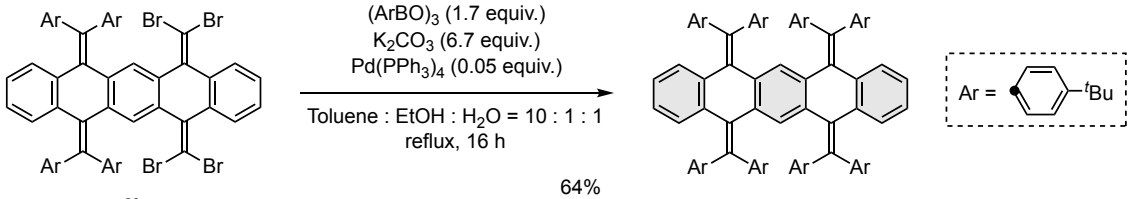

6b **2b**

A mixture of **6b** (802 mg, 682 μmol), tris(4-*tert*-butylphenyl)boroxin (558 mg, 1.16 mmol), K_2CO_3 (631 mg, 4.57 mmol), and $Pd(PPh_3)_4$ (39.4 mg, 34.1 μmol) in toluene (13 mL), EtOH (1.3 mL), and H_2O (1.3 mL) was heated at reflux for 16 h. After cooling to 25 °C, the mixture was diluted with water and extracted with CH_2Cl_2 five times. The combined organic layers were washed with water and brine, and dried over anhydrous Na_2SO_4. After filtration, the solvent was concentrated under reduced pressure. The crude product was washed with hexane/CH_2Cl_2 =1 five times, and dried *in vacuo* to give **2b** (611 mg) as a white solid in 64 % yield.

2b; Mp: > 300 °C; ^{1}H NMR ($CDCl_3$): δ/ppm 7.29 (8H, d, *J* = 8.3 Hz), 7.19 (8H, d, *J* = 8.5 Hz), 7.19 (8H, d, *J* = 8.5 Hz), 7.04 (8H, d, *J* = 8.3 Hz), 6.73 (4H, dd, *J* = 3.3, 5.8 Hz), 6.59 (4H, dd, *J* = 3.3, 5.8 Hz), 6.32 (2H, s), 1.35 (36H, s), 1.26 (36H, s); ^{13}C NMR ($CDCl_3$): δ/ppm 149.13, 148.91, 140.08, 139.79, 138.52, 138.05, 134.50, 133.62, 129.33, 129.22, 128.28, 127.51, 124.87, 124.81, 124.43, 34.52, 34.39, 31.57, 31.36; IR (ATR): ν/cm^{-1} 3081, 3026, 2959, 2901, 2864, 1508, 1460, 1402, 1393, 1362, 1267, 1202, 1145, 1109, 1090, 1022, 942, 913, 854, 843, 816, 796, 785, 760, 752, 728, 719, 695, 643, 637, 583, 562, 542, 504, 463, 456; LR-MS (FD) m/z (%): 1390.91 (8), 1389.91 (28), 1388.91 (61), 1387.90 (bp), 1386.90 (M^+, 86); HR-MS (FD) Calcd. for $C_{106}H_{114}$: 1386.89205; Found: 1386.89042; UV/Vis (CH_2Cl_2): λ_{max}/nm (ε/L mol^{-1} cm^{-1}) 317 (39100).

Reduction of **2b**$^{4+}$(SbCl$_6^-$)$_4$ to **2b**:

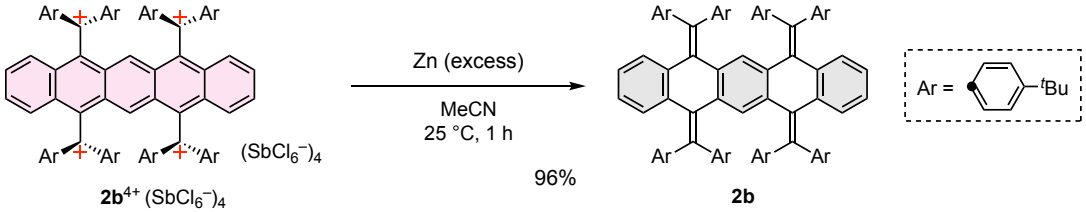

2b^{4+} (SbCl$_6^-$)$_4$ **2b**

To a solution of **2b**$^{4+}$(SbCl$_6^-$)$_4$ (139 mg, 50.9 μmol) in dry MeCN (2.5 mL) was added activated zinc powder (333 mg, 5.09 mmol) at 25 °C. The mixture was stirred at 25 °C for 1 h, and then diluted with water. The whole mixture was extracted with CH_2Cl_2 five times. The combined organic layers were washed with water and brine, and dried over anhydrous Na_2SO_4. After filtration through silica gel, the solvent was concentrated under reduced pressure to give **2b** (68.2 mg) as a white solid in 96% yield.

Reduction of **2b**$^{2+}$(SbCl$_6^-$)$_2$ to **2b**:

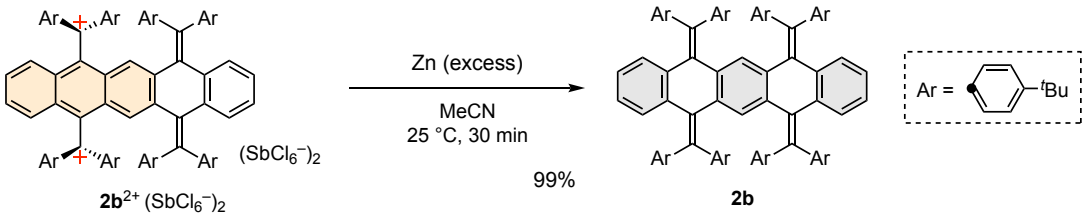

2b^{2+} (SbCl$_6^-$)$_2$ **2b**

To a solution of **2b**$^{2+}$(SbCl$_6^-$)$_2$ (18.9 mg, 9.19 μmol) in dry MeCN (2.0 mL) was added activated zinc powder (61.0 mg, 933 μmol) at 25 °C. The mixture was stirred at 25 °C for 30 min, and then diluted with water. The whole mixture was extracted with CH_2Cl_2 five times. The combined organic layers were washed with water and brine, and dried over anhydrous Na_2SO_4. After filtration through silica gel, the solvent was concentrated under reduced pressure to give **2b** (12.6 mg) as a white solid in 99% yield.

Pentacene-5,7,12,14-tetrayl-tetrakis[bis(4-*tert*-butylphenyl)methylium] tetrakis(hexachloroantimonate) $\mathbf{2b}^{4+}(SbCl_6^-)_4$

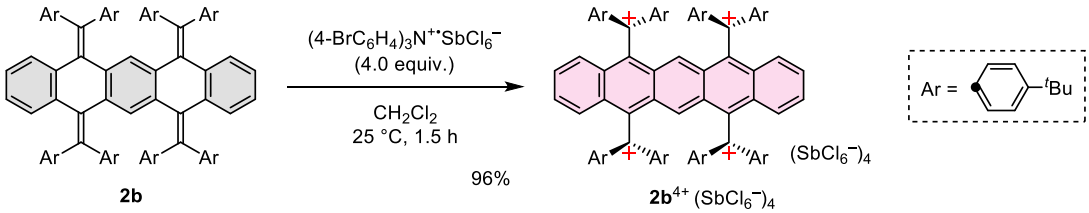

2b **2b**$^{4+}$ $(SbCl_6^-)_4$

To a solution of **2b** (215 mg, 155 μmol) in dry CH_2Cl_2 (20 mL) was added tris(4-bromophenyl)aminium hexachloroantimonate (505 mg, 619 μmol) at 25 °C to generate a deep red solution, and the mixture was stirred at 25 °C for 1.5 h. The addition of dry ether led to precipitation of the tetracation salt. The precipitates were collected, washed with dry ether three times, and dried *in vacuo* to give $\mathbf{2b}^{4+}(SbCl_6^-)_4$ (403 mg) as a reddish brown powder in 96% yield.

$\mathbf{2b}^{4+}(SbCl_6^-)_4$; Mp: 154 °C (decomp.); ^{1}H NMR (CD_3CN containing 5 vol% TFAA): δ/ppm 8.04 (2H, s), 7.95 (16H, brs), 7.78 (16H, brs), 7.33 (4H, dd, J = 3.2, 7.2 Hz), 7.11 (4H, dd, J = 3.2, 7.2 Hz), 1.35 (72H, s); IR (ATR): ν/cm^{-1} 3096, 2968, 2907, 2869, 1597, 1578, 1528, 1487, 1423, 1360, 1264, 1192, 1165, 1103, 1064, 1023, 1003, 976, 913, 850, 823, 769, 754, 727, 708, 686, 626, 608, 543, 522; LR-MS (FD) m/z (%): 1392.79 (6), 1391.87 (5), 1390.89 (16), 1389.88 (35), 1388.87 (63), 1387.87 (bp), 1386.87 ([M^{4+}+3e$^-$]$^+$, 71), 1385.86 (7); HR-MS (FD) Calcd. for $C_{106}H_{114}$: 1386.89205; Found: 1386.89027; UV/Vis/NIR (CH_2Cl_2): λ_{max}/nm (ε/L mol^{-1} cm^{-1}) 1094 (12800), 498 (120000), 348 (53900), 313 (99300), 275 (73700); elemental analysis calcd (%) for $C_{106}H_{114}Cl_{24}Sb_4 \cdot CH_2Cl_2$: C 45.72, H 4.16; found: C 45.87, H 4.05

Oxidation of $\mathbf{2b}^{2+}(SbCl_6^-)_2$ to $\mathbf{2b}^{4+}(SbCl_6^-)_4$:

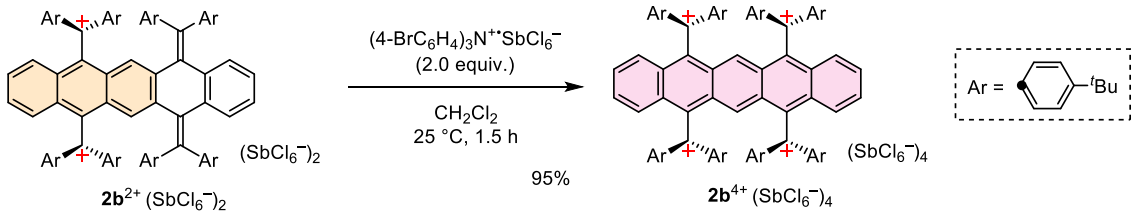

$\mathbf{2b}^{2+}$ $(SbCl_6^-)_2$ $\mathbf{2b}^{4+}$ $(SbCl_6^-)_4$

To a solution of $\mathbf{2b}^{2+}(SbCl_6^-)_2$ (62.7 mg, 30.5 μmol) in dry CH_2Cl_2 (5.0 mL) was added tris(4-bromophenyl)aminium hexachloroantimonate (50.0 mg, 61.2 μmol) at 25 °C to generate a deep red solution, and the mixture was stirred at 25 °C for 1.5 h. The addition of dry ether led to precipitation of the tetracation salt. The precipitates were collected, washed with dry ether three times, and dried *in vacuo* to give $\mathbf{2b}^{4+}(SbCl_6^-)_4$ (78.8 mg) as a reddish brown powder in 95% yield.

7,12-bis[bis(4-*tert*-butylphenyl)methylene]-7,12-dihydropentacene-5,14-diyl-bis[bis(4-*tert*-butylphenyl)methylium] bis(hexachloroantimonate) $\mathbf{2b}^{2+}$ $(SbCl_6^-)_2$

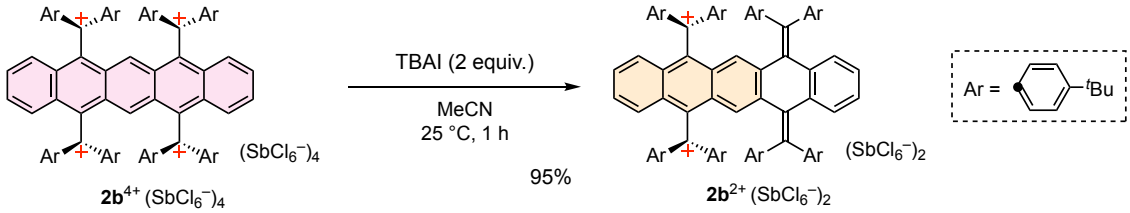

$\mathbf{2b}^{4+}$ $(SbCl_6^-)_4$ $\mathbf{2b}^{2+}$ $(SbCl_6^-)_2$

To a solution of $\mathbf{2b}^{4+}(SbCl_6^-)_4$ (187 mg, 68.6 µmol) in dry MeCN (5.0 mL) was added tetrabutylammonium iodide (TBAI, 51.2 mg, 139 µmol) at 25 °C, and the mixture was stirred at 25 °C for 1 h. The addition of dry ether led to precipitation of the dication salt. The precipitates were washed with dry ether three times and dried *in vacuo* to give $\mathbf{2b}^{2+}(SbCl_6^-)_2$ (134 mg) as a reddish brown powder in 95 % yield.

$\mathbf{2b}^{2+}(SbCl_6^-)_2$; Mp: 165-168 °C (decomp.); ^{1}H NMR (CD_3CN containing 5 vol% TFAA): δ/ppm 8.30-7.58 (16H, brm), 7.37 (4H, d, J = 8.2 Hz), 7.28 (2H, dd, J = 3.0, 6.8 Hz), 7.25 (4H, d, J = 8.2 Hz), 7.18 (4H, d, J = 8.2 Hz), 7.15-7.07 (6H, m), 7.13 (2H, s), 6.82-6.70 (4H, m), 1.58 (18H, s), 1.48 (18H, s), 1.28 (18H, s), 1.02 (18H, s); IR (ATR): ν/cm^{-1} 3072, 2962, 2903, 2867, 1597, 1579, 1488, 1423, 1360, 1260, 1194, 1102, 1020, 1004, 844, 820, 797, 752, 719, 692, 635, 605, 583, 543, 525; LR-MS (FD) m/z (%): 1390.82 (18), 1389.82 (39), 1388.82 (69), 1387.82 (bp), 1386.81 ($[M^{2+}+e^-]^+$, 80), 694.40 (6), 693.91 (5), 693.39 (M^{2+}, 4); HR-MS (FD) Calcd. for $C_{106}H_{114}$: 1386.89205; Found: 1386.89226; elemental analysis calcd (%) for $C_{106}H_{114}Cl_{12}Sb_2 \cdot CH_2Cl_2$: C 60.00, H 5.46; found: C 59.93, H 5.41; UV/Vis/NIR (CH_2Cl_2): λ_{max}/nm (ε/L mol^{-1} cm^{-1}) 1007 (10800), 509 (66200).

11,11,12,12-Tetrakis(4-*tert*-butylphenyl)-9,10-anthraquinodimethane 1b

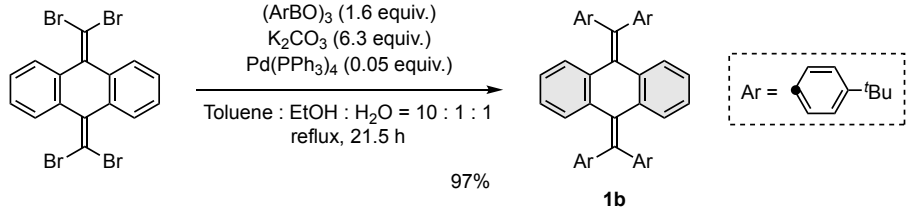

A mixture of 11,11,12,12-tetrabromo-9,10-anthraquinodimethane[53] (335 mg, 683 μmol), tris(4-*tert*-butylphenyl)boroxin (525 mg, 1.09 mmol), K_2CO_3 (594 mg, 4.30 mmol), and $Pd(PPh_3)_4$ (37.5 mg, 32.5 μmol) in toluene (6.5 mL), EtOH (0.65 mL), and H_2O (0.65 mL) was heated at reflux for 22 h. After cooling to 25 °C, the mixture was diluted with water and extracted with EtOAc three times. The combined organic layers were washed with water and brine, and dried over anhydrous Na_2SO_4. After filtration, the solvent was concentrated under reduced pressure. The crude product was washed with hexane/CH_2Cl_2 =1.5 five times, and dried *in vacuo* to give **1b** (459 mg) as a white solid in 97 % yield.

1b; ^{1}H NMR data were identical to those in literature.[55] UV/Vis (CH_2Cl_2): λ_{max}/nm (ε/L mol^{-1} cm^{-1}) 313 (21400), 294 (sh, 20200).

Reduction of **1b**$^{2+}$($SbCl_6^-$)$_2$ to **1b**:

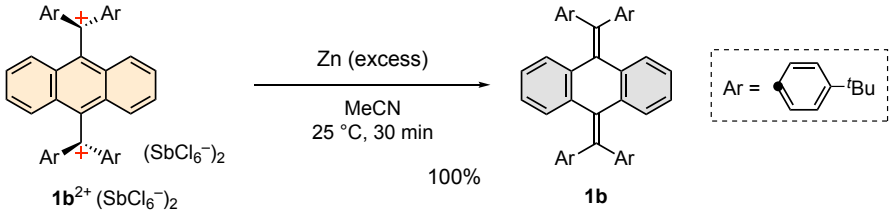

To a solution of **1b**$^{2+}$($SbCl_6^-$)$_2$ (24.0 mg, 17.1 μmol) in dry MeCN (1.7 mL) was added activated zinc powder (112.0 mg, 1.71 mmol) at 25 °C. The mixture was stirred at 25 °C for 30 min, and then diluted with water. The whole mixture was extracted with CH_2Cl_2 five times. The combined organic layers were washed with water and brine, and dried over anhydrous Na_2SO_4. After filtration through silica gel, the solvent was concentrated under reduced pressure to give **1b** (12.5 mg) as a white solid in 100% yield.

Anthracene-9,10-diyl-bis[bis(4-*tert*-butylphenyl)methylium] bis(hexachloroantimonate) $\mathbf{1b}^{2+}(SbCl_6^-)_2$

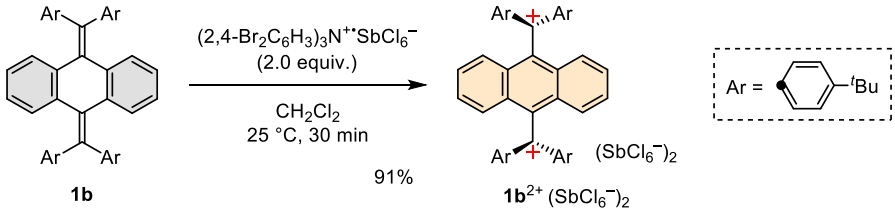

To a solution of **1b** (67.4 mg, 91.9 μmol) in dry CH_2Cl_2 (7.0 mL) was added tris(2,4-dibromophenyl)aminium hexachloroantimonate (194 mg, 184 μmol) at 25 °C to generate a deep orange solution, and the mixture was stirred at 25 °C for 30 min. The addition of dry ether led to precipitation of the dication salt. The precipitates were collected, washed with dry ether three times, and dried *in vacuo* to give $\mathbf{1b}^{2+}(SbCl_6^-)_2$ (117 mg) as an orange powder in 91% yield.

$\mathbf{1b}^{2+}(SbCl_6^-)_2$; Mp: 149-153 °C; ^{1}H NMR (CD_3CN containing 5 vol% TFAA): δ/ppm 7.98 (16H, brs), 7.49 (8H, s), 1.47 (36H, s); IR (ATR): ν/cm^{-1} 3078, 2963, 2937, 2905, 2868, 1601, 1578, 1522, 1487, 1477, 1444, 1423, 1316, 1263, 1195, 1103, 1019, 1000, 981, 928, 882, 845, 831, 824, 772, 727, 681, 635, 617, 596, 539, 522; LR-MS (FD) m/z (%): 735.54 (6), 734.53 (22), 733.53 (67), 732.53 ($[M^{2+}+e^-]^+$, bp), 367.27 (6), 366.76 (16), 366.26 (M^{2+}, 28); HR-MS (FD) Calcd. for $C_{56}H_{60}$: 732.46950; Found: 732.47083; UV/Vis/NIR (CH_2Cl_2): λ_{max}/nm (ε/L mol^{-1} cm^{-1}) 836 (8900), 506 (95600), 406 (15000), 387 (14700), 346 (20500), 258 (81400); elemental analysis calcd (%) for $C_{56}H_{60}Cl_{12}Sb_2 \cdot 0.5CH_2Cl_2$: C 46.72, H 4.16; found: C 46.98, H 4.26

5,7,12,14-Tetrakis[bis(4-dimethylaminophenyl)methylene]-5,7,12,14-tetrahydropentacene (2f)

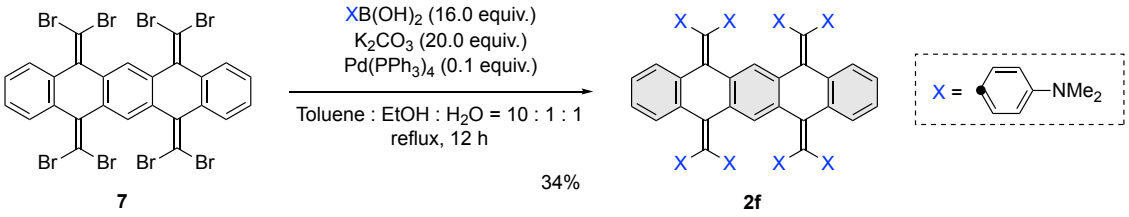

7 **2f**

A mixture of 5,7,12,14-tetrakis(dibromomethylene)-5,7,12,14-tetrahydropentacene **7** (147 mg, 153 µmol), 4-dimethylaminophenylboronic acid (402 mg, 2.44 mmol), K_2CO_3 (421 mg, 3.05 mmol), and $Pd(PPh_3)_4$ (17.6 mg, 15.2 µmol) in toluene (7.6 mL), EtOH (0.76 mL), and H_2O (0.76 mL) was heated at reflux for 12 h. After cooling to 25 °C, the mixture was diluted with water and extracted with CH_2Cl_2 five times. The combined organic layers were washed with water and brine, and dried over anhydrous Na_2SO_4. After filtration, the solvent was concentrated under reduced pressure. The crude product was purified by column chromatography on silica gel (hexane/EtOAc = 2, containing 0.5 vol% Et_3N) to give **2f** (67.7 mg) as a yellow solid in 34 % yield.

2f; Mp: 239-278 °C (decomp.); ^{1}H NMR (400 MHz, $CDCl_3$): δ/ppm 7.06 (8H, d, J = 8.8 Hz), 6.96 (8H, d, J = 8.7 Hz), 6.90 (4H, dd, J = 3.3, 5.8 Hz), 6.69 (2H, s), 6.64 (4H, dd, J = 3.3, 5.8 Hz), 6.58 (8H, d, J = 8.8 Hz), 6.57 (8H, d, J = 8.8 Hz), 2.92 (24H, s), 2.89 (24H, s); ^{13}C NMR (100 MHz, $CDCl_3$): δ/ppm 149.05, 148.76, 139.19, 138.21, 134.62, 133.86, 132.30, 132.07, 130.88, 130.67, 127.97, 127.66, 123.92, 112.44, 112.12, 40.93, 40.66; IR (ATR): ν/cm^{-1} 3086, 3030, 2879, 2851, 2794, 1606, 1514, 1478, 1442, 1344, 1219, 1190, 1163, 1125, 1091, 1058, 945, 905, 830, 809, 797, 784, 753, 729, 714, 646, 636, 579, 555, 518; LR-MS (FD) m/z (%): 1286.67 (6), 1285.67 (19), 1284.66 (53), 1283.66 (bp), 1282.66 (M^+, 93), 643.31 (7), 642.82 (21), 642.32 (49), 641.82 (bp), 641.32 (M^{2+}, 89), 634.81 (5); HR-MS (FD) Calcd. for $C_{90}H_{90}N_8$: 1282.72884; Found: 1282.72815; UV/Vis (CH_2Cl_2): λ_{max}/nm (ε/Lmol^{-1}cm^{-1}) 362 (40700), 267 (97100).

5,7,12,14-Tetrakis[bis(4-morpholinophenyl)methylene]-5,7,12,14-tetrahydropentacene (2g)

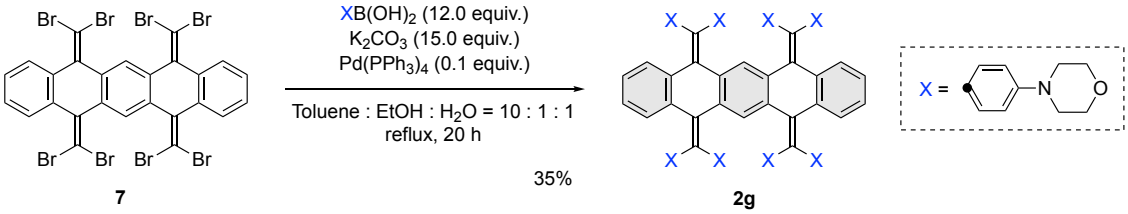

A mixture of 5,7,12,14-tetrakis(dibromomethylene)-5,7,12,14-tetrahydropentacene **7** (208 mg, 217 µmol), 4-dimethylaminophenylboronic acid (539 mg, 2.60 mmol), K_2CO_3 (580 mg, 3.25 mmol), and $Pd(PPh_3)_4$ (25.0 mg, 21.6 µmol) in toluene (10.5 mL), EtOH (1.0 mL), and H_2O (1.0 mL) was heated at reflux for 20 h. After cooling to 25 °C, the mixture was diluted with water and extracted with CH_2Cl_2 five times. The combined organic layers were washed with water and brine, and dried over anhydrous Na_2SO_4. After filtration, the solvent was concentrated under reduced pressure. The crude product was purified by column chromatography on silica gel (EtOAc/acetone = 30) to give **2g** (122 mg) as a yellow solid in 35 % yield.

2g; Mp: 204-234 °C (decomp.); ^{1}H NMR (400 MHz, $CDCl_3$): δ/ppm 7.09 (8H, d, J = 8.8 Hz), 6.98 (8H, d, J = 8.8 Hz), 6.86 (4H, dd, J = 3.4, 5.8 Hz), 6.75 (8H, d, J = 8.8 Hz), 6.74 (8H, d, J = 8.8 Hz), 6.65 (4H, dd, J = 3.4, 5.8 Hz), 6.55 (2H, s), 3.96-3.74 (32H, m), 3.24-3.00 (32H, m); ^{13}C NMR (100 MHz, $CDCl_3$): δ/ppm 149.68, 149.45, 138.50, 138.01, 134.69, 134.42, 134.37, 130.72, 130.56, 128.00, 127.71, 124.40, 115.31, 115.04, 67.02, 66.93, 49.61, 49.20; IR (ATR): ν/cm^{-1} 3057, 3031, 2956, 2910, 2890, 2853, 2819, 1605, 1449, 1378, 1333, 1303, 1282, 1258, 1229, 1193, 1118, 1069, 1050, 1032, 924, 839, 814, 798, 755, 730, 661, 638, 625, 602, 565, 528; LR-MS (FD) m/z (%): 1622.94 (11), 1621.94 (29), 1620.94 (66), 1619.94 (bp), 1618.93 (M^+, 87), 811.98 (5), 811.49 (10), 810.98 (23), 810.48 (52), 809.98 (79), 809.48 (M^{2+}, 67), 808.98 (5); HR-MS (FD) Calcd. for $C_{106}H_{106}N_8O_8$: 1618.81336; Found: 1618.81264; UV/Vis (CH_2Cl_2): λ_{max}/nm (ε/Lmol^{-1}cm^{-1}) 349 (44600), 262 (103600).

7,12-Bis[bis(4-methoxyphenyl)methylene]-5,14-bis[bis(4-dimethylaminophenyl)methylene]-5,7,12,14-tetrahydropentacene (2af)

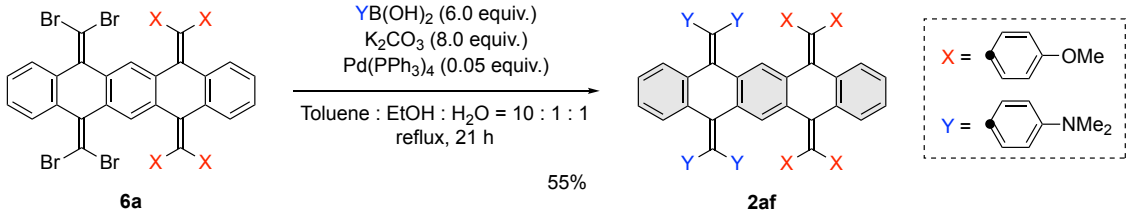

A mixture of 5,14-bis(dibromomethylene)-7,12-bis[bis(4-methoxyphenyl)methylene]-5,7,12,14-tetrahydropentacene **6a** (535 mg, 500 µmol), 4-dimethylaminophenylboronic acid (495 mg, 3.30 mmol), K_2CO_3 (553 mg, 4.00 mmol), and $Pd(PPh_3)_4$ (28.9 mg, 25.0 µmol) in toluene (20 mL), EtOH (2.0 mL), and H_2O (2.0 mL) was heated at reflux for 21 h. After cooling to 25 °C, the mixture was diluted with water and extracted with CH_2Cl_2 three times. The combined organic layers were washed with water and brine, and dried over anhydrous Na_2SO_4. After filtration, the solvent was concentrated under reduced pressure. The crude product was purified by column chromatography on silica gel (hexane/EtOAc = 2) to give **2af** (338 mg) as a greenish yellow solid in 55 % yield.

2af; Mp: 302.3-317.7 °C (decomp.); ^{1}H NMR (400 MHz, $CDCl_3$): δ/ppm 7.10 (4H, d, J = 8.8 Hz), 7.07 (4H, d, J = 8.8 Hz), 7.04 (4H, d, J = 8.8 Hz), 6.94 (4H, d, J = 8.8 Hz), 6.79 (2H, dd, J = 3.3, 5.8 Hz), 6.76 (4H, d, J = 8.8 Hz), 6.75 (4H, d, J = 8.8 Hz), 6.75 (2H, dd, J = 3.3, 5.8 Hz), 6.67 (2H, dd, J = 3.3, 5.8 Hz), 6.64 (2H, dd, J = 3.3, 5.8 Hz), 6.62 (2H, s), 6.58 (8H, d, J = 8.8 Hz), 3.76 (6H,s), 3.75 (6H, s), 2.93 (12H, s), 2.90 (12H, s); ^{13}C NMR (100 MHz, $CDCl_3$): δ/ppm 158.09, 157.96, 149.11, 148.86, 138.91, 138.88, 138.63, 137.28, 135.84, 135.35, 135.06, 135.00, 134.01, 133.49, 132.01, 131.87, 130.99, 130.85, 130.82, 130.56, 128.07, 127.87, 127.72, 124.37, 124.16, 113.49, 113.38, 112.40, 112.14, 55.28, 55.18, 40.90, 40.64; IR (ATR): ν/cm^{-1} 3029, 2930, 2833, 2795, 1736, 1604, 1505, 1452, 1441, 1348, 1286, 1242, 1170, 1127, 1105, 1061, 1032, 946, 901, 811, 754, 729, 647, 634, 588, 563, 518, 454, 431; LR-MS (FD) m/z (%): 1233.69 (6), 1232.69 (15), 1231.69 (31), 1230.68 (M^+, 31), 617.35 (8), 616.85 (20), 616.35 (53), 615.85 (99), 615.35 (M^{2+}, bp); HR-MS (FD) Calcd. for $C_{86}H_{78}O_4N_4$: 1230.60230; Found: 1230.60157; UV/Vis (CH_2Cl_2): λ_{max}/nm (ε/Lmol^{-1}cm^{-1}) 347 (38500).

7,12-Bis[bis(4-methoxyphenyl)methylene]-5,14-bis[bis(4-morpholinophenyl)methylene]-5,7,12,14-tetrahydropentacene (2ag)

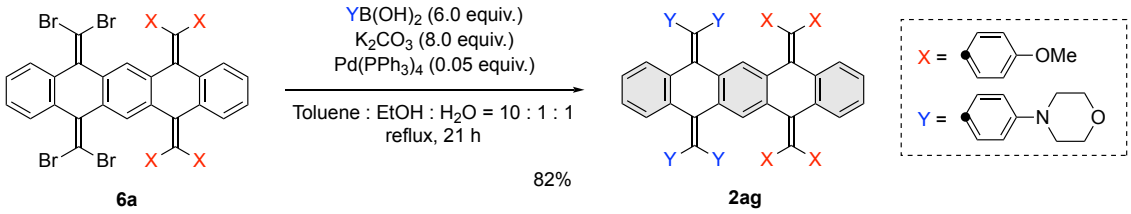

6a **2ag**

A mixture of 5,14-bis(dibromomethylene)-7,12-bis[bis(4-methoxyphenyl)methylene]-5,7,12,14-tetrahydropentacene **6a** (304 mg, 280 µmol), 4-morpholinophenylboronic acid (497 mg, 2.40 mmol), K_2CO_3 (442 mg, 3.20 mmol), and $Pd(PPh_3)_4$ (23.1 mg, 20.0 µmol) in toluene (5 mL), EtOH (0.5 mL), and H_2O (0.5 mL) was heated at reflux for 21 h. After cooling to 25 °C, the mixture was diluted with water and extracted with CH_2Cl_2 three times. The combined organic layers were washed with water and brine, and dried over anhydrous Na_2SO_4. After filtration, the solvent was concentrated under reduced pressure. The crude product was purified by column chromatography on silica gel (hexane/EtOAc = 1/4) to give **2ag** (320 mg) as a yellow solid in 82 % yield.

2ag; Mp: 293.5-297.0°C (decomp.); ^{1}H NMR (400 MHz, $CDCl_3$): δ/ppm 7.11 (4H, d, J = 8.8 Hz), 7.10 (4H, d, J = 8.8 Hz), 7.01 (4H, d, J = 8.8 Hz), 6.99 (4H, d, J = 8.8 Hz), 6.88 (2H, dd, J = 3.3, 5.8 Hz), 6.82 (2H, dd, J = 3.3, 5.8 Hz), 6.75 (8H, d, J = 8.8 Hz), 6.75 (8H, d, J = 8.8 Hz), 6.66 (4H, ddd, J = 3.3, 5.8 Hz), 6.55 (2H, s), 3.87 (8H, t, J = 6.4 Hz), 3.83 (8H, t, J = 4.8 Hz), 3.77 (6H, s), 3.75 (6H, s), 3.14 (8H, t, J = 6.4 Hz), 3.12 (8H, t, J = 4.8 Hz); ^{13}C NMR (100 MHz, $CDCl_3$): δ/ppm 158.18, 158.13, 149.71, 149.44, 138.43, 138.37, 138.25, 137.79, 135.53, 135.28, 134.73, 134.71, 134.67, 134.56, 134.32, 134.29, 130.90, 130.75, 130.74, 130.52, 128.03, 127.92, 127.73, 124.52, 124.47, 115.29, 115.06, 113.52, 113.49, 67.01, 66.93, 55.29, 55.19, 49.58, 49.24; IR (ATR): ν/cm^{-1} 3030, 2951, 2907, 2815, 1603, 1506, 1449, 1377, 1332, 1301, 1283, 1340, 1228, 1173, 1121, 1070, 1032, 922, 902, 816, 801, 775, 755, 726, 628, 621, 591, 564, 525; LR-MS (FD) m/z (%): 1402.69 (7), 1401.68 (19), 1400.68 (46), 1399.68 (80), 1398.68 (M^+, 77), 701.84 (5), 701.35 (11), 700.85 (25), 700.35 (60), 699.85 (bp), 699.34 (M^{2+}, 97), 698.83 (12), 698.33 (11); HR-MS (FD) Calcd. for $C_{94}H_{86}N_4O_8$: 1398.64456; Found: 1398.64380; UV/Vis (CH_2Cl_2): λ_{max}/nm (ε/Lmol^{-1}cm^{-1}) 337 (40200).

7,12-Bis[bis(4-methoxyphenyl)methylene]-7,12-dihydropentacene-5,14-diyl-bis[bis(4-dimethylaminophenyl)methylium] bis(hexachloroantimonate) [2af^{2+}(SbCl$_6^-$)$_2$]

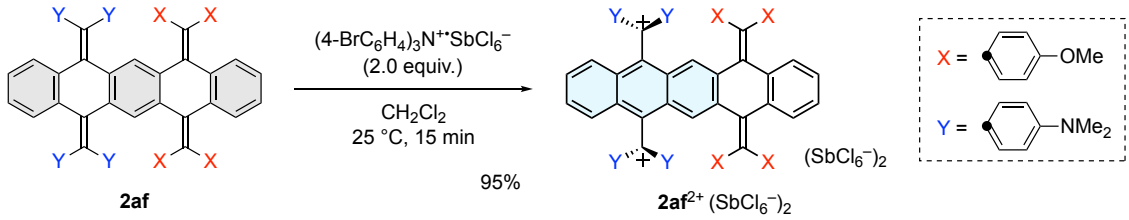

To a solution of **2af** (24.6 mg, 20.0 μmol) in dry CH_2Cl_2 (1.0 mL) was added tris(4-bromophenyl)aminium hexachloroantimonate (32.7 mg, 40.0 μmol) at 25 °C to generate a deep blue solution, and the mixture was stirred at 25 °C for 15 min. The addition of dry ether led to precipitation of the dication salt. The precipitates were washed with dry ether three times, and collected by filtration to give **2af**$^{2+}$(SbCl$_6^-$)$_2$ (35.9 mg) as a dark blue powder in 95% yield.

2af^{2+}(SbCl$_6^-$)$_2$; Mp: 212.1-227.7°C (decomp.); ^{1}H NMR (400 MHz, CD_3CN): δ/ppm 7.50 (2H, s), 7.48 (4H, d, J = 8.8 Hz), 7.42 (2H, dd, J = 3.0, 7.0 Hz), 7.26 (2H, dd, J = 3.0, 7.0 Hz), 7.21 (4H, d, J = 8.8 Hz), 7.15 (4H, d, J = 8.8 Hz), 6.96 (4H, d, J = 8.8 Hz), 6.91 (2H, dd, J = 3.2, 5.8 Hz), 6.89 (4H, d, J = 8.8 Hz), 6.84 (4H, d, J = 8.8 Hz), 6.75 (2H, dd, J = 3.2, 5.8 Hz), 6.64 (8H, d, J = 8.8 Hz), 3.75 (6H, s), 3.59 (6H, s), 3.38 (12H, s), 3.30 (12H, s); ^{13}C NMR (100 MHz, CD_3CN): δ/ppm 170.83, 159.21, 158.85, 157.75, 157.44, 142.16, 139.52, 139.52, 138.21, 137.71, 136.56, 135.74, 135.17, 134.21, 131.19, 131.05, 130.51, 129.02, 128.92, 128.55, 128.50, 127.67, 126.72, 126.27, 125.22, 115.29, 115.18, 114.40, 114.16, 55.52, 55.46, 41.20, 41.12; IR (ATR): ν/cm^{-1} 3064, 2926, 2861, 2810, 1616, 1576, 1506, 1477, 1437, 1352, 1280, 1242, 1157, 1026, 936, 907, 881, 847, 824, 786, 756, 728, 590, 518; LR-MS (FD) m/z (%): 1232.60 (7), 1231.61 (12), 1230.60 ([M^{2+}+e$^-$]$^+$, 13), 616.81 (49), 616.31 (78), 615.81 (bp), 615.31 (M^{2+}, 86); HR-MS (FD) Calcd. for $C_{86}H_{78}N_4O_4$: 1230.60230; Found: 1230.60419; UV/Vis (CH_2Cl_2): λ_{max}/nm (ε/Lmol^{-1}cm^{-1}) 640 (237000), 425 (30300), 417 (28700), 354 (30200), 309 (69200), 265 (85300).

7,12-Bis[bis(4-methoxyphenyl)methylene]-7,12-dihydropentacene-5,14-diyl-bis[bis(4-morpholinophenyl)methylium] bis(hexachloroantimonate) [2ag^{2+}(SbCl$_6^-$)$_2$]

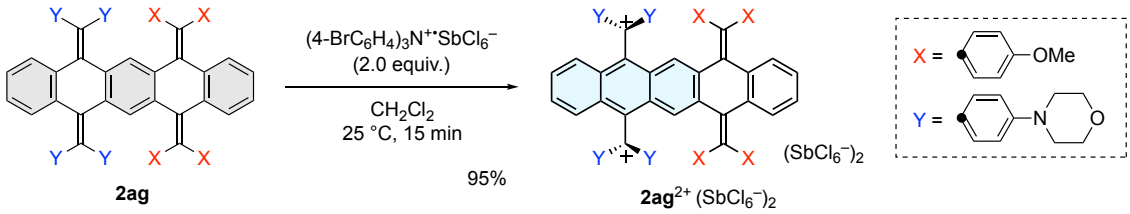

To a solution of **2ag** (112 mg, 80.0 μmol) in dry CH_2Cl_2 (4.0 mL) was added tris(4-bromophenyl)aminium hexachloroantimonate (131 mg, 160 μmol) at 24 °C to generate a deep blue solution, and the mixture was stirred at 24 °C for 15 min. The addition of dry ether led to precipitation of the dication salt. The precipitates were washed with dry ether three times, and collected by filtration to give **2ag**$^{2+}$(SbCl$_6^-$)$_2$ (157 mg) as a dark blue powder in 95% yield.

2ag^{2+}(SbCl$_6^-$)$_2$; Mp: 187.1-190.5 °C (decomp.); ^{1}H NMR (400 MHz, CD_3CN): δ/ppm 7.51 (4H, d, *J* = 9.2 Hz), 7.49 (2H, s), 7.41 (2H, dd, *J* = 3.0, 7.0 Hz), 7.28 (2H, dd, *J* = 3.0, 7.0 Hz), 7.22 (4H, d, *J* = 8.8 Hz), 7.18 (4H, d, *J* = 8.4 Hz), 7.15 (4H, d, *J* = 8.4 Hz), 7.10 (4H, d, *J* = 9.2 Hz), 7.02 (4H, d, *J* = 8.8 Hz), 6.93 (2H, dd, *J* = 3.2, 6.0 Hz), 6.85 (4H, d, *J* = 8.8 Hz), 6.77 (2H, dd, *J* = 3.2, 6.0 Hz), 6.65 (4H, d, *J* = 8.8 Hz), 3.89 (8H, t, *J* = 4.3 Hz), 3.83 (8H, t, *J* = 4.2 Hz), 3.81 (8H, t, *J* = 4.3 Hz), 3.76 (6H, s), 3.74 (8H, t, *J* = 4.2 Hz), 3.60 (6H, s); ^{13}C NMR (100 MHz, CD_3CN): δ/ppm 171.06, 159.23, 158.87, 157.20, 157.10, 142.30, 140.01, 139.97, 139.86, 139.83, 139.16, 137.92, 136.46, 135.64, 135.22, 134.20, 131.18, 131.04, 130.54, 129.03, 128.47, 127.83, 126.69, 126.31, 125.14, 115.84, 115.75, 114.45, 114.19, 66.60, 66.58, 55.71, 55.52, 48.43, 48.34; IR (ATR): ν/cm^{-1} 3061, 2960, 2839, 1611, 1573, 1506, 1374, 1299, 1280, 1237, 1174, 1108, 1027, 924, 907, 820, 758, 715, 596, 505; LR-MS (FD) m/z (%): 1402.63 (8), 1401.62 (21), 1400.62 (49), 1399.62 (94), 1398.61 ([M^{2+}+e$^-$]$^+$, bp), 1397.61 (44), 1396.60 (42), 1395.59 (10), 1394.59 (11), 701.32 (10), 700.81 (20), 700.31 (43), 699.80 (72), 699.30 (M^{2+}, 72), 698.79 (33), 698.30 (33), 697.79(8), 697.29 (9); HR-MS (FD) Calcd. for $C_{94}H_{86}N_4O_8$: 1398.64456; Found: 1398.64233; UV/Vis (CH_2Cl_2): λ_{max}/nm (ε/Lmol^{-1}cm^{-1}) 642 (209000), 428 (35600), 416 (30600), 316 (79300), 266 (102000).

Pentacene-5,7,12,14-tetrayl-tetrakis[bis(4-dimethylaminophenyl)methylium] tetrakis(triiodide) [$2f^{4+}(I_3^-)_4$]

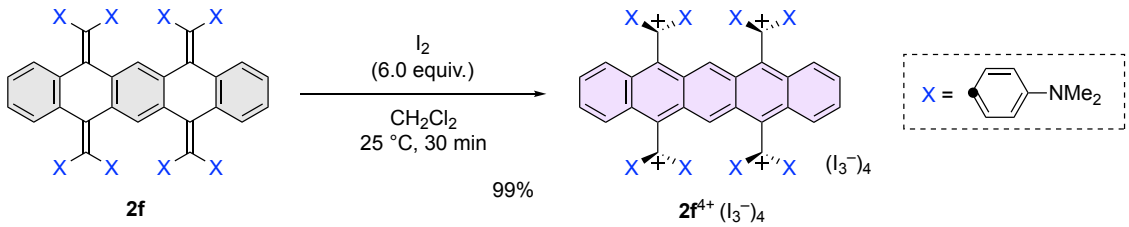

2f **$2f^{4+}(I_3^-)_4$**

To a solution of **2f** (66.7 mg, 51.6 µmol) in dry CH_2Cl_2 (6 mL) was added iodine (80.1 mg, 316 µmol) at 25 °C to generate a deep blue solution, and the mixture was stirred at 25 °C for 30 min. The addition of dry ether led to precipitation of the tetracation salt. The precipitates were washed with dry ether three times, and collected by filtration to give **$2f^{4+}(I_3^-)_4$** (145 mg) as a dark blue powder in 99% yield.

$2f^{4+}(I_3^-)_4$; Mp: 270-288 °C (decomp.); ^{1}H NMR (400 MHz, DMSO-*d*^{6}): δ/ppm 7.87 (2H, s), 7.49 (4H, dd, *J* = 3.2, 7.2 Hz), 7.39-7.29 (20H, m), 6.86 (16H, d, *J* = 9.2 Hz), 3.23 (48H, s); ^{13}C NMR (100 MHz, DMSO-*d*^{6}): δ/ppm 168.26, 156.42, 139.55, 137.05, 131.30, 128.69, 128.47, 128.36, 126.77, 125.89, 114.94, 41.14; IR (ATR): *ν*/cm^{-1} 3077, 2915, 2853, 2806, 1618, 1581, 1476, 1391, 1167, 1059, 963, 937, 908, 827, 785, 759, 728, 701, 675, 518; LR-MS (FD) m/z (%): 1286.72 (7), 1285.71 (18), 1284.72 (35), 1283.72 (40), 1282.71 ([M^{4+}+3e$^-$]$^+$, 40), 642.84 (69), 642.35 (87), 641.85 (bp), 641.35 ([M^{4+}+2e$^-$]$^{2+}$, 75); HR-MS (FD) Calcd. for $C_{90}H_{90}N_8$: 1282.72884; Found: 1282.72669; UV/Vis (MeCN): λ_{max}/nm (ε/Lmol^{-1}cm^{-1}) 567 (101000), 356 (40900), 296 (116000), 247 (43800).

Pentacene-5,7,12,14-tetrayl-tetrakis[bis(4-morpholinophenyl)methylium] tetrakis(triiodide) [$2g^{4+}(I_3^-)_4$]

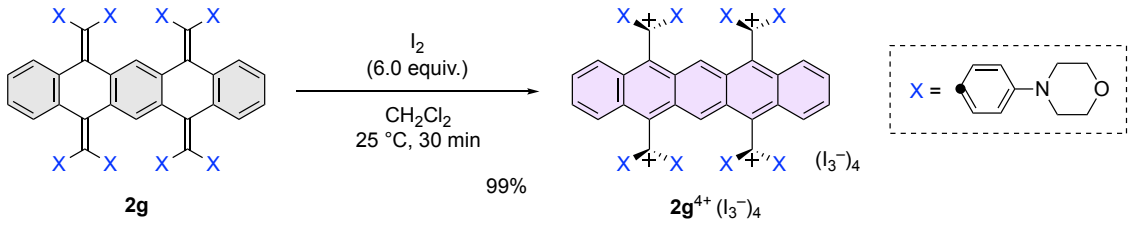

2g **$2g^{4+}$ $(I_3^-)_4$**

To a solution of **2g** (32.4 mg, 20.0 µmol) in dry CH_2Cl_2 (1 mL) was added iodine (30.5 mg, 120 µmol) at 25 °C to generate a deep blue solution, and the mixture was stirred at 25 °C for 30 min. The addition of dry ether led to precipitation of the tetracation salt. The precipitates were washed with dry ether three times, and collected by filtration to give **$2g^{4+}$**$(I_3^-)_4$ (62.5 mg) as a dark blue powder in 99% yield.

$2g^{4+}$ $(I_3^-)_4$; Mp: 264-294 °C (decomp.); ^{1}H NMR (400 MHz, DMSO-d^6): δ/ppm 7.99 (2H, s), 7.53-7.34 (20H, m), 7.31 (4H, dd, J = 2.6, 7.0 Hz), 7.09 (16H, d, J = 9.2 Hz), 3.75 (32H, brs), 3.67 (32H, brs); ^{13}C NMR (100 MHz, DMSO-d^6): δ/ppm 168.67, 156.05, 140.23, 137.36, 132.01, 129.63, 128.89, 128.63, 126.90, 125.69, 115.33, 66.29, 47.78; IR (ATR): ν/cm^{-1} 3073, 2961, 2893, 2851, 1612, 1579, 1377, 1301, 1269, 1238, 1183, 1108, 1030, 925, 909, 825, 781, 717, 695, 642, 624, 594, 507; LR-MS (FD) m/z (%): 1621.91 (7), 1620.92 (14), 1619.90 (21), 1618.90 ([M^{4+}+3e$^-$]$^+$, 17), 811.45 (23), 810.95 (42), 810.46 (68), 809.96 (bp), 809.46 ([M^{4+}+2e$^-$]$^{2+}$, 76), 808.95 (18), 808.45 (13); HR-MS (FD) Calcd. for $C_{106}H_{106}N_8O_8$: 1618.81336; Found: 1618.81441; UV/Vis (CH_2Cl_2): λ_{max}/nm (ε/Lmol^{-1}cm^{-1}) 830 (13600), 600 (194400), 363 (112300), 296 (263700).

Pentacene-5,7,12,14-tetrayl-7,12-bis[bis(4-methoxyphenyl)methylium]-5,14-bis[bis(4-dimethylaminophenyl)methylium] tetrakis(hexachloroantimonate) [$2af^{4+}(SbCl_6^-)_4$]

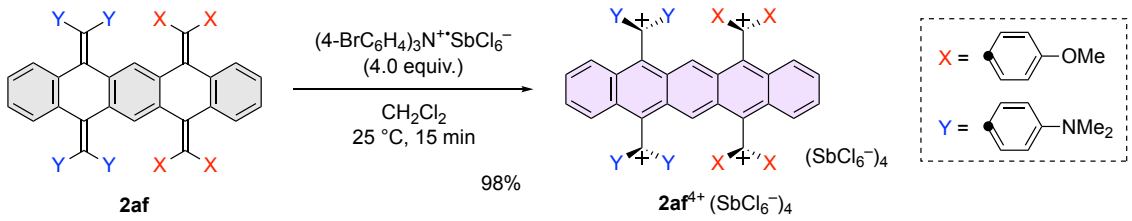

2af **$2af^{4+}$ $(SbCl_6^-)_4$**

To a solution of **2af** (49.2 mg, 39.9 μmol) in dry CH_2Cl_2 (2.0 mL) was added tris(4-bromophenyl)aminium hexachloroantimonate (131 mg, 160 μmol) at 25 °C to generate a deep blue solution, and the mixture was stirred at 25 °C for 15 min. The addition of dry ether led to precipitation of the tetracation salt. The precipitates were washed with dry ether three times, and collected by filtration to give **$2af^{4+}$**$(SbCl_6^-)_4$ (101 mg) as a dark violet powder in 98% yield.

$2af^{4+}$ $(SbCl_6^-)_4$; Mp: 116.0-140.1°C (decomp.); ^{1}H NMR (400 MHz, CD_3CN): δ/ppm 7.84 (2H, s), 7.75 (8H, d, J = 8.8 Hz), 7.54 (2H, dd, J = 3.2, 7.0 Hz), 7.41 (2H, dd, J = 3.0, 7.3 Hz), 7.36 (2H, dd, J = 3.0, 7.3 Hz), 7.33 (2H, dd, J = 3.2, 7.0 Hz), 7.29 (8H, d, J = 8.8 Hz), 7.21 (8H, d, J = 8.8 Hz), 6.80 (8H, d, J = 8.8 Hz), 4.11 (12H, s), 3.28 (24 H, s); ^{13}C NMR (100 MHz, CD_3CN): δ/ppm 189.53, 174.57, 157.27, 146.52, 144.74, 139.68, 138.89, 137.26, 134.97, 132.78, 132.23, 131.06, 129.95, 129.79, 129.27, 129.13, 128.84, 126.92, 126.87, 118.88, 115.17, 58.83, 41.32; IR (ATR): ν/cm^{-1} 3085, 2931, 2858, 1617, 1577, 1478, 1449, 1357, 1277, 1154, 997, 937, 908, 845, 827, 787, 757, 729, 702, 608, 521; LR-MS (FD) m/z (%): 616.79 (6), 616.30 (11), 615.79 (15), 615.30 ($[M^{4+}+2e^-]^{2+}$, 14); HR-MS (FD) Calcd. for $C_{86}H_{78}N_4O_4$: 1230.60230; Found: 1230.60419; UV/Vis (CH_2Cl_2): λ_{max}/nm (ε/Lmol^{-1}cm^{-1}) 1025 (5160), 656 (93700), 532 (171000), 316 (110000), 279 (88700).

Pentacene-5,7,12,14-tetrayl-7,12-bis[bis(4-methoxyphenyl)methylium]-5,14-bis[bis(4-morpholinophenyl)methylium] tetrakis(hexachloroantimonate) [2ag^{4+}(SbCl$_6^-$)$_4$]

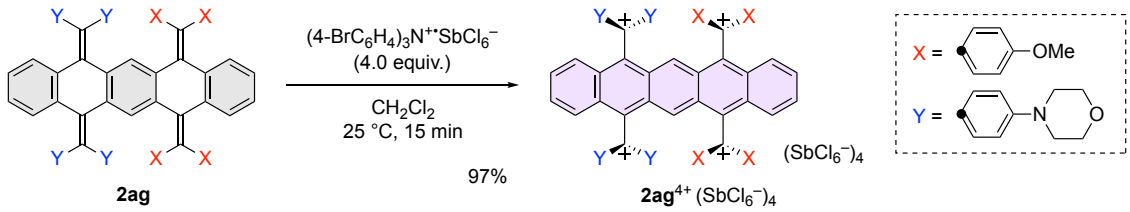

2ag **2ag**$^{4+}$ (SbCl$_6^-$)$_4$

To a solution of **2ag** (42.0 mg, 30.0 μmol) in dry CH_2Cl_2 (2.0 mL) was added tris(4-bromophenyl)aminium hexachloroantimonate (98.0 mg, 120 μmol) at 25 °C to generate a deep blue solution, and the mixture was stirred at 25 °C for 15 min. The addition of dry ether led to precipitation of the tetracation salt. The precipitates were washed with dry ether three times, and collected by filtration to give **2ag**$^{4+}$(SbCl$_6^-$)$_4$ (79.4 mg) as a dark violet powder in 97% yield.

2ag^{4+}(SbCl$_6^-$)$_4$; Mp: 89.5-98.8 °C (decomp.); ^{1}H NMR (400 MHz, CD_3CN): δ/ppm 7.93 (2H, dd, *J* = 2.8, 5.8 Hz), 7.76 (8H, d, *J* = 8.0 Hz), 7.61 (2H, s), 7.52 (2H, dd, *J* = 3.0, 7.0 Hz), 7.38 (2H, dd, *J* = 2.8, 5.8 Hz), 7.35 (2H, dd, *J* = 3.0, 7.0 Hz), 7.32 (8H, d, *J* = 5.2 Hz), 7.24 (8H, d, *J* = 5.2 Hz), 6.96 (8H, d, *J* = 8.0 Hz), 4.13 (12H, s), 3.83 (16H, t, *J* = 3.6 Hz), 3.72 (16H, t, *J* = 3.6 Hz); ^{13}C NMR (100 MHz, CD_3CN): δ/ppm 189.38, 174.58, 169.03, 156.87, 144.71, 140.05, 139.03, 137.04, 135.07, 133.06, 132.09, 130.03, 129.89, 129.74, 129.69, 129.28, 129.17, 126.90, 126.84, 119.03, 115.65, 66.71, 58.91, 48.47; IR (ATR): *ν*/cm^{-1} 3085, 2931, 2858, 1617, 1577, 1478, 1449, 1357, 1277, 1154, 997, 937, 908, 845, 827, 787, 757, 729, 702, 608, 521; LR-MS (FD) m/z (%): 1402.59 (11), 1401.62 (23), 1400.62 (46), 1399.61 (86), 1398.61 ([M^{4+}+3e$^-$]$^+$, bp), 1397.59 (51), 1396.59 (54), 1395.58 (19), 1394.59 (16), 701.74 (7), 701.29 (15), 700.81 (25), 700.30 (49), 699.80 (82), 699.30 ([M^{4+}+2e$^-$]$^{2+}$, 95), 698.80 (57), 698.30 (58), 697.79 (17), 697.29 (20); HR-MS (FD) Calcd. for $C_{94}H_{86}N_4O_8$: 1398.64456; Found: 1398.64201; UV/Vis (CH_2Cl_2): λ_{max}/nm (ε/Lmol^{-1}cm^{-1}) 1000 (5100), 659 (103000), 534 (166000), 315 (114000), 278 (90000).

Oxidation of dication salt **2af**$^{2+}$($SbCl_6^-$)$_2$ to tetracation salt **2af**$^{4+}$($SbCl_6^-$)$_4$:

To a solution of **2af**$^{2+}$($SbCl_6^-$)$_2$ (28.5 mg, 15.0 μmol) in dry CH_2Cl_2 (1.0 mL) was added tris(4-bromophenyl)aminium hexachloroantimonate (24.5 mg, 30.0 μmol) to generate a deep violet solution, and the mixture was stirred at 24 °C for 15 min. The addition of dry ether led to precipitation of the dication salt. The precipitates were washed with dry ether three times, and collected by filtration to give **2af**$^{4+}$($SbCl_6^-$)$_4$ (36.4 mg) as a dark violet powder in 96% yield.

Oxidation of dication salt **2ag**$^{2+}$($SbCl_6^-$)$_2$ to tetracation salt **2ag**$^{4+}$($SbCl_6^-$)$_4$:

To a solution of **2ag**$^{2+}$($SbCl_6^-$)$_2$ (30.8 mg, 14.9 μmol) in dry CH_2Cl_2 (1.0 mL) was added tris(4-bromophenyl)aminium hexachloroantimonate (24.4 mg, 29.9 μmol) to generate a deep violet solution, and the mixture was stirred at 24 °C for 15 min. The addition of dry ether led to precipitation of the dication salt. The precipitates were washed with dry ether three times, and collected by filtration to give **2ag**$^{4+}$($SbCl_6^-$)$_4$ (39.6 mg) as a dark violet powder in 97% yield.

Reduction of tetracation salt **2f**$^{4+}$(I_3^-)$_4$ to **2f**:

To a solution of **2f**$^{4+}$(I_3^-)$_4$ (32.8 mg, 11.7 μmol) in dry MeCN (12 mL) was added activated zinc powder (306 mg, 4.68 mmol). The mixture was stirred at 25 °C for 2 h, and then diluted with water. The whole mixture was extracted with CH_2Cl_2 five times. The combined organic layers were washed with water and brine, and dried over anhydrous Na_2SO_4. After filtration through silica gel, the solvent was concentrated under reduced pressure to give **2f** (14.9 mg) as a yellow solid in 99% yield.

Reduction of tetracation salt **2g**$^{4+}$(I_3^-)$_4$ to **2g**:

To a solution of **2g**$^{4+}$(I_3^-)$_4$ (22.5 mg, 7.16 μmol) in dry MeCN (1.0 mL) was added activated zinc powder (187 mg, 2.86 mmol). The mixture was stirred at 25 °C for 2 h, and then diluted with water. The whole mixture was extracted with CH_2Cl_2 five times. The combined organic layers were washed with water and brine, and dried over anhydrous Na_2SO_4. After filtration through silica gel, the solvent was concentrated under reduced pressure to give **2g** (11.2 mg) as a yellow solid in 97% yield.

Reduction of tetracation salt **2af**$^{4+}$($SbCl_6^-$)$_4$ to **2af**:

To a solution of **2af**$^{4+}$($SbCl_6^-$)$_4$ (24.0 mg, 9.47 μmol) in dry MeCN (1.0 mL) was added activated zinc powder (61.7 mg, 944 μmol). The mixture was stirred at 24 °C for 15 min, and then diluted with water. The whole mixture was extracted with CH_2Cl_2 five times. The combined organic layers were washed with water and brine, and dried over anhydrous Na_2SO_4. After filtration through silica gel, the solvent was concentrated under reduced pressure to give **2af** (11.7 mg) as a yellow solid in 100% yield.

Reduction of tetracation salt **2ag**$^{4+}$($SbCl_6^-$)$_4$ to **2ag**:

To a solution of **2ag**$^{4+}$($SbCl_6^-$)$_4$ (27.4 mg, 10.0 μmol) in dry MeCN (1.0 mL) was added activated zinc powder (65.4 mg, 1.00 mmol). The mixture was stirred at 25 °C for 15 min, and then diluted with water. The whole mixture was extracted with CH_2Cl_2 five times. The combined organic layers were washed with water and brine, and dried over anhydrous Na_2SO_4. After filtration through silica gel, the solvent was concentrated under reduced pressure to give **2ag** (14.0 mg) as a yellow solid in 100% yield.

Reduction of tetracation salt **2af**$^{4+}$($SbCl_6^-$)$_4$ to dication salt **2af**$^{2+}$($SbCl_6^-$)$_2$:

To a solution of **2af**$^{4+}$($SbCl_6^-$)$_4$ (32.2 mg, 12.7 μmol) in dry MeCN (1.0 mL) was added cobaltocene (4.8 mg, 25.4 μmol) to generate a deep blue solution, and the mixture was stirred at 24 °C for 15 min. The addition of dry ether led to precipitation of the dication salt. The precipitates were washed with dry ether ten times, and collected by filtration to give **2af**$^{2+}$($SbCl_6^-$)$_2$ (21.4 mg) as a dark blue powder in 88% yield.

Reduction of tetracation salt **2ag**$^{4+}$($SbCl_6^-$)$_4$ to dication salt **2ag**$^{2+}$($SbCl_6^-$)$_2$:

To a solution of **2ag**$^{4+}$($SbCl_6^-$)$_4$ (36.3 mg, 13.3 μmol) in dry MeCN (1.0 mL) was added cobaltocene (5.0 mg, 26.4 μmol) to generate a deep blue solution, and the mixture was stirred at 25 °C for 15 min. The addition of dry ether led to precipitation of the dication salt. The precipitates were washed with dry ether ten times, and collected by filtration to give **2ag**$^{2+}$($SbCl_6^-$)$_2$ (22.5 mg) as a dark blue powder in 82% yield.

Reduction of dication salt **2af**$^{2+}$($SbCl_6^-$)$_2$ to **2af**:

To a solution of **2af**$^{2+}$($SbCl_6^-$)$_2$ (57.0 mg, 30.0 μmol) in dry MeCN (5.0 mL) was added activated zinc powder (196 mg, 3.00 mmol). The mixture was stirred at 25 °C for 15 min, and then diluted with water. The whole mixture was extracted with CH_2Cl_2 five times. The combined organic layers were washed with water and brine, and dried over anhydrous Na_2SO_4. After filtration through silica gel, the solvent was concentrated under reduced pressure to give **2af** (36.8 mg) as a yellow solid in 100% yield.

Reduction of dication salt **2ag**$^{2+}$($SbCl_6^-$)$_2$ to **2ag**:

To a solution of **2ag**$^{2+}$($SbCl_6^-$)$_2$ (41.4 mg, 20.0 μmol) in dry MeCN (2.0 mL) was added activated zinc powder (130 mg, 2.00 mmol). The mixture was stirred at 26 °C for 15 min, and then diluted with water. The whole mixture was extracted with CH_2Cl_2 five times. The combined organic layers were washed with water and brine, and dried over anhydrous Na_2SO_4. After filtration through silica gel, the solvent was concentrated under reduced pressure to give **2ag** (26.8 mg) as a yellow solid in 96% yield.

3-4-3. Crystal data

Method

A suitable crystal was selected and measured on a Rigaku XtaLAB Synergy (Cu-Kα radiation, λ = 1.54184 Å) with HyPix diffractometer. The crystal was kept at 150 K or 100 K during data collection. Using Olex2,[52] the structure was solved with the SHELXT[53] structure solution program using Intrinsic Phasing and refined with the SHELXL[54] refinement package using Least Squares minimisation. Solvent mask procedure was used for the analyses of **2a**$^{2+}$($SbCl_6^-$)$_2$, **2a**$^{4+}$($SbCl_6^-$)$_4$, **2b**$^{2+}$($SbCl_6^-$)$_2$, **2b**$^{4+}$($SbCl_6^-$)$_4$, **2g**, **2f**$^{4+}$(I_3^-)$_4$, **2g**$^{4+}$(I_3^-)$_4$, **2af**, **2af**$^{2+}$($SbCl_6^-$)$_2$, **2ag**, **2ag**$^{4+}$($SbCl_6^-$)$_4$, and **7**.

Crystal data of **2a**

Crystals were obtained by recrystallization from CH_2Cl_2/hexane. MF: $C_{82}H_{66}O_8 \cdot 4CH_2Cl_2$, FW: 1519.05, colorless plate, 0.60 × 0.30 × 0.05 mm, triclinic $P\bar{1}$, a = 10.93126(17) Å, b = 13.6025(2) Å, c = 15.05682(19) Å, α = 65.6392(13)°, β = 85.0560(11)°, γ = 72.3703(14)°, V = 1941.77(5) Å^3, ρ (Z = 1) = 1.299 g cm^{-1}. A total 21801 reflections were measured at T = 150 K. Numerical absorption correction was applied (μ = 3.097 mm^{-1}). The final *R1* and *wR*2 values are 0.0829 (I > 2σI) and 0.2923 (all data) for 7823 reflections and 410 parameters. Estimated standard deviations are 0.003-0.005 Å for bond lengths and 0.2-0.3° for bond angles. CCDC 2051602

Crystal data of **2a**$^{4+}$($SbCl_6^-$)$_4$

Crystals were obtained by recrystallization from $MeNO_2$/Et_2O. MF: $C_{82}H_{66}O_8Cl_{24}Sb_4$, FW: 2517.14, red needle, 0.20 × 0.02 × 0.02 mm^3, triclinic $P\bar{1}$, a = 11.6462(3) Å, b = 13.6587(3) Å, c = 17.4887(3) Å, α = 105.8247(18)°, β = 100.681(2)°, γ = 91.778(2)°, V = 2620.34(11) Å^3, ρ (Z = 1) = 1.595 g cm^{-1}. A total 29777 reflections were measured at T = 150 K. Numerical absorption correction was applied (μ = 14.105 mm^{-1}). The final *R1* and *wR*2 values are 0.0862 (I > 2σI) and 0.2437 (all data) for 10510 reflections and 577 parameters. Estimated standard deviations are 0.002-0.016 Å for bond lengths and 0.08-1.0° for bond angles. CCDC 2051604

Crystal data of **2a**$^{2+}$($SbCl_6^-$)$_2$

Crystals were obtained by recrystallization from 1,2-dichloroethane/Et_2O. MF: $C_{82}H_{66}O_8Cl_{12}Sb_2$, FW: 1848.24, red plate, 0.15 × 0.10 × 0.03 mm^3, monoclinic $P2_1/m$, a = 13.8452(3) Å, b = 18.8420(3) Å, c = 17.3907(4) Å, β = 111.367(3)°, V = 4224.91(17) Å^3, ρ (Z = 2) = 1.453 g cm^{-1}. A total 23154 reflections were measured at T = 150 K. Numerical absorption correction was applied (μ = 8.981 mm^{-1}). The final *R1* and *wR*2 values are 0.0759 (I > 2σI) and 0.2346 (all data) for 7782 reflections and 482 parameters. Estimated standard deviations are 0.002-0.011 Å for bond lengths and 0.07-0.16° for bond angles. CCDC 2051603

Crystal data of **2b**

Crystals were obtained by recrystallization from CH_2Cl_2/hexane. MF: $C_{106}H_{114}\cdot 4CH_2Cl_2$, FW: 1727.67, colorless block, 0.50 × 0.50 × 0.20 mm, triclinic $P\bar{1}$, a = 13.6799(2) Å, b = 14.0528(4) Å, c = 14.9128(3) Å, α = 63.165(2)°, β = 77.3078(17)°, γ = 81.6011(17)°, V = 2491.98(11) Å^3, ρ (Z = 1) = 1.151 g cm^{-1}. A total 30676 reflections were measured at T = 150 K. Numerical absorption correction was applied (μ = 2.403 mm^{-1}). The final *R1* and *wR*2 values are 0.0607 (I > 2σI) and 0.1766 (all data) for 10071 reflections and 544 parameters. Estimated standard deviations are 0.002-0.005 Å for bond lengths and 0.13-0.3° for bond angles. CCDC 2051605

Crystal data of **2b**$^{4+}$($SbCl_6^-$)$_4$

Crystals were obtained by recrystallization from $MeNO_2$/benzene with TFAA/HFIP MF: $C_{106}H_{114}Cl_{24}Sb_4$, FW: 2725.77, red needle, 0.10 × 0.02 × 0.02 mm^3, monoclinic *I2/m*, a = 20.361(3) Å, b = 19.1322(15) Å, c = 19.793(3) Å, β = 91.165(14)°, V = 7708.8(17) Å^3, ρ (Z = 2) = 1.174 g cm^{-3}. A total 21484 reflections were measured at T = 150 K. Numerical absorption correction was applied (μ = 9.583 mm^{-1}). The final *R1* and *wR*2 values are 0.1385 (I > 2σI) and 0.3922 (all data) for 7061 reflections and 330 parameters. Estimated standard deviations are 0.004-0.04 Å for bond lengths and 0.2-3.0° for bond angles. CCDC 2051607

Crystal data of **2b**$^{2+}$($SbCl_6^-$)$_2$

Crystals were obtained by recrystallization from CH_2Cl_2/hexane with TFAA/HFIP. MF: $C_{106}H_{114}Cl_{12}Sb_2$, FW: 2056.87, red plate, 0.30 × 0.04 × 0.01 mm^3, orthorhombic *Pnma*, a = 21.1362(10) Å, b = 19.0387(13) Å, c = 30.281(3) Å, V = 12185.3(15) Å^3, ρ (Z = 4) = 1.121 g cm^{-3}. A total 40883 reflections were measured at T = 150 K. Numerical absorption correction was applied (μ = 6.220 mm^{-1}). The final *R1* and *wR*2 values are 0.1627 (I > 2σI) and 0.4308 (all data) for 11161 reflections and 564 parameters. Estimated standard deviations are 0.002-0.011 Å for bond lengths and 0.004-0.05° for bond angles. CCDC 2051606

Crystal data of **7**

Crystals were obtained by recrystallization from CH_2Cl_2/hexane. MF: $C_{26}H_{10}Br_8$, FW: 961.62, colorless block, 0.30 × 0.10 × 0.10 mm, tetragonal $I4_1cd$, a = 24.06405(12) Å, b = 24.06405(12) Å, c = 38.4600(3) Å, V = 22271.4(3) Å^3, ρ (Z = 1) = 2.294 g cm^{-1}. A total 29787 reflections were measured at T = 150 K. Numerical absorption correction was applied (μ = 13.900 mm^{-1}). The final *R1* and *wR*2 values are 0.0779 (I > 2σI) and 0.2061 (all data) for 7558 reflections and 613 parameters. Estimated standard deviations are 0.016-0.03 Å for bond lengths and 0.8-1.9° for bond angles.

Crystal data of **2f**·2CH_2Cl_2

Crystals were obtained by recrystallization from CH_2Cl_2/hexane. MF: $C_{90}H_{90}N_8 \cdot C_2H_4Cl_4$, FW: 1453.55, yellow plate, 0.301 × 0.134 × 0.06 mm^3, triclinic $P\bar{1}$, a = 10.9504(2) Å, b = 13.9833(3) Å, c = 15.0254(3) Å, α = 103.5137(19)°, β = 109.948(2)°, γ = 106.4565(19)°, V = 1929.83(8) $Å^3$, ρ (Z = 1) = 1.251 g cm^{-3}. A total 25166 reflections were measured at T = 150 K. Numerical absorption correction was applied (μ = 1.797 mm^{-1}). The final R_1 and wR_2 values are 0.0646 (I > 2σI) and 0.1974 (all data) for 7888 reflections and 477 parameters. Estimated standard deviations are 0.002-0.005 Å for bond lengths and 0.15-0.3° for bond angles. CCDC 2247038.

Crystal data of **2g**·EtOAc

Crystals were obtained by recrystallization from $CHCl_3$/EtOAc. MF: $C_{110}H_{114}N_8O_{10}$, FW: 1708.09, yellow block, 0.209 × 0.087 × 0.049 mm^3, triclinic $P\bar{1}$, a = 15.60686(15) Å, b = 16.21001(13) Å, c = 18.99287(15) Å, α = 79.4079(7), β = 77.1179(7)°, γ = 88.6293(7), V = 4603.48(7) $Å^3$, ρ (Z = 2) = 1.232 g cm^{-3}. A total 87037 reflections were measured at T = 150 K. Numerical absorption correction was applied (μ = 0.625 mm^{-1}). The final R_1 and wR_2 values are 0.0988 (I > 2σI) and 0.2993 (all data) for 18841 reflections and 1117 parameters. Estimated standard deviations are 0.003-0.007 Å for bond lengths and 0.2-0.5° for bond angles. CCDC 2247039.

Crystal data of **2f**$^{4+}$(I_3^-)$_4$ · 2C_6H_6

Crystals were obtained by recrystallization from DMSO/benzene. MF: $C_{102}H_{102}N_8 \cdot I_{12}$, FW: 2962.71, blue plate, 0.30 × 0.05 × 0.02 mm^3, triclinic $P\bar{1}$, a = 12.5558(3) Å, b = 16.3819(5) Å, c = 16.4000(5) Å, α = 113.976(3)°, β = 94.079(2)°, γ = 109.299(2)°, V = 2825.28(16) $Å^3$, ρ (Z = 1) = 1.741 g cm^{-3}. A total 30632 reflections were measured at T = 150 K. Numerical absorption correction was applied (μ = 26.157 mm^{-1}). The final R_1 and wR_2 values are 0.0642 (I > 2σI) and 0.1843 (all data) for 11442 reflections and 558 parameters. Estimated standard deviations are 0.0006-0.02 Å for bond lengths and 0.02-1.2° for bond angles. CCDC 2247040.

Crystal data of **2g**$^{4+}$(I_3^-)$_4$· 2MeOH

Crystals were obtained by recrystallization from DMSO/MeOH. MF: $C_{108}H_{114}N_8O_{10} \cdot I_{12}$, FW: 3206.87, dark blue block, 0.606 × 0.143 × 0.082 mm^3, triclinic $P\bar{1}$, a = 13.89682(14) Å, b = 13.98565(15) Å, c = 16.17905(13) Å, α = 74.0222(8), β = 80.1972(8)°, γ = 88.7049(8), V = 2977.91(5) $Å^3$, ρ (Z = 1) = 1.788 g cm^{-3}. A total 55560 reflections were measured at T = 150 K. Numerical absorption correction was applied (μ = 24.937 mm^{-1}). The final R_1 and wR_2 values are 0.0789 (I > 2σI) and 0.2435 (all data) for 12143 reflections and 740 parameters. Estimated standard deviations are 0.002-0.02 Å for bond lengths and 0.06-3.0° for bond angles. CCDC 2247041.

Crystal data of **2af**·2CH_2Cl_2

Crystals were obtained by recrystallization from CH_2Cl_2/hexane. MF: $C_{88}H_{82}Cl_4N_4O_4$, FW: 1401.37, yellow plate, 0.206 × 0.101 × 0.029 mm^3, monoclinic $P2_1/m$, a = 10.4107(2) Å, b = 25.8244(5) Å, c = 14.2451(3) Å, β = 97.282(2)°, V = 3798.92(13) $Å^3$, ρ (Z = 2) = 1.225 g cm^{-3}. A total of 7758 reflections were measured at T = 150 K. Numerical absorption correction was applied (μ = 1.834 mm^{-1}). The final R_1 and wR_2 values are 0.0783 (I > 2σI) and 0.2488 (all data) for 7758 reflections and 494 parameters. Estimated standard deviations are 0.003-0.015 Å for bond lengths and 0.14-1.7° for bond angles. CCDC 2247042.

Crystal data of **2ag**·0.5EtOAc

Crystals were obtained by recrystallization from EtOAc/hexane. MF: $C_{96}H_{90}N_4O_9$, FW: 1443.71, green plate, 0.477 × 0.06 × 0.039 mm^3, triclinic $P\bar{1}$, a = 20.06409(14) Å, b = 20.23110(14) Å, c = 22.02718(13) Å, β = 90.4577(5)°, V = 7836.40(10) $Å^3$, ρ (Z = 4) = 1.224 g cm^{-3}. A total of 101485 reflections were measured at T = 150 K. Numerical absorption correction was applied (μ = 0.619 mm^{-1}). The final R_1 and wR_2 values are 0.0686 (I > 2σI) and 0.2020 (all data) for 31736 reflections and 2040 parameters. Estimated standard deviations are 0.003-0.02 Å for bond lengths and 0.17-1.5° for bond angles. CCDC 2247043.

Crystal data of **2af**$^{2+}$($SbCl_6^-$)$_2$·MeCN

Crystals were obtained by recrystallization from MeCN/^{t}BuMeEther. MF: $C_{88}H_{81}N_5O_4 \cdot Cl_{12}Sb_2$, FW: 1941.47, dark blue plate, 0.20 × 0.10 × 0.03 mm^3, orthorhombic $Cmc2_1$, a = 17.3527(4) Å, b = 31.0712(6) Å, c = 34.7088(8) Å, β = 90°, V =18713.9(7) $Å^3$, ρ (Z = 8) = 1.378 g cm^{-3}. A total of 33444 reflections were measured at T = 150 K. Numerical absorption correction was applied (μ = 8.119 mm^{-1}). The final R_1 and wR_2 values are 0.0695 (I > 2σI) and 0.2057 (all data) for 13544 reflections and 1146 parameters. Estimated standard deviations are 0.003-0.09 Å for bond lengths and 0.12-4.0° for bond angles. CCDC 2247044.

Crystal data of **2ag**$^{4+}$($SbCl_6^-$)$_4$·4C_6H_6·3.5$ClCH_2CH_2Cl$

Crystals were obtained by recrystallization from CH_2Cl_2/benzene. MF: $C_{125}H_{124}Cl_7N_4O_8 \cdot Cl_{24}Sb_4$, FW: 3396.22, dark violet plate, 0.28 × 0.09 × 0.04 mm^3, monoclinic $C2/m$, a = 24.2324(3) Å, b =20.0172(3) Å, c = 29.1766(4) Å, β = 96.3054(14)°, V = 14066.9(3) $Å^3$, ρ (Z = 4) = 1.604 g cm^{-3}. A total 65061 reflections were measured at T = 100 K. Numerical absorption correction was applied (μ = 11.883 mm^{-1}). The final R_1 and wR_2 values are 0.0470 (I > 2σI) and 0.1319 (all data) for 14625 reflections and 771 parameters. Estimated standard deviations are 0.0009-0.014 Å for bond lengths and 0.06-1.8º for bond angles. CCDC 2247045.

3-4-4. (TD-)DFT calculations at the CAM-B3LYP/6-31G* level

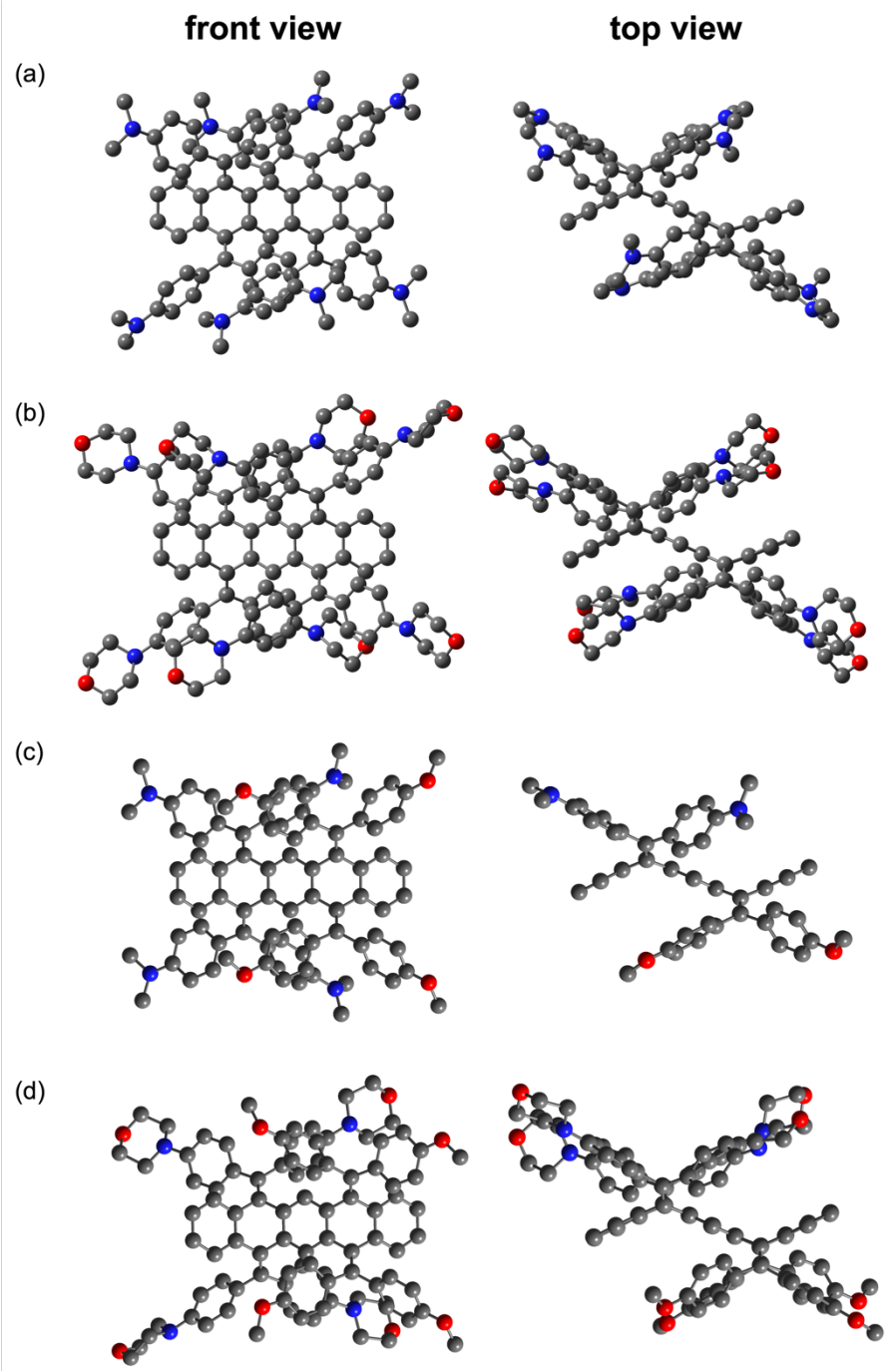

Figure 3-22. Optimized structures of (a) **2f**, (b) **2g**, (c) **2af**, and (d) **2ag** obtained by DFT calculations (CAM-B3LYP/6-31G*). Hydrogen atoms are omitted for clarity. [**2f**: X = Y = 4-$Me_2NC_6H_4$; **2g**: X = Y = 4-$O(C_2H_4)_2NC_6H_4$; **2af**: X = 4-$MeOC_6H_4$, Y = 4-$Me_2NC_6H_4$; **2ag**: X = 4-$MeOC_6H_4$, Y = 4-$O(C_2H_4)_2NC_6H_4$]

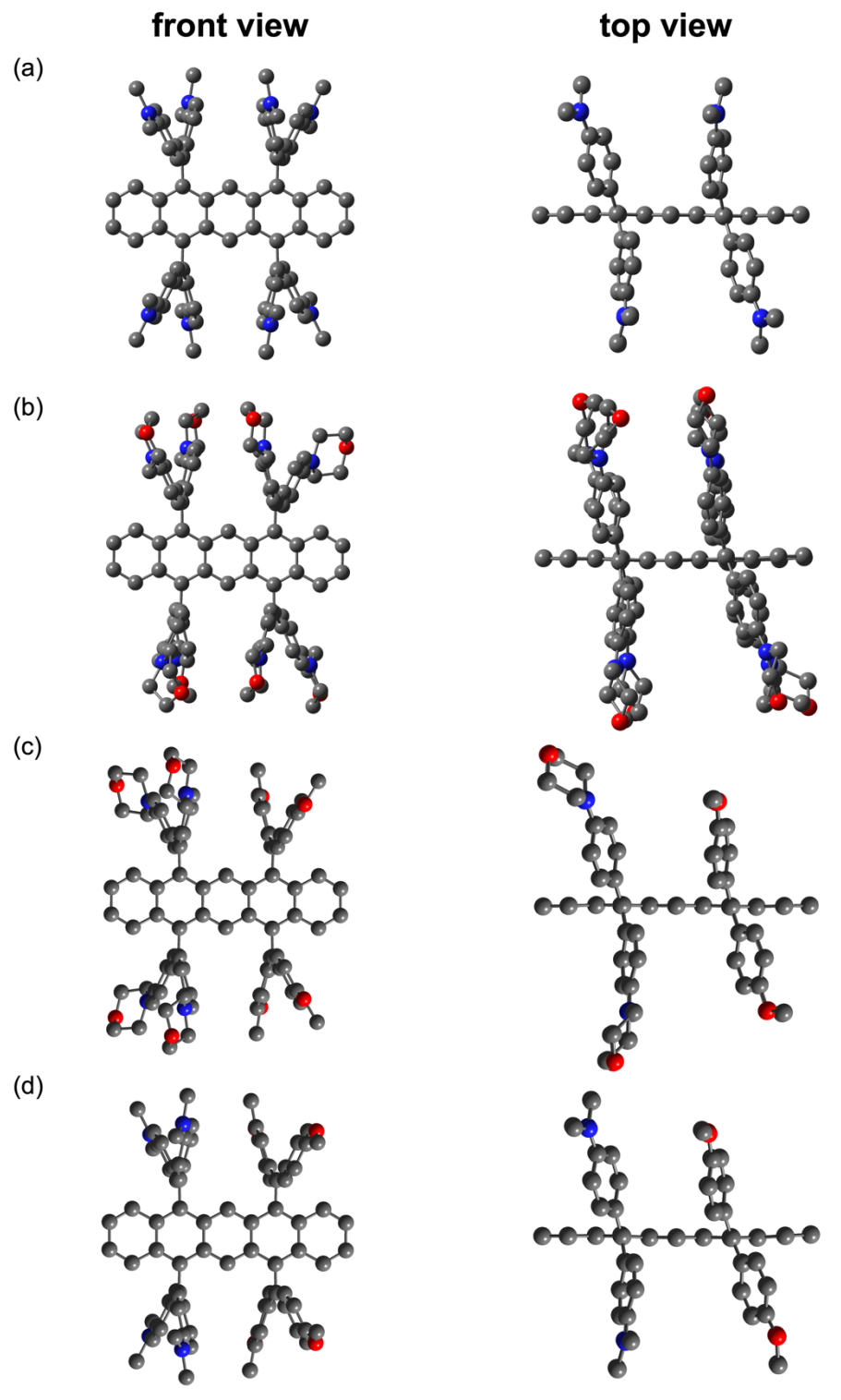

Figure 3-23. Optimized structures of (a) $\mathbf{2f}^{4+}$, (b) $\mathbf{2g}^{4+}$, (c) $\mathbf{2af}^{4+}$, and (d) $\mathbf{2af}^{4+}$ obtained by DFT calculations (CAM-B3LYP/6-31G*). Hydrogen atoms are omitted for clarity. [$\mathbf{2f}^{4+}$: X = Y = 4-$Me_2NC_6H_4$; $\mathbf{2g}^{4+}$: X = Y = 4-$O(C_2H_4)_2NC_6H_4$; $\mathbf{2af}^{4+}$: X = 4-$MeOC_6H_4$, Y = 4-$Me_2NC_6H_4$; $\mathbf{21g}^{4+}$: X = 4-$MeOC_6H_4$, Y = 4-$O(C_2H_4)_2NC_6H_4$]

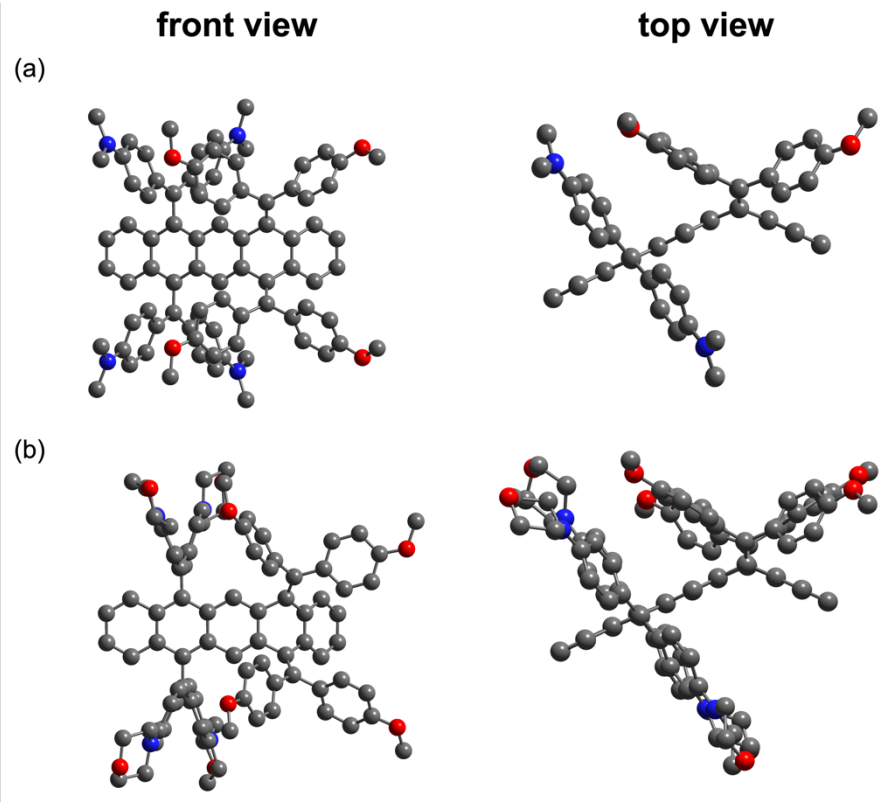

Figure 3-24. Optimized structures of (a) **2af**$^{2+}$, and (b) **2ag**$^{2+}$ obtained by DFT calculations (CAM-B3LYP/6-31G*). Hydrogen atoms are omitted for clarity. [**2af**$^{2+}$: X = 4-$MeOC_6H_4$, Y = 4-$Me_2NC_6H_4$; **2ag**$^{2+}$: X = 4-$MeOC_6H_4$, Y = 4-$O(C_2H_4)_2NC_6H_4$]

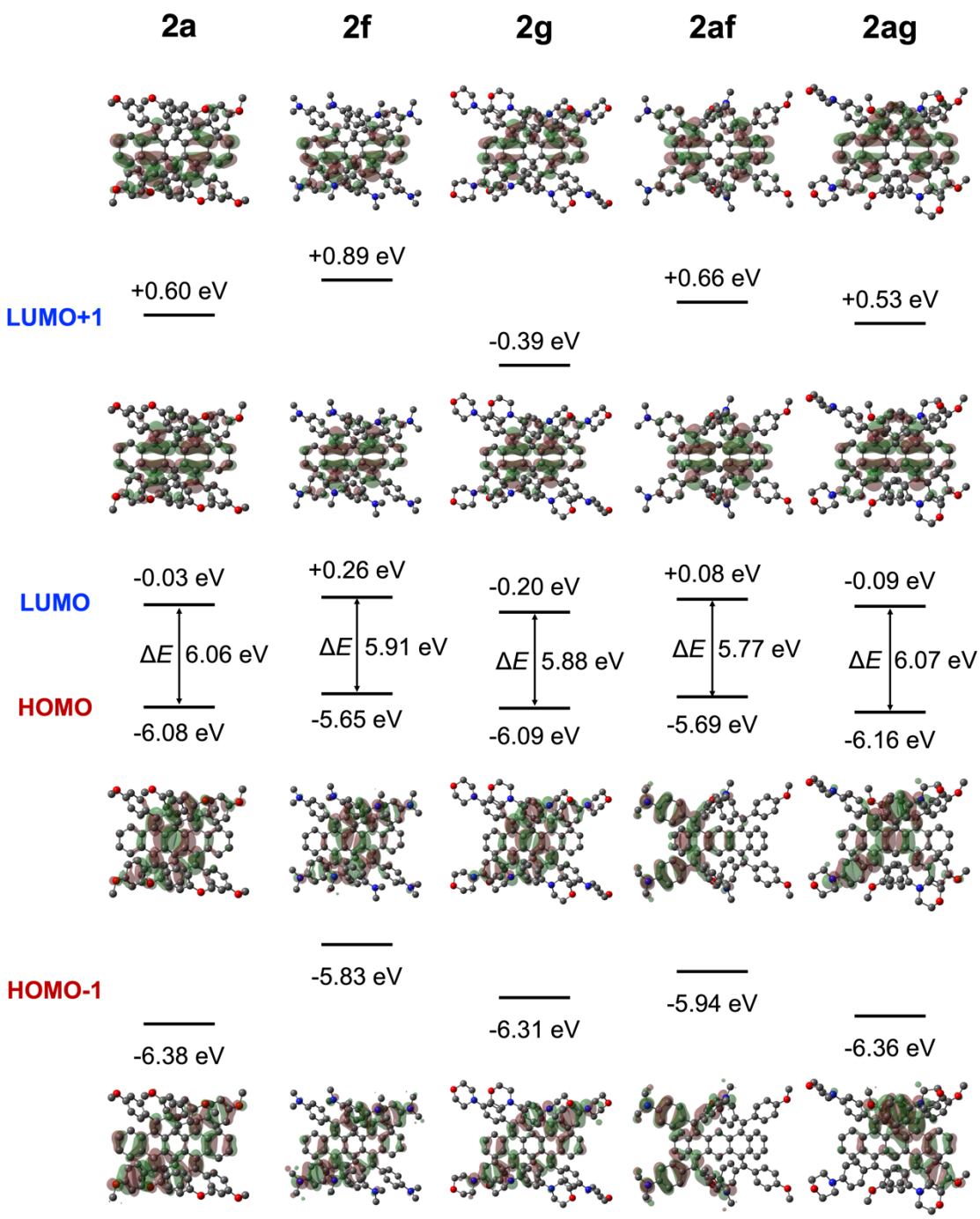

Figure 3-25. HOMO and LUMO levels calculated by the DFT method (CAM-B3LYP/6-31G*) based on the optimized structures of **2a**, **2f**, **2g**, **2af**, and **2ag**. [**2a**: X = Y = 4-$MeOC_6H_4$; **2f**: X = Y = 4-$Me_2NC_6H_4$; **2g**: X = Y = 4-$O(C_2H_4)_2NC_6H_4$; **2af**: X = 4-$MeOC_6H_4$, Y = 4-$Me_2NC_6H_4$; **2ag**: X = 4-$MeOC_6H_4$, Y = 4-$O(C_2H_4)_2NC_6H_4$]

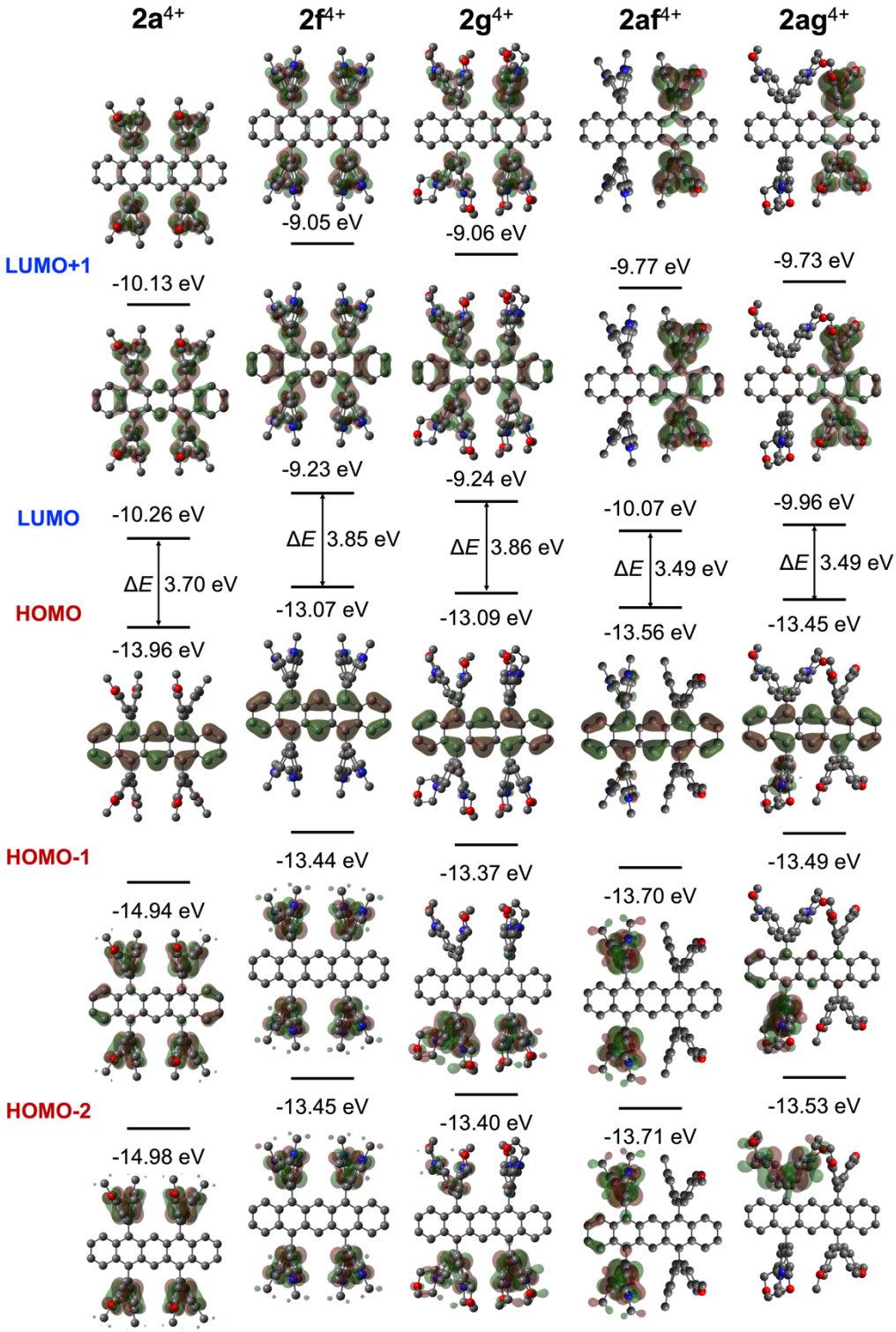

Figure 3-26. HOMO and LUMO levels calculated by the DFT method (CAM-B3LYP/6-31G*) based on the optimized structures of **2a**$^{4+}$, **2f**$^{4+}$, **2g**$^{4+}$, **2af**$^{4+}$, and **2ag**$^{4+}$. [**2a**$^{4+}$: X = Y = 4-MeOC$_6$H$_4$; **2f**$^{4+}$: X = Y = 4-Me$_2$NC$_6$H$_4$; **2g**$^{4+}$: X = Y = 4-O(C$_2$H$_4$)$_2$NC$_6$H$_4$; **2af**$^{4+}$: X = 4-MeOC$_6$H$_4$, Y = 4-Me$_2$NC$_6$H$_4$; **2ag**$^{4+}$: X = 4-MeOC$_6$H$_4$, Y = 4-O(C$_2$H$_4$)$_2$NC$_6$H$_4$]

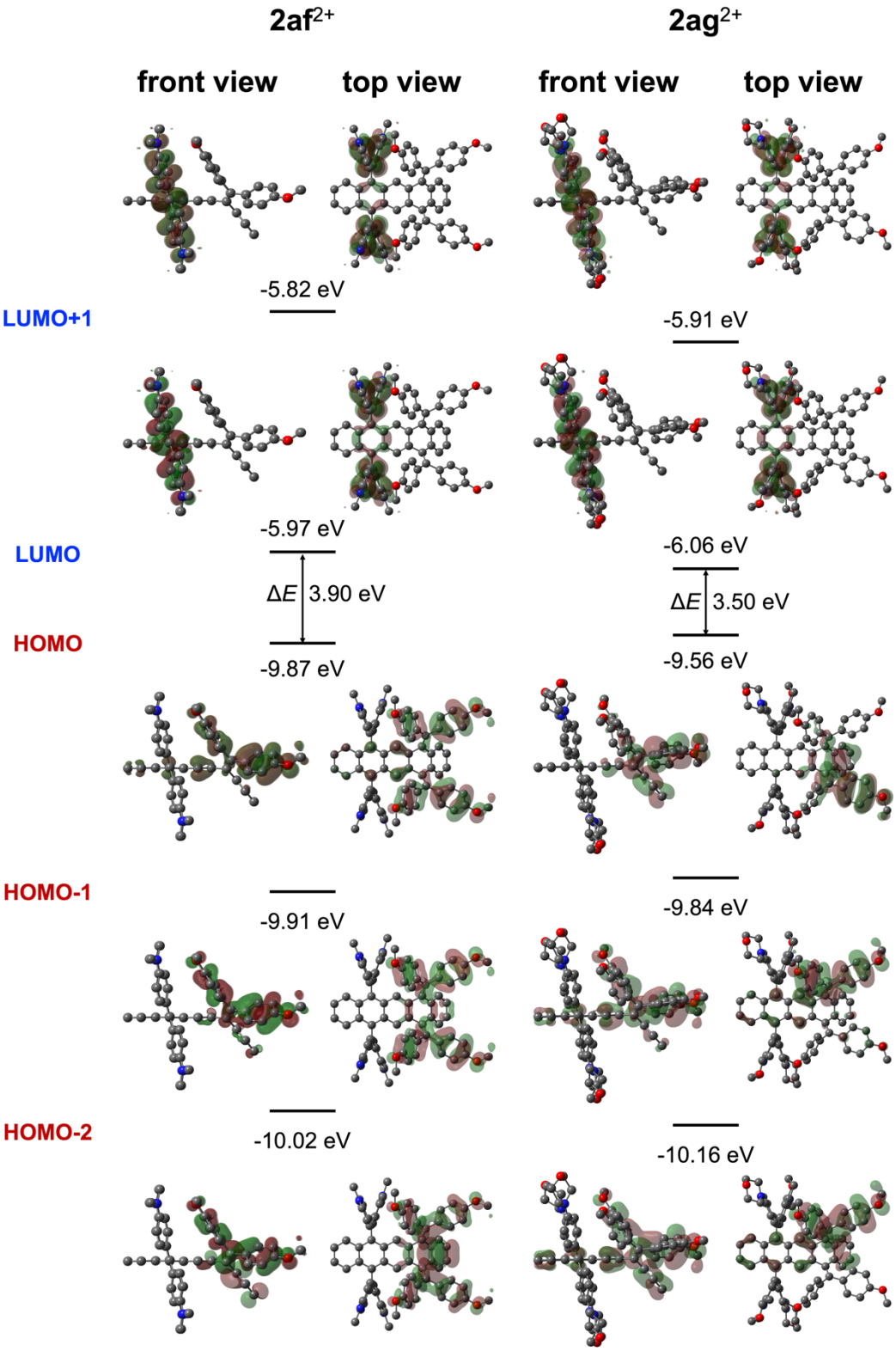

Figure 3-27. HOMO and LUMO levels calculated by the DFT method (CAM-B3LYP/6-31G*) based on the optimized structures of **2af**$^{2+}$ and **2ag**$^{2+}$. [**2af**$^{2+}$: X = 4-$MeOC_6H_4$, Y = 4-$Me_2NC_6H_4$; **2ag**$^{2+}$: X = 4-$MeOC_6H_4$, Y = 4-$O(C_2H_4)_2NC_6H_4$]

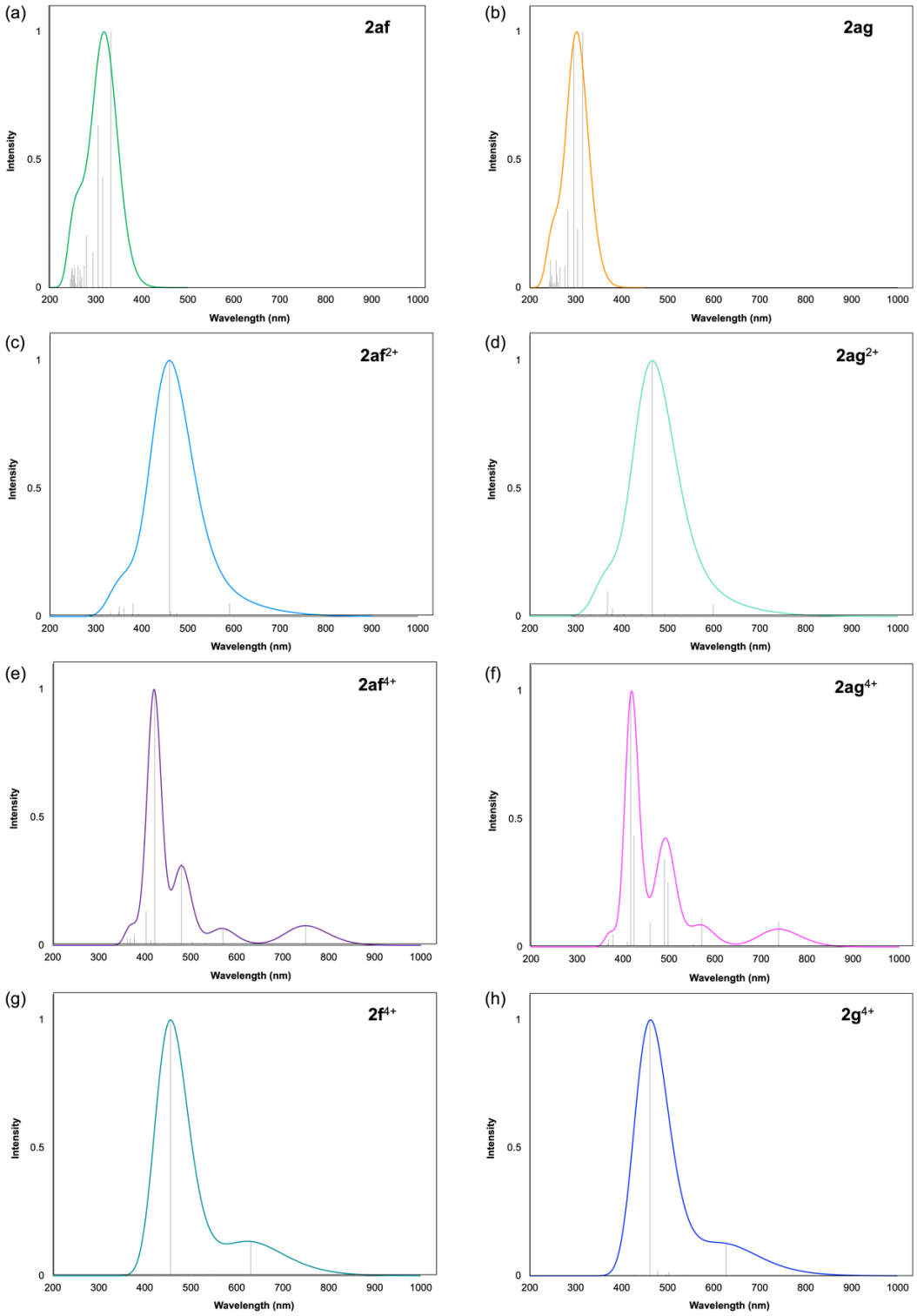

Figure 3-28. Simulated UV/Vis/NIR spectra by TD-DFT calculations (CAM-B3LYP/6-31G*) for (a) **2af**, (b) **2ag**, (c) **2af**$^{2+}$, (d) **2ag**$^{2+}$, (e) **2af**$^{4+}$, (f) **2ag**$^{4+}$, (g) **2f**$^{4+}$, and (h) **2g**$^{4+}$. [**2f**: X = Y = 4-$Me_2NC_6H_4$; **2g**: X = Y = 4-$O(C_2H_4)_2NC_6H_4$; **2af**: X = 4-$MeOC_6H_4$, Y = 4-$Me_2NC_6H_4$; **2ag**: X = 4-$MeOC_6H_4$, Y = 4-$O(C_2H_4)_2NC_6H_4$] For detailed information on excitation energies and oscillator strengths, see Ref. [50].

3-5. References

[1] Dang, H.; Garcia-Garibay, M. A., *J. Am. Chem. Soc.* **2001**, *123*, 355–356.

[2] Anthony, J. E.; Brooks, J. S.; Eaton, D. L.; Parkin, S. R., *J. Am. Chem. Soc.* **2001**, *123*, 9482−9483.

[3] Sakamoto, Y.; Suzuki, T.; Kobayashi, M.; Gao, Y.; Fukai, Y.; Inoue, Y.; Sato, F.; Tokito, S., *J. Am. Chem. Soc.* **2004**, *126*, 8138−8140.

[4] Payne, M. M.; Parkin, S. R.; Anthony, J. E., *J. Am. Chem. Soc.* **2005**, *127*, 8028−8029.

[5] Purushotham, U.; Sastry, G. N., *Phys. Chem. Chem. Phys*. **2013**, *15*, 5039−5048.

[6] Naibi Lakshminarayana, A.; Chang, J.; Luo, J.; Zheng, B.; Huang, K.-W.; Chi, C., *Chem. Commun.* **2015**, *51*, 3604−3607.

[7] Bheemireddy, S. R.; Ubaldo, P. C.; Rose, P. W.; Finke, A. D.; Zhuang, J.; Wang, L.; Plunkett, K. N. *Angew. Chem. Int. Ed.* **2015**, *54*, 15762−15766.

[8] Hu, Y.; Thomas, M. B.; Webre, W. A.; Moss, A.; Jinadasa, R. G. W.; Nesterov, V. N.; D'Souza, F.; Wang, H., *Angew. Chem. Int. Ed.* **2020**, *59*, 20075−20082.

[9] Pascal, R. A. *Chem. Rev.* **2006**, *106*, 4809−4819.

[10] Clevenger, R. G.; Kumar, B.; Menuey, E. M.; Kilway, K. V. *Chem. - Eur. J.* **2018**, *24*, 3113−3116.

[11] Bedi, A.; Shimon, L. J. W.; Gidron, O., *J. Am. Chem. Soc.* **2018**, *140*, 8086−8090.

[12] Anthony, J. E., *Chem. Rev.* **2006**, *106*, 5028−5048.

[13] Pilevarshahri, R.; Rungger, I.; Archer, T.; Sanvito, S.; Shahtahmassebi, N., P*hys. Rev. B: Condens. Matter Mater. Phys.* **2011**, *84*, 174437.

[14] Paulus, F.; Engelhart, J. U.; Hopkinson, P. E.; Schimpf, C.; Leineweber, A.; Sirringhaus, H.; Vaynzof, Y.; Bunz, U. H. F., *J. Mater. Chem. C* **2016**, *4*, 1194−1200.

[15] Pham, H. D.; Hu, H.; Wong, F.-L.; Lee, C.-S.; Chen, W.-C.; Feron, K.; Manzhos, S.; Wang, H.; Motta, N.; Lam, Y. M.; Sonar, P., *J. Mater. Chem. C* **2018**, *6*, 9017− 9029.

[16] Brega, V.; Yan, Y.; Thomas, S. W., *Org. Biomol. Chem.* **2020**, *18*, 9191−9209.

[17] McDaniel, D. K.; Jo, A.; Ringel-Scaia, V. M.; Coutermarsh-Ott, S.; Rothschild, D. E.; Powell, M. D.; Zhang, R.; Long, T. E.; Oestreich, K. J.; Riffle, J. S.; Davis, R. M.; Allen, I. C., *Nanomedicine* **2017**, *13*, 1255−1266.

[18] Uchiyama, Y.; Watanabe, R.; Kurotaki, T.; Kuniya, S.; Kimura, S.; Sawamura, Y.; Ohtsuki, T.; Kikuchi, Y.; Matsuzawa, H.; Uchiyama, K.; Itakura, M.; Kawakami, F.; Maruyama, H., *ACS Omega* **2017**, *2*, 3371−3379.

[19] Wilson, M. W. B.; Rao, A.; Johnson, K.; Gélinas, S.; di Pietro, R.; Clark, J.; Friend, R. H., *J. Am. Chem. Soc.* **2013**, *135*, 16680−16688.

[20] Basel, B. S.; Hetzer, C.; Zirzlmeier, J.; Thiel, D.; Guldi, R.; Hampel, F.; Kahnt, A.; Clark, T.; Guldi, D. M.; Tykwinski, R. R., *Chem. Sci.* **2019**, *10*, 3854−3863.

[21] Yablon, L. M.; Sanders, S. N.; Li, H.; Parenti, K. R.; Kumarasamy, E.; Fallon, K. J.; Hore, M. J. A.; Cacciuto, A.; Sfeir, M. Y.; Campos, L. M., *J. Am. Chem. Soc.* **2019**, *141*, 9564−9569.

[22] Papadopoulos, I.; Gao, Y.; Hetzer, C.; Tykwinski, R. R.; Guldi, D. M., *ChemPhotoChem.* **2020**, *4*, 5168−5174.

[23] Lijina, M. P.; Benny, A.; Ramakrishnan, R.; Nair, N. G.; Hariharan, M., *J. Am. Chem. Soc.* **2020**, *142*, 17393−17402.
[24] Fallon, K. J.; Churchill, E. M.; Sanders, S. N.; Shee, J.; Weber, J. L.; Meir, R.; Jockusch, S.; Reichman, D. R.; Sfeir, M. Y.; Congreve, D. N.; Campos, L. M., *J. Am. Chem. Soc.* **2020**, *142*, 19917−19925.
[25] Bergman, H. M.; Kiel, G. R.; Witzke, R. J.; Nenon, D. P.; Schwartzberg, A. M.; Liu, Y.; Tilley, T. D., *J. Am. Chem. Soc.* **2020**, *142*, 19850−19855.
[26] Dorel, R.; Echavarren, A. M., *Eur. J. Org. Chem.* **2017**, *2017*, 14−24.
[27] Chen, K.-Y.; Hsieh, H.-H.; Wu, C.-C.; Hwang, J.-J.; Chow, T. J., *Chem. Commun*. **2007**, 1065−1067.
[28] Watanabe, M.; Chang, Y. J.; Liu, S.-W.; Chao, T.-H.; Goto, K.; Islam, M. M.; Yuan, C.-H.; Tao, Y.-T.; Shinmyozu, T.; Chow, T. J., *Nat. Chem.* **2012**, *4*, 574−578.
[29] Hayashi, H.; Hieda, N.; Yamauchi, M.; Chan, Y. S.; Aratani, N.; Masuo, S.; Yamada, H., *Chem. - Eur. J.* **2020**, *26*, 15079−15083.
[30] Yamada, H.; Kuzuhara, D.; Suzuki, M.; Hayashi, H.; Aratani, N., *Bull. Chem. Soc. Jpn.* **2020**, *93*, 1234−1267.
[31] Kaur, I.; Jazdzyk, M.; Stein, N. N.; Prusevich, P.; Miller, G. P., *J. Am. Chem. Soc.* **2010**, *132*, 1261−1263.
[32] Tykwinski, R. R., *Acc. Chem. Res.* **2019**, *52*, 2056−2069.
[33] Berg, O.; Chronister, E. L.; Yamashita, T.; Scott, G. W.; Sweet, R. M.; Calabrese, J., *J. Phys. Chem. A* **1999**, *103*, 2451−2459.
[34] Zade, S. S.; Zamoshchik, N.; Reddy, A. R.; Fridman-Marueli, G.; Sheberla, D.; Bendikov, M., *J. Am. Chem. Soc.* **2011**, *133*, 10803−10816.
[35] Einholz, R.; Fang, T.; Berger, R.; Grüninger, P.; Früh, A.; Chassé, T.; Fink, R. F.; Bettinger, H. F., *J. Am. Chem. Soc.* **2017**, *139*, 4435−4442.
[36] Dong, S.; Ong, A.; Chi, C., *J. Photochem. Photobiol., C* **2019**, *38*, 27−46.
[37] Fudickar, W.; Linker, T., *J. Am. Chem. Soc.* **2012**, *134*, 15071−15082.
[38] Gao, Z.; Han, Y.; Wang, F., *Nat. Commun.* **2018**, *9*, 3977.
[39] Liu, K.; Lalancette, R. A.; Jäkle, F., *J. Am. Chem. Soc.* **2019**, *141*, 7453−7462.
[41] Ishigaki, Y.; Hayashi, Y.; Suzuki, T., *J. Am. Chem. Soc*. **2019**, *141*, 18293−18300.
[42] Ishigaki, Y.; Hashimoto, T.; Sugawara, K.; Suzuki, S.; Suzuki, T., *Angew. Chem. Int. Ed.* **2020**, *59*, 6581−6584.
[43] Sakamaki, D.; Ito, A.; Tsutsui, Y.; Seki, S., *J. Org. Chem.* **2017**, *82*, 13348−13358.
[44] Nguyen, M. T.; Ferris, D. P.; Pezzato, C.; Wang, Y.; Stoddart, J. F., *Chem* **2018**, *4*, 2329−2344.
[45] Ni, Y.; Gopalakrishna, T. Y.; Phan, H.; Kim, T.; Herng, T. S.; Han, Y.; Tao, T.; Ding, J.; Kim, D.; Wu, J., *Nat. Chem.* **2020**, *12*, 242−248.
[46] Ni, Y.; Gordillo-Gámez, F.; Peña Alvarez, M.; Nan, Z.; Li, Z.; Wu, S.; Han, Y.; Casado, J.; Wu, J., *J. Am. Chem. Soc*. **2020**, *142*, 12730−12742.

[47] Suzuki, T.; Tamaoki, H.; Nishida, J.; Higuchi, H.; Iwai, T.; Ishigaki, Y.; Hanada, K.; Katoono, R.; Kawai, H.; Fujiwara, K.; Fukushima, T., *Organic Redox Systems*; Wiley: Hoboken, NJ, **2015**; pp 13−37.
[48] Ishigaki, Y.; Harimoto, T.; Sugawara, K.; Suzuki, T., *J. Am. Chem. Soc*. **2021**, *143*, 3306−3311.
[49] Ishigaki, Y.; Fukagawa, R.; Sugawara, K.; Harimoto, T.; Suzuki, T., *Chem Asian J.* **2022**, *17*, e202200914.
[50] Harimoto, T.; Sugai, Y.; Sugawara, K.; Suzuki, T.; Ishigaki, Y., *Chem Eur J.* **2023**, *29*, e202301476.
[51] Frisch, M. J.; Trucks, G. W.; Schlegel, H. B.; Scuseria, G. E.; Robb, M. A.; Cheeseman, J. R.; Scalmani, G.; Barone, V.; Petersson, G. A.; Nakatsuji, H.; Li, X.; Caricato, M.; Marenich, A. V.; Bloino, J.; Janesko, B. G.; Gomperts, R.; Mennucci, B.; Hratchian, H. P.; Ortiz, J. V.; Izmaylov, A. F.; Sonnenberg, J. L.; Williams-Young, D.; Ding, F.; Lipparini, F.; Egidi, F.; Goings, J.; Peng, B.; Petrone, A.; Henderson, T.; Ranasinghe, D.; Zakrzewski, V. G.; Gao, J.; Rega, N.; Zheng, G.; Liang, W.; Hada, M.; Ehara, M.; Toyota, K.; Fukuda, R.; Hasegawa, J.; Ishida, M.; Nakajima, T.; Honda, Y.; Kitao, O.; Nakai, H.; Vreven, T.; Throssell, K.; Montgomery, J. A., Jr.; Peralta, J. E.; Ogliaro, F.; Bearpark, M. J.; Heyd, J. J.; Brothers, E. N.; Kudin, K. N.; Staroverov, V. N.; Keith, T. A.; Kobayashi, R.; Normand, J.; Raghavachari, K.; Rendell, A. P.; Burant, J. C.; Iyengar, S. S.; Tomasi, J.; Cossi, M.; Millam, J. M.; Klene, M.; Adamo, C.; Cammi, R.; Ochterski, J. W.; Martin, R. L.; Morokuma, K.; Farkas, O.; Foresman, J. B.; Fox, D. J. *Gaussian 16, Revision A.03*; Gaussian, Inc.: Wallingford, CT, 2016.
[52] Dolomanov, O. V.; Bourhis, L. J.; Gildea, R. J.; Howard, J. A. K.; Puschmann, H., *J. Appl. Crystallogr.* **2009**, *42*, 339–341.
[53] Sheldrick, G. M., *Acta Crystallogr. Sect. A Found. Adv.* **2015**, *71*, 3–8.
[54] Sheldrick, G. M., *Acta Crystallogr. Sect. C Struct. Chem.* **2015**, *71*, 3–8.
[55] Ko, F.; Hirabayashi, K.; Shimizu, T.; Sugiura, K. *Tetrahedron Lett.* **2018**, *59*, 4251–4254.

Chapter 4

Domino-Redox Reaction Induced by a Conformational Change Based on Dithiin Bisquinodimethane Skeleton

4-1. Introduction

Domino reactions are intramolecular reactions in which a single event triggers the conversion of a starting material to a product, which then provides a substrate for the next reaction until a stable final product is obtained (Figure 4-1a).[1–8] They have contributed greatly to green chemistry such as by improving the reaction efficiency (atom economy) and simplifying the workup process, thanks to the generation of multiple bonds in a single step. By expanding the concept of domino reactions to intermolecular reactions, various advanced strategies have been established, such as multicomponent reactions for medicinal and combinatorial chemistry,[9–15] chain-growth polymerization for precision macromolecular construction,[16–21] domino-type crystal growth and phase transition for crystal engineering,[22–26] and bottom-up genome assembly for synthetic biology.[27–29]

However, it is difficult to apply the concept of domino reactions to redox reactions due to electrostatic reasons (Figure 4-1b),[30–34] since in general, an electron transfer (ET) reaction produces a positively or negatively charged species. As a result, the oxidation/reduction reaction proceeds in a stepwise manner with an anodic/cathodic shift of the electric potential for the subsequent process.[35]

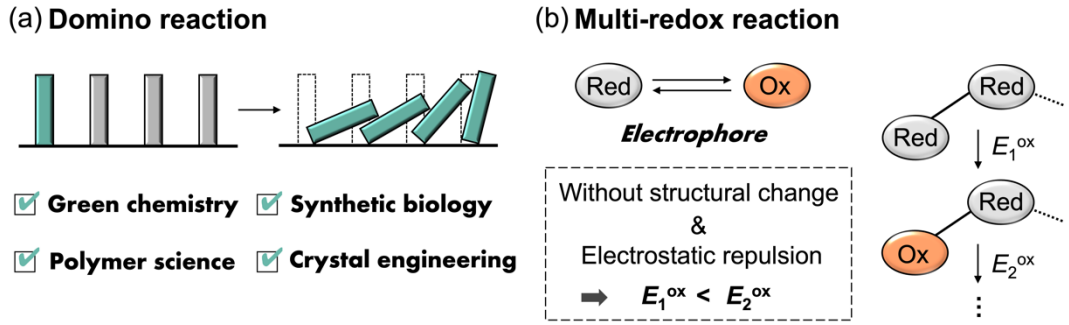

Figure 4-1. (a) The concept of domino reactions. (b) General Scheme for a multi-redox reaction without a change in the structure of the electrophore.

One of the exceptions is the "dyrex (dynamic redox)" system,[36] such as tetraarylanthraquinodimethane (AQD, **1**), in which the first oxidation of **1** with a folded geometry generates $\mathbf{1}^{+\bullet}$ that undergoes a rapid structural change into $(\mathbf{1'})^{+\bullet}$ with a twisted geometry (Figure 4-2). Since $(\mathbf{1'})^{+\bullet}$ (twisted) is more easily oxidized than $\mathbf{1}^{+\bullet}$ (folded) or even than **1** (folded), the second oxidation occurs nearly at the same potential to generate $(\mathbf{1'})^{2+}$ (twisted). This process is akin to the domino process, however, **1** could undergo only two-electron (2e) oxidation, and thus the first ET only facilitates the second ET but could not continue the process, so that it is not a domino process. In

addition, organic systems constructed by the assembly of multiple redox-active units (electrophores) are attracting much attention since it could exhibit superior charge transport properties based on their potential to interconvert with multivalent ionic species.[37–49]

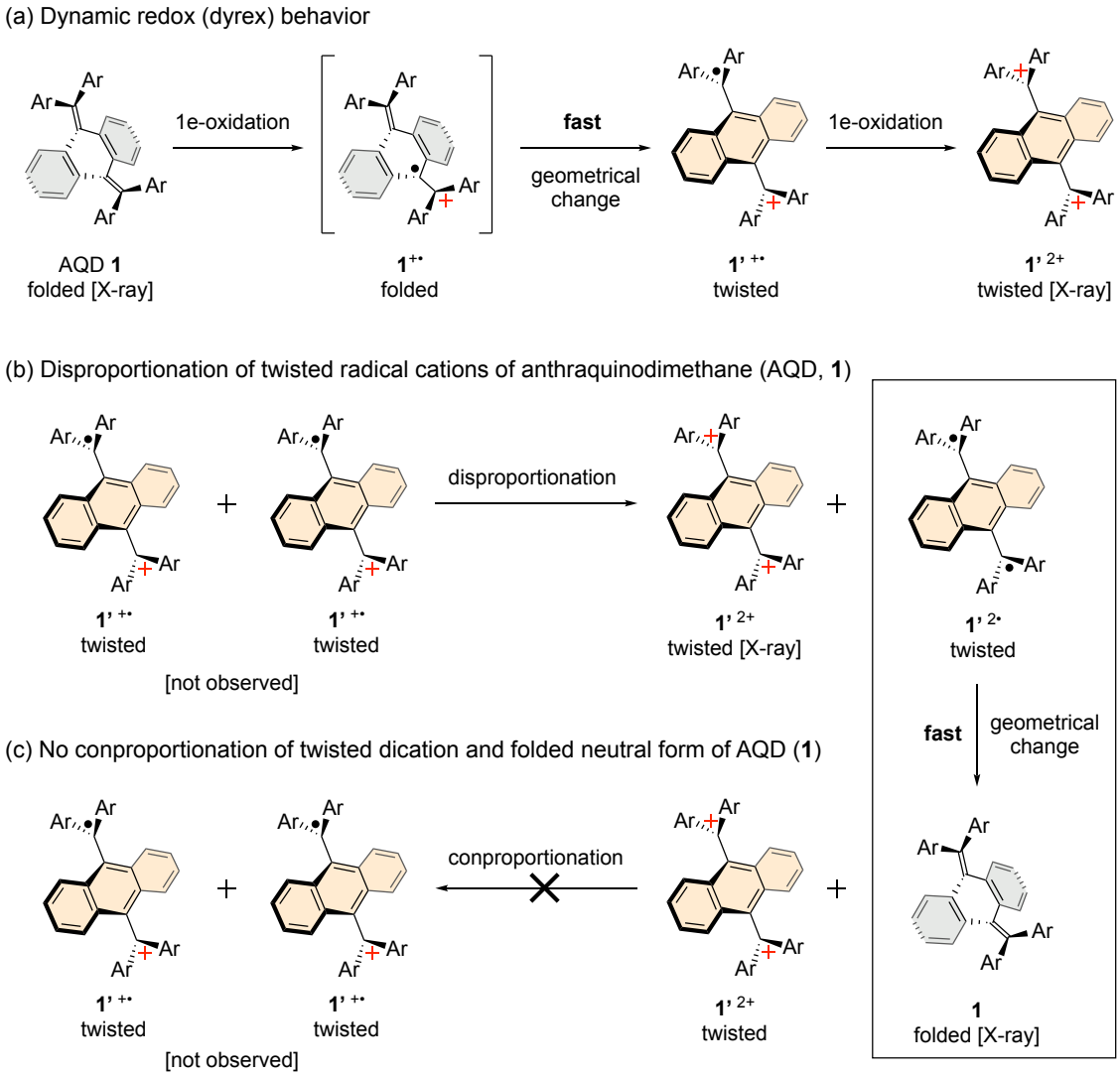

Figure 4-2. Redox interconversion of AQD **1**.

To realize domino-redox reactions in multi-redox systems consisting of the same kinds of electrophores, some novel mechanism is necessary, so that the initial redox reaction in one electrophore facilitates the subsequent redox reaction of the neighboring unit. As the simplest model of the multi-chromophoric systems, the author recently studied octaarylbisquinodimethane (BQD) derivatives **2** as shown in chapter 3, which have two units of the folded-shaped quinodimethane (QD) connected by a rigid π-linker (Figure 4-3).[50] If they exhibit the domino process, the same idea could be applied for the much larger multi-redox systems to facilely generate oligo/poly-cations. In fact, **2**

underwent one-wave four-electron (4e) oxidation to give tetracation $\mathbf{2}^{4+}$, however, this did not lead to the domino-redox reaction, because the oxidation potential of **2** is similar to that of monomeric AQD **1** with the same aryl groups,[36,51–53] which undergoes one-wave 2e-oxidation. Thus, the oxidation behavior of multi-redox system **2** could instead be explained by the independent ET process of two QD units. To achieve a domino redox reaction, mutual steric repulsion and/or electronic interaction between the electrophores is important, while it is prevented due to rigidity of the spacer in **2**.

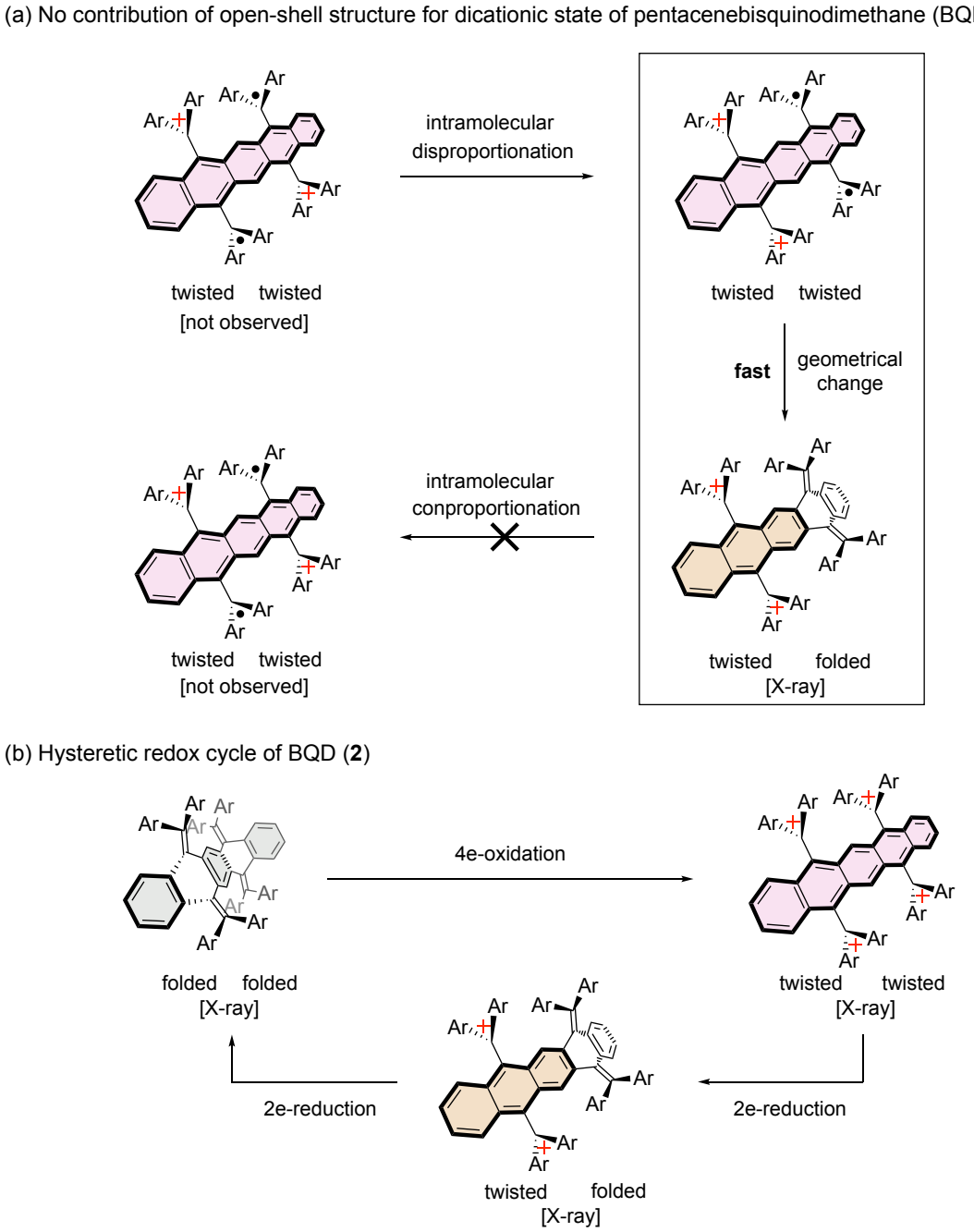

Figure 4-3. Redox interconversion of BQD **2**.

Thus, the author anticipated that, instead of fusing the QD units with a rigid π-skeleton, bridging two electrophores with a more flexible nonplanar linker would be promising (Figure 4-4). The author chose the dithiin skeleton, which was used to construct several nanohoops and nanobelts.[33–35] Herein, the author newly designed SS-BQD **3**, which consists of two QD units fused with a dithiin skeleton. The backbone of SS-BQD **3** is expected to exhibit higher flexibility, allowing close proximity of two QD units for mutual communication, thus affecting the structural preference of a QD unit while adopting one of multiple conformations, such as folded (**F**) and twisted (**T**) forms, with different electronic structures. In many cases, the AQD electrophore prefers the folded form with a low HOMO level whereas the high-energy twisted form has a much higher HOMO.[15]

A detailed investigation of the effects of changes in the conformation of QD units on the redox behavior indicated that, after the initial oxidation of SS-BQD, subsequent oxidation of the second unit is facilitated by raising the HOMO level, which is caused by a dynamic change in conformation of the intermediary dicationic state. In addition, this domino process could be clearly demonstrated since the initial oxidation process of the neutral species is activated by raising the temperature through the thermal equilibrium among the conformers in SS-BQD, thanks to the redox properties of a QD unit being drastically modified by adopting the high-energy twisted form. In this chapter, the author describes the first example of a domino-redox reaction induced by a drastic change in conformation that is accompanied by a domino-type change in the HOMO level.

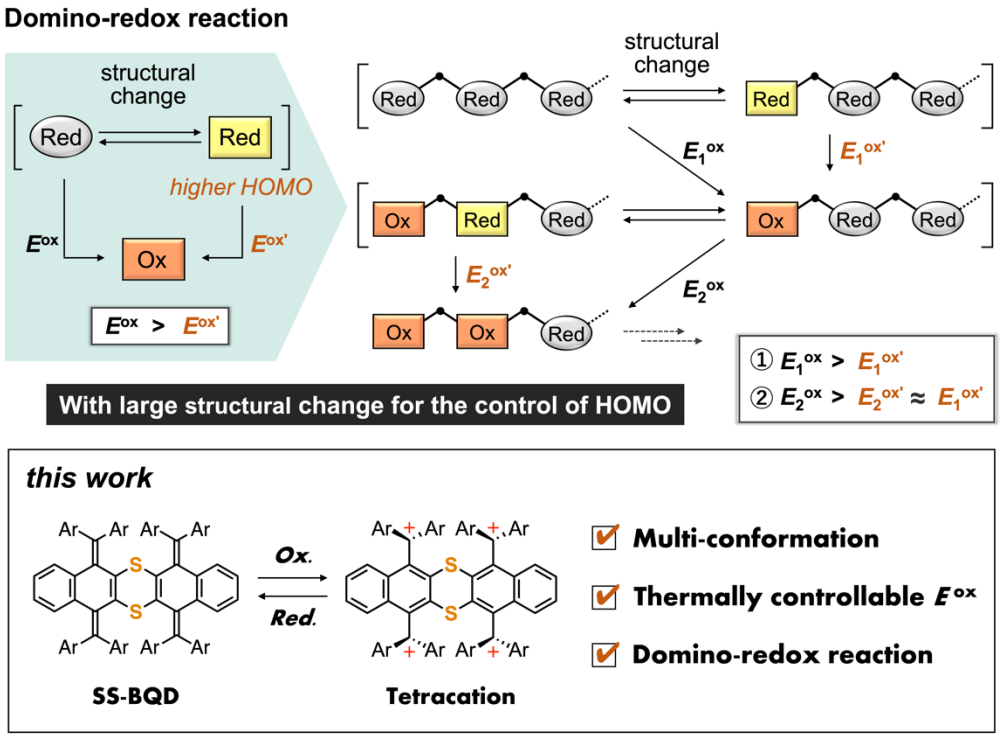

Figure 4-4. This work: realizing a domino-redox reaction by a large change in the structure of the electrophore after oxidation of the neighboring unit.

4-2. Results and Discussion

4-2-1. Preparation and X-ray analysis

To construct SS-BQD-based redox systems, the author selected a 4-methoxyphenyl group as the aryl group, since it has enough electron-donating ability to stabilize the cationic states. By an eight-fold Suzuki-Miyaura cross-coupling reaction, SS-BQD **3a** with 4-methoxyphenyl groups was prepared in 92% yield in a one-step manner from tetrakis(dibromomethylene) precursor **3Br$_8$**, which was prepared from SS-tetraone[36] (Figure4-5a). In addition, to investigate the effect of a restricted change in the structure of the QD unit,[32] the author prepared the reference compound **3d** with a chlorine atom at the 2-position of the 4-methoxyphenyl group in a similar manner (56% yield). X-ray analysis of SS-BQD **3a** using a benzene-solvated single crystal obtained by recrystallization from benzene/hexane showed that SS-BQD **3a** contains two units of folded QD, which are connected by a boat-shaped dithiin spacer (Figure 4-5b). Thus, **3a** adopts a U-shaped conformation (**F-F$_{syn}$**) in which the concave faces of the QD units are directed to the same sides.

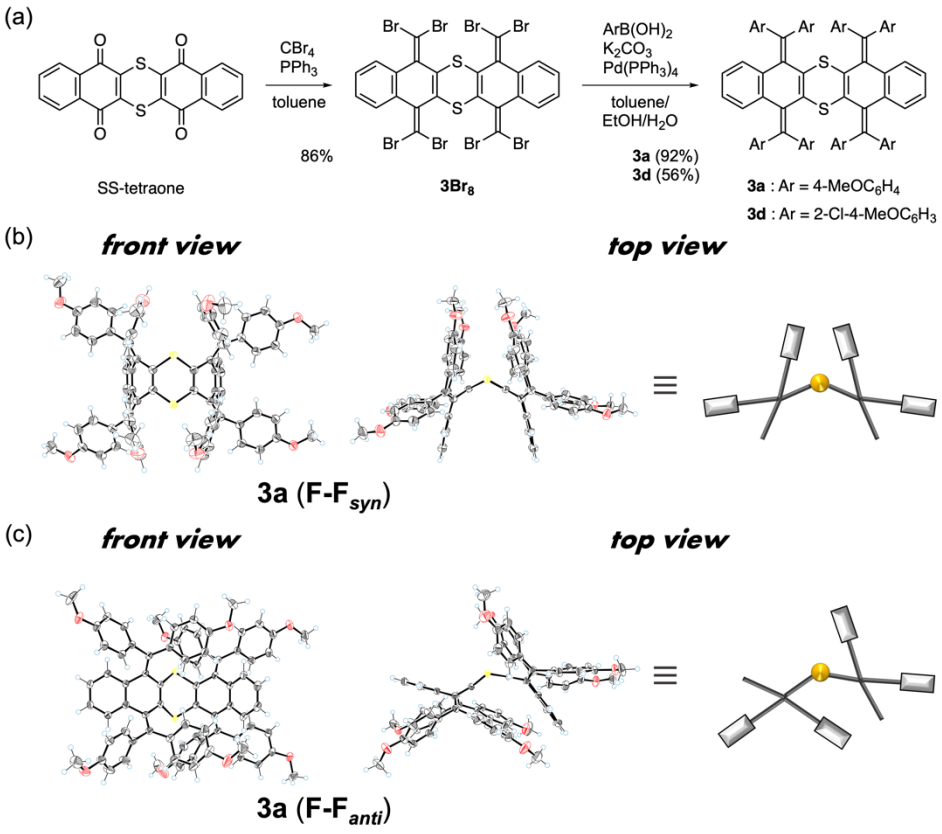

Figure 4-5. (a) Preparation of newly designed SS-BQDs **3**. X-ray crystal structures (ORTEP drawings) of (b) **3a** (**F-F$_{syn}$**)$^{\#}$ and (c) **3a** (**F-F$_{anti}$**) determined at 150 K. The solvent molecules and disordered atoms are omitted for clarity. Thermal ellipsoids are shown at the 50 % probability level. $^{\#}$One of the two crystallographically independent molecules.

On the other hand, X-ray analysis of a $CHCl_3$-solvated single crystal obtained from $CHCl_3$/hexane revealed that SS-BQD **3a** adopts a Z-shaped conformation (**F-F**$_{anti}$) with the two folded QD units (Figure 4-5c), while their concave faces are directed to the opposite side. These results clearly show that two conformers with QD units in different orientations can exist as stable species in the crystals. The observation of both conformers by X-ray analysis indicated that **3a** exists in a state of rapid equilibrium of the **F-F**$_{syn}$ and **F-F**$_{anti}$ conformations in solution.

4-2-2. Redox interconversion and X-ray analysis

Thanks to the electron-donating nature of the 4-methoxyphenyl and 2-chloro-4-methoxyphenyl groups, upon treatment of **3a** and **3d** with four equivalents of $(4\text{-}BrC_6H_4)_3N^{+\bullet}SbCl_6^-$, the tetracation salts $\mathbf{3a}^{4+}(SbCl_6^-)_4$ and $\mathbf{3d}^{4+}(SbCl_6^-)_4$ were obtained quantitatively (Figure 4-6). When tetracations $\mathbf{3a}^{4+}$ and $\mathbf{3d}^{4+}$ were reduced with Zn powder, neutral species **3a** and **3d** were recovered quantitatively. X-ray analysis of tetracation salt $\mathbf{3a}^{4+}(SbCl_6^-)_4$ showed that tetracation adopts almost orthogonally twisted structures, with large dihedral angles between the central pentacyclic skeleton and each diarylmethylium unit [64.7(8)°-82.3(8)°]. These results indicate that the tetracation adopts a perpendicular geometry, whereas the QD units in the neutral state prefer a folded geometry.

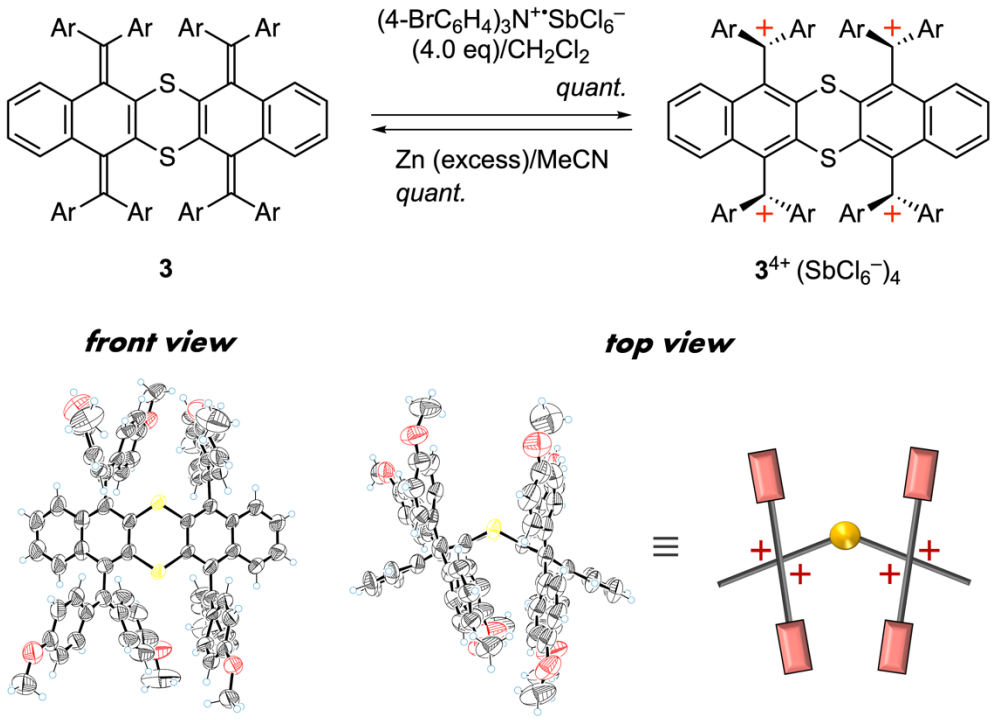

Figure 4-6. Redox interconversion between neutral donors and tetracations. Four equivalents of $(4\text{-}BrC_6H_4)_3N^{+\bullet}SbCl_6^-$ were used for the oxidation of **3a** and **3d**, respectively. X-ray crystal structures (ORTEP drawings) of $\mathbf{3a}^{4+}(SbCl_6^-)_4$ determined at 100 K. The counterions, solvent molecules, and disordered atoms are omitted for clarity. Thermal ellipsoids are shown at the 50% probability level.

4-2-3. Redox behavior

Such a change in structures between the neutral and cationic states is common with AQD derivatives **1a** and **1d**,[15,32] which is reflected in the redox behavior with large separation of the oxidation and reduction peaks (Figure 4-7). This would also be the case for SS-BQD. Indeed, a cyclic voltammogram of **3d** in CH_2Cl_2 exhibited one-wave 4e-redox peaks at quite different potentials, each of which corresponds to the oxidation of **3d** and the reduction of $\mathbf{3d}^{4+}$, respectively (Figure 4-7). The redox behaviors of **1a** and **3d** do not change when measured at other scan rates or at other temperatures. However, quite different and rather reversible redox waves were observed for **3a** at 298 K. A cathodic shift of the oxidation wave compared to that of AQD **1a** with 4-methoxyphenyl groups suggests that **3a** has a much higher HOMO than AQD **1a** (Figure 4-7).

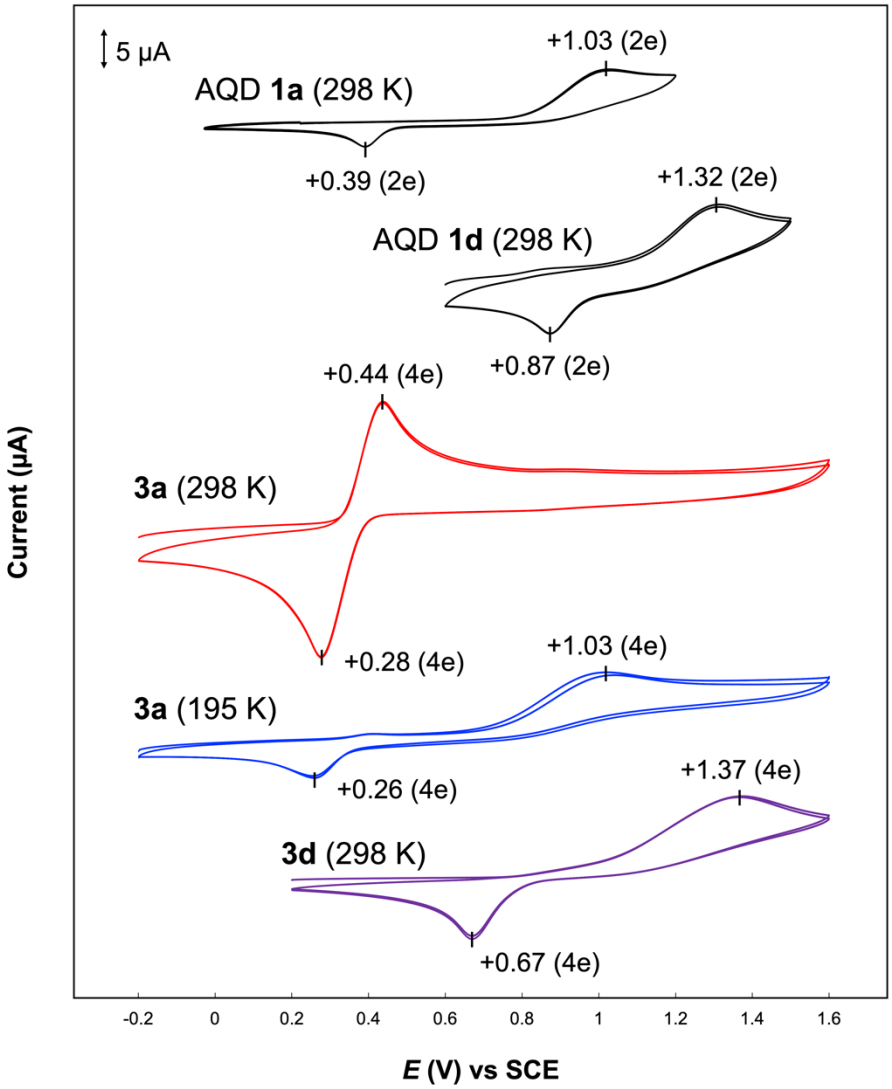

Figure 4-7. Cyclic voltammograms of neutral donors **1a**, **1d**, **3a**, and **3d** measured in CH_2Cl_2 containing 0.1 M Bu_4NBF_4 as a supporting electrolyte (scan rate 100 mV s^{-1}, Pt electrodes). [**1a** and **3a**: Ar = 4-$MeOC_6H_4$; **1d** and **3d**: Ar = 2-Cl-4-$MeOC_6H_3$]

The nearly reversible redox waves imply that there is almost no change in structure between before and after the oxidation of neutral species **3a** in solution. Considering that tetracation $\mathbf{3a}^{4+}$ only adopts a perpendicularly twisted structure as suggested by an X-ray analysis, NMR and UV/Vis spectra, and theoretical calculations (see below), the oxidation of neutral species **3a** should occur from the conformations other than those observed in crystal by X-ray, so that one or both of the two QD units adopt a twisted form.

The author considered that a more stable folded form and a metastable twisted form in the QD units of **3a** would be in thermal equilibrium at 298 K. To validate this hypothesis, the cyclic voltammogram was measured at 195 K in CH_2Cl_2. As expected from the general view that the metastable form makes less of a contribution at a lower temperature, the voltammogram showed a large separation of redox peaks, indicating that the QD units with a folded form are dominant in solution at 195 K, and thus a large change in structure between the neutral donor and the tetracation was indicated (Figure 4-7). A continuous change was observed by measuring the voltammogram of **3a** at different temperatures between 195 K and 298 K (Figures 4-8a and 4-9a). Similarly, when the scan rate was increased during the measurements at 298 K, the similar continuous change was observed showing large separation of redox peaks at higher scan speeds (Figures 4-8b and 4-9b). The above results show that the less populated but easily-oxidized form is supplied from the most stable forms at higher temperature and/or at slower scan rate.

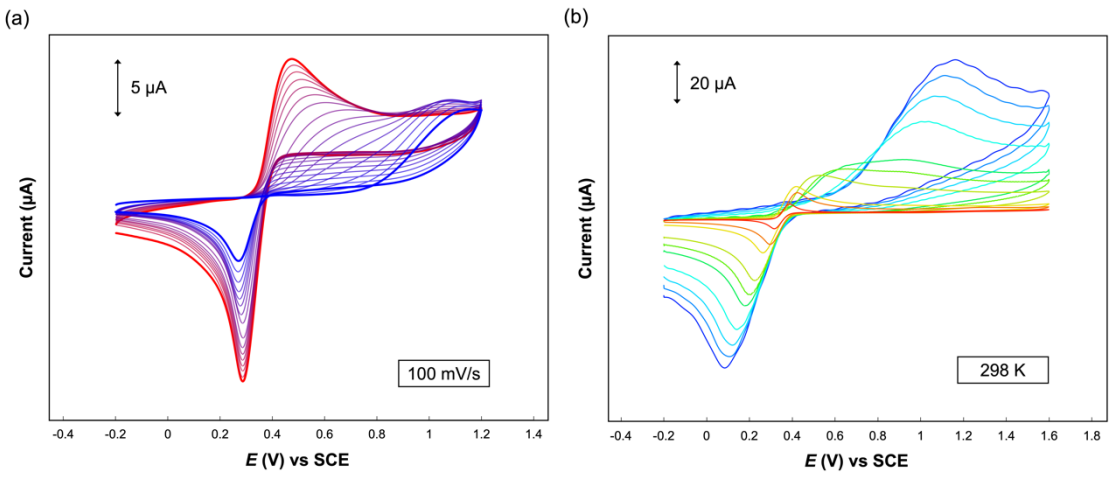

Figure 4-8. Cyclic voltammograms of SS-BQD **3a** in CH_2Cl_2 containing 0.1 M Bu_4NBF_4 as a supporting electrolyte (Pt electrodes). (a) Measured at various temperatures varied continuously from 195 K (blue) to 298 K (red). (b) Measured at various scan rates varied from 10 mV s^{-1} (red) to 5 V s^{-1} (blue).

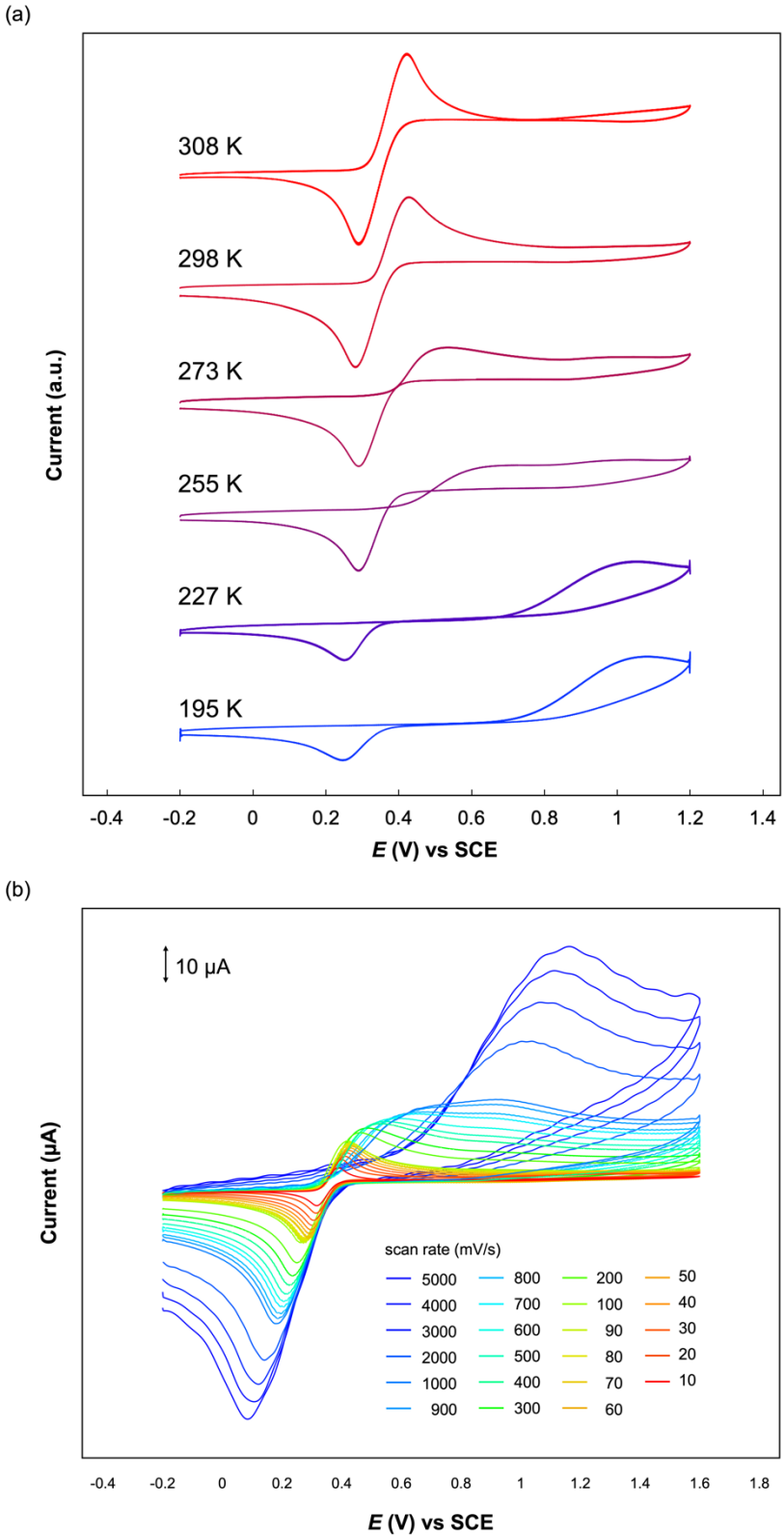

Figure 4-9. Cyclic voltammograms of SS-BQD **3a** measured in CH_2Cl_2 containing 0.1 M Bu_4NBF_4 as a supporting electrolyte (Pt electrodes) (a) at various temperatures (195 K–298 K, scan rate 100 mV s^{-1}) and (b) with scan rates varied from 10 mV s^{-1} to 5 V s^{-1} at 298 K.

4-2-4. Plausible redox mechanism

Based on the thermally activatable redox behavior observed in SS-BQD **3a**, the author can propose a mechanism for the redox process shown in Scheme 4-1. The two conformers **F-F**$_{syn}$ and **F-F**$_{anti}$, in which both QD units adopt the folded form, are in equilibrium in solution via the rapid flipping motion of QD units. At 195K, the voltammogram of **3a** is similar to that of **3d**, in the latter of which the twisted QD unit does not need to be considered due to the substituents at the 2-position of aryl groups even at 298 K. These results indicate that the contribution of the metastable conformation with a twisted QD unit of **3a** is negligibly small at lower temperatures. When the temperature was raised to 298 K, some contribution from the conformer containing a twisted QD unit (e.g., **T-F**) is expected with a change in redox behavior. While its proportion should be small, the high HOMO of the **T-F** conformer allows facile oxidation of **3a** since **F-F**$_{syn}$ and **F-F**$_{anti}$ are in rapid equilibrium with **T-F**. After the **T-F** conformer undergoes an apparent 2e-oxidation, the as-generated dication **3a**$^{2+}$ adopts the **T**$^{2+}$**-F** conformation, which has a twisted bis(diarylmethylium) moiety and the neutral QD unit of the folded form. Importantly, due to the steric repulsion between electrophores, the folded QD unit in the dication **3a**$^{2+}$ could further undergo a rapid change in conformation into the twisted QD, with the formation of a doubly twisted conformer **T**$^{2+}$**-T** with a higher HOMO level than **T**$^{2+}$**-F** (see below). Moreover, in the **T**$^{2+}$**-T** conformer, the HOMO and LUMO are delocalized in the orthogonally attached diarylmethylene/methylium units, suggesting the presence of interelectrophore interactions. In this way, the change in conformation can facilitate subsequent 2e-oxidation so that it happens at nearly the same potential as for **T-F**, resulting in the formation of tetracation **3a**$^{4+}$ with the **T**$^{2+}$**-T**$^{2+}$ conformation.

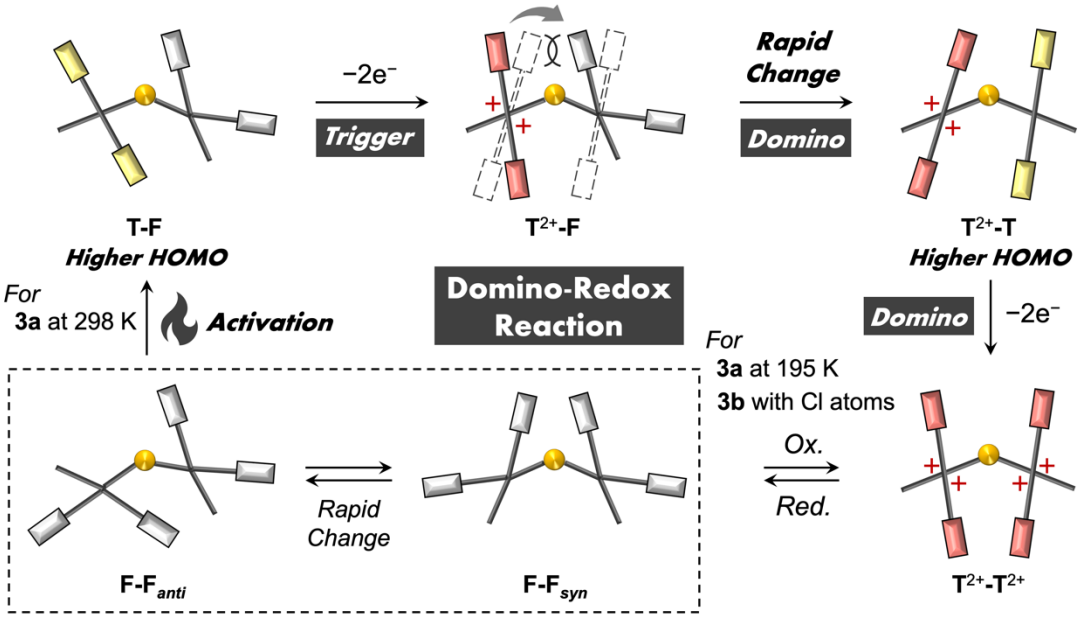

Scheme 4-1. A plausible mechanism for domino-redox reaction induced by an electrochemically triggered conformational change.

This scenario for the domino-redox reaction is most likely to account for the one-wave 4e-oxidation process of **3a** at the cathodically shifted potential compared to AQD **1a**. The change in conformation of the as-generated $\mathbf{3a}^{2+}$ is the key for the success of the domino process. The $\mathbf{T}^{2+}$**-F** conformer of $\mathbf{3a}^{2+}$ generated by the initial oxidation exhibits steric repulsion between two electrophores as in the case of neutral **T-F**. However, the repulsion in the dicationic state cannot be released as in the neutral state, since the $\mathbf{T}^{2+}$ part cannot convert to the folded form. The only way to relieve the repulsion in $\mathbf{T}^{2+}$**-F** is by a change in the conformation of the QD unit to the twisted form, which warrants the downstream change in conformation from $\mathbf{T}^{2+}$**-F** to $\mathbf{T}^{2+}$**-T**. When a spectral change was followed by UV/Vis spectroscopy upon electrochemical oxidation in CH_2Cl_2, a clean conversion of **3a** to tetracation $\mathbf{3a}^{4+}$ (Figure 4-10) was observed with isosbestic points at 314 and 347 nm. At the early-stage of oxidation, a slightly red-shifted absorption maximum (529 nm) was observed, which merged into the absorption of $\mathbf{3a}^{4+}$ at 507 nm, suggesting that the dicationic intermediate could be transiently detected under the constant-current electrolytic condition. Then, to observe transient dication $\mathbf{3a}^{2+}$ more clearly, the author conducted electrochemical oxidation of **3a** in MeCN, which can stabilize the intermediary cationic species by an effective solvation. Indeed, stepwise oxidation processes were observed via the intermediary dication with several isosbestic points in each oxidation process (Figure 4-11), indicating that the transient $\mathbf{T}^{2+}$**-F** form can be long-lived in MeCN, which was supported by DFT calculations (see below).

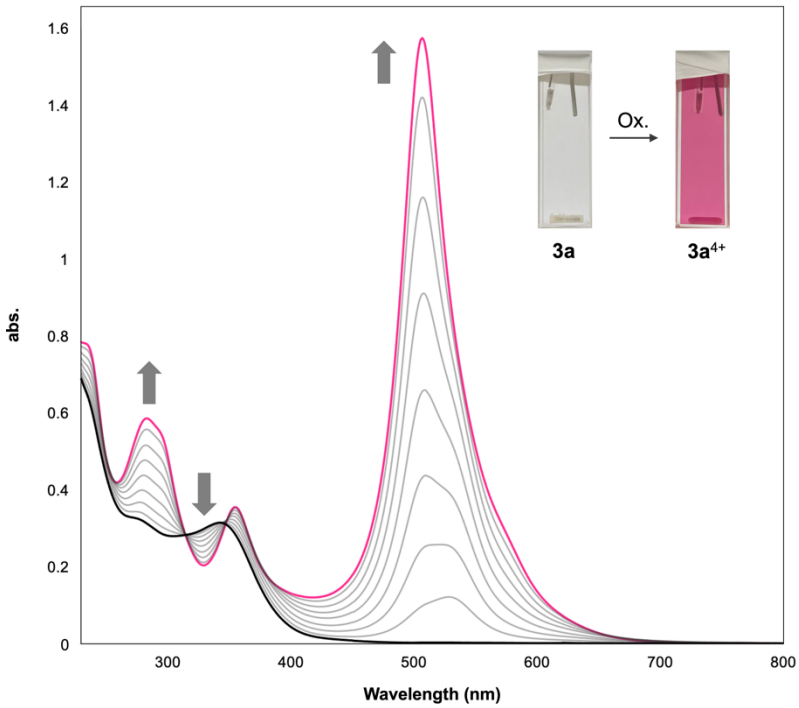

Figure 4-10. A change in UV/Vis spectrum upon constant-current electrochemical oxidation of SS-BQD **3a** (8.1 μM, 30 μA, every 4 min) in CH_2Cl_2 containing 0.05 M Bu_4NBF_4 as a supporting electrolyte. [**3a**: Ar= 4-$MeOC_6H_4$]

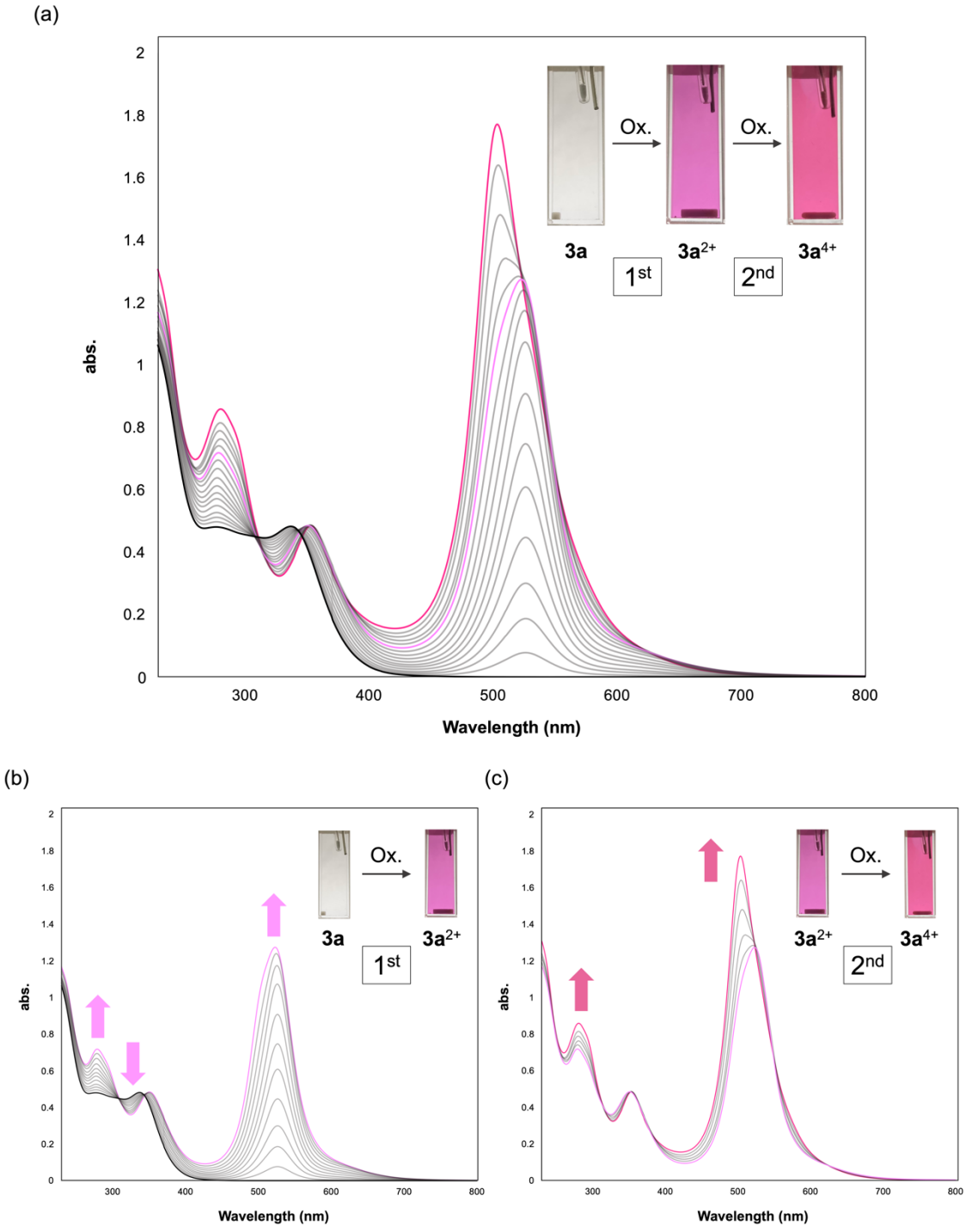

Figure 4-11. (a) Changes in UV/Vis spectrum upon constant-current electrochemical oxidation of SS-BQD **3a** (11.6 μM, 30 μA, every 2 min) in MeCN containing 0.05 M Et_4NClO_4 as a supporting electrolyte. (b) The 1st process corresponding to the oxidation of **3a** and (c) the 2nd process corresponding to the oxidation of as-prepared $\mathbf{3a}^{2+}$. [**3a**: Ar= 4-$MeOC_6H_4$]

4-2-5. DFT calculations

To validate the domino-redox scenario by evaluating the relative energies (E_{rel}) of the conformers, DFT calculations were performed at the (U)B3LYP-D3/6-31G* level. Since the variable temperature (VT)-NMR measurements (see below) did not show any biradical character, open-shell species would be energetically overestimated and can be excluded. The results showed that not only the **F-F**$_{syn}$ and **F-F**$_{anti}$ conformations with folded QD units but also the **T-F** conformation with a twisted QD unit were obtained as energy-minimized structures for **3a** (Figures 4-12a and 4-15, see p. 146). The energy difference between **F-F**$_{syn}$ and **F-F**$_{anti}$ (3.19 kcal/mol) suggests that there is some steric repulsion/dispersion attraction between electrophores over the dithiin skeleton. The **T-F** conformer with a higher HOMO level has an E_{rel} value of 5.90 kcal/mol, which is small enough to consider the contribution from this conformer with an increase in temperature. On the other hand, the **T-T** conformer is much less stable (E_{rel}: 20.2 kcal/mol), so the contribution of the **T-T** conformer is negligible (Figure 4-15, see p. 146). In the case of dication **3a**$^{2+}$, the **T**$^{2+}$**-T** form is more stable than **T**$^{2+}$**-F** (E_{rel}: 6.76 kcal/mol), as discussed above based on the interelectrophore interaction (Figures 4-12b and 4-16, see p. 147). Again, the **T**$^{2+}$**-T** form has a higher HOMO level than **T**$^{2+}$**-F** (Figure 4-22), indicating that subsequent oxidation of **3a**$^{2+}$ to **3a**$^{4+}$ would readily occur to accomplish the domino-redox reaction.

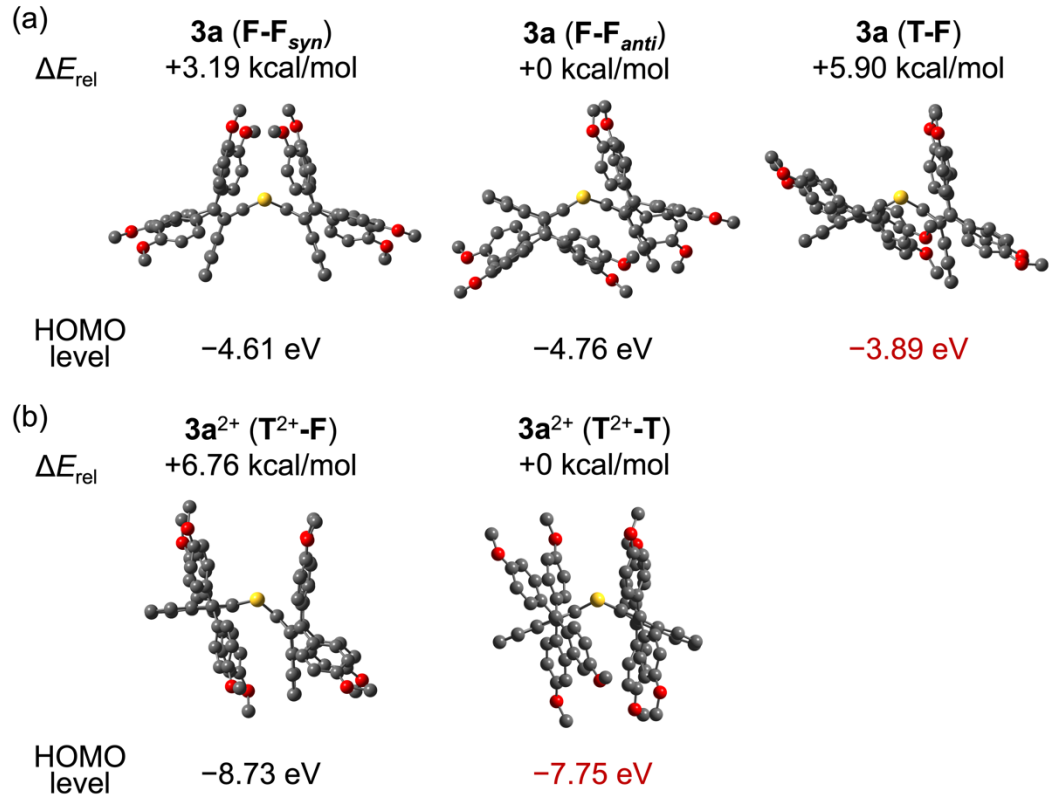

Figure 4-12. Optimized structures of possible isomers of (a) **3a** and (b) **3a**$^{2+}$ obtained by DFT calculations at the B3LYP-D3/6-31G* level. Hydrogen atoms are omitted for clarity.

On the other hand, the calculation for **3d** with a 2-chloro substituent on the aryl group showed a considerable change in the relative stability of conformers. In the neutral state, the author tried to find other conformations with a twisted QD unit, but both the **T-T** and **T-F** conformations were not obtained as energy-minimized structures (Figure 4-18, see p. 148). Furthermore, in the dicationic state, $\mathbf{T}^{2+}$**-F** conformer should be dominant because of the very large E_{rel} value (17.5 kcal/mol) for the $\mathbf{T}^{2+}$**-T** conformer of $\mathbf{3d}^{2+}$ (Figure 4-19, see p. 149). These theoretical results can account for the absence of a domino-redox reaction in the reference compound **3d**.

4-2-6. Study on dynamic motion in solution

Finally, VT-^{1}H NMR analyses were conducted to evaluate the energy barrier for the interconversion among the conformers in **3a** and **3d**. Although the less-populated conformer (**T-F**) with a twisted QD unit was not detected in the spectrum, the energy barrier for the conversion of **F-F** and **T-F** should be smaller than that for exomethylene rotation. Indeed, the ^{1}H NMR spectrum of **3a** at 298 K in CD_2Cl_2 showed a single broad signal of the methoxy protons (δ=3.8 ppm) (Figure 4-13a). Upon cooling to 258 K, the corresponding methoxy signal splits into two sharp signals and their resonances are assigned to a closed-shell species with C_{2v}-symmetry; this observation indicates that rotation of the exomethylene bond of SS-BQD **3a** can be suppressed at lower temperatures. Based on the coalescence temperature T_c (293 K) for the methoxy protons on the aryl groups, the $\Delta G^{\neq}$ value was estimated to be 14.6 kcal/mol, which is sufficiently small for free rotation of the exomethylene bond under ambient conditions. At even lower temperatures, the dynamic motion of major **F-F**$_{anti}$ conformer can be suppressed in solution at 193 K due to the slow ring-flip of the dithiin unit for SS-BQD **3a** (Figure 4-14a). Based on the coalescence of aromatic proton signals, the energy barrier $\Delta G^{\neq}$ of the ring-flip was estimated to be 10.1 kcal/mol, suggesting that the ring-flip motion proceeds more easily than rotation of the exomethylene bond for SS-BQD **3a**. In addition, even at higher temperatures in DMSO-d_6 (Figure 4-14b), very sharp signals were observed, which suggests that the open-shell character is negligible in SS-BQD **3a**.

In contrast to **3a**, no coalescence of the methoxy proton signals was observed even at 393 K in DMSO-d_6 for reference compound **3d** (Figure 4-13b), suggesting that the introduction of a sterically hindered chlorine atom at the 2-position increases the energy barrier, which prevents free rotation of the exomethylene bond. The difference in the rotational dynamics of the exomethylene bonds between **3a** and **3d** revealed by the above VT-^{1}H NMR analyses should be closely related to the results of electrochemical measurements, in which **3a** exhibited a dynamic change in redox properties, unlike **3d**. Thus, based on the easy rotation of the exomethylene bond of **3a**, the interconversion from **F-F**$_{syn}$ and/or **F-F**$_{anti}$ to the **T-F** conformation would be fully feasible in solution, resulting in the first observation of a domino-redox reaction.

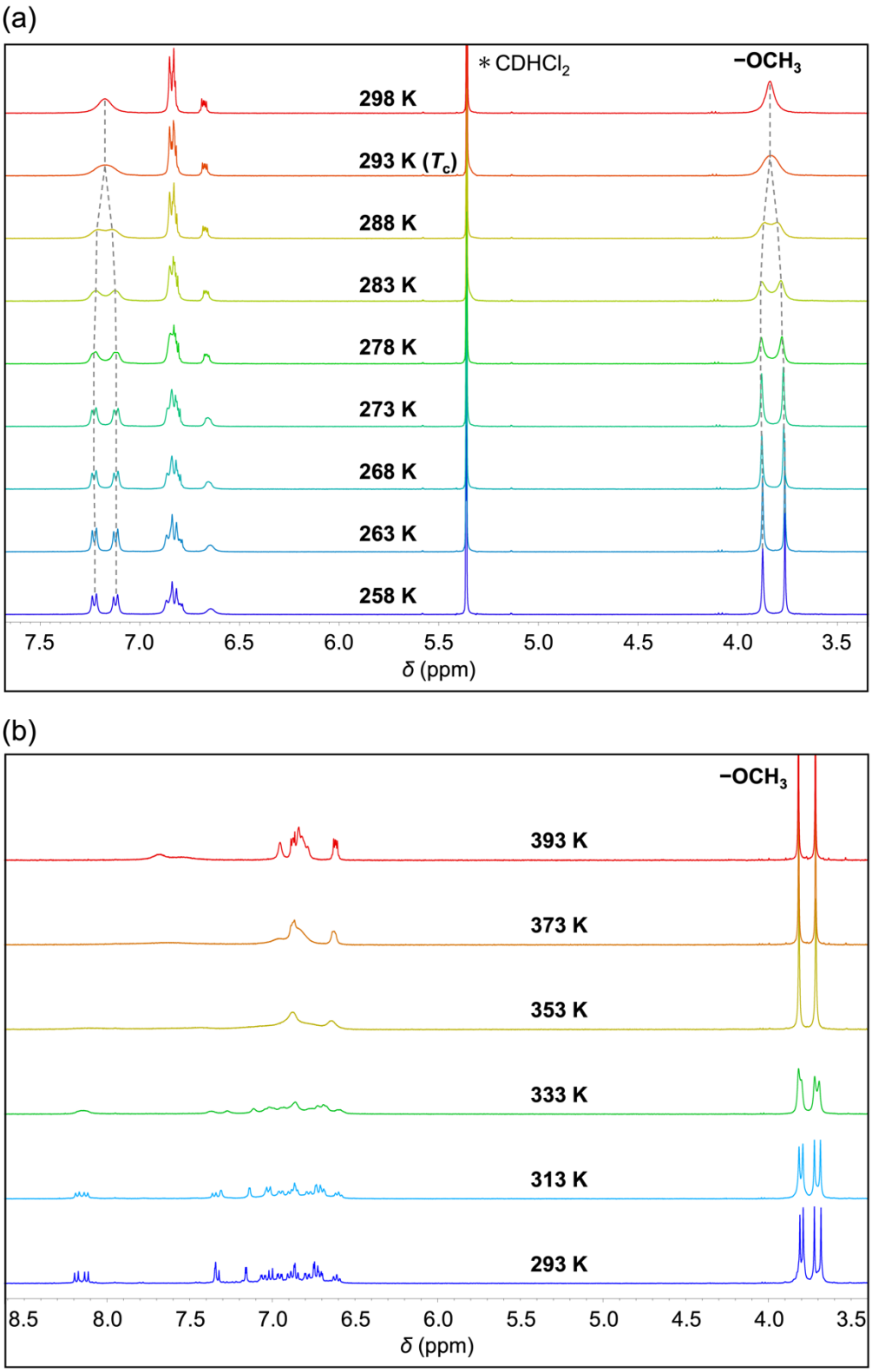

Figure 4-13. VT-^{1}H NMR spectra of (a) **3a** in CD_2Cl_2 (258–298 K) and (b) **3d** in DMSO-d_6 (293–393 K).

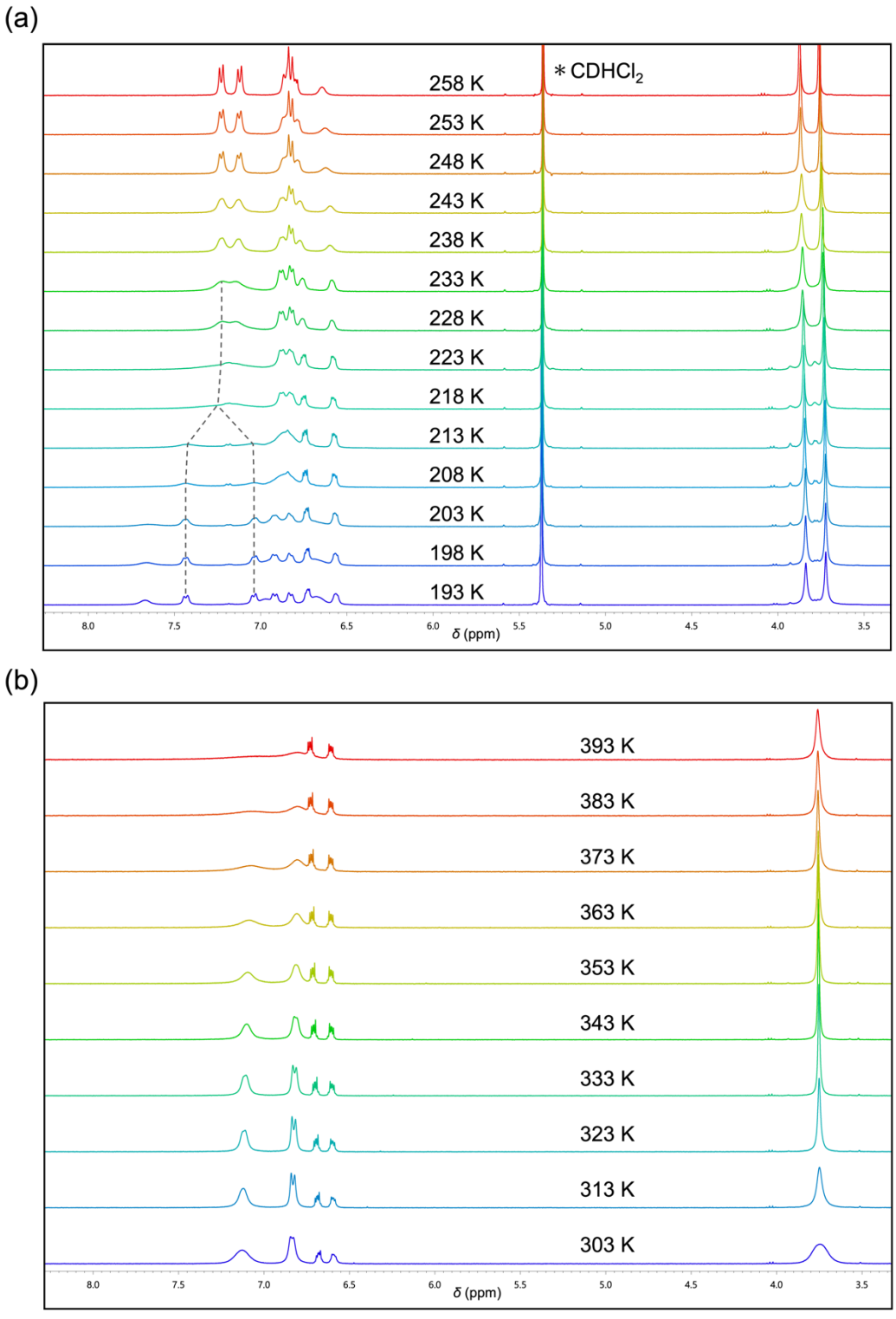

Figure 4-14. VT-^{1}H NMR spectra of (a) **3a** in CD_2Cl_2 (193–258 K) and (b) in DMSO-d_6 (303–393 K).

4-3. Conclusion

In conclusion, the author designed and synthesized the SS-BQD derivative, in which the redox-active QD units are connected by a nonplanar dithiin skeleton, which allows steric repulsion and/or electronic interaction between electrophores for specific conformers.[41] VT-electrochemical measurements showed that **3a** with a flexible structure exhibits temperature-dependent redox properties, unlike *ortho*-substituted **3d**, which is less flexible. VT-^{1}H NMR measurements revealed that **3a** undergoes a smooth change in conformation, and thus the metastable **T-F** conformer can be partially generated with an increase in temperature (activation), and undergoes facile apparent 2e-transfer (trigger). In the resulting dication **3a**$^{2+}$, the steric repulsion and interelectrophore interaction cause a facile change in structure from the as-generated **T**$^{2+}$**-F** conformer to the **T**$^{2+}$**-T** conformer (domino), which facilitates the subsequent oxidation (domino) to **3a**$^{4+}$ of the **T**$^{2+}$**-T**$^{2+}$ conformer. This is the first successful demonstration of the domino-redox reaction of multi-redox systems consisting of the same kind of electrophores. This work presents a new molecular design concept for organic systems containing multiple redox-active units, so that they can exhibit superior charge transport properties based on facile and nearly simultaneous multiple-electron transfer to generate multivalent ionic species.

4-4. Experimental Section

4-4-1. General

All reactions were carried out under an argon atmosphere. All commercially available compounds were used without further purification. Dry MeCN was obtained by distillation from CaH_2 prior to use. Column chromatography was performed on silica gel 60N (KANTO KAGAKU, spherical neutral) of particle size 40-50 μm or Wakogel® 60N (neutral) of particle size 38-100 μm. ^1H and ^{13}C NMR spectra were recorded on a BRUKER Ascend™ 400 (^1H/400 MHz and ^{13}C/100MHz) spectrometer at 296 K unless otherwise indicated. IR spectra were measured on a Shimadzu IRAffinity-1S spectrophotometer using the attenuated total reflection (ATR) mode. Mass spectra were recorded on a JMS-T100GCV spectrometer in FD mode or a Q Exactive Plus in ESI positive mode by Dr. Eri Fukushi and Mr. Yusuke Takata (GS-MS & NMR Laboratory, Research Faculty of Agriculture, Hokkaido University). Melting points were measured on a Yamato MP-21 and are uncorrected. UV/Vis/NIR spectra were recorded on a JASCO V-770 spectrophotometer. Redox potentials (E^{ox} and E^{red}) were measured on a BAS ALS-612EX by cyclic voltammetry in dry CH_2Cl_2 containing 0.1 M Bu_4NBF_4 as a supporting electrolyte. All of the values shown in the text are in E/V vs. SCE measured at the scan rate of 100 mVs^{-1}. Pt electrodes were used as the working (disk) and counter electrodes. The working electrode was polished using a water suspension of aluminum oxide (0.05 μm) before use. DFT calculations were performed with the Gaussian 16W program package.[37] The geometries of the compounds were optimized by using the B3LYP-D3 method in combination with the 6-31G* basis set unless otherwise indicated. A suitable crystal was selected and measured on a Rigaku XtaLAB Synergy (Cu-Kα radiation, λ = 1.54184 Å) with HyPix diffractometer. The crystal was kept at 150 K or 100 K during data collection. Using Olex2,[38] the structure was solved with the SHELXT[39] structure solution program using Intrinsic Phasing and refined with the SHELXL[40] refinement package using Least Squares minimization.

4-4-2. Synthetic procedures

5,7,12,14-Tetrakis(dibromomethylene)-5,7,12,14-tetrahydrodibenzo[*b*,*i*]thianthrene

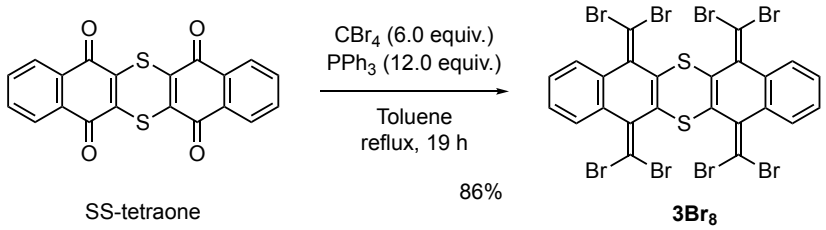

A mixture of CBr_4 (19.9 g, 60.0 mmol) and PPh_3 (31.5 g, 120 mmol) in dry toluene (200 mL) was stirred at 25 °C for 1.5 h. To a suspension was added dibenzo[*b*,*i*]thianthrene-5,7,12,14-tetraone[36] (3.76 g, 10.0 mmol), and the mixture was heated at reflux for 19 h. After cooling to 25 °C, the reaction mixture was diluted with water. Then, the solvent was concentrated under reduced pressure and the resulting residue was extracted with CH_2Cl_2 five times. The combined organic layers were washed with water and brine, and dried over anhydrous $MgSO_4$. After filtration, the solvent was concentrated under reduced pressure. The crude product was purified by column chromatography on silica gel (hexane/CH_2Cl_2 = 4) to give a mixture of **F-F** conformers **3Br$_8$** (8.62 g) as a white solid in 86 % yield.

3Br$_8$; Mp: 272-296 °C (decomp.) ^{1}H NMR (400 MHz, $CDCl_3$): δ/ppm **F-F$_{anti}$**: 7.76 (4H, dd, *J* = 3.3, 5.9 Hz), 7.28 (4H, dd, *J* = 3.3, 5.9 Hz); **F-F$_{syn}$**: 7.64 (4H, dd, *J* = 3.3, 5.8 Hz), 7.10 (4H, dd, *J* = 3.3, 5.9 Hz); ^{13}C NMR (100 MHz, $CDCl_3$): δ/ppm **F-F$_{anti}$**: 142.22, 138.32, 135.85, 127.38, 127.12, 93.40; **F-F$_{syn}$**: 140.98, 139.55, 135.11, 127.17, 126.75, 92.72; IR (ATR): *ν*/cm^{-1} 3056, 2950, 2922, 2856, 1559, 1496, 1450, 1371, 1293, 1260, 1238, 1163, 1150, 1085, 1037, 949, 908, 892, 855, 758, 746, 739, 648, 631, 610, 603, 521; LR-MS (FD) m/z (%):1007.28 (5), 1006.28 (5), 1005.28 (17), 1004.28 (13), 1003.28 (44), 1002.28 (26), 1001.28 (85), 1000.29 (30), 999.28 (bp), 998.28 (24), 997.28 (80), 996.29 (12), 995.29 (40), 994.29 (3), 993.29 (12), 991.29 (M^+, 2); HR-MS (FD) Calcd. for $C_{24}H_8{}^{79}Br_4{}^{81}Br_4S_2$: 999.34535; Found: 999.34700.

5,7,12,14-Tetrakis[bis(4-methoxyphenyl)methylene]-5,7,12,14-tetrahydrodibenzo[*b*,*i*]thianthrene (3a)

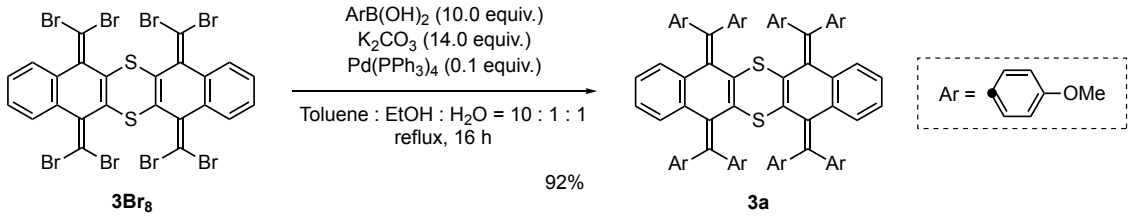

A mixture of 5,7,12,14-tetrakis(dibromomethylene)-5,7,12,14-tetrahydrodibenzo[*b*,*i*]thianthrene **3Br8** (200 mg, 200 μmol), 4-methoxyphenylboronic acid (305 mg, 2.01 mmol), K_2CO_3 (389 mg, 2.81 mmol), and $Pd(PPh_3)_4$ (23.3 mg, 20.1 μmol) in toluene (4.0 mL), EtOH (0.40 mL), and H_2O (0.40 mL) was heated at reflux for 12 h. After cooling to 25 °C, the mixture was diluted with water and extracted with CH_2Cl_2 five times. The combined organic layers were washed with water and brine, and dried over anhydrous Na_2SO_4. After filtration, the solvent was concentrated under reduced pressure. The crude product was purified by column chromatography on silica gel (hexane/EtOAc = 3) to give **3a** (224 mg) as a yellow solid in 92 % yield.

3a; Mp: 288-298 °C (decomp.); ^{1}H NMR (400 MHz, $CDCl_3$): δ/ppm 7.11 (16H, brs), 6.77 (4H, dd, J = 3.2, 5.8 Hz), 6.76 (16H, d, J = 7.6 Hz), 6.65 (4H, dd, J = 3.2, 5.8 Hz), 3.79 (24H, s); ^{13}C NMR (100 MHz, $CDCl_3$, 318 K): δ/ppm 157.68, 138.98, 136.24, 135.71, 134.32, 132.97, 129.69, 126.99, 123.39, 112.89, 54.37; IR (ATR): ν/cm^{-1} 3089, 3059, 3032, 2999, 2952, 2929, 2905, 2833, 1604, 1571, 1505, 1462, 1451, 1440, 1412, 1286, 1240, 1171, 1109, 1031, 848, 817, 762, 744, 691, 587, 550, 518; LR-MS (FD) m/z (%): 1220.39 (10), 1219.39 (23), 1218.39 (53), 1217.38 (92), 1216.38 (M^+, bp); HR-MS (FD) Calcd. for $C_{80}H_{64}O_8S_2$: 1216.40426; Found: 1216.40627; UV/Vis (CH_2Cl_2): λ_{max}/nm (ε/Lmol^{-1}cm^{-1}) 343 (39100), 272 (sh, 39200); UV/Vis (MeCN): λ_{max}/nm (ε/Lmol^{-1}cm^{-1}) 340 (41400).

5,7,12,14-Tetrakis[bis(2-chloro-4-methoxyphenyl)methylene]-5,7,12,14-tetrahydrodibenzo[*b*,*i*]thianthrene (3d)

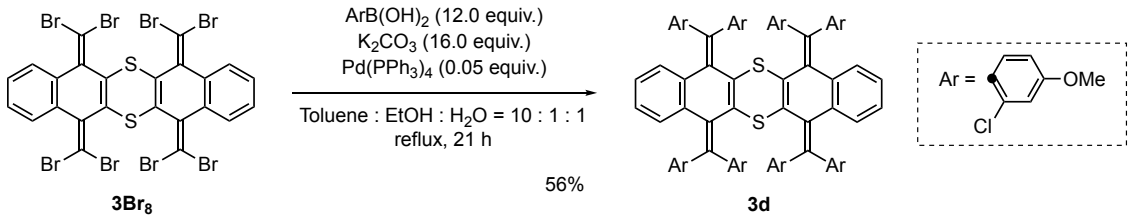

A mixture of 5,7,12,14-tetrakis(dibromomethylene)-5,7,12,14-tetrahydrodibenzo[*b*,*i*]thianthrene **3Br$_8$** (330 mg, 330 μmol), 2-chloro-4-methoxyphenylboronic acid (739 mg, 3.96 mmol), K_2CO_3 (730 mg, 5.28 mmol), and $Pd(PPh_3)_4$ (19.1 mg, 16.5 μmol) in toluene (7.0 mL), EtOH (0.7 mL), and H_2O (0.7 mL) was heated at reflux for 21 h. After cooling to 25 °C, the mixture was diluted with water and extracted with CH_2Cl_2 five times. The combined organic layers were washed with water and brine, and dried over anhydrous Na_2SO_4. After filtration, the solvent was concentrated under reduced pressure. The crude product was purified by column chromatography on silica gel (hexane/EtOAc = 2) to give **3d** (276 mg) as a pale yellow solid in 56 % yield.

3d; Mp: >300 °C; ^{1}H NMR (400 MHz, $CDCl_3$): δ/ppm 8.26 (4H, dd, *J* = 3.2, 8.8 Hz), 7.53 (2H, d, *J* = 8.8 Hz), 7.16 (2H, d, *J* = 8.8 Hz), 7.04 (2H, d, *J* = 2.4 Hz), 6.94 (2H, d, *J* = 2.4 Hz), 6.93 (4H, m, *J* = 7.2 Hz), 6.86 (2H, dd, *J* = 2.4, 8.8 Hz), 6.83 (2H, dd, *J* = 2.4, 8.8 Hz), 6.74 (2H, d, *J* = 2.4 Hz), 6.70-6.61 (6H, m), 6.60-6.49 (4H, m), 3.78 (6H, s), 3.76 (6H, s), 3.70 (6H, s), 3.70 (6H, s); ^{13}C NMR (100 MHz, $CDCl_3$): δ/ppm 159.16, 159.07, 158.99, 158.99, 140.84, 139.96, 139.91, 138.21, 136.02, 135.83, 134.55, 134.40, 134.01, 133.88, 133.65, 133.34, 132.87, 132.77, 132.37, 132.37, 132.26, 131.79, 130.97, 127.27, 126.40, 125.15, 124.99, 124.84, 117.52, 115.11, 114.77, 114.56, 113.35, 112.73, 112.37, 111.73, 55.35, 55.35, 55.21, 55.10; IR (ATR): ν/cm^{-1} 3073, 2999, 2958, 2936, 2904, 2835, 1734, 1599, 1559, 1490, 1459, 1437, 1391, 1285, 1223, 1181, 1036, 924, 841, 811, 790, 760, 718, 684, 669, 610, 594, 555, 481; LR-MS (FD) m/z (%): 1499.96 (6), 1498.96 (11), 1497.97 (19), 1496.97 (30), 1495.97 (46), 1494.97 (56), 1493.97 (84), 1492.97 (74), 1491.97 (bp), 1490.97 (61), 1489.97 (72), 1488.98 (M^+, 21), 1487.97 (24); HR-MS (FD) Calcd. for $C_{80}H_{56}Cl_8O_8S_2$: 1488.09248; Found: 1488.09202; UV/Vis (CH_2Cl_2): λ_{max}/nm (ε/Lmol^{-1}cm^{-1}) 332 (36100), 278 (sh, 39400).

Dibenzo[*b*,*i*]thianthrene-5,7,12,14-tetrayl-tetrakis[bis(4-methoxyphenyl)methylium] tetrakis(hexachloroantimonate) [$3a^{4+}(SbCl_6^-)_4$]

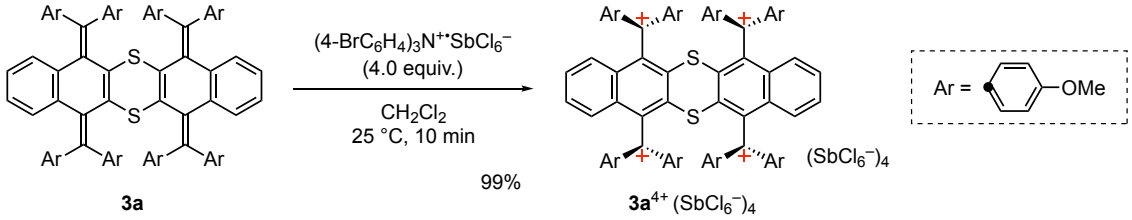

3a **$3a^{4+}$ $(SbCl_6^-)_4$**

To a solution of **3a** (33.7 mg, 27.7 µmol) in dry CH_2Cl_2 (2 mL) was added tris(4-bromophenyl)aminium hexacholoroantimonate (90.4 mg, 111 µmol) at 25 °C to generate a deep red solution, and the mixture was stirred at 25 °C for 10 min. The addition of dry ether led to precipitation of the tetracation salt. The precipitates were washed with dry ether five times, and collected by filtration to give **$3a^{4+}$**$(SbCl_6^-)_4$ (70.2 mg) as a dark red powder in 99% yield.

$3a^{4+}$ $(SbCl_6^-)_2$; Mp: 189-197 °C (decomp.); ^{1}H NMR (400 MHz, CD_3CN): δ/ppm 7.73 (16H, brs), 7.44 (4H, dd, J = 3.2, 6.4 Hz), 7.28 (16H, brs), 7.19 (4H, dd, J = 3.2, 6.4 Hz), 4.19 (24H, s); ^{13}C NMR (100 MHz, CD_3CN): δ/ppm 186.01, 175.07, 144.75, 139.92, 134.01, 133.07, 133.03, 130.55, 127.07, 119.34, 58.93; IR (ATR): ν/cm^{-1} 3100.62, 3019.61, 2984.89, 2941.49, 2847.95, 1608.66, 1572.01, 1506.43, 1447.60, 1373.34, 1307.76, 1274.00, 1186.24, 1149.59, 1132.23, 1071.48, 990.46, 911.38, 887.27, 846.76, 831.33, 799.51, 786.97, 758.04, 619.16, 604.69, 591.19, 567.08, 524.65; LR-MS (ESI) m/z (%): 593.18 (5, $[M-2CH_3]^{2+}$), 418.46 (6), 418.12 (12), 417.79 (22), 417.46 (24), 417.12 (27, $[M+Cl]^{3+}$), 401.46 (6), 401.13 (16), 400.79 (31), 400.46 (33, $[M-CH_3]^{3+}$), 305.10 (6), 304.85 (19), 304.60 (46), 304.35 (87), 304.10 (M^{4+}, bp); HR-MS (ESI) Calcd. for $C_{80}H_{64}O_8S_2$: 304.10052 (M^{4+}); Found: 304.10077; UV/Vis (CH_2Cl_2): λ_{max}/nm (ε/Lmol^{-1}cm^{-1}) 513 (247100), 358 (46000), 296 (sh, 77300), 279 (98200); UV/Vis (MeCN): λ_{max}/nm (ε/Lmol^{-1}cm^{-1}) 500 (205200), 354 (44400), 295 (sh, 77100), 278 (100500).

Dibenzo[*b*,*i*]thianthrene-5,7,12,14-tetrayl-tetrakis[bis(2-chloro-4-methoxyphenyl)methylium] tetrakis(hexachloroantimonate) [$3d^{4+}(SbCl_6^-)_4$]

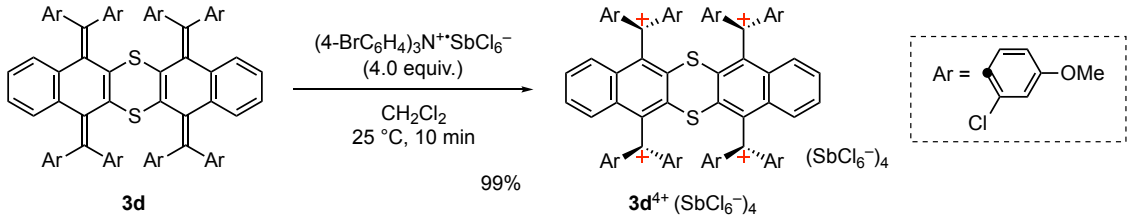

3d **$3d^{4+}$ $(SbCl_6^-)_4$**

To a solution of **3d** (42.4 mg, 28.4 µmol) in dry CH_2Cl_2 (2 mL) was added tris(4-bromophenyl)aminium hexacholoroantimonate (92.1 mg, 114 µmol) at 25 °C to generate a deep violet solution, and the mixture was stirred at 25 °C for 10 min. The addition of dry ether led to precipitation of the tetracation salt. The precipitates were washed with dry ether five times, and collected by filtration to give **$3d^{4+}(SbCl_6^-)_4$** (70.2 mg) as a dark violet powder in 99% yield.

$3d^{4+}(SbCl_6^-)_2$; Mp: 182-187 °C (decomp.); ^{1}H NMR (400 MHz, 1,1,2,2-tetrachloroethane-d_2, 353 K): δ/ppm 7.76 (4H, brs), 7.67-7.27 (24H, m), 7.18 (4H, brs), 4.5 (24H, s); ^{13}C NMR could not be recorded due to its poor solubility.; IR (ATR): ν/cm^{-1} 3092, 3023, 2942, 2843, 1597, 1569, 1521, 1476, 1436, 1358, 1293, 1206, 1176, 1138, 1078, 1030, 1001, 922, 862, 815, 755, 722, 610, 546, 438; LR-MS (ESI) m/z (%): 770.04 (5), 769.54 (6), 769.04 (8), 768.54 (7), 768.04 (10), 767.54 (6), 767.04 (7), 757.01 (5), 756.52 (5), 756.02 (6), 755.53 (5), 755.03 (6), 754.54 (6), 754.04 (7), 748.04 (5), 747.54 (6), 747.04 (9), 746.54 (8), 746.04 (11), 745.55 (6), 745.04 (8) , 744.05 (4, M^{2+}), 740.03 (5), 739.53 (8), 739.03 (7), 738.53 (9), 738.03 (5), 737.53 (8), 734.52 (5), 734.02 (10), 733.52 (15), 733.02 (29), 732.52 (34), 732.02 (51), 731.52 (46), 731.02 (60), 730.52 (37), 730.02 (48), 729.52 (13), 729.02 (15, $[M-2CH_3]^{2+}$), 509.68 (6), 509.02 (6), 508.35 (5), 498.69 (6), 498.36 (9), 498.03 (12), 497.70 (12), 497.36 (14), 497.03 (10), 496.70 (11), 496.36 (5), 496.03 (4, M^{3+}), 494.69 (7), 494.35 (14), 494.02 (27), 493.69 (43), 493.35 (53), 493.02 (78), 492.69 (70), 492.35 (bp), 492.02 (59), 491.69 (71), 491.36 (21), 491.02 (22, $[M-CH_3]^{3+}$), 374.52 (7), 374.27 (9), 374.02 (17), 373.77 (21), 373.52 (31), 373.27 (27), 373.02 (41), 372.77 (20), 372.52 (28), 372.27 (10), 372.02 (M^{4+}, 14); HR-MS (ESI) Calcd. for $C_{80}H_{56}Cl_8O_8S_2$: 372.02257 (M^{4+}); Found: 372.02249; UV/Vis/NIR (CH_2Cl_2): λ_{max}/nm (ε/Lmol^{-1}cm^{-1}) 725 (sh, 12800), 567 (138900), 378 (46900).

Reduction of tetracation salt **3a**$^{4+}$(SbCl$_6^-$)$_4$ to **3a**:

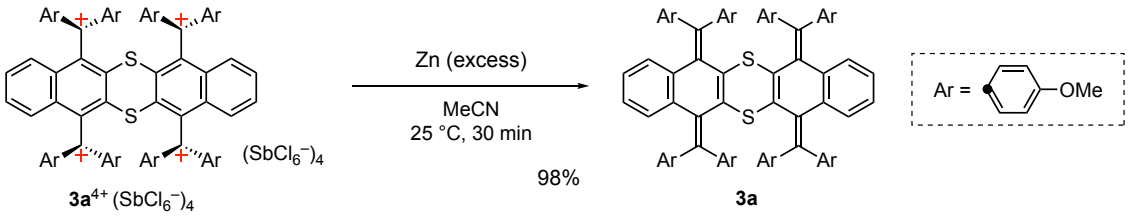

3a^{4+} (SbCl$_6^-$)$_4$ **3a**

To a solution of **3a**$^{4+}$(SbCl$_6^-$)$_4$ (22.9 mg, 8.96 μmol) in dry MeCN (1.0 mL) was added activated zinc powder (58.6 mg, 896 μmol). The mixture was stirred at 25 °C for 30 min, and then diluted with water. The whole mixture was extracted with CH_2Cl_2 five times. The combined organic layers were washed with water and brine, and dried over anhydrous Na_2SO_4. After filtration through silica gel, the solvent was concentrated under reduced pressure to give **3a** (10.7 mg) as a yellow solid in 98% yield.

Reduction of tetracation salt **3d**$^{4+}$(SbCl$_6^-$)$_4$ to **3d**:

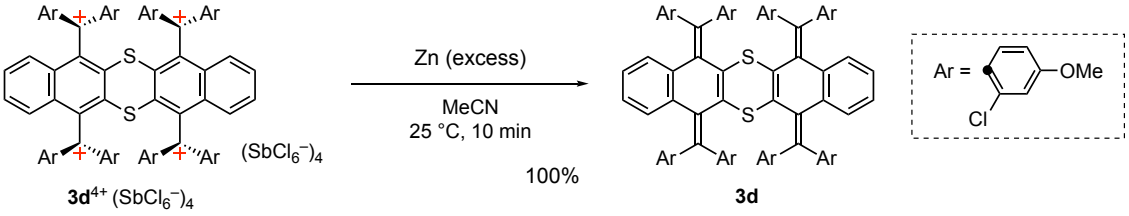

3d^{4+} (SbCl$_6^-$)$_4$ **3d**

To a solution of **3d**$^{4+}$(SbCl$_6^-$)$_4$ (39.2 mg, 13.8 μmol) in dry MeCN (1.0 mL) was added activated zinc powder (90.6 mg, 139 μmol). The mixture was stirred at 25 °C for 10 min, and then diluted with water. The whole mixture was extracted with CH_2Cl_2 five times. The combined organic layers were washed with water and brine, and dried over anhydrous Na_2SO_4. After filtration through silica gel, the solvent was concentrated under reduced pressure to give **3d** (20.7 mg) as a pale yellow solid in 100% yield.

4-4-3. Crystal data

Compounds	**3a (F-F*syn*)**	**3a (F-F*anti*)**	**3d (F-F*syn*)**[a]	**3a**$^{4+}$$(SbCl_6^-)_4$ [a]	**3Br8 (F-F*syn*)**
Solvent system	benzene/hexane	$CHCl_3$/hexane	CH_2Cl_2/hexane	CH_2Cl_2/1,4-dioxane	CH_2Cl_2/Et_2O
Empirical formula	$C_{80}H_{64}O_8S_2$• $3C_6H_6$	$C_{80}H_{64}O_8S_2$• $CHCl_3$	$C_{80}H_{56}Cl_8O_8S_2$• $4CH_2Cl_2$	$C_{80}H_{64}O_8S_2Cl_{24}Sb_4$	$C_{24}H_8S_2Br_8$• $CHCl_3$
Formula weight	1451.75	1336.80	1832.67	2555.23	1119.07
Temperature/K	150	150	150	100	150
Crystal system	triclinic	triclinic	triclinic	monoclinic	triclinic
Space group	*P*-1	*P*-1	*P*-1	*C*2/*c*	*P*-1
a/Å	16.37614(16)	11.18890(15)	13.39047(10)	35.5458(5)	9.21584(10)
b/Å	22.6038(2)	16.9660(3)	18.95474(14)	15.34011(18)	9.73646(11)
c/Å	23.8053(2)	18.2902(3)	18.99515(15)	47.7807(7)	21.2959(2)
α/°	111.0908(9)	99.7646(14)	93.3536(6)	90	79.1968(9)
β/°	100.5175(8)	93.6116(12)	110.3136(7)	105.7823(15)	88.9340(8)
γ/°	99.3229(8)	99.9493(13)	105.9748(7)	90	64.2521(11)
Volume/Å^3	7830.47(14)	3355.03(9)	4282.85(6)	25071.5(6)	1686.38(3)
Z	4	2	2	8	2
ρ_{calc} g/cm^3	1.231	1.323	1.421	1.354	2.204
μ/mm^{-1}	1.085	2.29	5.595	12.105	14.862
Color and shape	colorless block	light yellow plate	light yellow plate	dark red block	colorless plate
Crystal size/mm^3	0.107 × 0.08 × 0.078	0.377 × 0.104 × 0.049	0.532 × 0.097 × 0.044	0.15 × 0.15 × 0.06	0.62 × 0.06 × 0.02
Reflections collected	60221	41647	68247	122653	17227
R_{int}	R_{int} = 0.0501	Rint = 0.0217	R_{int} = 0.0470	R_{int} = 0.0783	R_{int} = 0.0540
Data/restraints/ parameters	60221/12/1993	13576/207/929	17442/2/1017	25615/785/1436	6613/0/344
GOF	1.036	1.035	1.038	1.045	1.073
R_1 [I>=2σ(I)]	0.0485	0.0554	0.0544	0.0989	0.0460
wR_2 [I>=2σ(I)]	0.1263	0.1633	0.1543	0.2733	0.1322
R_1 [all data]	0.0651	0.0585	0.0593	0.1190	0.0485
wR_2 [all data]	0.1365	0.1666	0.1582	0.2914	0.1348
Largest diff.peak /hole/e Å^{-3}	0.30/-0.28	1.06/-1.27	1.54/-0.91	1.17/-1.17	1.33/-1.12
Solvent mask	None	None	Used for the analysis	Used for the analysis	Used for the analysis
CCDC No.	2288937	2288938	2288939	2288940	2288941

[a] Some B-level alerts were found in the checkCIF file.

Authors response: These alerts are a consequence of disorders in chlorine atoms and counterions for **3d** (**F-F*syn***) and **3a**$^{4+}$$(SbCl_6^-)_4$, respectively.

4-4-4. (TD-)DFT calculations at the B3LYP-D3/6-31G* level

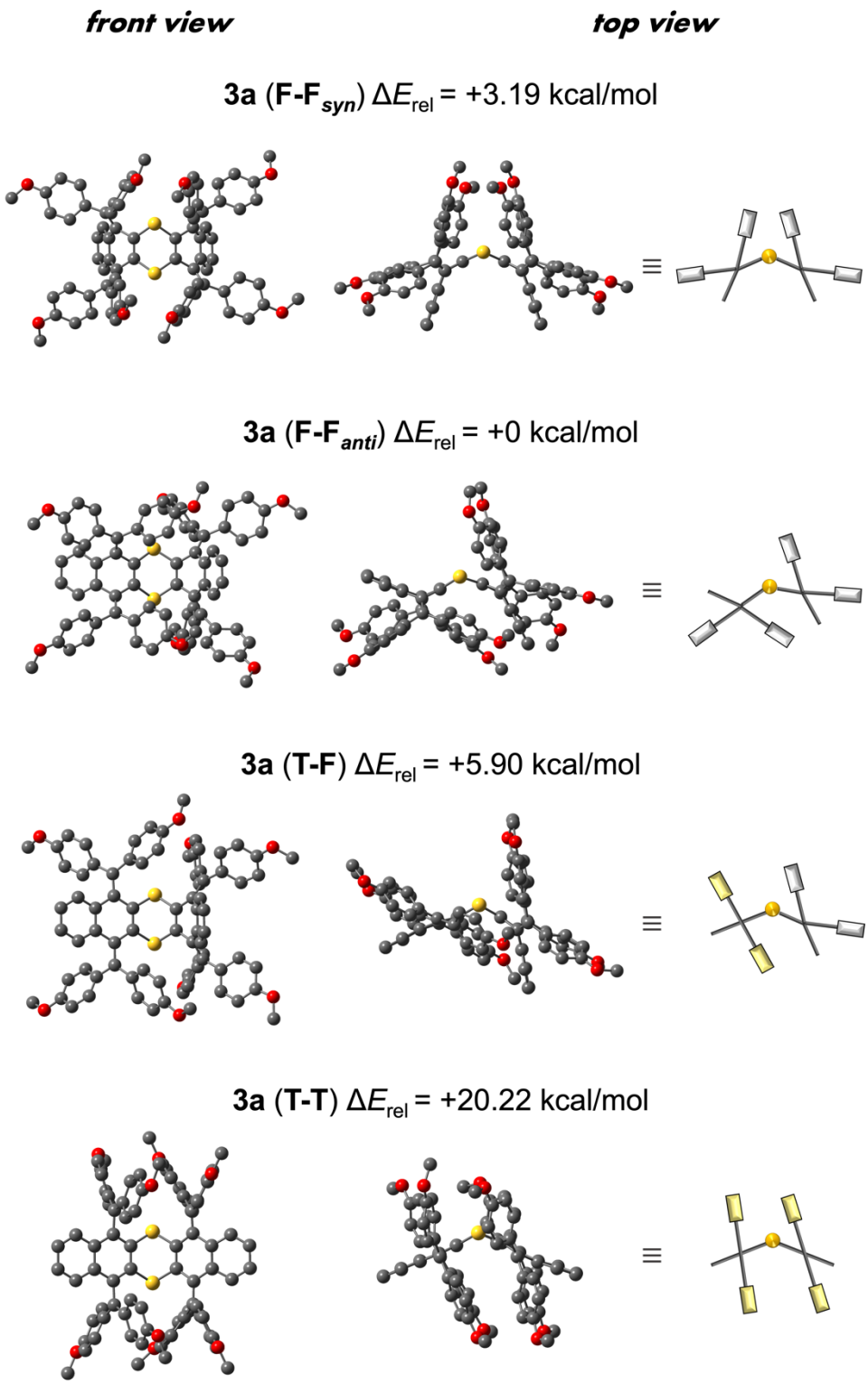

Figure 4-15. Optimized structures and their relative energies of possible isomers for neutral donor **3a** obtained by DFT calculations at the B3LYP-D3/6-31G* level (0 kcal/mol for **F-F**$_{anti}$ form). Hydrogen atoms are omitted for clarity. [**3a**: Ar = 4-MeOC$_6$H$_4$]

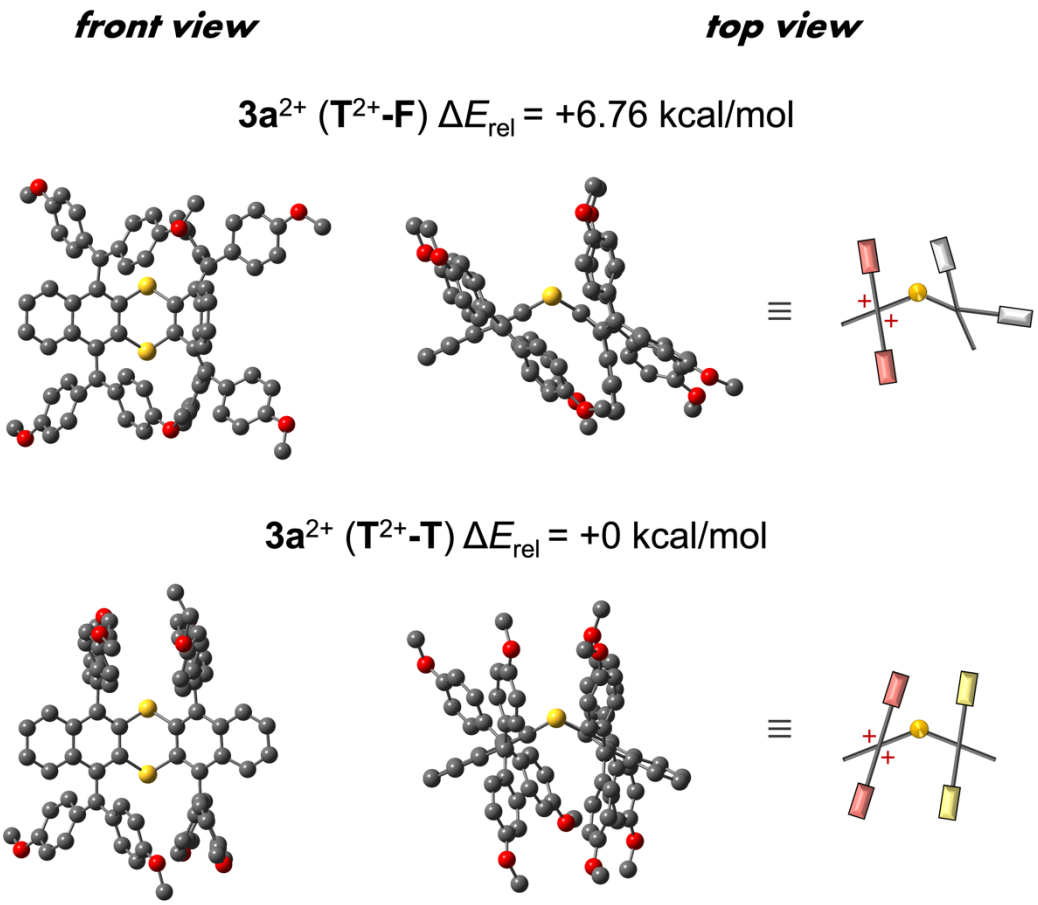

Figure 4-16. Optimized structures and their relative energies of possible isomers for dication **3a**$^{2+}$ obtained by DFT calculations at the B3LYP-D3/6-31G* level (0 kcal/mol for **T**$^{2+}$**-T** form). Hydrogen atoms are omitted for clarity. [**3a**$^{2+}$: Ar = 4-MeOC$_6$H$_4$]

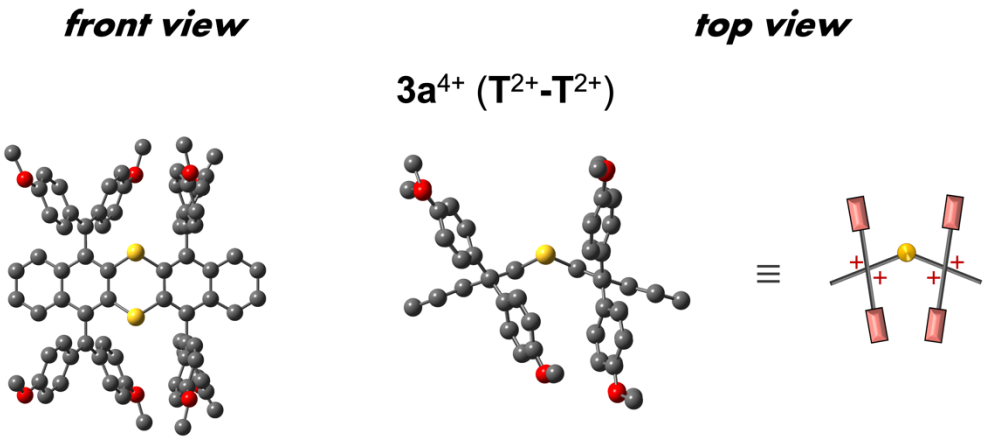

Figure 4-17. Optimized structure of tetracation **3a**$^{4+}$ obtained by DFT calculations at the B3LYP-D3/6-31G* level. Hydrogen atoms are omitted for clarity. [**3a**$^{4+}$: Ar = 4-MeOC$_6$H$_4$]

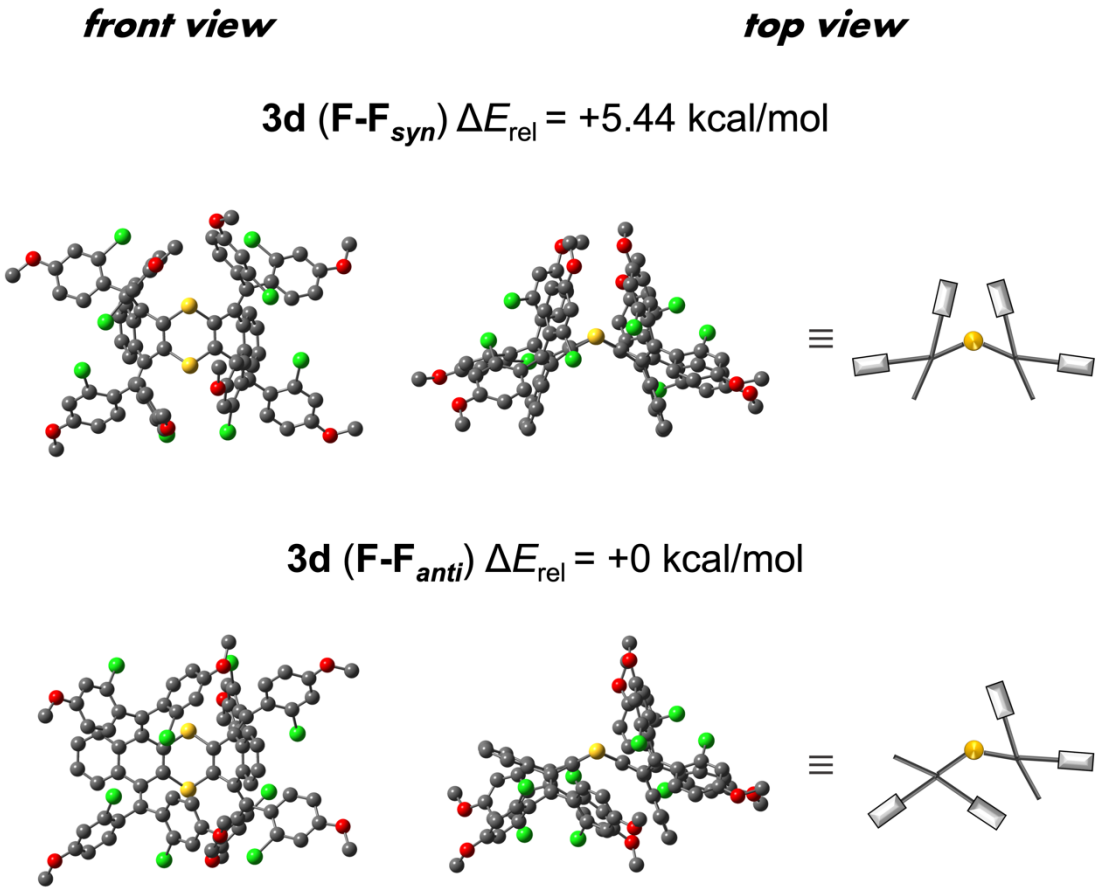

Figure 4-18. Optimized structures and their relative energies of possible isomers for neutral donor **3d** obtained by DFT calculations at the B3LYP-D3/6-31G* level (0 kcal/mol for **F-F**$_{anti}$ form). Hydrogen atoms are omitted for clarity. [**3d**: Ar = 2-Cl-4-MeOC$_6$H$_3$] In the cases of **T-F** and **T-T** forms, energy-minimized structures were not obtained probably due to the large steric strain by *ortho*-chlorine atoms.

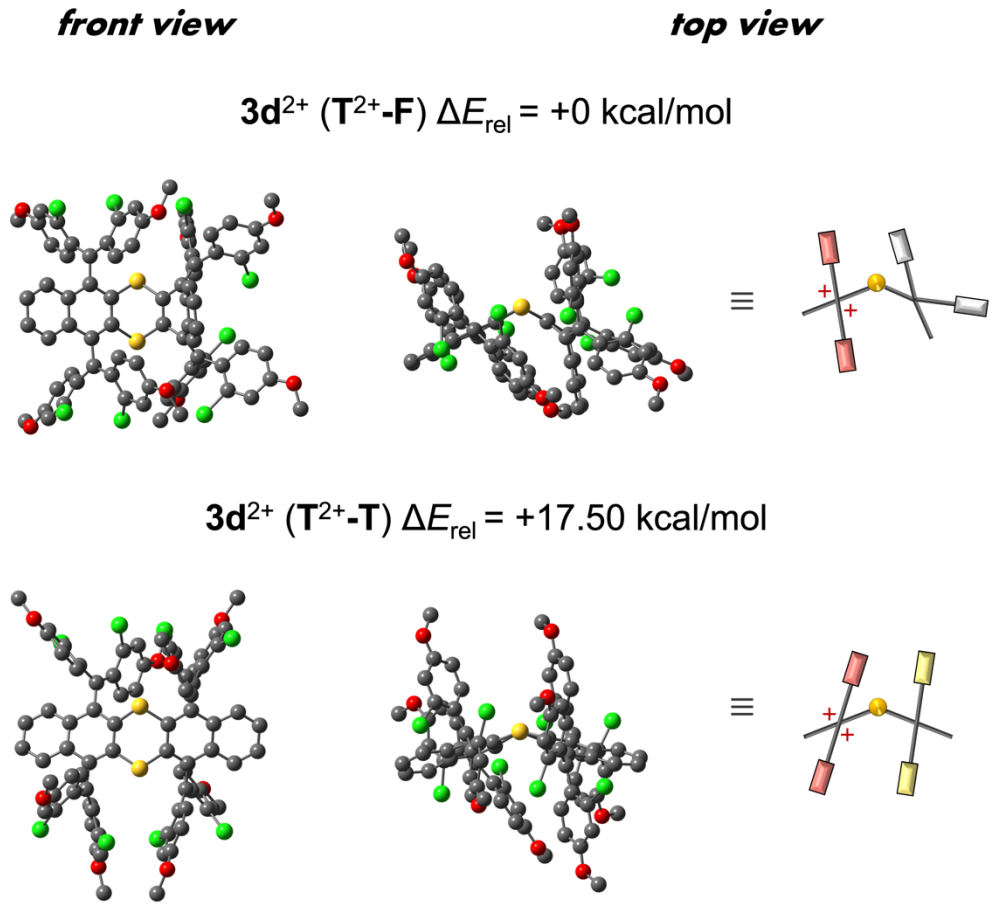

Figure 4-19. Optimized structures and their relative energies of possible isomers for dication **3d**$^{2+}$ obtained by DFT calculations at the B3LYP-D3/6-31G* level (0 kcal/mol for **T**$^{2+}$**-F** form). Hydrogen atoms are omitted for clarity. [**3d**$^{2+}$: Ar = 2-Cl-4-MeOC$_6$H$_3$]

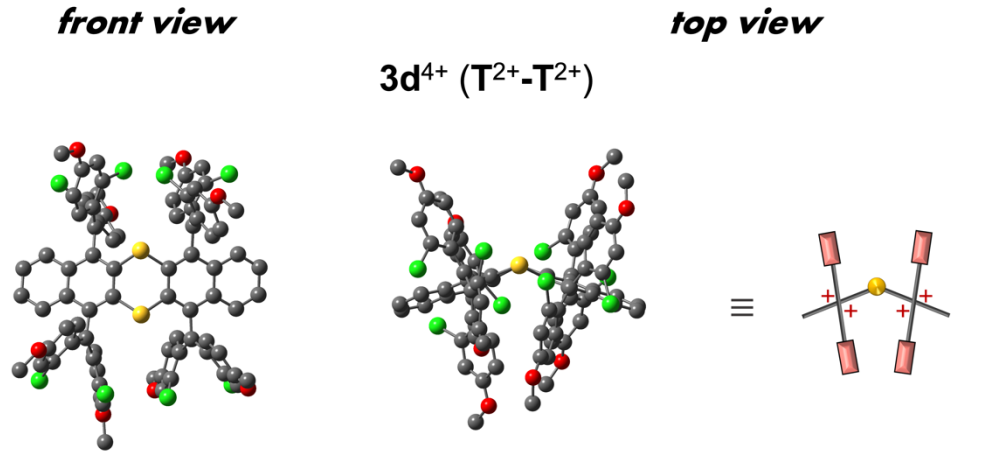

Figure 4-20. Optimized structure of tetracation **3d**$^{4+}$ obtained by DFT calculations at the B3LYP-D3/6-31G* level. Hydrogen atoms are omitted for clarity. [**3d**$^{4+}$: Ar = 2-Cl-4-MeOC$_6$H$_3$]

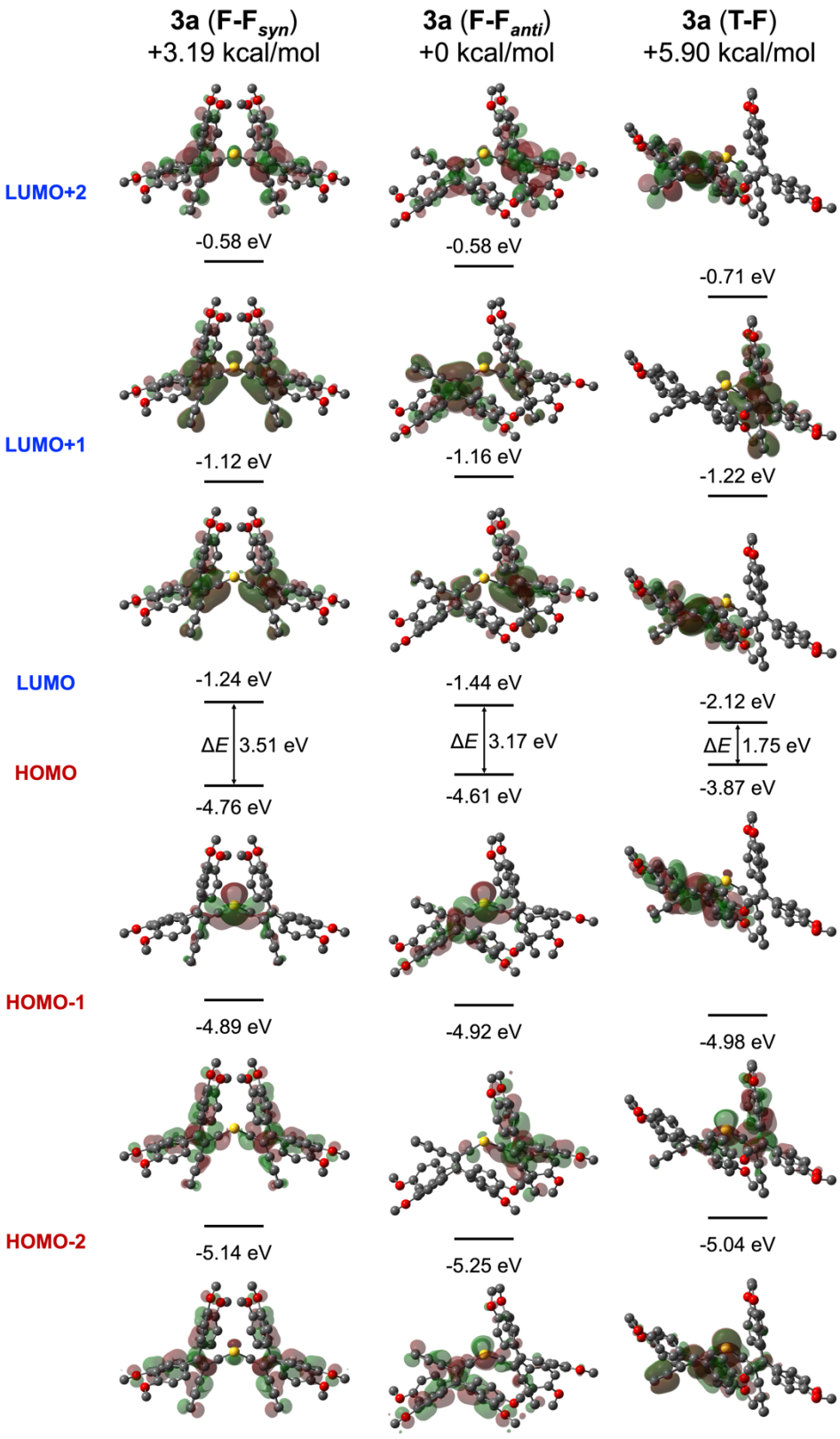

Figure 4-21. HOMO and LUMO levels calculated by the DFT method (B3LYP-D3/6-31G*) based on the optimized structures of possible isomers for neutral donor **3a**. [**3a**: Ar= 4-MeOC$_6$H$_4$]

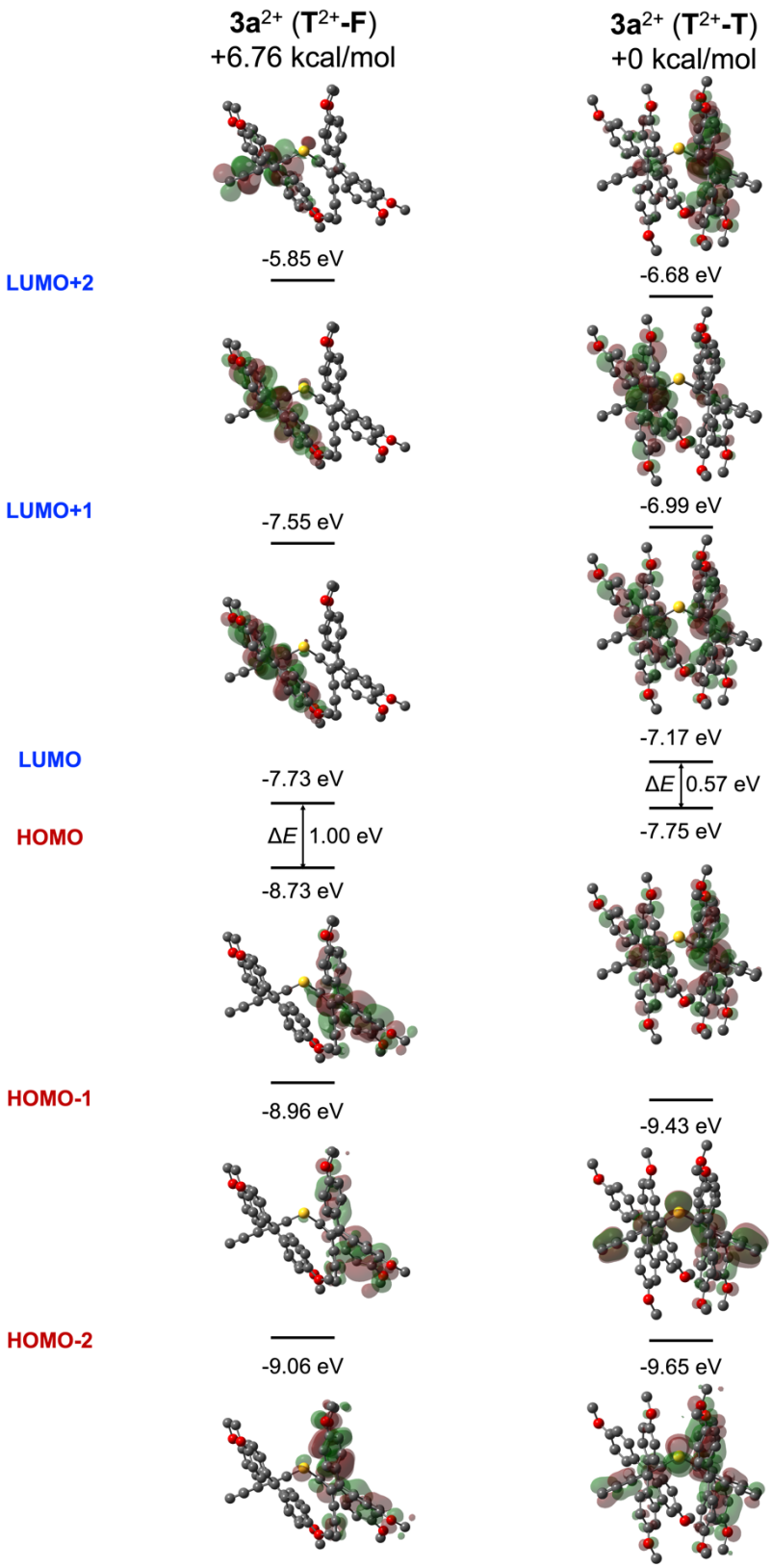

Figure 4-22. HOMO and LUMO levels calculated by the DFT method (B3LYP-D3/6-31G*) based on the optimized structures of possible isomers for dication **3a**$^{2+}$. [**3a**$^{2+}$: Ar= 4-MeOC$_6$H$_4$]

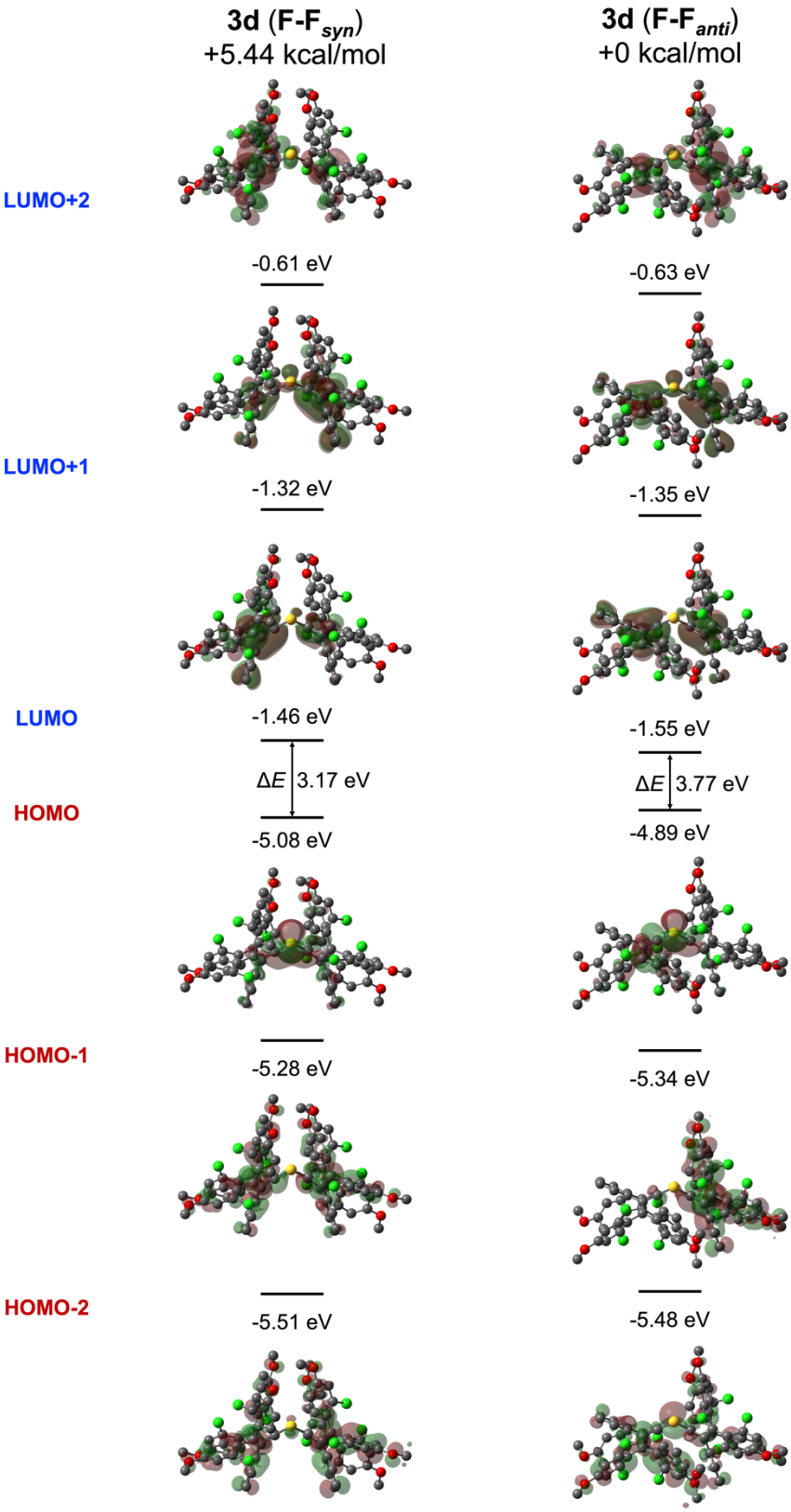

Figure 4-23. HOMO and LUMO levels calculated by the DFT method (B3LYP-D3/6-31G*) based on the optimized structures of possible isomers for neutral donor **3d**. [**3d**: Ar= 2-Cl-4-MeOC$_6$H$_3$]

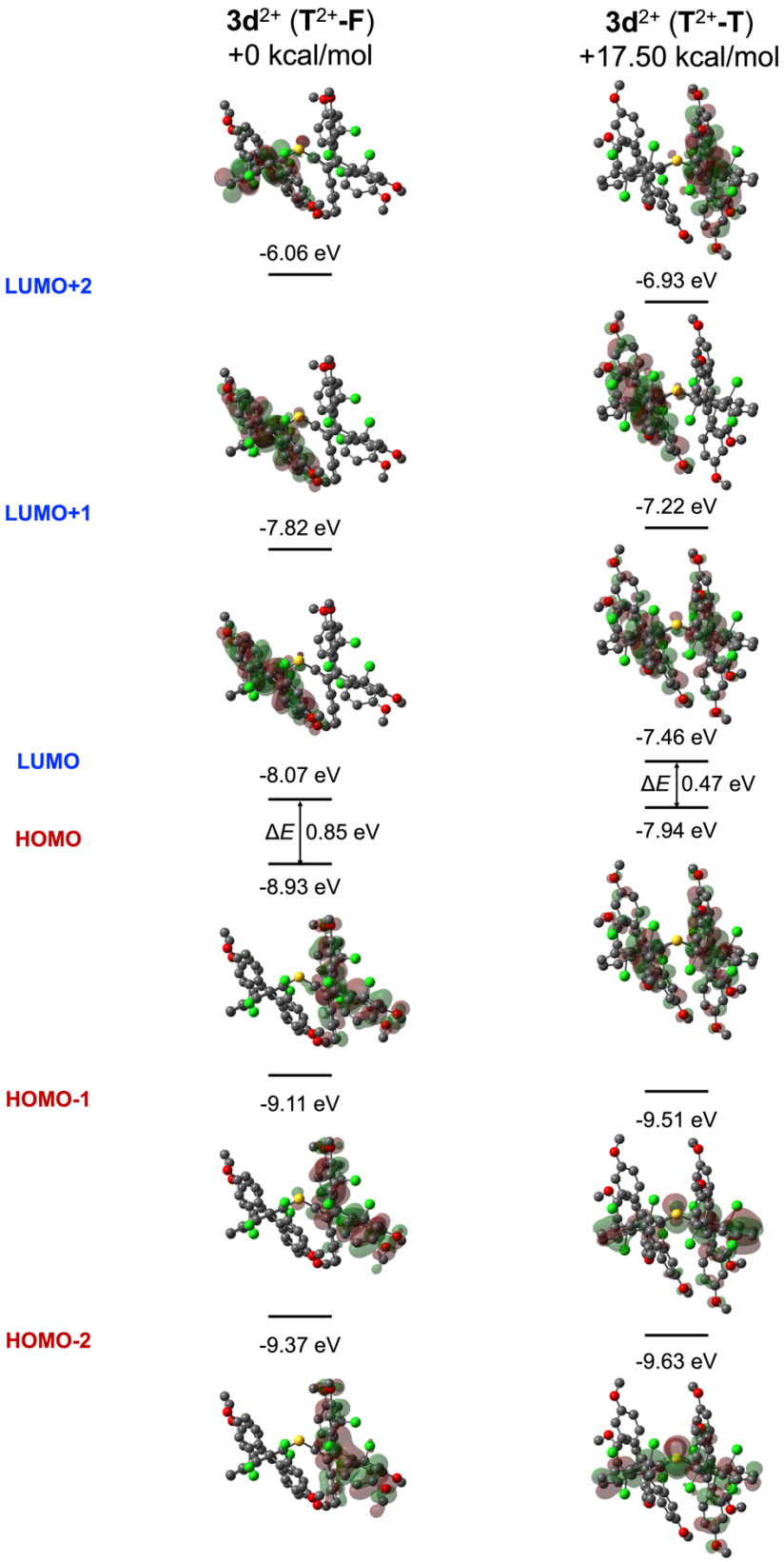

Figure 4-24. HOMO and LUMO levels calculated by the DFT method (B3LYP-D3/6-31G*) based on the optimized structures of possible isomers for dication **3d**$^{2+}$. [**3d**$^{2+}$: Ar= 2-Cl-4-MeOC$_6$H$_3$]

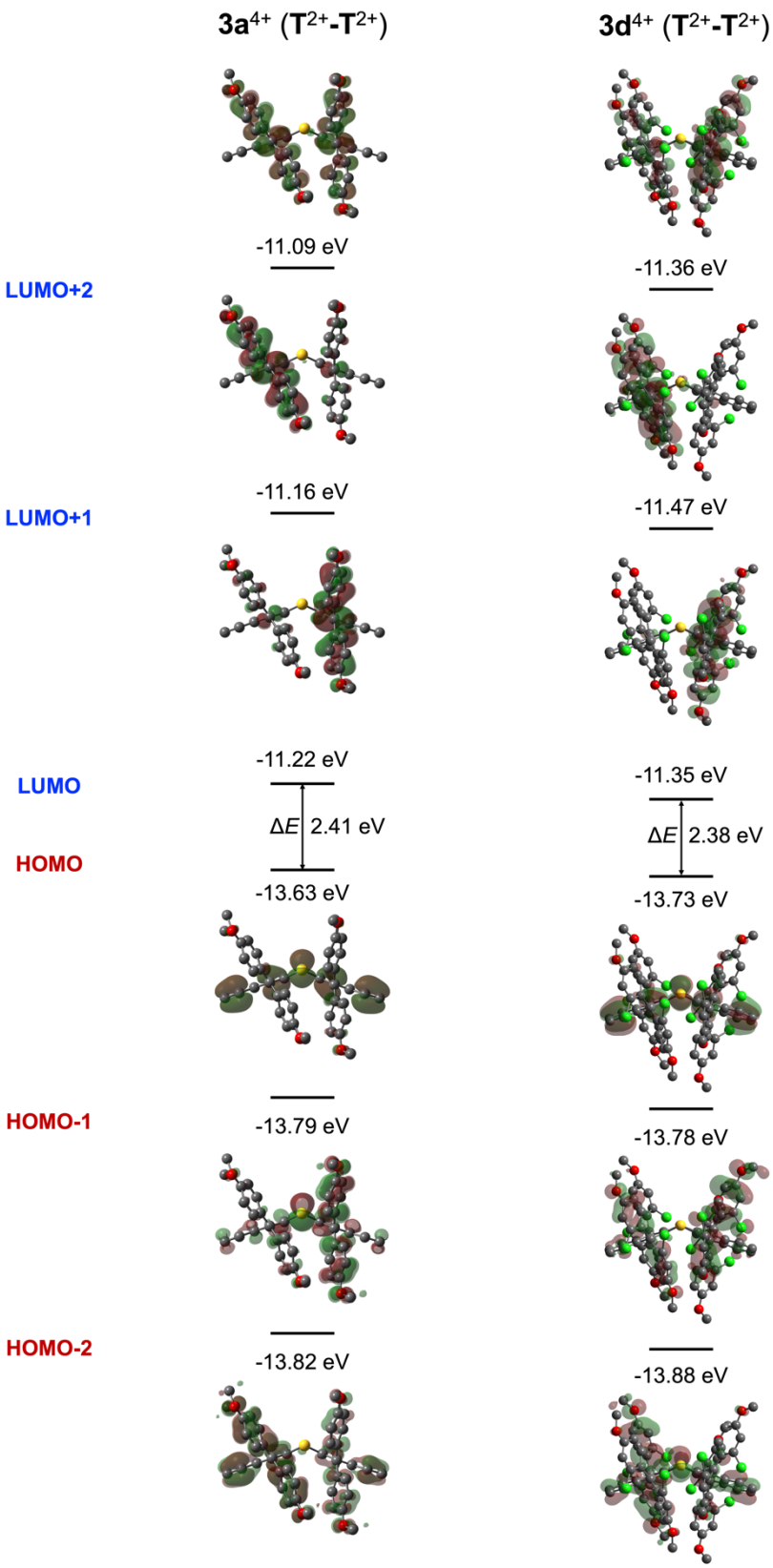

Figure 4-25. HOMO and LUMO levels calculated by the DFT method (B3LYP-D3/6-31G*) based on the optimized structures of tetracations **3a**$^{4+}$ and **3d**$^{4+}$. [**3a**$^{4+}$: Ar= 4-MeOC$_6$H$_4$, **3d**$^{4+}$: Ar= 2-Cl-4-MeOC$_6$H$_3$]

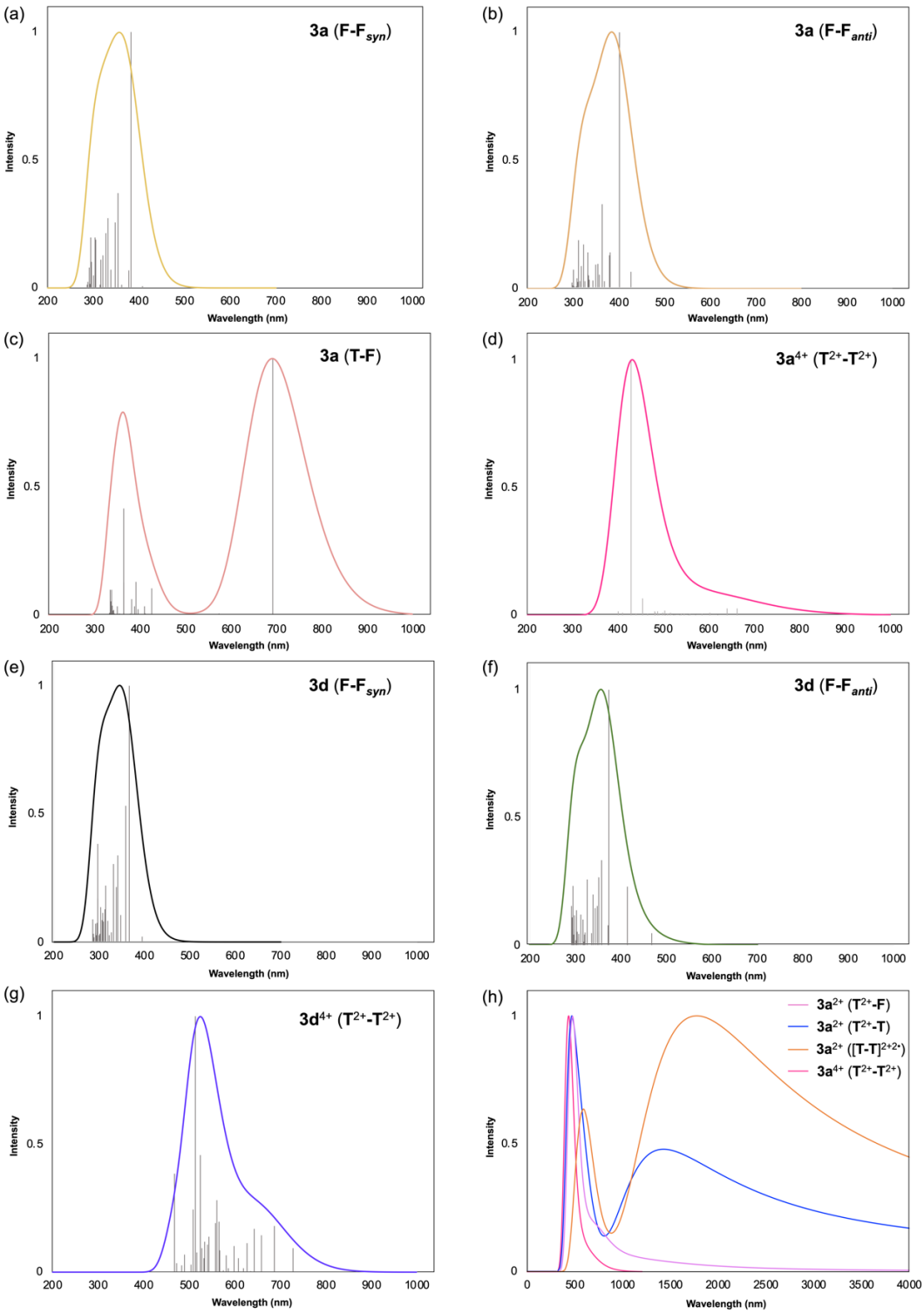

Figure 4-26. Simulated UV/Vis/NIR spectra by TD-DFT calculations (B3LYP-D3/6-31G*) for (a) **3a** (**F-F**$_{syn}$), (b) **3a** (**F-F**$_{anti}$), (c) **3a** (**T-F**), (d) **3a**$^{4+}$ (**T**$^{2+}$-**T**$^{2+}$), (e) **3d** (**F-F**$_{syn}$), (f) **3d** (**F-F**$_{anti}$), (g) **3d**$^{4+}$ (**T**$^{2+}$-**T**$^{2+}$), and (h) **3a**$^{2+}$ (**T**$^{2+}$-**F**), **3a**$^{2+}$ (**T**$^{2+}$-**T**, closed-shell), **3a**$^{2+}$ ([**T-T**]$^{2+2\bullet}$, open-shell, singlet), and **3a**$^{4+}$ (**T**$^{2+}$-**T**$^{2+}$). [**3a**: Ar= 4-MeOC$_6$H$_4$, **3d**: Ar= 2-Cl-4-MeOC$_6$H$_3$] For detailed information on excitation energies and oscillator strengths, see Ref. [62].

4-5. References

[1] L. F. Tietze, *Chem. Rev.* **1996**, *96*, 115–136.

[2] L. F. Tietze, *Domino Reactions : Concepts for Efficient Organic Synthesis.*, Wiley, **2014**.

[3] K. C. Nicolaou, T. Montagnon, S. A. Snyder, *Chem. Commun.* **2003**, *3*, 551–564.

[4] K. C. Nicolaou, D. J. Edmonds, P. G. Bulger, *Angew. Chem. Int. Ed.* **2006**, *45*, 7134–7186.

[5] D. Enders, C. Grondal, M. R. M. Hüttl, *Angew. Chem. Int. Ed.* **2007**, *46*, 1570–1581.

[6] A. Grossmann, D. Enders, *Angew. Chem. Int. Ed.* **2012**, *51*, 314–325.

[7] H. Pellissier, *Adv. Synth. Catal.* **2012**, *354*, 237–294.

[8] R. Westphal, E. Venturini Filho, F. Medici, M. Benaglia, S. J. Greco, *Synthesis (Stuttg).* **2022**, *54*, 2927–2975.

[9] R. W. Armstrong, A. P. Combs, P. A. Tempest, S. D. Brown, T. A. Keating, *Acc. Chem. Res.* **1996**, *29*, 123–131.

[10] A. Dömling, I. Ugi, *Angew. Chem.* **2000**, *39*, 3168–3210.

[11] A. Dömling, W. Wang, K. Wang, *Chem. Rev.* **2012**, *112*, 3083–3135.

[12] R. P. Herrera, E. Marqués-López, Eds. , *Multicomponent Reactions: Concepts and Applications for Design and Synthesis*, John Wiley & Sons, Inc, Hoboken, NJ, **2015**.

[13] R. O. Rocha, M. O. Rodrigues, B. A. D. Neto, *ACS Omega* **2020**, *5*, 972–979.

[14] S. Morita, T. Yoshimura, J. Matsuo, *Green Chem.* **2021**, *23*, 1160–1164.

[15] K. Fujii, Y. Nagashima, T. Shimokawa, J. Kanazawa, H. Sugiyama, K. Masutomi, H. Uekusa, M. Uchiyama, K. Tanaka, *Nat. Synth.* **2022**, *1*, 365–375.

[16] T. Yokozawa, A. Yokoyama, *Polym. J.* **2004**, *36*, 65–83.

[17] M. Ouchi, T. Terashima, M. Sawamoto, *Chem. Rev.* **2009**, *109*, 4963–5050.

[18] J. Kang, D. Miyajima, T. Mori, Y. Inoue, Y. Itoh, T. Aida, *Science (80-.).* **2015**, *347*, 646–651.

[19] R. B. Grubbs, R. H. Grubbs, *Macromolecules* **2017**, *50*, 6979–6997.

[20] M. Schnitte, A. Staiger, L. A. Casper, S. Mecking, *Nat. Commun.* **2019**, *10*, 2592.

[21] Y.-N. Zhou, J.-J. Li, T.-T. Wang, Y.-Y. Wu, Z.-H. Luo, *Prog. Polym. Sci.* **2022**, *130*, 101555.

[22] H. Ito, M. Muromoto, S. Kurenuma, S. Ishizaka, N. Kitamura, H. Sato, T. Seki, *Nat. Commun.* **2013**, *4*, 2009.

[23] T. Seki, K. Sakurada, H. Ito, *Angew. Chem. Int. Ed.* **2013**, *52*, 12828–12832.

[24] S.-H. Lo, L. Feng, K. Tan, Z. Huang, S. Yuan, K.-Y. Wang, B.-H. Li, W.-L. Liu, G. S. Day, S. Tao, C.-C. Yang, T.-T. Luo, C.-H. Lin, S.-L. Wang, S. J. L. Billinge, K.-L. Lu, Y. J. Chabal, X. Zou, H.-C. Zhou, *Nat. Chem.* **2020**, *12*, 90–97.

[25] Y. Hino, S. Hayashi, *Chem. – A Eur. J.* **2021**, *27*, 17595–17600.

[26] Q. Gao, J. Ai, S. Tang, M. Li, Y. Chen, J. Huang, H. Tong, L. Xu, L. Xu, H. Tanaka, P. Tan, *Nat. Mater.* **2021**, *20*, 1431–1439.

[27] M. Itaya, K. Fujita, A. Kuroki, K. Tsuge, *Nat. Methods* **2008**, *5*, 41–43.

[28] N. Ohtani, M. Hasegawa, M. Sato, M. Tomita, S. Kaneko, M. Itaya, *Biotechnol. J.* **2012**, *7*, 867–876.

[29] M. Juhas, J. W. Ajioka, *Crit. Rev. Biotechnol.* **2017**, *37*, 277–286.
[30] K. Deuchert, S. Hünig, *Angew. Chem. Int. Ed. Engl.* **1978**, *17*, 875–886.
[31] T. Nishinaga, *Organic Redox Systems*, John Wiley & Sons, Inc, Hoboken, NJ, **2015**.
[32] G. Kwon, S. Lee, J. Hwang, H.-S. Shim, B. Lee, M. H. Lee, Y. Ko, S.-K. Jung, K. Ku, J. Hong, K. Kang, *Joule* **2018**, *2*, 1771–1782.
[33] J. Shukla, V. P. Singh, P. Mukhopadhyay, *ChemistryOpen* **2020**, *9*, 304–324.
[34] H. Ueda, S. Yoshimoto, *Chem. Rec.* **2021**, *21*, 2411–2429.
[35] D. H. Evans, *Chem. Rev.* **2008**, *108*, 2113–2144.
[36] Y. Ishigaki, K. Sugawara, T. Tadokoro, Y. Hayashi, T. Harimoto, T. Suzuki, *Chem. Commun.* **2021**, *57*, 7201–7214.
[37] K. Katsuma, Y. Shirota, *Adv. Mater.* **1998**, *10*, 223–226.
[38] M. Kivala, C. Boudon, J.-P. Gisselbrecht, P. Seiler, M. Gross, F. Diederich, *Angew. Chem. Int. Ed.* **2007**, *46*, 6357–6360.
[39] J. C. Barnes, A. C. Fahrenbach, D. Cao, S. M. Dyar, M. Frasconi, M. A. Giesener, D. Benítez, E. Tkatchouk, O. Chernyashevskyy, W. H. Shin, H. Li, S. Sampath, C. L. Stern, A. A. Sarjeant, K. J. Hartlieb, Z. Liu, R. Carmieli, Y. Y. Botros, J. W. Choi, A. M. Z. Slawin, J. B. Ketterson, M. R. Wasielewski, W. A. Goddard, J. F. Stoddart, *Science (80-.).* **2013**, *339*, 429–433.
[40] G. Zhang, V. Lami, F. Rominger, Y. Vaynzof, M. Mastalerz, *Angew. Chem. Int. Ed.* **2016**, *55*, 3977–3981.
[41] S. Dong, T. Y. Gopalakrishna, Y. Han, H. Phan, T. Tao, Y. Ni, G. Liu, C. Chi, *J. Am. Chem. Soc.* **2019**, *141*, 62–66.
[42] W. Nojo, Y. Ishigaki, T. Takeda, T. Akutagawa, T. Suzuki, *Chem. – A Eur. J.* **2019**, *25*, 7759–7765.
[43] C. R. Bridges, A. M. Borys, V. A. Béland, J. R. Gaffen, T. Baumgartner, *Chem. Sci.* **2020**, *11*, 10483–10487.
[44] L. Ueberricke, B. Punja Benke, T. Kirschbaum, S. Hahn, F. Rominger, U. H. F. Bunz, M. Mastalerz, *Chem. – A Eur. J.* **2021**, *27*, 2043–2049.
[45] V. Bliksted Roug Pedersen, J. Granhøj, A. Erbs Hillers-Bendtsen, A. Kadziola, K. V. Mikkelsen, M. Brøndsted Nielsen, *Chem. – A Eur. J.* **2021**, *27*, 8315–8324.
[46] P. W. Antoni, C. Golz, M. M. Hansmann, *Angew. Chem. Int. Ed.* **2022**, *61*, e202203064.
[47] R. Kumar, P. J. Chmielewski, T. Lis, D. Volkmer, M. Stępień, *Angew. Chem. Int. Ed.* **2022**, *61*, e202207486.
[48] Y. Hayashi, S. Suzuki, T. Suzuki, Y. Ishigaki, *J. Am. Chem. Soc.* **2023**, *145*, 2596–2608.
[49] M. Hayakawa, N. Sunayama, S. I. Takagi, Y. Matsuo, A. Tamaki, S. Yamaguchi, S. Seki, A. Fukazawa, *Nat. Commun.* **2023**, *14*, 2741.
[50] Y. Ishigaki, T. Harimoto, K. Sugawara, T. Suzuki, *J. Am. Chem. Soc.* **2021**, *143*, 3306–3311.
[51] Y. Sakano, R. Katoono, K. Fujiwara, T. Suzuki, *Chem. Lett.* **2014**, *43*, 1143–1145.
[52] Y. Ishigaki, K. Sugawara, M. Yoshida, M. Kato, T. Suzuki, *Bull. Chem. Soc. Jpn.* **2019**, *92*, 1211–1217.

[53] T. Harimoto, T. Suzuki, Y. Ishigaki, *Chem. – A Eur. J.* **2023**, *29*, e202203899.
[54] S. Wang, J. Yuan, J. Xie, Z. Lu, L. Jiang, Y. Mu, Y. Huo, Y. Tsuchido, K. Zhu, *Angew. Chem. Int. Ed.* **2021**, *60*, 18443–18447.
[55] S. I. Etkind, T. M. Swager, *Synthesis (Stuttg).* **2022**, *54*, 4843–4863.
[56] M. Lin, L. Bian, Q. Chen, H. Xu, Z. Liu, K. Zhu, *Angew. Chem. Int. Ed.* **2023**, *62*, e202303035.
[57] M. Matsuoka, A. Iwamoto, T. Kitao, *J. Heterocycl. Chem.* **1991**, *28*, 1445–1447.
[58] M. J. Frisch, G. W. Trucks, H. B. Schlegel, G. E. Scuseria, M. A. Robb, J. R. Cheeseman, G. Scalmani, V. Barone, G. A. Petersson, X. Nakatsuji, H.; Li, M. Caricato, A. V. Marenich, J. Bloino, B. G. Janesko, R. Gomperts, B. Mennucci, H. P. Hratchian, J. V. Ortiz, A. F. Izmaylov, J. L. Sonnenberg, D. Williams-Young, F. Ding, F. Lipparini, F. Egidi, J. Goings, B. Peng, A. Petrone, T. Henderson, D. Ranasinghe, V. G. Zakrzewski, J. Gao, N. Rega, G. Zheng, W. Liang, M. Hada, M. Ehara, K. Toyota, R. Fukuda, J. Hasegawa, M. Ishida, T. Nakajima, Y. Honda, O. Kitao, H. Nakai, T. Vreven, K. Throssell, J. A. J. Montgomery, J. E. Peralta, F. Ogliaro, M. J. Bearpark, J. J. Heyd, E. N. Brothers, K. N. Kudin, V. N. Staroverov, T. A. Keith, R. Kobayashi, J. Normand, K. Raghavachari, A. P. Rendell, J. C. Burant, S. S. Iyengar, J. Tomasi, M. Cossi, J. M. Millam, M. Klene, C. Adamo, R. Cammi, J. W. Ochterski, R. L. Martin, K. Morokuma, O. Farkas, J. B. Foresman, D. J. Fox, *Gaussian 16, Revision B.01*, Gaussian, Inc., Wallingford CT, 2016, **n.d.**
[59] O. V. Dolomanov, L. J. Bourhis, R. J. Gildea, J. A. K. Howard, H. Puschmann, *J. Appl. Crystallogr.* **2009**, *42*, 339–341.
[60] G. M. Sheldrick, *Acta Crystallogr. Sect. A Found. Adv.* **2015**, *71*, 3–8.
[61] G. M. Sheldrick, *Acta Crystallogr. Sect. C Struct. Chem.* **2015**, *71*, 3–8.
[62] T. Harimoto, T. Tadokoro, S. Sugiyama, T. Suzuki, Y. Ishigaki, *Angew. Chem. Int. Ed.* **2023**, e202316753.

Acknowledgements

The research described in this dissertation was carried out under the guidance of Associate Professor Dr. Yusuke Ishigaki (Department of Chemistry, Faculty of Science, Hokkaido University). The author is grateful to Associate Professor Ishigaki for his consistent guidance, kind suggestions, valuable discussions, enthusiastic encouragement, and much help throughout the course of this work. It is the author's sincere pleasure to have been able to pursue this work with Associate Professor Ishigaki.

The author would like to express his sincere gratitude to Professor Dr. Takanori Suzuki (Department of Chemistry, Faculty of Science, Hokkaido University) for his helpful guidance, insightful comments, precious discussions, tremendous encouragement, and so much help throughout the course of this work. Professor Takanori Suzuki guided the author to the field of "Physical Organic Chemistry" and inspired the author to pursue a career in research.

The author deeply grateful to Assistant Professor Dr. Ryo Katoono (Department of Chemistry, Faculty of Science, Hokkaido University) for his perceptive point of view, precious comments, and so much help throughout the course of this work. Dr. Ryo Katoono shared with the author how to take a break when the author gets stuck in this work.

The author would like to be thankful to Assistant Professor Dr. Takuya Shimajiri (Department of Chemistry, Faculty of Science, Hokkaido University) for his helpful guidance, critical suggestion, valuable comments, and so much help throughout the course of this work. The author was always encouraged by Dr. Shimajiri's enthusiasm for his research.

The author would like to thank Professor Dr. Aiichiro Nagaki, Professor Dr. Takeshi Ohkuma, Professor Dr. Keiji Tanino and Professor Dr. Masaya Sawamura, for their valuable suggestions and discussions.

The author gives special thanks to Dr. Wataru Nojo, Mr. Keisuke Sugimoto, Dr. Kazuma Sugawara, Dr. Yuki Hayashi, Mr. Masataka Saito, Dr. Su-Gi Chong, Mr. Takuya Tachibana, Mr. Takumi Hashimoto, Mr. Takumi Tanioka, Mr. Kota Asai, Mr. Masaki Takata, and other members in Suzuki Laboratory for their valuable discussion and irreplaceable time.

The author is very grateful to Mr. Rikumaru Saito, Mr. Kojiro Machi, Mr. Kiyohisa Shimizu, Mr. Yoju Kato, Mr. Kaoru Hayashi, Mr. Yusuke Mizunoue, Mr. Yuki Shibata, Mr. Kanta Suzuki, Mr. Akira Niizato, Mr. Satoshi Hasegawa, Mr. Junki Ikeguchi, and other members in Kowa Clerk dormitory for their exciting times.

The author is grateful to members in Hokkaido Univ. Youth Hostel Club for sharing great times together.

The author is deeply indebted to Iwamoto sensei and other teachers in TOKO GAKUEN for teaching him how to approach things.

The author is in acknowledgement of Research Fellowship of the Japan Society for the Promotion of Science (JSPS) for Young Scientists for Financial Support and TOBE MAKI Scholarship Foundation.

Finally, the author would like to express his deep and sincere gratitude to his family, Kae Harimoto, Hiroshi Harimoto and Akina Harimoto, for their continuous financial help and encouragement.